Machine Learning-enhanced feasibility studies on the production of new particles with preferential couplings to third generation fermions at the LHC

Thesis submitted in partial fulfillment

of the requirements for the degree of

Doctor in Sciences - Physics

Presented by:
Cristian Fernando Rodríguez Cruz

Directed by:
Prof. Andrés Florez (advisor)
Universidad de los Andes

Prof. Joel Jones-Perez (co-advisor)
Pontificia Universidad Católica del Perú

Uniandes - High Energy Physics Research Group
Phenomenology of Particle Physics

Universidad de los Andes
Faculty of Sciences
Department of Physics
Bogotá D.C., Colombia
October 24, 2025. Pre-alpha version

Abstract

The Standard Model (SM) of particle physics is the most successful framework for describing the subatomic world. It is continuously tested in experiments worldwide, with the Large Hadron Collider (LHC) being the flagship project in this endeavor. One of the primary goals of the LHC is to precisely measure SM parameters and search for deviations that could signal new physics.

In recent years, reported anomalies, such as those in B-meson decays from LHCb, BaBar, and Belle experiments, along with the potential discrepancy in the muon's magnetic moment $(g-2)$ from Fermilab, suggest a violation of lepton flavor universality (LFU). These observations provide a compelling window into physics beyond the SM. Among the proposed SM extensions to explain LFU violation, many introduce new particles with preferential couplings to third and second-generation fermions. Popular candidates include heavy states such as Z' bosons, ϕ' scalars, and leptoquarks (LQs), among others.

This work presents two phenomenological studies proposing different strategies to probe new models, such as the 4321 [1], $U(1)_{T^3_R}$ [2], that extend the SM particle content to explain clues on LFU violation. The studies use benchmark scenarios in which the structure of the model and the couplings of the new particle fields determine preferential interactions with second- and third-generation SM fermions. The hypothetical signal and background samples are generated using Monte Carlo simulations, emulating the current running conditions of the LHC and the performance of the CMS detector. The expected sensitivity for the different signal models under study is obtained by performing a detailed analysis of the available (non-excluded) experimental phase-space, boosted by machine learning (ML) techniques to optimize the discovery potential for these exotic states.

Dedication

to be added

Acknowledgements

to be added

CONTENTS

INTRODUCTION

The pursuit of a fundamental description of nature's building blocks and their interactions is a central endeavor of modern physics. This quest has led to the development of the Standard Model (SM) of particle physics, a quantum field theory that encapsulates our current understanding of the subatomic world. With breathtaking precision, the SM describes the electromagnetic, weak, and strong nuclear forces, and classifies all known elementary particles. Its triumphs are undeniable, crowned by the landmark discovery of the Higgs boson at the Large Hadron Collider (LHC) in 2012, which confirmed the mechanism for generating the masses of elementary particles, and represented the final piece of the SM puzzle.

Yet, for all its success, the SM is universally acknowledged to be an incomplete theory. It offers no candidate for dark matter, does not explain the origin of small neutrino masses, cannot account for the matter–antimatter asymmetry in the universe, does not incorporate gravity, and leaves the mass of the Higgs boson itself unnaturally unstable under quantum corrections—a problem known as the hierarchy problem. These profound theoretical shortcomings provide a clear motivation for physics beyond the SM (BSM). However, the most compelling guide for this search has always come from experimental data itself.

The primary mission of the LHC is not only to consolidate the SM but to probe its boundaries and search for new physics. While no direct evidence of new particles has been found so far, a series of subtle but persistent discrepancies—termed "anomalies"—have emerged from experiments worldwide, suggesting a potential crack in the SM's foundation.

A particularly intriguing set of these anomalies points towards a violation of Lepton Flavor Universality (LFU). In the SM, the electroweak force couples with identical strength to the three charged leptons (electrons, muons, and taus), a fundamental principle known as LFU. The most significant and long-standing hints of LFU violation come from measurements of semileptonic B-meson decays. The ratios $R(D^{(*)}) = \mathcal{B}(B \to D^{(*)}\tau\nu_\tau)/\mathcal{B}(B \to D^{(*)}\ell\nu_\ell)$, where ℓ is a muon or electron, have been measured by the BaBar, Belle, and LHCb collaborations to consistently exceed the SM predictions by a combined significance of approximately 3σ–4σ. This deviation suggests that B mesons are more likely to decay to a final state containing a tau lepton than the SM allows, providing a compelling hint of new physics that couples preferentially to the third generation fermions. Furthermore, the longstanding discrepancy in the muon's anomalous magnetic moment $(g-2)$, recently confirmed with increased precision by the Fermilab experiment, adds another layer of intrigue, as it also hints at new physics potentially coupled preferentially to the second generation[1].

While each anomaly individually requires careful scrutiny, their collective persistence has generated significant excitement, as they seem to point towards new physics that breaks lepton flavor universality, potentially involving enhanced couplings to heavier fermions.

The pattern of these LFU-violating anomalies has inspired a vast landscape of theoretical models extending the SM. A common thread among the most promising explanations is the introduction of new heavy particles that mediate interactions with non-universal couplings to the different generations of fermions. This generational hierarchy is crucial to evade tight constraints from precision measurements on electrons (first generation) while affecting processes involving muons and taus.

In this thesis, we contextualize and present two of our phenomenological studies that propose different strategies to probe new physics models, such as the 4321 [1] and $U(1)_{T^3_R}$ [2] models, which extend the SM particle content to explain the hints of LFU violation. These models introduce new particles with preferential couplings to second and third-generation fermions, making them prime candidates for explaining the experimental anomalies.

The experimental challenge lies in probing these models at the LHC. The proposed new particles are often heavy, leading to low production rates, and their decay signatures are complex and overwhelmed by enormous backgrounds from SM processes. Given the immense number of theoretical possibilities and the finite resources available to experimental collaborations, it is impossible to pursue every potential signature with equal vigor. This is where **phenomenological feasibility studies** becomes critical. They provide a vital bridge between theory and experiment by performing a detailed *a priori* assessment of the discovery potential for a given signal model. By using Monte Carlo simulations to emulate the detector response and analysis chain, these studies can identify the most promising signatures, optimize event selection criteria, and estimate the sensitivity achievable with the available data. This process is essential for prioritizing the experimental program, justifying the dedication of significant computing and human resources to a particular search, and ultimately guiding the LHC experiments towards the most well-motivated and detectable signals of new physics.

This thesis contributes to this effort by presenting two dedicated phenomenological studies that propose and develop novel strategies to probe signatures typical of the 4321 and $U(1)_{T^3_R}$ models at the LHC. The work is situated at the intersection of theoretical model-building and experimental high-energy physics, with the explicit goal of assessing the feasibility of these searches.

[1] Recent theoretical updates of the Standard Model prediction for the muon anomalous magnetic moment, including improved lattice-QCD results for the hadronic vacuum polarization, indicate that the discrepancy with experiment appears less significant; see [**arXiv:2505.21476**].

The core methodology of this research involves:

1. Defining **benchmark scenarios** within each model, selecting specific mass points and coupling structures that explain the LFU anomalies while remaining experimentally viable.

2. Using **Monte Carlo simulation** to accurately generate the hypothetical signal processes alongside the dominant SM background processes, emulating the run conditions of the LHC and the performance of the CMS detector.

3. Performing a detailed analysis of the available experimental phase-space. Given the high-dimensionality of the final states (e.g., involving multiple jets, leptons, and missing energy) and the complex, overlapping kinematical distributions of signal and background, traditional "cut-and-count" analyses are often sub-optimal. To overcome this, we employ advanced **Machine Learning (ML) techniques**, specifically supervised learning algorithms such as Boosted Decision Trees (BDTs) or Deep Neural Networks (DNNs). These algorithms are trained to learn the complex, non-linear correlations between many kinematic variables (e.g., invariant masses, angular separations, transverse momenta) to construct powerful discriminators that optimally separate the rare signal events from the large and diverse SM backgrounds. This ML-enhanced approach significantly boosts the analysis sensitivity, allowing for the detection of weaker signals or the setting of more stringent limits than would otherwise be possible.

4. Deriving the **expected sensitivity** for each model, establishing the exclusion limits or discovery potential that the LHC experiments could achieve with the current dataset. This final step is the ultimate quantitative measure of the search's feasibility.

The structure of this thesis is as follows. We begin by establishing the theoretical foundation with a review of the SM in Chapter 1. Then, Chapter 2 details the experimental context, describing the LHC and the CMS detector, and introduces the general analysis techniques employed, including a discussion on the application of Machine Learning in high-energy physics. The original phenomenological work of this thesis is presented in the subsequent chapters: Chapter 3 details a search for new physics in the process $pp \to t\bar{t}\mu^+\mu^-$, while Chapter 4 presents a search for vector leptoquarks in the process $pp \to \tau^+\tau^- + b$-jets. Finally, Chapter **??** concludes by summarizing our findings and discussing their implications for the field, along with an outlook on future prospects.

1

STANDARD MODEL OF PARTICLE PHYSICS

The Standard Model (SM) of particle physics is a quantum field theory (QFT) that describes matter as fermionic particles and their fundamental interactions. The forces are incorporated through the gauge principle, where force-carrying particles—vector bosons with spin one, arising from the adjoint representation of symmetry groups (*gauge groups*)—mediate the interactions between matter particles [3, 4]. However, this elegant formulation is not sufficient to account for particle masses. These are generated through Yukawa interactions, which are scalar-fermion couplings between the Higgs field and the fermion fields. While the Yukawa interactions themselves are not gauge interactions, their allowed structure—specifically, which fermions they can couple and their transformation properties—is strictly dictated by the gauge symmetry of the theory. This combined framework of gauge and Yukawa sectors successfully describes three of the four fundamental forces in nature.

In this chapter, we contextualize the SM by introducing the basic concepts of quantum field theory, including the notion of fields and symmetries. We then present the particle content of the SM, its gauge group, and the Lagrangian density that describes its dynamics. The Higgs mechanism and its role in providing mass to the weak gauge bosons and fermions are also discussed. Finally, we address the main deficiencies of the SM and review the experimental evidence that motivates the search for physics beyond the SM.

1.1 FIELDS

Relativistic quantum fields are degrees of freedom in QFT. Formally, they are *operator-valued functions on spacetime that transform under a representation of the Lorentz group on an invariant subspace* [5]. The different representations of the Lorentz group are mainly characterized by their spin, and their fields obey a different equation of motion (see table 1.1).

In classical field theory, a variational principle is established which generates the equations that govern the dynamics of the different fields in a theory, *the equations of motion*. Hamilton's principle, or principle of minimal action, indicates that all possible physical configurations for a set of fields φ^I, with $I = 1, 2, 3, \cdots, n$, are those for which the action S is minimal [6, 7]:

$$S = \int \mathcal{L}(\varphi^I, \partial_\mu \varphi^I) d^4x. \tag{1.1}$$

Here, $d^4x = dx^0 dx^1 dx^2 dx^3$ and $x \equiv (ct, x^1, x^2, x^3) \equiv (x^0, x^1, x^2, x^3) \in \mathcal{M}^4$, are the space-time coordinates in the Minkowskian spacetime ($\mathcal{M}^4$), and the function $\mathcal{L}(\varphi^I, \partial_\mu \varphi^I)$ is called *the Lagrangian density* of a theory [3, 6]. The problem in classical field dynamics is to find the functions $\varphi^I(x)$ in a space-time $\mathcal{M}^4$, fixing their boundary conditions. The solution to this classical problem is given by the Euler-Lagrange equations:

$$\frac{\partial \mathcal{L}}{\partial \varphi^I} - \frac{\partial}{\partial x^\mu} \frac{\partial \mathcal{L}}{\partial\left(\partial_\mu \varphi^I\right)} = 0, \tag{1.2}$$

and they are used to obtain the equations of motion of the set of fields φ^I [7].

While in classical field theory the Euler–Lagrange equations directly determines the dynamics of the system, in QFT the approach changes: if we adopt the path-integral formulation [8, 9], the idea of an equation of motion vanishes and we move on to searching for correlations between free particle states. However, the notion of action remains the cornerstone in the description of these observables.

Explicitly, the correlation functions are calculated through the Lehmann-Symanzik-Zimmermann (LSZ) reduction formula, which connects these correlators with physical scattering amplitudes. These are computed from the path integral [10, 11]:

$$\begin{aligned} Z[J] &= \langle \text{ out}, 0|0, \text{ in } \rangle \\ &= \mathcal{N} \int \mathcal{D}(\varphi, \bar{\varphi}) e^{iS[\varphi]} e^{i\int J_I \varphi^I d^4x} \\ &= \mathcal{N} \int \mathcal{D}(\varphi, \bar{\varphi}) e^{i\int d^4x \mathcal{L}} e^{i\int J_I \varphi^I d^4x}, \end{aligned} \tag{1.3}$$

taken over the space of fields φ with an appropriate measure $\mathcal{D}(\varphi, \bar{\varphi})$ and normalized by $\mathcal{N}$. The quantity Z is known as the partition function of the theory and gives the transition amplitude from the initial vacuum $|0, \text{ in}\rangle$ to the final vacuum $|0, \text{ out}\rangle$ in the presence of a source $J(x)$ producing particles [12].

Name	Field	Spin	Free-Lagrangian
Klein-Gordon	ϕ	0	$\mathcal{L} = \frac{1}{2}\left(\partial^\mu \phi \partial_\mu \phi - m^2 \phi \phi\right)$
Dirac	χ	1/2	$\mathcal{L} = \bar{\chi}\left(i\boldsymbol{\gamma}^\mu \partial_\mu - m\mathbf{1}\right)\chi$
Proca (Massive Vector)	A^μ	1	$\mathcal{L} = -\frac{1}{4} F^{\mu\nu} F_{\mu\nu} + \frac{1}{2} m^2 A^\mu A_\mu$

Table 1.1: Some relevant representations of the Lorentz group in 4-dimensional space-time. In this notation $\eta_{\mu\nu} = \text{diag}(1, -1, -1, -1)$, $\boldsymbol{\gamma}^\mu$ are the Dirac matrices, $F_{\mu\nu} = \partial_\mu A_\nu - \partial_\nu A_\mu$ is the abelian field strength tensor. All equations are written in natural units with $c = \hbar = 1$. Fields are shown in their standard representations.

Therefore, the dynamics, at both the classical and quantum levels, are entirely determined by the Lagrangian density. For free fields (i.e., non-interacting), the Lagrangian is quadratic in the fields and the path integral can be evaluated exactly. Tab. 1.1 records the Lagrangian density for these free fields. However, to describe physics, we must include interactions, which render the path integral impossible to compute exactly.

The framework of *perturbation theory* addresses this by expanding the interaction part of the Lagrangian as a power series. This expansion is organized using *Feynman diagrams*, which provides a pictorial representation of each term, and a set of *Feynman rules*, which provides a precise dictionary to translate these diagrams into mathematical expressions for scattering amplitudes [9, 11]. The importance of these rules cannot be overstated, as they are the practical computational tools of perturbative QFT.

In this paradigm, our task is to propose a Lagrangian density for a set of fields that correctly models the propagation and interactions of fundamental particles. The free part defines the particle content and propagators, while the interaction part defines the vertices and possible scattering processes.

1.1.1 INTERACTIONS AND SYMMETRIES

The structure of the Lagrangian density in a quantum field theory is not arbitrary; it is constrained by fundamental principles that ensure the theory is physically consistent and mathematically well-defined. These principles act as "rules" that guide the construction of viable theories. In what follows, we systematically develop these constraints, starting from the practical requirements of perturbation theory and building up to the fundamental symmetry principles.

To perform calculations, we typically split the Lagrangian into a free part, which describes non-interacting fields, and an interaction part:

$$\mathcal{L} = \mathcal{L}_0 + \mathcal{L}_{\text{int}}. \tag{1.4}$$

This splitting is the starting point for perturbation theory. In the path integral formulation, the generating functional $Z[J]$ can then be expressed as an operator acting on the free functional $Z_0[J]$:

$$Z[J] = \mathcal{N} \exp\left[i \int d^4x \, \mathcal{L}_{\text{int}} \left(-i \frac{\delta}{\delta J(x)}\right)\right] Z_0[J]. \tag{1.5}$$

The exponential operator generates an infinite series known as the perturbation series. The n-point correlation function is found by taking functional derivatives of $Z[J]$ with respect to the sources $J(x_i)$ and setting $J = 0$. Each term in this series is represented by a **Feynman diagram**, whose components are:

- **External Lines:** Represent incoming and outgoing physical particles.
- **Internal Lines:** Represent virtual particles propagating between interactions, corresponding to the free-field propagators derived from $\mathcal{L}_0$.

- **Vertices:** Represent interactions, derived from the terms in $\mathcal{L}_{\text{int}}$. Each vertex has an associated coupling constant and enforces momentum conservation.

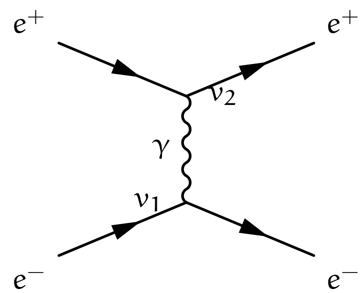

Figure 1.1: Example of a Feynman diagram for $e^+e^- \to e^+e^-$ scattering. **External lines** (solid arrows at the edges) represent the incoming and outgoing electrons and positrons. The **internal line** (wavy line) represents the virtual photon propagator. The **vertices** (v_1 and v_2) represent the electromagnetic interaction points where the coupling constant e (electric charge) enters and momentum is conserved.

For this perturbation series to be a predictive computational tool, it must yield finite physical results. However, individual terms in the series (i.e., individual Feynman diagrams) often lead to divergent integrals when loop corrections are included. The key is that in a *renormalizable* theory, these divergences from all diagrams can be systematically absorbed into a finite number of parameters (like masses and coupling constants) through a redefinition procedure known as renormalization. It is important to note that while individual Feynman diagrams may diverge, the requirement is that the combination of all contributions at a given order yields finite, physically meaningful results after renormalization.

This requirement of renormalizability imposes a powerful constraint on the form of $\mathcal{L}_{\text{int}}$. Through power-counting arguments, one finds that only operators of mass dimension $\leqslant 4$ lead to renormalizable interactions. In natural units, where $\mathcal{L}$ has dimension $[\text{mass}]^4$, this means that $\mathcal{L}_{\text{int}}$ can be expressed as a truncated polynomial containing only terms up to dimension 4. Specifically, this allows Yukawa couplings (dim 4), quartic scalar interactions (dim 4), and gauge interactions (dim 4), while forbidding non-renormalizable operators like ϕ^6 (dim 6). Higher-dimensional operators are still allowed in effective field theories, but they correspond to interactions that are suppressed at low energies and signal the presence of new physics at higher scales [9, 11].

This is why we express $\mathcal{L}_{\text{int}}$ as a truncated polynomial: renormalizability demands that we include only a finite set of operators with dimension $\leqslant 4$, ensuring that the theory remains predictive at all accessible energy scales.

An additional crucial requirement is the *stability of the vacuum*. For a theory to be physically meaningful, it must possess a stable ground state. This is ensured by demanding that the scalar potential, which governs the self-interactions of scalar fields, is bounded from below. If the potential were unbounded, the system could lower its energy indefinitely by evolving toward field configurations of ever-greater magnitude, meaning no stable vacuum would exist.

For a renormalizable theory, the scalar potential can contain at most quartic terms. The stability condition requires that the quartic couplings satisfy certain positivity constraints to ensure that the potential raises with the scalar fields in any direction in field space. This is why the scalar potential is a polynomial of at most order four: renormalizability forbids higher-order terms, and stability demands that the quartic terms dominate at large field values with the correct sign.

It is important to note that this condition must hold not just at tree level but also at the quantum level, as running couplings can change sign at different energy scales, potentially leading to metastability or instability of the vacuum.

A fundamental requirement from quantum mechanics is *Hermiticity*: the Lagrangian density must be Hermitian to ensure that observables are real and the time evolution of the theory is unitary [11, 13]. This is the most basic constraint that quantum theory imposes on the Lagrangian. Without Hermiticity, the theory would predict complex-valued probabilities and violate the fundamental probabilistic interpretation of quantum mechanics.

Beyond the quantum mechanical requirement of Hermiticity, special relativity imposes a fundamental constraint: *Poincaré invariance*. This symmetry demands that the equations of motion remain the same in all inertial frames. Mathematically, this is implemented by requiring the action to be globally invariant under Poincaré transformations [13]. Equivalently, the Lagrangian density must transform as a Lorentz scalar and may change under translations at most by a total derivative [7].

In QFT, Poincaré invariance is assumed to be global. Promoting it to a local symmetry leads to gravity, with spin-2 fields (the graviton) as mediators. Perturbatively, such a theory is not renormalizable, so it lacks predictivity at high energies, although it can still be understood as an effective field theory.

This constraint is extremely powerful: it eliminates all possible interaction terms that would depend on the choice of reference frame. For instance, terms that explicitly depend on spacetime coordinates or preferred directions are forbidden. Furthermore, *dimensional analysis* places additional restrictions. In natural units, $\mathcal{L}$ carries dimensions of mass to the fourth power ($[\mathcal{L}] = [\text{mass}]^4$), which corresponds to an energy density. Combined with Lorentz invariance, this means that the interaction terms must be constructed from Lorentz-covariant combinations of fields and their derivatives, with the correct overall mass dimension.

The symmetries discussed so far—Poincaré invariance, Hermiticity, and dimensional analysis—are universal requirements that any relativistic quantum field theory must satisfy. However, they still leave a vast array of possible interaction terms. To further constrain the Lagrangian and to describe the fundamental forces of nature, we must consider *internal symmetries*: transformations that act on the fields' internal degrees of freedom rather than on spacetime coordinates.

Internal symmetries can be either *global* (where the transformation parameters are constant throughout spacetime) or *local* (gauge symmetries, where the parameters can vary from point to point). The procedure for constructing gauge theories—where global symmetries are "promoted" to local ones by introducing gauge fields—is systematic and will be described in detail below. This gauge principle has proven to be the most powerful organizing principle in particle physics, determining not only which interactions are realized in nature but also their precise mathematical structure.

A classical symmetry of the Lagrangian may not always survive the process of quantization. If it fails to do so, it is said to be anomalous. *Chiral anomalies*, specifically, arise from the regularization of fermion loops in triangle diagrams and can break gauge symmetries at the quantum level. Since gauge symmetry is the very principle that dictates the form of interactions and removes unphysical states, its violation would destroy the renormalizability and unitarity of the theory. Therefore, the particle content must be carefully chosen so that these potential anomalies cancel among fermions, a non-trivial condition famously satisfied by the quarks and leptons of the Standard Model [9, 11, 14].

In summary, the construction of a consistent relativistic quantum field theory proceeds through a hierarchy of constraints:

1. **Perturbative renormalizability:** power-counting arguments restrict operators to mass dimension $\leqslant 4$, ensuring $\mathcal{L}_{\text{int}}$ is a truncated polynomial.

2. **Vacuum stability:** the scalar potential must be bounded from below, requiring appropriate positivity conditions on quartic couplings.

3. **Hermiticity:** quantum mechanics demands $\mathcal{L}$ be Hermitian for real observables and unitary evolution.

4. **Poincaré invariance:** special relativity requires the action to be invariant under Lorentz transformations and translations, eliminating frame-dependent terms.

5. **Internal symmetries:** global and gauge symmetries further constrain the form of interactions and determine the structure of fundamental forces.

6. **Anomaly cancellation:** the particle content must be chosen such that chiral anomalies cancel, preserving gauge symmetry at the quantum level.

These constraints drastically reduce the number of possible terms in the Lagrangian. The renormalizable interaction structures that survive are limited to: Yukawa couplings between fermions and scalars, quartic scalar self-interactions, and gauge interactions between matter/scalar fields and vector bosons. The precise form of these interactions is then determined by the internal (gauge) symmetries of the theory, which we now describe in detail.

Gauge theories

The procedure is systematic: first, the spin-0 and spin$-1/2$ fields are organized into representations of a unitary (gauge) group G, such that the Lagrangian density is globally invariant under G. This global symmetry is then "promoted" to a *local symmetry* (where the group parameters can vary in spacetime) by replacing the ordinary derivatives ∂_μ with *covariant derivatives* $\mathcal{D}_\mu$ that incorporate new *gauge fields* B_μ^A [4, 15–18]. This "promotion" is described in more detail below.

Given a Lagrangian density $\mathcal{L}(\varphi^I, \partial_\mu \varphi^I)$, where I is an index enumerating the different fields φ^I in the model, it is said to be *globally symmetric* under unitary transformations if the action remains invariant under field variations. At infinitesimal level, these variations are given by:

$$\delta_G \varphi^I = i\theta^A (T_A)^I_J \varphi^J, \tag{1.6}$$

where θ^A are constant parameters of the transformation and the T_A are the generators of the group G in the appropriate representation. The corresponding finite unitary transformation is

$$\mathcal{U}_G \equiv U(\theta) = \exp\bigl(i\theta^A T_A\bigr). \tag{1.7}$$

Note that the T_A generators satisfy the same Lie algebra of the group G:

$$[T_A, T_B] = i f_{AB}^{\;C} T_C, \tag{1.8}$$

where $f_{AB}^{\;C}$ are the structure constants of G.

To promote the global symmetry to a local one ($\theta^A \to \theta^A(x)$), the ordinary derivative ∂_μ is replaced by a *covariant derivative* $\mathcal{D}_\mu$. This new derivative is designed to transform covariantly under the gauge group, meaning $\mathcal{D}_\mu \varphi \to U(x)(\mathcal{D}_\mu \varphi)$, so that the kinetic terms $\mathcal{L}_{kin} \sim (\mathcal{D}_\mu \varphi)^\dagger (\mathcal{D}^\mu \varphi)$ remain invariant. This is achieved by introducing a gauge field B_μ^A for each generator T_A and defining:

$$\mathcal{D}_\mu = \partial_\mu - igB_\mu^A T_A, \tag{1.9}$$

where g is the gauge coupling constant. The transformation law for the gauge fields that ensures the covariant transformation of $\mathcal{D}_\mu$ is:

$$\delta B_\mu^A = \frac{1}{g}\partial_\mu \theta^A + f_{BC}{}^A \theta^B B_\mu^C. \tag{1.10}$$

The introduction of the gauge fields B_μ^A requires the addition of a kinetic term for them to the Lagrangian. This is constructed from the *field strength tensor* $F_{\mu\nu}^A$, defined as the curvature of the covariant derivative:

$$F_{\mu\nu}^A T_A = -\frac{i}{g}[\mathcal{D}_\mu, \mathcal{D}_\nu] = \partial_\mu B_\nu^A - \partial_\nu B_\mu^A + g f_{BC}{}^A B_\mu^B B_\nu^C. \tag{1.11}$$

The gauge-invariant kinetic Lagrangian is then:

$$\mathcal{L}_{gauge} = -\frac{1}{4}\delta_{AB} F_{\mu\nu}^A F^{\mu\nu B}. \tag{1.12}$$

A general, archetypal Lagrangian, embodying these structures, can be written as:

$$\mathcal{L} = -\frac{1}{4}F^A_{\mu\nu}F^{A\mu\nu} + i\bar{\psi}^i\gamma^\mu\mathcal{D}_\mu\psi^i + \left(\bar{\psi}^j_L\,\Gamma^j_k\,\Phi\,\psi^k_R + \text{h.c.}\right) + |\mathcal{D}_\mu\Phi|^2 - V(\Phi) \tag{1.13}$$

The terms correspond to: the kinetic term for gauge fields ($F^A_{\mu\nu}$), the kinetic term for fermions ψ^i, the Yukawa interactions between left- and right-handed fermions and scalars (Γ^j_k is a Yukawa coupling matrix and Φ is a scalar field), the kinetic term for scalars, and the scalar potential $V(\Phi)$. For a renormalizable and stable theory $V(\Phi) = \mu^2|\Phi|^2 + \lambda|\Phi|^4$ with $\lambda > 0$.

Note the absence of explicit mass terms for the gauge fields ($\sim M^2 B_\mu B^\mu$) and fermions ($\sim m\bar{\psi}\psi$). These are forbidden by gauge invariance and for chiral fermions. Mass terms can be generated via spontaneous symmetry breaking, as discussed below.

It is important to emphasize that while the Yukawa interactions do not involve gauge bosons directly, their structure is nonetheless *completely determined by the gauge symmetry*. Specifically, gauge invariance dictates which fermion fields can couple to which scalar fields, and constrains the form of the coupling matrix Γ^j_k. For a Yukawa term to be gauge-invariant, the product $\bar{\psi}^j_L\,\Phi\,\psi^k_R$ must be a singlet under the gauge group. This requirement arises because the left-handed and right-handed fermions typically transform in different representations of the gauge group, and the scalar field Φ must carry the appropriate quantum numbers to make the overall combination invariant. In the Standard Model, for instance, the left-handed fermions are $SU(2)_L$ doublets while the right-handed fermions are singlets, and the Higgs doublet provides the necessary quantum numbers to form gauge-invariant Yukawa couplings. Thus, even though Yukawa interactions are scalar-mediated rather than gauge-mediated, the gauge principle is the fundamental organizing principle that determines their allowed structure.

Example

Note that for this vector-like $U(1)$ theory, the explicit fermion mass term $m\bar{\psi}\psi$ is gauge-invariant. This will not be the case for chiral gauge theories like the Standard Model.

To illustrate these concepts, let us consider a renormalizable theory with a real scalar ϕ and a Dirac spinor ψ, and suppose that this theory is globally invariant under $U(1)$ phase transformations, i.e. the fields $\varphi \in \{\phi, \psi\}$ transform as $\varphi \mapsto e^{i\theta\hat{Q}}\varphi$ such that $\hat{Q}\psi = q\psi$ and $\hat{Q}\phi = 0$. The free Lagrangian density is

$$\mathcal{L}_{\text{free}} = \frac{1}{2}\partial^\mu\phi\partial_\mu\phi - \frac{1}{2}\mu^2\phi^2 + \bar{\psi}(i\gamma_\mu\partial^\mu - m)\psi. \tag{1.14}$$

To add globally symmetric interaction terms, we must consider operators of mass dimension $\leqslant 4$. The most general renormalizable Lagrangian, invariant under the global $U(1)$ symmetry, is

$$\mathcal{L}_{\text{global-int}} = k_1\,\phi\bar{\psi}\psi - \underbrace{\left(\frac{\alpha}{3!}\phi^3 + \frac{\lambda}{4!}\phi^4\right)}_{V(\phi)-\frac{1}{2}\mu^2\phi^2} \tag{1.15}$$

Here, $V(\phi)$ is the scalar potential containing both the mass term ($\mu^2\phi^2$, which is part of the free theory) and the self-interaction terms (ϕ^3 and ϕ^4, which are genuine interactions). All terms in $V(\phi)$ are allowed because ϕ is a real scalar field and thus a $U(1)$ singlet (charge 0). However, For stability of the potential, we require $\lambda > 0$. With $\mu^2 > 0$ as shown, the vacuum is unique at $\langle\phi\rangle = 0$. The sign of μ^2 will become crucial for spontaneous symmetry breaking in the Higgs mechanism. Finally, the Yukawa coupling $k_1\phi\bar{\psi}\psi$ is also gauge-invariant since the charges of $\bar{\psi}$, ϕ, and ψ sum to zero ($-q + 0 + q = 0$).

Promoting the global symmetry to a local one ($\theta \to \theta(x)$) requires introducing a gauge field A_μ and replacing ordinary derivatives with covariant derivatives:

$$\mathcal{D}_\mu\varphi = (\partial_\mu - igA_\mu\hat{Q})\varphi \quad \Longrightarrow \quad \begin{cases} \mathcal{D}_\mu\phi = \partial_\mu\phi, & (\text{since } \hat{Q}\phi = 0) \\ \mathcal{D}_\mu\psi = (\partial_\mu - igqA_\mu)\psi. \end{cases} \tag{1.16}$$

The field strength tensor for the abelian $U(1)$ field is defined as $F_{\mu\nu} = \partial_\mu A_\nu - \partial_\nu A_\mu$. The locally invariant Lagrangian is then:

$$\mathcal{L}_{\text{local}} = \frac{1}{2}\partial^\mu\phi\partial_\mu\phi - V(\phi) + \bar{\psi}i\gamma_\mu\mathcal{D}^\mu\psi - m\bar{\psi}\psi + k_1\phi\bar{\psi}\psi - \frac{1}{4}F_{\mu\nu}F^{\mu\nu}. \tag{1.17}$$

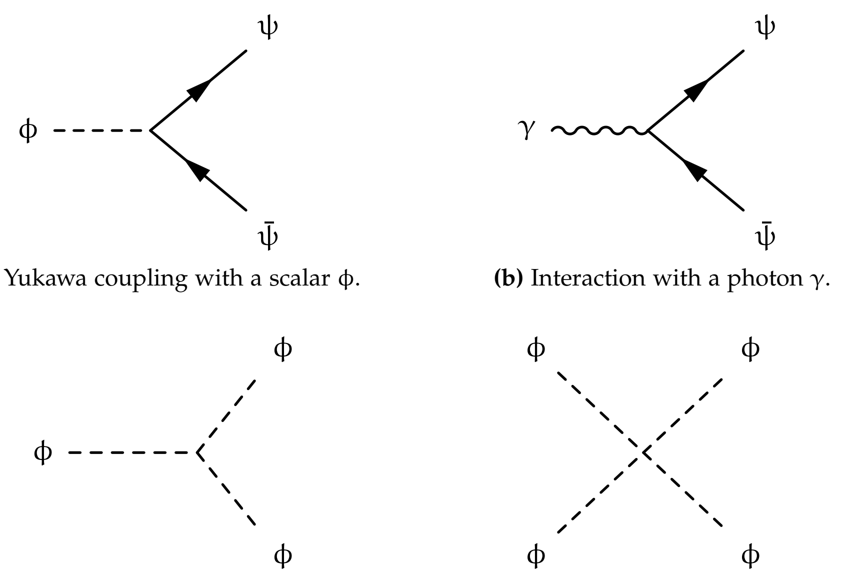

(a) Yukawa coupling with a scalar ϕ.

(b) Interaction with a photon γ.

(c) Triple scalar coupling.

(d) Quartic scalar coupling.

Figure 1.2: Feynman diagrams for Yukawa coupling, gauge boson coupling and quartic scalar coupling.

The interaction terms in this Lagrangian give rise to distinct vertices in Feynman diagrams. Figure 1.2a illustrates the Yukawa coupling $k_1\phi\bar{\psi}\psi$, which allows the scalar field to mediate fermion interactions. Figure 1.2b shows the gauge interaction arising from the covariant derivative term $\bar{\psi}i\gamma_\mu\mathcal{D}^\mu\psi$, where the photon couples to the charged fermion with strength

gq. Finally, Figures 1.2c and 1.2d depict the cubic ($\alpha\phi^3$) and quartic ($\lambda\phi^4$) scalar self-interactions from the potential $V(\phi)$, which are essential for the theory's renormalizability and vacuum stability.

With these ingredients and principles, we are now equipped to understand the structure of the SM Lagrangian, which will be discussed in the next section.

1.2 STANDARD MODEL

Fragment extracted and adapted from [19]

In 1965, Tomonaga, Feynman, and Schwinger were awarded the Nobel Prize for their independent formulation of Quantum Electrodynamics (QED) [20]. Their work established renormalization as a consistent method to separate infinities from finite, physically meaningful results in quantum field theory. QED provided predictions, such as the anomalous magnetic moment of the electron, that later experiments confirmed with remarkable precision [21, 22]. It became the prototypical example of a successful quantum field theory.

This success, however, did not extend to other fundamental interactions. The weak interaction was described by the chiral $V-A$ model, in which processes such as the beta decay were represented by four-fermion contact terms. This framework was not renormalizable: divergences could not be absorbed into a finite set of parameters, restricting its validity to low energies. A fundamental description within the quantum field theory framework was still missing.

The issue was linked to the short-range character of the weak and strong forces. In quantum field theory, the range of an interaction depends on the mass of its mediating boson. A massless boson, such as the photon, generates a long-range force with an inverse-square dependence. A massive boson, in contrast, produces a Yukawa potential of the form $\exp(-mr)/r$, which falls off rapidly with distance. Therefore, a consistent theory for weak interactions required massive gauge bosons.

Here lay the apparent obstacle. A mass term for a gauge boson, such as $m_A^2 A_\mu A^\mu$ in the Lagrangian, explicitly breaks gauge invariance, since it is not preserved under the transformation $A_\mu \mapsto A_\mu + \partial_\mu \epsilon$. This seemed to rule out gauge theories as candidates for describing short-range forces. The problem was recognized early on. For instance, in a 1954 seminar where Chen Ning Yang introduced non-Abelian gauge theories, Wolfgang Pauli objected that assigning masses to the gauge bosons would violate gauge invariance, and without such masses the theory could not describe nuclear forces. This skepticism reflected a widely shared view: gauge symmetry appeared incompatible with short-range interactions.

The resolution of this problem came from two developments that allowed gauge bosons to behave as if they had mass, without explicitly breaking gauge symmetry:

1. The Higgs mechanism. In this framework, a scalar field permeates the vacuum. While the underlying Lagrangian remains gauge invariant, the vacuum state does not respect this symmetry. Gauge bosons interacting with this vacuum acquire mass in a renormalizable way. This mechanism explains the masses of the W and Z bosons.

2. Dynamical mass generation in non-Abelian gauge theories. In Quantum Chromodynamics (QCD), gluons and nearly massless quarks are confined into hadrons with substantial masses. The appearance of a mass gap is a nonperturbative consequence of confinement. Understanding this mechanism in a rigorous way is at the core of the Yang–Mills existence and mass gap Millennium Prize problem.......AF: Considero que esto debe extenderse un poco, Por ejemlo, se podría mencionar que la mayor parte de la "masa" proviene entonces de interaccione , es lo que usted dice, pero de manera muy técnica para mi gusto. Por otro lado, introduce "Yang–Mills existence", pero en nigún momento explica que esto en escencia se asocia con la inotroducción de simetrías no-abelinas en el lagrangiano del SM para incorporar terminos de auto-interacción de bosones gauge. En general, para mi es importante que el documento se lo más claro y autocontendo a nivel conceptual, dentro de lo que es razoble. Por favor incluya por lo menos una referencia en esta parte.

The SM incorporates both solutions. Electroweak theory relies on the Higgs mechanism (1), which provides a renormalizable description of the weak interaction. For the strong interaction, QCD employs dynamical mass generation (2), where most of the mass of hadrons arises from confinement rather than from the small quark masses introduced by the Higgs field.

1.2.1 PARTICLE CONTENT AND GAUGE GROUP

First, let us talk about the chiral nature of particles: massive half-spin particles are described at the fundamental level by a Dirac spinorial field, see table 1.1. However, Dirac spinors do not transform under an irreducible representation of the Lorentz group. Spinors can be decomposed into two components that do transform under irreducible representations of the Lorentz group: two *Weyl spinors*. The left and right chiral projectors, P_L and P_R, take a Dirac spinor and project it onto each of these invariant subspaces. For a massless Dirac spinor, the left and right components are dynamically decoupled, *i.e.* are independent fields obeying independent Lagrangian densities. For example, the left component of a massless spinor has the Lagrangian $\mathcal{L} = -i\bar{\psi}\not{\partial}P_L\psi$ (for more details see Appendix A at [23]).

The discovery of parity asymmetry in radioactive decays [24] indicates that the chiral description of weak interactions couples differently to the left and right chiral components of half-spin particles. Indeed, the chirality of the fermionic spectrum is possibly one of the deepest properties of the Standard Model. Describing particles in terms of Dirac spinors, it means that left- and right-chirality components actually have different EW quantum numbers. This is compatible with a gauge symmetry only if half-spin particles are considered to be massless, at least without a Dirac mass $m\overline{f_R}f_L +$ h.c. Nevertheless, half-integer spin fundamental particles, such as the electron, have a well-measured mass. Therefore, the reconciliation of chiral asymmetry and mass lies in the Higgs mechanism, where the masses of the particles result from an effective Yukawa coupling with a scalar, the Higgs boson.

With this in mind, the SM has a content of matter fields from three generations (or families) of quarks q and leptons ℓ, described as Weyl 2-component spinors, with the structure

$$q_L = \begin{pmatrix} u_L^i \\ d_L^i \end{pmatrix}, u_R^i, d_R^i, \quad \ell_L = \begin{pmatrix} \nu_L^i \\ e_L^i \end{pmatrix}, e_R^i; \quad i = 1, 2, 3. \tag{1.18}$$

All these particles transform under a $U(1)$ group with different associated (hyper) charges. The doublets formed by the left components of the fields transform under the representation of two components of a $SU(2)$ group. The right components do not transform under $SU(2)$, therefore they are singlets. In addition, each quark in q_L transforms as color triplets under $SU(3)$, while u_R, d_R transforms as conjugate triplets. In the case of leptons, they are considered colored singlets estates. The gauge quantum numbers of the SM fermions are summarized in table 1.2.

Field	$SU(3)_C$	$SU(2)_L$	$U(1)_Y$	$U(1)_{EM}$
$q_L^i = (u^i, d^i)_L$	$\mathbf{3}$	$\mathbf{2}$	$+1/3$	$(2/3, -1/3)$
u_R^i	$\bar{\mathbf{3}}$	$\mathbf{1}$	$+4/3$	$+2/3$
d_R^i	$\bar{\mathbf{3}}$	$\mathbf{1}$	$-2/3$	$-1/3$
$\ell_L^i = (\nu^i, e^i)_L$	$\mathbf{1}$	$\mathbf{2}$	-1	$(0, -1)$
e_R^i	$\mathbf{1}$	$\mathbf{1}$	-2	-1
$H = (H^+, H^0)$	$\mathbf{1}$	$\mathbf{2}$	$+1$	$(+1, 0)$

Table 1.2: Gauge quantum numbers of Standard Model quarks, leptons and the Higgs scalar.

Then, with these symmetry groups in mind, we consider the SM as a quantum field theory based on a gauge group

$$G_{SM} = SU(3)_C \times SU(2)_L \times U(1)_Y, \tag{1.19}$$

with $SU(3)_C$ describing strong interactions via QCD, and $SU(2)_L \times U(1)_Y$ describing electroweak (EW) interactions. Gauge vector bosons that result from taking this group locally are eight gluons (G^a) from each t^a color-generator of $SU(3)_C$, and a linear combination of the three $(W^\pm, Z)$ weak bosons and the (γ) electromagnetic photon from the three T^i isospin-generators of $SU(2)_L$ and Y hyper-charge-generator of $U(1)_Y$.....AF: Esto no está bien escrito. No se articulan bien la ideas. Resulta incluso confuso cuando se coloca en contexto con la línea anterior. Por favor corregir. Por otor lado, he notado un cambio en el manejo del inglés en esta parte, en referencia a la redacción usada hasta la página 13.

The electroweak symmetry, $SU(2)_L \times U(1)_Y$, is spontaneously broken, leaving the unbroken electromagnetic symmetry $U(1)_{EM}$. This process occurs via the Higgs mechanism, whose associated quantum is the Higgs boson H. The hypercharges (Y) of the SM fermions in table 1.2 are related to their usual electric charges by the Gell-Mann–Nishijima relation [25]

$$Q_{EM} = \frac{1}{2}Y + T_3, \tag{1.20}$$

where $T_3 \doteq \mathrm{diag}\left(\frac{1}{2}, -\frac{1}{2}\right)$ is an $SU(2)_L$ generator. Thus, they reproduce electric charge quantization, e.g. the equality in magnitude of the proton and electron charges. Although these hypercharge assignments look rather ad hoc, their values are dictated by the quantum consistency of the theory.

It is indeed easy to check that these are (module an irrelevant overall normalization) the only (family independent) assignments canceling all potential triangle gauge anomalies.

1.2.2 GAUGE BOSONS

The Lie algebra of the gauge group $SU(3)_C \times SU(2)_L \times U(1)_Y$ follows

$$\begin{aligned} \left[t^a, t^b\right] &= i f^{abc} t_c, \\ \left[T^i, T^j\right] &= i\epsilon^{ijk} T_k, \\ \left[T^i, Y\right] &= \left[t^a, T^j\right] = [t^a, Y] = 0, \end{aligned} \tag{1.21}$$

where f^{abc} and ϵ^{ijk} are the structure constants of $SU(3)$ and $SU(2)$. Therefore, the gauge fields G_μ, W_μ, and B_μ must transform in the adjoint representation:

$$\begin{aligned} \delta B_\mu &= \partial_\mu \theta, \\ \delta W^i_\mu &= \partial_\mu \theta^i - g\epsilon^{ijk}\theta^j W^k_\mu, \\ \delta G^a_\mu &= \partial_\mu \epsilon^a - g_s f^{abc} \epsilon^b G^c_\mu. \end{aligned} \tag{1.22}$$

Then, the curvature strength tensors are

$$\begin{aligned} G^a_{\mu\nu} &= \partial_\mu G^a_\nu - \partial_\nu G^a_\mu + g_s f^{abc} G^b_\mu G^c_\nu \\ W^i_{\mu\nu} &= \partial_\mu W^i_\nu - \partial_\nu W^i_\mu + g\epsilon^{ijk} W^j_\mu W^k_\nu \\ B_{\mu\nu} &= \partial_\mu B_\nu - \partial_\nu B_\mu \end{aligned} \tag{1.23}$$

and the "kinetic" term for gauge fields in the Lagrangian is

$$\mathcal{L}_{\text{Gauge}} = -\frac{1}{4} G^a_{\mu\nu} G^{\mu\nu}_a - \frac{1}{4} W^i_{\mu\nu} W^{\mu\nu}_i - \frac{1}{4} B_{\mu\nu} B^{\mu\nu}. \tag{1.24}$$

These kinetic terms induce vertices between gauge bosons and in turn do not take into account the masses for such vector bosons. Their masses are generated via the Higgs mechanism, thorough linear combinations, giving rise to the physical $W^{\pm}$, Z, and γ bosons. The field redefinitions leading to mass eigenstates are

$$\begin{cases} W^+_\mu = \frac{1}{\sqrt{2}}\left(W^1_\mu - iW^2_\mu\right) \\ W^-_\mu = \frac{1}{\sqrt{2}}\left(W^1_\mu + iW^2_\mu\right) \\ Z_\mu = c_w W^3_\mu - s_w B_\mu \\ A_\mu = s_w W^3_\mu + c_w B_\mu \end{cases} \quad \text{where} \quad \begin{cases} s_w = \sin\theta_w = \frac{g}{\sqrt{g^2 + g\prime 2}} \\ c_w = \cos\theta_w = \frac{g'}{\sqrt{g^2 + g\prime 2}} \end{cases} \tag{1.25}$$

To avoid confusions with the Dirac matrices, we denote the electromagnetic potential as A_μ.

Before symmetry breaking we work in a general renormalizable R_ξ gauge; for the discussion of observable tree-level vertices below we will adopt the unitary gauge, in which the unphysical Goldstone bosons are removed from the spectrum and only the physical transverse and longitudinal polarizations of $W^{\pm}$ and Z remain. (Ghost and Goldstone interactions present in a covariant gauge are therefore omitted from the figures.)

Due to the non-abelian nature of the $SU(3)_C$ and $SU(2)_L$ gauge groups, the corresponding gauge bosons also interact among themselves. From the strength tensors in Eq. (1.23) in the kinetic term of the gauge Lagrangian in Eq. (1.24), we obtain three- and four-point self-interaction vertices for vector bosons from the $SU(3)_C$ and $SU(2)_L$ sectors (see Fig. 1.3), whose structure follows directly from the commutation relations of the Lie algebra.

1.2.3 MATTER FIELDS

We refer to the fermionic fields of the SM as the matter fields. We distinguish fermions in these two categories: leptons, fermions that do not have strong interaction, and quarks that interact both strongly and electroweakly. In table 1.3, we can see that there are six leptons, three charged and three neutral: each charged lepton has an associated neutrino. Therefore, the electrically charged and the associated neutral leptons can be arranged as $SU(2)_L$ doublets. In the case of quarks, we can divide these particles as up-and-down-type quarks, also arranged as $SU(2)_L$ doublets, one per generation.

Fermion categories		**Elementary particle generation**		
Type	Subtype	First	Second	Third
Quarks (q)	up-type	(u) up	(c) charm	(t) top
	down-type	(d) down	(s) strange	(b) bottom
Leptons (ℓ)	charged	(e) electron	(μ) muon	(τ) tauon
	neutrino	(ν_e)	(ν_μ)	(ν_τ)

Table 1.3: Three generations of fermions according to the SM of particle physics. Each generation containing two types of leptons and two types of quarks.

According to the SM, there are three generations (families) of fermions. Each generation contains a doublet of leptons and a doublet of quarks. Among generations, particles differ by their flavour quantum number and

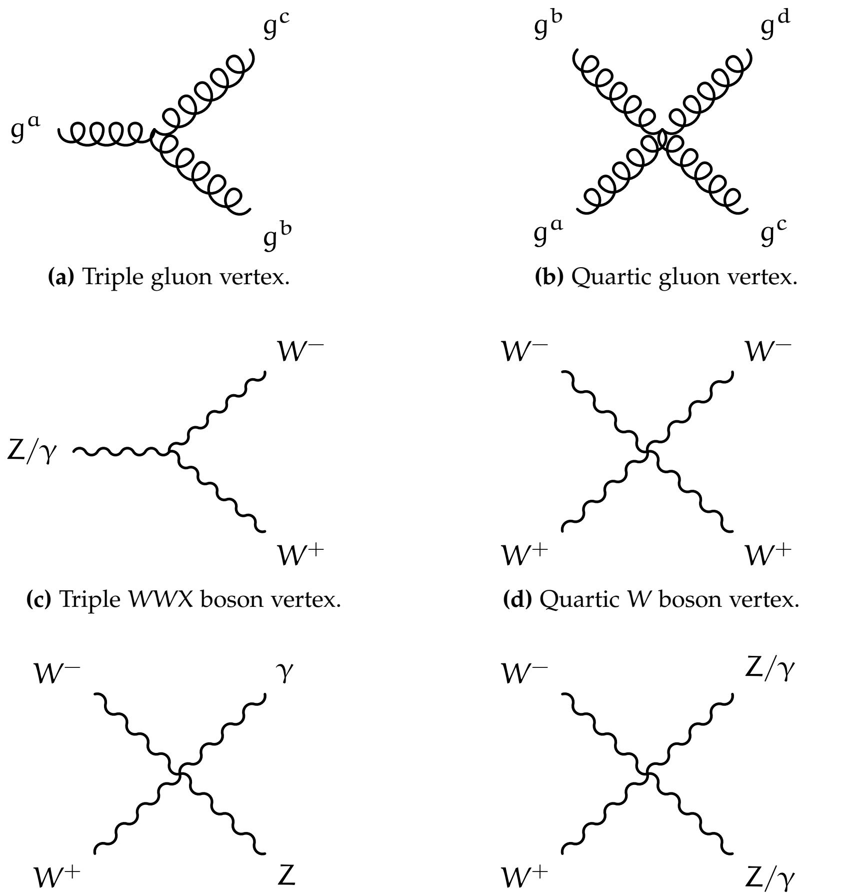

(a) Triple gluon vertex.

(b) Quartic gluon vertex.

(c) Triple WWX boson vertex.

(d) Quartic W boson vertex.

(e) Quartic $WWZ\gamma$ vertex.

(f) Quartic $WWXX$ vertex ($X = Z, \gamma$).

Figure 1.3: Feynman diagrams for gauge boson self-interactions (unitary gauge). We denote by $X = Z, \gamma$ a neutral electroweak gauge boson.

mass, but their strong and electrical interactions are identical. Moreover, the flavour quantum number is a quantity conserved by all interactions except for the weak interaction. Each generation is more massive than the previous one. The second and third generations are unstable and they disintegrate into the first generation. This is why ordinary matter is composed of first generation fermions. All three generations are produced in nuclear reactors, colliders, and cosmic rays.

Under all the constraints on local gauge invariance and renormalizability of the theory, the fermionic Lagrangian for SM is given by

$$\mathcal{L}_{\text{Fer}} = i\bar{\ell}^j_L \not{\mathcal{D}} \ell^j_L + i\bar{e}^j_R \not{\mathcal{D}} e^j_R + i\bar{q}^j_L \not{\mathcal{D}} q^j_L + i\bar{u}^j_R \not{\mathcal{D}} u^j_R + i\bar{d}^j_R \not{\mathcal{D}} d^j_R \tag{1.26}$$

where $\not{\mathcal{D}} \equiv \gamma^\mu \mathcal{D}_\mu$, for the covariant derivative

$$\mathcal{D}_\mu = \partial_\mu - i g_s t_a G^a_\mu - i g T_i W^i_\mu - i g' \frac{Y}{2} B_\mu, \tag{1.27}$$

with the gauge fields G^a, W^i, and B acting on each kind of fermion via

$$\begin{aligned}
\mathcal{D}_\mu \ell_L^i &= \left(\partial_\mu - igT_j W_\mu^j + i\frac{g'}{2}B_\mu\right)\ell_L^i \\
\mathcal{D}_\mu e_R^i &= \left(\partial_\mu - ig'B_\mu\right)e_R^i \\
\mathcal{D}_\mu q_L^i &= \left(\partial_\mu - ig_s t_a G_\mu^a - igT_j W_\mu^j - i\frac{g'}{6}B_\mu\right)q_L^i \\
\mathcal{D}_\mu u_R^i &= \left(\partial_\mu - ig_s t_a G_\mu^a - i\frac{2g'}{3}B_\mu\right)u_R^i \\
\mathcal{D}_\mu d_R^i &= \left(\partial_\mu - ig_s t_a G_\mu^a + i\frac{g'}{3}B_\mu\right)d_R^i,
\end{aligned} \tag{1.28}$$

coupling the fermions to the gauge bosons. As we will show below, after electroweak symmetry breaking, these interactions give rise to the familiar electromagnetic, weak, and strong forces, where the physical γ, Z, and W bosons are a superposition of the original B and W fields, as it was mentioned before. Representative tree-level gauge–fermion interaction vertices are displayed in Fig. 1.4.

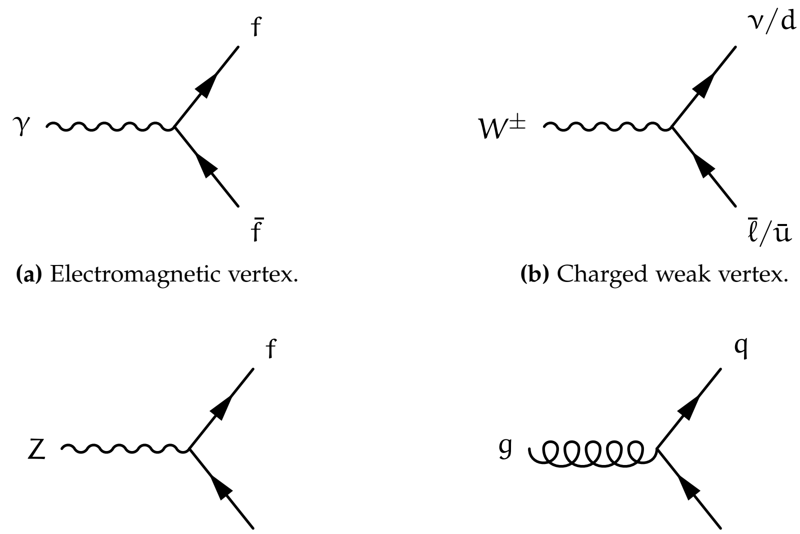

(a) Electromagnetic vertex. **(b)** Charged weak vertex.

(c) Neutral weak vertex. **(d)** Strong interaction.

Figure 1.4: Feynman diagrams for gauge boson interactions in the Standard Model.

1.2.4 ELECTROWEAK SYMMETRY BREAKING

As it was mentioned in Section 1.2.1, in the SM the EW symmetry, $SU(2)_L \times U(1)_Y$, is spontaneously broken down to the electromagnetic $U(1)_{EM}$ group by a complex scalar Higgs field. This field transforms as an $SU(2)_L$ doublet, $H = (H^+, H^0)$, with hypercharge $+1$. Its dynamics is governed by the Mexican-hat potential ......AF: Si se va a nombrar el sombrero mexicano, sería deacuado incluir una figura del potencial (the resulting scalar self-interactions are shown in Fig. 1.5):

$$V(H) = -\mu^2|H|^2 + \lambda|H|^4 \quad \Rightarrow \quad v^2 \equiv \langle H^\dagger H\rangle = \mu^2/2\lambda. \tag{1.29}$$

The vacuum expectation value (vev) aligns with the electrically neutral component, $\langle H^0\rangle = v/\sqrt{2} \simeq 174\,\text{GeV}$, generating masses for the weak gauge bosons while preserving $U(1)_{EM}$.

We adopt the Kibble (polar) parametrization of the Higgs doublet in terms of one physical scalar h and three would-be Goldstone bosons $G^\pm, G^0$:

$$H = \begin{pmatrix} G^+ \\ \frac{1}{\sqrt{2}}(v + h + iG^0) \end{pmatrix}, \tag{1.30}$$

which in a unitary gauge reduces to $H = \frac{1}{\sqrt{2}}(0, v+h)^T$ after gauging away $G^\pm, G^0$.

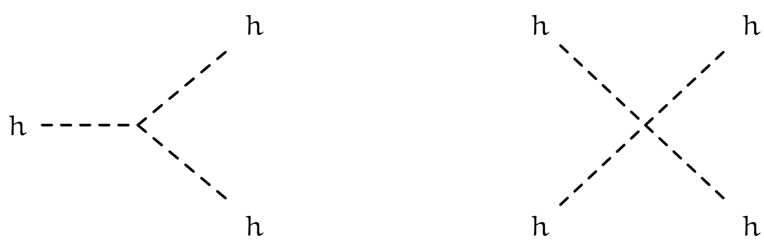

(a) Higgs triple self-coupling. **(b)** Higgs quartic self-coupling.

Figure 1.5: Feynman diagrams for Higgs self-interactions arising from the potential $V(H^\dagger, H) = -\mu^2|H|^2 + \lambda|H|^4$ in the Higgs Lagrangian.

Fermion masses arise through Yukawa couplings, which represent the most general renormalizable interactions between the Higgs field and the fermion fields (see the diagrammatic decomposition in Fig. 1.6a–1.6d):

$$\mathcal{L}_{\text{Yuk}} = y_u^{ij}\bar{q}_L^i u_R^j \tilde{H} + y_d^{ij}\bar{q}_L^i d_R^j H + y_\ell^{ij}\bar{\ell}_L^i e_R^j H + \text{h.c.}, \tag{1.31}$$

where $\tilde{H} = i\sigma_2 H^*$, and y_u, y_d, y_ℓ are arbitrary 3×3 complex matrices in flavor space. When the Higgs acquires its vev,

$$\langle H\rangle = \begin{pmatrix} 0 \\ \frac{v}{\sqrt{2}} \end{pmatrix}, \tag{1.32}$$

these couplings generate Dirac mass terms for the fermions.

The quark mass matrices are proportional to the Yukawa matrices: $M_u = y_u v/\sqrt{2}$, $M_d = y_d v/\sqrt{2}$. Since y_u and y_d are general complex matrices, they cannot be simultaneously diagonalized. The physical quark masses and states are found by performing separate unitary transformations on the left- and right-handed fields:

$$u_L \to V_L^u u_L, \quad u_R \to V_R^u u_R, \quad d_L \to V_L^d d_L, \quad d_R \to V_R^d d_R, \tag{1.33}$$

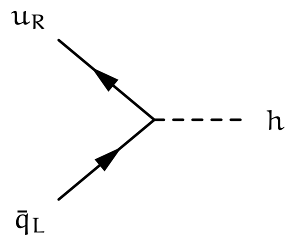

(a) Up-type Yukawa coupling.

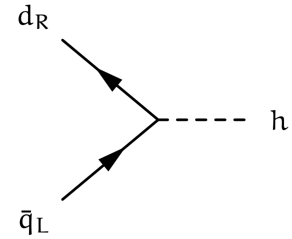

(b) Down-type Yukawa coupling.

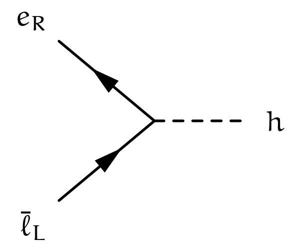

(c) Lepton Yukawa coupling.

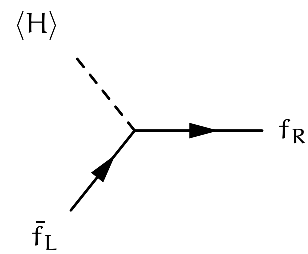

(d) Fermion mass term from vev.

Figure 1.6: Feynman diagrams for Yukawa couplings.

such that $V_L^u M_u V_R^{u\dagger} = M_u^{\text{diag}}$ and $V_L^d M_d V_R^{d\dagger} = M_d^{\text{diag}}$ are diagonal with real, positive entries.

This diagonalization procedure has a direct consequence for the charged-current interactions mediated by the $W^\pm$ bosons. In the flavor basis the interaction reads

$$\mathcal{L}_W \supset -\frac{g}{\sqrt{2}}(\bar{u}_L, \bar{c}_L, \bar{t}_L)\gamma^\mu W_\mu^+ (d_L, s_L, b_L)^T + \text{h.c.} \tag{1.34}$$

After moving to the mass basis, the left-handed up- and down-type quarks rotate differently ($u_L \to V_L^u u_L$, $d_L \to V_L^d d_L$), and the interaction becomes

$$\mathcal{L}_W \supset -\frac{g}{\sqrt{2}}(\bar{u}_L, \bar{c}_L, \bar{t}_L)\gamma^\mu W_\mu^+ V_{\text{CKM}} (d_L, s_L, b_L)^T + \text{h.c.}, \tag{1.35}$$

where the Cabibbo–Kobayashi–Maskawa (CKM) matrix appears as the mismatch between the two rotations:

$$V_{\text{CKM}} \equiv V_L^u V_L^{d\dagger} = \begin{pmatrix} V_{ud} & V_{us} & V_{ub} \\ V_{cd} & V_{cs} & V_{cb} \\ V_{td} & V_{ts} & V_{tb} \end{pmatrix}. \tag{1.36}$$

This unitary matrix encodes flavor mixing in charged-current weak interactions, and its non-diagonal structure is the origin of all quark flavor-changing processes in the SM.

The situation is different for leptons in the minimal SM without right-handed neutrinos. The charged-lepton mass matrix $M_\ell = y_\ell v/\sqrt{2}$ can be diagonalized by field redefinitions, but since neutrinos are massless in this framework, there is no additional rotation in the neutrino sector. As a result, the charged-current interaction

$$\mathcal{L}_W \supset -\frac{g}{\sqrt{2}}\bar{\nu}_L \gamma^\mu W_\mu^+ \ell_L + \text{h.c.} \tag{1.37}$$

remains diagonal in the mass basis. This implies *Lepton Flavor Universality* (LFU): the electroweak gauge bosons couple to all three lepton families with identical strength. In particular, the W boson couples to each $\bar{\nu}_L \gamma^\mu \ell_L$ current with coefficient $-g/\sqrt{2}$, and the Z boson couplings to ℓ_L and ℓ_R are flavor-independent because the hypercharge assignments are the same for all families.

LFU means that processes differing only by the lepton flavor, such as leptonic decays or semileptonic transitions, are predicted to occur with the same rates up to well-understood effects: differences in phase space, helicity suppression, lepton-mass dependence, and small radiative corrections. The assumption of LFU is central in the extraction of CKM parameters, since experimental determinations from decays involving electrons, muons, and tau leptons can be consistently combined.

Precision tests of LFU focus on ratios of decay widths or branching fractions where theoretical and experimental uncertainties cancel to a large extent. Agreement with these tests confirms the gauge structure of the SM, while deviations would point to new physics.

The Lagrangian of the scalar sector is

$$\mathcal{L}_H = \mathcal{D}_\mu H^\dagger \mathcal{D}^\mu H - V\left(H^\dagger, H\right), \tag{1.38}$$

with the covariant derivative defined as $\mathcal{D}_\mu H = \left(\partial_\mu + igT_a W_\mu^a + ig'\frac{Y}{2}B_\mu\right) H$. Substituting the Higgs vacuum expectation value, one obtains

$$\begin{aligned}\mathcal{L}_{\langle H \rangle} &= -\frac{1}{8} \begin{pmatrix} 0 & v \end{pmatrix} \begin{pmatrix} gW_\mu^3 - g'B_\mu & g\left(W_\mu^1 - iW_\mu^2\right) \\ g\left(W_\mu^1 + iW_\mu^2\right) & -gW_\mu^3 - g'B_\mu \end{pmatrix}^2 \begin{pmatrix} 0 \\ v \end{pmatrix} \\ &= -\frac{1}{8} v^2 V_\mu^T \begin{pmatrix} g^2 & 0 & 0 & 0 \\ 0 & g^2 & 0 & 0 \\ 0 & 0 & g^2 & -g'g \\ 0 & 0 & -g'g & g'^2 \end{pmatrix} V^\mu,\end{aligned} \tag{1.39}$$

where $V_\mu^T = \left(W_\mu^1, W_\mu^2, W_\mu^3, B_\mu\right)$. Diagonalizing this mass matrix yields the following eigenvalues

$$0,\ -\tfrac{1}{8}v^2 g^2,\ -\tfrac{1}{8}v^2 g^2,\ \text{and}\ -\tfrac{1}{8}v^2\left(g^2 + g'^2\right).$$

The massless state corresponds to the photon, the heaviest to the Z boson, and the two degenerate intermediate states to the charged bosons $W^\pm$, which transform under the representation of the unbroken generator Q_{EM}. The resulting Higgs–vector boson interaction structures are summarized in Fig. 1.7.

This suffices to illustrate how the SM, formulated as a relativistic quantum field theory, describes the interactions of matter fields through the fundamental forces, mediated by vector bosons. The Higgs boson, also part of the SM spectrum, plays the central role in generating masses for the

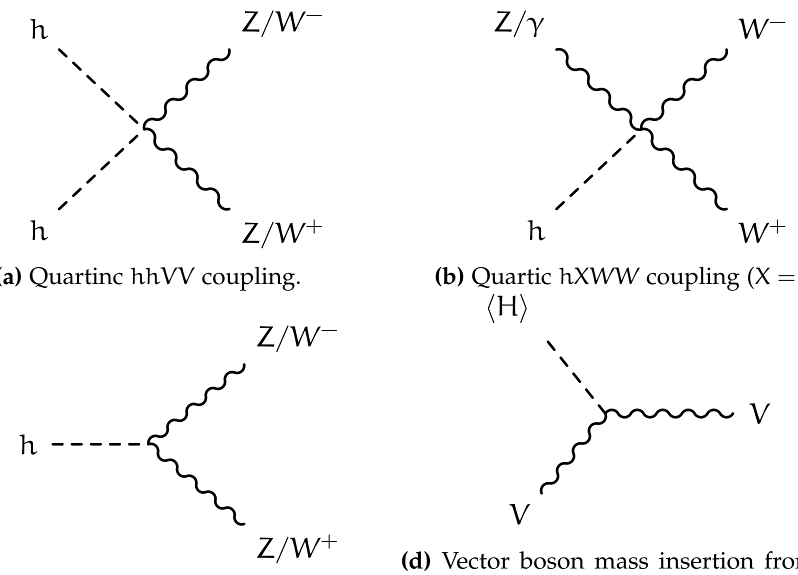

(a) Quartinc $hhVV$ coupling.

(b) Quartic $hXWW$ coupling ($X = Z, \gamma$).

(c) Triple hVV coupling ($V = W^{\pm}, Z$).

(d) Vector boson mass insertion from the vev ($V = W^{\pm}, Z$).

Figure 1.7: Feynman diagrams for Higgs–gauge boson interactions (unitary gauge) arising from $\mathcal{D}_{\mu}H^{\dagger}\mathcal{D}^{\mu}H$ and a vev insertion. Here $V = W^{\pm}, Z$ and $X = Z, \gamma$.

weak bosons and the fermions, while indirectly distinguishing the photon as the only massless gauge boson of the EW sector.

Since its formulation, the SM has been tested extensively and has shown remarkable success, both in explaining existing data and in making accurate predictions. A well-known example is the agreement between its prediction and the experimental measurement of the electron magnetic dipole moment, consistent to twelve significant figures [26]. The discovery of the Higgs boson in 2012 was the culmination of almost fifty years of experimental efforts, confirming the mechanism incorporated into the SM in the late 1960s through the unification of the electromagnetic and weak interactions by Glashow, Weinberg, and Salam [27, 28]. With this discovery, the full particle spectrum predicted by the SM was finally observed.

1.3 DEFICIENCIES OF SM AND NEW PHYSICS

While these and other successes of the SM are an achievement for the field of particle physics, it is well known that this cannot be the ultimate theory of fundamental particles and interactions. Even though the SM is currently the best description there is of the subatomic world, it does not explain the complete picture; there are important questions that it does not answer and it is also surrounded by different irregularities. Some of them are completely incompatible with the current SM, and strongly suggest that it requires a consistent extension to solve experimental and theoretical problems that we will label as the cosmological problems, phenomenological problems, and theoretical problems. We proceed to list briefly some of the main open conundrums.

1.3.1 Cosmological problems

Gravity and the cosmological-constant problem A UV-complete quantum theory of gravity remains unknown. At low energies, general relativity can be treated as an effective field theory, but it is non-renormalizable [29, 30]. Moreover, the observed vacuum energy (cosmological constant) driving cosmic acceleration is many orders of magnitude smaller than naive quantum-field-theory estimates, posing a severe naturalness problem [31].

Dark matter Cosmological and astrophysical data require a cold, non-baryonic, component with $\Omega_c h^2 \simeq 0.12$ [32], consistent with the thermal weakly interacting massive particle (WIMP) production hypothesis. The SM does not have a suitable dark matter particle candidate: active neutrinos are too light and hot, and baryons are limited by BBN/CMB (Baryon Acoustic Oscillations / Cosmic Microwave Background) AF: Por favor incluir algunas referencias. This points to new degrees of freedom BSM. Dark matter direct-detection experiments continue to improve sensitivity with null results. Recent LZ and XENONnT runs set the strongest spin-independent limits over a wide mass range [33–35].

Matter–antimatter asymmetry (baryon asymmetry) The Universe exhibits a nonzero baryon asymmetry, $\eta_B \simeq 6 \times 10^{-10}$ from CMB/BBN [32]. The SM fails quantitatively: for $m_H = 125$ GeV the electroweak transition is a crossover (no sufficient departure from equilibrium), and CKM CP violation is many orders of magnitude too small to generate the observed asymmetry. Therefore, additional CP violation and/or new dynamics are required, e.g. leptogenesis or electroweak baryogenesis [36–38].

Dark energy Late-time acceleration is consistent with a cosmological constant with $w \approx -1$ [39]. In SM+GR there is no mechanism to obtain such a tiny but nonzero vacuum energy; naive quantum-field-theory estimates are vastly larger, implying extreme fine-tuning (the cosmological-constant problem) [31]. The H_0 tension persists and could reflect systematics or new physics.

1.3.2 Theoretical problems

Hierarchy problem Is the problem concerning the large discrepancy between aspects of the weak force and gravity. Both of these forces involve constants of nature: the Fermi constant for the weak force and the Newtonian constant of gravitation for gravity. If the SM is used to calculate the quantum corrections to Fermi's constant, it appears that Fermi's constant is surprisingly large and is expected to be closer to Newton's constant, unless there is a delicate cancellation between the bare value of Fermi's constant and the quantum corrections to it.

In the SM context, the Higgs boson mass is much lighter than the energy scale on which the SM is considered valid (ideally, around the Plank mass at 1.221×10^{19} GeV), and the quantum corrections to the Higgs mass are on the order of this energy scale. This would inevitably make the Higgs and fermions masses huge, comparable to the scale at which new physics appears, unless there is an incredible fine-tuning cancellation between the quadratic radiative corrections and the bare mass. This level of fine-tuning is deemed unnatural.

STRONG CP PROBLEM The QCD Lagrangian supports a term associated with the strength tensor dual for gluons that break CP symmetry in the strong interaction sector. Experimentally, however, no such violation has been found, implying that the coefficient of this term is fine tunned to zero.

QUANTUM TRIVIALITY Suggests that it may not be possible to create a consistent quantum field theory involving elementary scalar Higgs particles, because, for high momentum particles, the renormalization presents inconsistencies unless the renormalization of the charges becomes null, and therefore not interacting, *i.e.* trivial. Nevertheless, because the Higgs boson plays a central role in the SM of particle physics, the question of triviality in Higgs models is of great importance.

NUMBER OF PARAMETERS AND UNEXPLAINED RELATIONS In total, the SM has too many free parameters (19 in total) that are obtained experimentally. There are indications that several of these free parameters may be correlated. However, the origin of these correlations is beyond the SM. For example, Yoshio Koide's empirical formula [40]

$$\frac{m_e + m_\mu + m_\tau}{\left(\sqrt{m_e} + \sqrt{m_\mu} + \sqrt{m_\tau}\right)^2} = 0.666661(7) \approx \frac{2}{3},$$

seems to indicate that there is a way to predict the masses of leptons.....AF: Esto se siente inconcluso: ¿cómo concluye esto?

1.3.3 PHENOMENOLOGICAL PROBLEMS

NEUTRINO MASSES Precision oscillation data continue to require nonzero neutrino masses and mixing. Global fits still prefer normal ordering, but the mass ordering and the Dirac CP phase remain unestablished; see the latest NuFIT summary [**NuFIT2024**]. Direct kinematic limits from KATRIN have pushed the effective electron-neutrino mass into the sub-eV regime (about 0.5 eV at 90% CL) [**KATRIN2022, KATRIN2024**].

ANOMALIES IN b-HADRON DECAYS The earlier hints of lepton-flavour universality violation in $b \to s\ell\ell$ (e.g. $R_{K^{(*)}}$) have largely subsided.

The 2022 LHCb analyses with the full Run 1+2 dataset report R_K and related ratios consistent with the SM within uncertainties [**LHCb:2022RK**]. Angular-observable tensions (e.g. P_5') persist at lower significance and are sensitive to hadronic uncertainties. For $b \to c\tau\nu$, updated averages (Belle/Belle II, HFLAV) have moved closer to the SM; any deviation is now at the ~2–3σ level depending on inputs [**HFLAV2023**, **BelleII:2023RDstar**].

ANOMALOUS MAGNETIC DIPOLE MOMENT OF THE MUON Fermilab's 2023 update improved the experimental precision [**FNALg2_2023**]. The significance of any discrepancy with the SM now depends on the hadronic vacuum polarization input: using the 2020 theory white paper gives a ~4σ deviation [**Aoyama:2020WhitePaper**], whereas lattice-QCD evaluations (e.g. BMW) and new $e^+e^- \to \pi^+\pi^-$ input from CMD-3 tend to reduce the tension [**BMW:2021Nature**, **CMD3:2023pipii**].

W-BOSON MASS The precise CDF II determination remains in strong tension with the SM and with other experiments [**CDFII:2022Wmass**]. Subsequent ATLAS and earlier LEP/LHCb results are compatible with the SM; see the PDG 2024 summary for a balanced overview [**PDG2024**].

CCA AND $q\bar{q} \mapsto e^+e^-$ First-row CKM unitarity tests still show a mild (~2–3σ) tension depending on treatment of radiative/nuclear corrections and kaon inputs [**PDG2024**, **Seng:2018PRL**, **HardyTowner:2020**]. High-mass Drell–Yan lepton universality measurements at the LHC with Run 2/3 data are generally consistent with the SM within uncertainties.

1.4 LEPTON FLAVOUR UNIVERSALITY: TESTS AND ANOMALIES

As established previously, gauge interactions of charged leptons are flavour-universal [21, 27, 28] in the SM: the $SU(2)_L \times U(1)_Y$ couplings are generation-independent [27, 28], meaning that after accounting for kinematic and mass effects, processes mediated by electroweak interactions predict identical couplings to electrons, muons, and tau leptons [21]. While small deviations can arise from well-understood mass-dependent, phase-space, and radiative corrections [21], genuine Lepton Flavour Universality Violation (LFUV) would constitute clear evidence of new physics beyond the Standard Model [41–43].

It is worth noting that total lepton flavour numbers are accidental symmetries of the renormalizable SM with massless neutrinos [21]. While neutrino oscillations demonstrate flavour violation in the neutral sector [44, 45], any significant charged-lepton flavour violation (cLFV) would unambiguously signal BSM physics [21]. This section focuses specifically on LFU tests and their current experimental status [21, 46].

An extensive experimental program probes LFU across various processes [21]:

- **Rare** B **decays** ($b \to s\ell^+\ell^-$): Clean ratios R_K and R_{K^*} comparing muon to electron modes [41, 47–52].
- **Charged-current** B **decays** ($b \to c\ell\nu$): Ratios R_D and R_{D^*} comparing τ to light leptons [53–59].
- **Light-meson decays**: Leptonic ($\pi, K \to \ell\nu$) y semileptonic ($K_{\ell 3}$) universality tests [21, 60].
- **Electroweak boson decays**: $W \to \ell\nu$ y $Z \to \ell^+\ell^-$ universality [61, 62].
- τ **decays**: Tests of $e/\mu/\tau$ universality in leptonic and semileptonic channels [21, 59].

Combinations of these measurements provide stringent constraints on flavour-dependent interactions beyond the SM [21].

Most LFU tests involving light mesons, W/Z bosons, and τ decays show agreement with SM predictions at the percent level [21]. The most significant tensions initially emerged in semileptonic B decays [41, 43, 63–65], particularly in the neutral-current ratios R_K and R_{K^*} and the charged-current ratios R_D and R_{D^*} (discussed in detail in the following subsection) [63, 66]. Recent analyses have brought $R_{K^{(*)}}$ measurements closer to SM predictions [46, 51, 52, 67], while the situation for $R_{D^{(*)}}$ remains actively investigated [59], with forthcoming data expected to provide decisive insights [68]. Collectively, these measurements delineate viable patterns of lepton non-universal interactions and provide crucial guidance for theoretical model building [42, 43, 69, 70].

In the renormalizable SM, any credible observation of LFV would require BSM physics [41, 42]. Various theoretical frameworks can accommodate such violations, including extended gauge sectors and other scenarios that generate non-universal couplings [71–73]. These models typically predict correlated signals across multiple precision observables [46, 67, 74] and, depending on their flavour structure, may also induce cLFV at potentially observable levels, subject to tight constraints from existing experimental limits [69, 75]. AF: Toda esta parte es una repetición de lo que se dijo arriba....: In recent years, significant attention has focused on precision measurements of B-meson decay rates [41, 43], particularly through ratios that test LFU [59]. The most prominent examples are the $R_{K^{(*)}}$ [47–50] and $R_{D^{(*)}}$ [53, 54, 56–58, 76–82] ratios, which compare decay rates to different lepton families [21, 59]. These measurements generated substantial theoretical interest, with numerous proposals for new physics scenarios that could explain potential deviations from SM predictions [42, 69, 83, 84]. Recent re-analyses of $R_{K^{(*)}}$ data have shown this ratio to be compatible with the SM prediction [46, 51, 52, 67], while the situation for $R_{D^{(*)}}$ remains an open question [59] that continues to motivate the study of scenarios where new particles might have preferential couplings to third-generation fermions [72, 85, 86]. The anomalous magnetic moment of the muon, $a_\mu \equiv (g-2)_\mu/2$, represents another benchmark precision observable sensitive to new virtual states [87]. The latest measurements from the Fermilab Muon $g-2$ experiment report a value with sub-ppm precision [88], broadly consistent with but more precise than the earlier BNL result [89]. This measurement shows sustained tension with certain Standard Model evaluations [87].

The theoretical prediction for a_μ combines QED, electroweak, and hadronic contributions [87], with the hadronic vacuum polarization and light-by-light scattering components driving the dominant uncertainties [21, 90]. The comparison between experimental results and theoretical predictions therefore serves as a powerful indirect probe of new physics scenarios that couple to leptons [87].

The complementarity between $(g-2)_\mu$, LFU tests in B decays, and direct searches provides a multifaceted approach to testing the Standard Model [46, 67]. Limits on charged lepton flavour violation further constrain possible chirality-flipping couplings that could also contribute to dipole moments [69, 75], highlighting the interconnected nature of these precision observables in the search for physics beyond the Standard Model [42].

Taken together, these precision observables underscore the importance of direct searches for new physics at colliders [91, 92]. While deviations from LFU in light-meson, τ, and electroweak boson decays remain consistent with SM expectations [21, 62], the persistent anomalies in B decays and the muon $(g-2)$ point to scenarios where new states may couple non-universally to leptons [43, 87]. A particularly well-motivated possibility is that new particles exhibit enhanced couplings to third-generation fermions [72, 93]. Such flavour structures naturally alleviate existing constraints from first- and second-generation processes while offering testable signatures in collider environments [70, 73].

Therefore, a dedicated experimental program to search for new particles with preferential couplings to the third generation is a crucial component of the BSM search strategy [91, 92]. This program requires not only powerful collider experiments [94, 95] but also detailed *feasibility studies* to assess the discovery potential of these non-standard signatures [96, 97]. Such studies are essential to optimize trigger strategies [94, 95], refine analysis techniques [98], and ultimately guide the exploration of the most promising regions of parameter space where these hypothetical particles might reveal themselves [42].

2

PHENOMENOLOGICAL FRAMEWORK FOR LHC SEARCHES

Since its formulation, the SM has proven remarkably successful in describing the fundamental particles and interactions, and its parameters have been measured with increasing precision over several decades [21, 27]. However, as discussed in the previous chapter, various theoretical and experimental observations suggest that the SM is incomplete [42, 99]. As outlined previously, this is motivated by theoretical shortcomings such as the hierarchy problem [100, 101] , the absence of a dark matter candidate [102], and non-zero neutrino masses [103], as well as by experimental anomalies [47, 48, 53]. These limitations motivate searches for physics beyond the SM [42, 43].

The search for BSM physics proceeds along two main axes: the construction of theoretical extensions to the SM [42, 43, 101], and the development of experimental methods to probe them [104–106]. A necessary condition for any viable BSM model is consistency with existing experimental data, which places strong constraints on its parameter space [21, 107, 108]. These constraints include lower limits on the masses of new particles from direct searches at high-energy colliders [107, 108], and upper bounds on couplings and mixing angles from precision measurements at both high and low energies [66, 109], which are sensitive to virtual corrections [46].

The area of particle physics phenomenology, connects theoretical models to experimental observables by calculating cross sections, decay rates, and other signatures for given model parameters [104, 110, 111]. A critical function of this field is to assess the experimental feasibility of BSM scenarios—evaluating whether predicted signals would be observable above background processes given the capabilities of current and future experiments [104–106]. This involves estimating production rates [104, 110, 112], modeling detector acceptance and efficiency [94, 95, 106, 113], and developing discrimination variables to maximize the likelihood of observing new signals above known SM backgrounds [114–117]. This feasibility assessment is essential for designing analysis strategies, particularly at LHC, where signals of new physics must be discriminated from large SM backgrounds [94, 95, 104, 106, 118].

The LHC has provided data at center-of-mass energies from 7 TeV to 13.6 TeV [108, 113]. During Run I (2010–2013), operations at 7–8 TeV led to the discovery of the Higgs boson using a dataset corresponding to an integrated luminosity of roughly 30 fb^{-1} [119, 120]. Run II (2015–2018) significantly expanded this dataset, collecting approximately 140 fb^{-1} at 13 TeV [108, 113]. Run III (2022–2025) is currently underway at 13.6 TeV and its target is to collect over 300 fb^{-1} [113]. Future operations will be dominated by the High-Luminosity LHC (HL-LHC), starting around 2029, which is designed to accumulate an unprecedented integrated luminosity of 3000 fb^{-1} [121, 122]. This vast increase in data volume enables searches for exceedingly rare processes but also requires discriminating potential signals of new physics from correspondingly large and complex SM backgrounds, making sophisticated phenomenological tools increasingly important [104, 106].

2.1 DETECTORS AND SUBSYSTEMS

When two particle bunches from colliding beams cross each other, they generate individual interactions known as events [94, 95]. At the LHC, the beam intensity is so high that multiple interactions can take place in a single event; this phenomenon is referred to as in-time pile-up [122, 123]. In other words, the probability that several proton-proton interactions occur within the same bunch crossing is non-negligible, leading to multiple overlapping events in a single detector readout [111, 124]. In addition, particles from other bunch crossings with respect to the primary collision of interest can be detected. This latter experimental feature is known as out-of-time pile-up. The sum of these two effects, in-time and out-of-time pile-up, is commonly referred to as PU.

The particle collisions at the LHC, pp and heavy-ions, occur at four main interaction points, each hosting a large particle detector designed to record and analyze the outcomes [94, 95]. The two largest and most comprehensive experiments [94, 95] are the Compact Muon Solenoid (CMS) and A Toroidal LHC ApparatuS (ATLAS). Both are multipurpose detectors with broad physics programs, capable of exploring a wide range of phenomena [94, 95]. They perform precision measurements within the electroweak sector of the SM [21], probe the dynamics of quarks and gluons (including through heavy-ion collisions) [106], and conduct extensive searches for BSM physics using pp collision data [119, 120]. While CMS and ATLAS differ in their detector designs and reconstruction strategies, their physics goals are largely overlapping, and their results are complementary [94, 95].

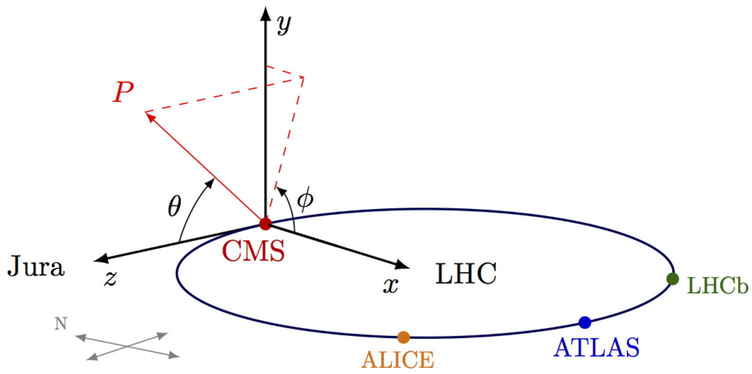

Figure 2.1: Coordinate system employed by the CMS experiment (retrieved from [125]).

Throughout this work, phenomenological studies and comparisons are primarily developed in the context of CMS, although several results from ATLAS are also referenced, given the close alignment in sensitivity and scope [94, 95]. Measurements performed at CMS adopt a right-handed coordinate system with its origin at the nominal collision point [95]. The z-axis is defined along the beam direction, the x-axis points radially inward toward the center of the LHC ring, and the y-axis points vertically upward [95]. The azimuthal angle ϕ is measured in the transverse (xy) plane from the x-axis, while the polar angle θ is measured from the z-axis, as shown in Fig. 2.1 [95]. Moreover, for kinematic analysis at hadron colliders, the Cartesian coordinate system is often reparameterized into quantities that are more physically meaningful and experimentally convenient as shown in Fig. 2.2 [126]:

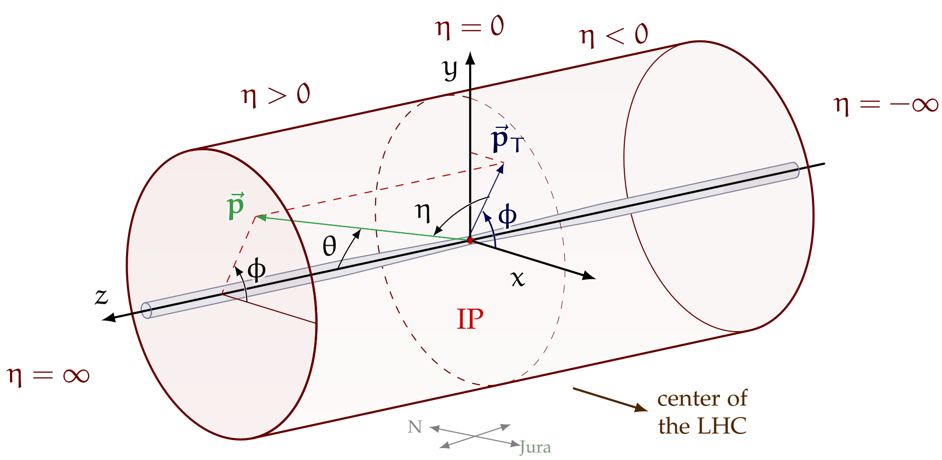

Figure 2.2: Detailed reparametrization of the coordinate system employed by the CMS experiment (retrieved from [125]).

PSEUDO-RAPIDITY (η) The polar angle is not a Lorentz invariant quantity. In addition, since the vast majority of particles are detected in the forward region of the detector, known as the endcap region, the distribution of the particle multiplicity as a function of θ is not uniform. This non-uniformity makes it difficult to study the agreement between the observed data and the background prediction in the central part of the detector. Therefore, the CMS experiment uses a variable known as pseudo-rapidity [21, 95], η, defined in terms of the polar angle as:

$$\eta = -\ln\left(\tan\frac{\theta}{2}\right)$$

Therefore, the main advantages of using η instead of θ are that it provides more uniform distributions than those over the polar angle [126], see Fig. 2.2. And, furthermore, the difference in η is a Lorentz boosts invariant quantity, along the beam direction [21].

TRANSVERSE MOMENTUM (p_T) It refers to the component of momentum which is perpendicular to the beam line [126]. It is usually preferred over full momentum because momentum along the beamline may just be left over from the beam particles, while the transverse momentum is always associated with whatever physics happened at the vertex [126], see Fig. 2.2.

AZIMUTHAL ANGLE (ϕ) it measures the angle in the transverse plane relative to the x-axis, providing the directional component perpendicular to the beam line [95].

Together, the triplet (p_T, ϕ, η) forms a natural coordinate system that fully describes a particle's three-momentum vector at a hadron collider [21, 126]. The full four-momentum (E, p_x, p_y, p_z) can be reconstructed from these quantities, typically supplemented by either the particle's mass hypothesis (for identified particles like electrons or muons) or the energy deposited in the calorimeters (for neutral objects like photons or jets) [111, 127, 128]. This (p_T, ϕ, η) system serves as the fundamental framework for defining physical objects, calculating event variables, and performing analyses at the LHC, providing both experimental convenience and physical insight into the collision dynamics [111, 126].

A key challenge is isolating the primary hard interaction from the additional concurrent PU interactions [122, 123]. This is accomplished by reconstructing distinct interaction vertices along the beam direction and associating charged particles to their point of origin using the CMS tracking and vertexing algorithms [126, 129]. The ultimate aim of the reconstruction chain is to identify all stable particles produced in the collision and measure their four-momenta, thereby enabling the identification of the underlying fundamental process [126].

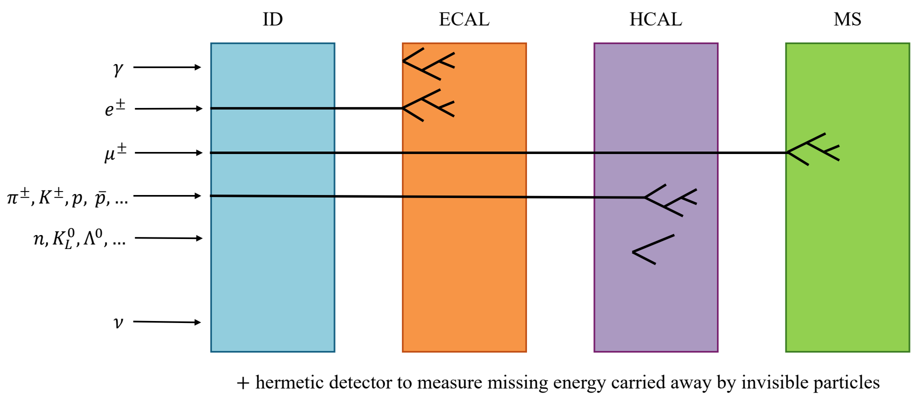

Figure 2.3: Illustration of high-energy particles being identified by consecutive types of subdetectors in a typical collider experiment. The curvature of the tracks in the magnetic field is not shown for simplicity. Representation of which particles and kinds of detectors are used in a multipurpose detector such as CMS or ATLAS. (retrieved from [130])

However, the reconstruction is complicated by several factors [95, 126]. The initial state of the colliding protons is not fully known, as they are composite particles made up of quarks and gluons (collectively referred to as partons) [112, 131]. The fraction of the proton's momentum carried by each parton is described by parton distribution functions (PDFs), which are determined experimentally. Among the available groups of PDFs, LHC analyses using Run II/III data have mainly implemented the PDF4LHC [112, 132] set. Consequently, the total momentum along the beam axis (z) is not balanced on an event-by-event basis [131]. Furthermore, not all particles are stable enough to reach the detector; some decay before being detected, and only their decay products are observed [21]. The design of a collider experiment, illustrated in Fig. 2.3, is optimized for the identification and energy measurement of the particles produced in high-energy collisions [95, 106]. Using the information from the different particle sub-detectors, it is possible to differentiate signatures from various particle types. This information is utilized by software algorithms, optimized for particle reconstruction and identification, to calculate the likelihood that a detector signature was created by a specific type of particle.

Finally, some hypothetical particles, such as those comprising dark matter, along with known neutrinos, interact very weakly with matter and escape direct detection [21, 102]. Therefore, a hermetic detector design is crucial to infer their presence by accurately measuring the imbalance of energy and momentum in the transverse plane, referred to as missing transverse momentum [126, 133].

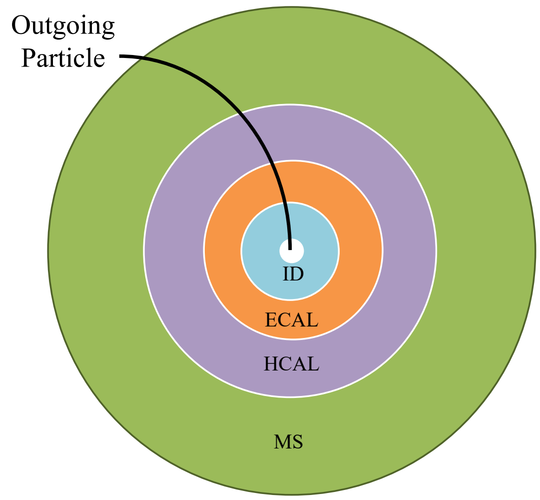

Figure 2.4: Schematic representation of a transverse section of a generic multipurpose detector. The inner detector (ID) is used to measure the trajectories of charged particles, the electromagnetic calorimeter (ECAL) measures the energy of photons and electrons, the hadronic calorimeter (HCAL) measures the energy of hadrons, and the muon system (MS) identifies and measures muons. The missing transverse momentum (MET) is inferred from the momentum imbalance in the transverse plane (retrieved from [134])

In this way, a typical collider experiment comprises several main detector subsystems that are used jointly to detect and measure the properties of particles produced in the collision [94, 95, 106, 126]. A *schematic representation* of such a generic multipurpose detector is shown in Fig. 2.4 [95, 106, 134]. The detector features an "onion-like" design of several concentric layers, each optimized to identify different types of particles and measure their properties [95, 126].

The innermost subsystem, the inner detector (ID) or tracker, is immersed in a strong axial magnetic field (typically 1–4 T) [95, 129]. It is designed to reconstruct the trajectories of charged particles, which are bent by the magnetic field [126, 129]. The direction and curvature of these trajectories, called **tracks**, allows to estimate the particle's momentum vector and electric charge [21, 129]. The most common long-lived charged particles from the SM are the so called light leptons (electrons e and muons μ) and hadrons (pions π, kaons K, and protons p) [21]. In some detectors, the ID is complemented by a Cherenkov light detector (RICH) to measure particle velocity and aid particle identification [21, 135]. Combined with the momentum measurement, this velocity helps determine the particle mass, allowing for differentiation between pions, kaons, and protons [21, 135].

After the tracker, particles enter the electromagnetic calorimeter (ECAL), which is designed to fully absorb photons, electrons, and positrons [95, 127]. These particles deposit all their energy in the ECAL by initiating an electromagnetic shower via bremsstrahlung and e^+e^- pair production [127]. Electrons are identified as charged tracks that point to a compact, high-energy deposit in the ECAL [127].

The hadronic calorimeter (HCAL) surrounds the ECAL and is built to absorb hadrons and measure their energy through hadronic interactions [95, 106]. High-energy quarks and gluons hadronize into collimated sprays of hadrons known as **jets**. The energy of jets is measured by combining calorimeter deposits with track momenta. The reconstruction of particles using the information of the different detector subsystems is formalized in particle-flow reconstruction [111, 124, 126].

Muons are unique as they can penetrate the calorimeters; a dedicated muon system outside the calorimeters identifies and measures muons, and muon tracks in the ID are matched to tracks in the muon chambers [95, 128]. Since the detector is nearly hermetic, momentum conservation in the transverse plane is a powerful tool: any significant imbalance (missing transverse momentum, MET) signals undetected neutral particles such as neutrinos or potential dark-matter candidates [126, 133].....AF: Esto es una versión no muy bien escrita del párrafo de abajo. Sugiero quitar.

Since the detector is nearly hermetic (covering almost the full solid angle), momentum conservation in the plane transverse to the beam line (x-y plane) is a powerful tool. The vector sum of the momenta in the transverse plane ($\vec{p}_T$) of all detected particles should be zero. Any significant imbalance indicates the presence of undetected neutral particles that did not interact with the detector, such as neutrinos or new hypothetical dark matter particles. This imbalance is referred to as missing transverse momentum ($\vec{p}_T^{\,\text{miss}}$) and is formally defined as:

$$\vec{p}_T^{\,\text{miss}} \equiv -\sum_i \vec{p}_{T,i}, \tag{2.1}$$

where the sum runs over all reconstructed particles (e.g., leptons, photons, jets) or calorimeter deposits in the event.

The detector design, optimized for identifying and measuring SM particles, also makes it a powerful instrument to search for BSM physics.

2.1.1 COLLISION PARAMETERS

One of the main objectives of particle physics experiments is to quantify how frequently different processes occur and to characterize the properties of the particles involved. The expected rate of a given process, either from the SM or from new physics, is quantified using production **cross-sections**, a theoretical estimate, and the **luminosity**, a parameter that accounts for the amount of data delivered by the accelerator.

In essence, the cross-section (σ) quantifies the probability for a specific process to occur. Formally, it represents the effective area of a target particle presented to an incoming beam particle for an interaction to happen. It has units of area, typically barn (b), where $1\,\text{b} = 10^{-28}\,\text{m}^2$.

In the context of pp collisions at the LHC, the concept is generalized. Since both colliding particles are composite, the cross-section for a specific process is calculated by considering the interactions between their constituent partons (quarks and gluons). The total cross-section for a process $pp \to X$ is given by the convolution of the PDFs and the partonic cross-section $\hat{\sigma}_{ij\to X}$:

$$\sigma(pp \to X) = \sum_{i,j} \int_0^1 dx_1 dx_2\, f_i(x_1, \mu_F^2) f_j(x_2, \mu_F^2)\, \hat{\sigma}_{ij\to X}(\hat{s}, \mu_F^2, \mu_R^2), \quad (2.2)$$

where:

- the sum runs over all possible parton types i, j (e.g., u, d, g) in the two protons.
- $f_i(x, \mu_F^2)$ is the PDF, representing the probability density to find a parton of type i carrying a fraction x of the proton's momentum at a factorization scale μ_F.
- $\hat{s} = x_1 x_2 s$ is the square of the center-of-mass energy for the colliding partons, with s being the square of the pp center-of-mass energy (e.g., 13.6 TeV).
- μ_R is the renormalization scale.
- $\hat{\sigma}_{ij\to X}$ is the partonic cross-section for the hard scattering process $ij \to X$.

Then, on one side, the cross-section σ is a theoretical quantity that encapsulates the fundamental physics of the interaction, independent of the accelerator's performance. On the other side, the **luminosity** ($\mathcal{L}$) is a property of the particle accelerator and beams. It measures the density of particles in the colliding beams and thus the rate at which interactions can occur. The instantaneous luminosity is defined by:

$$\mathcal{L} = \frac{\mathcal{F} n_1 n_2}{4\pi\sigma_x\sigma_y}, \quad (2.3)$$

where $\mathcal{F}$ is the revolution frequency of the bunches, n_1 and n_2 are the numbers of particles in each bunch, and σ_x and σ_y are the transverse dimensions of the beams at the interaction point. The integrated luminosity is the integral of the instantaneous luminosity over time:

$$L = \int \mathcal{L}\, dt. \quad (2.4)$$

The primary unit of integrated luminosity is the inverse barn (b^{-1}), commonly fb^{-1}.

Theoretically, the expected number of events of a SM or BSM process is estimated as

$$N_{\text{theory}} = \sigma \cdot L. \tag{2.5}$$

Under the context of a collider experiment one has to include the detector acceptance and efficiency of the particle identification and selection criteria used to discriminate the signal of interest among other processes. The variable ϵ is defined as the product of the acceptance ($\mathcal{A}$) and the cumulative efficiency of all the selection criteria used to estimate the signal rate above the backgrounds:

$$\epsilon = \left(\prod_i \epsilon_i\right) \times \mathcal{A}. \tag{2.6}$$

Therefore, the expected number of events of a process of interest, for either a SM or BSM process, is estimated using the following equation [106, 126]:

$$N = \sigma \cdot L \cdot \epsilon. \tag{2.7}$$

Equation 2.7 allows one to estimate the expected number of observed events, accounting for reconstruction, particle identification, detector resolution, and acceptance effects, among other experimental considerations [126].

Note that the integrated luminosity L is a parameter that can be measured from the accelerator's performance [113], while ϵ can be estimated using information from the detector calibration and simulation (including event generation, parton shower, and detector simulation) [104, 106, 110]. For a known process, if we know the expected number of events, we can use Equation 2.7 and solve for σ to extract a measurement of the production rate, through a statistical interpretation based on likelihood methods [98].

In the case of searches for BSM physics, we calculate the expected background N_{bkg} from known SM processes using Monte Carlo and data-driven techniques [104, 111]. Then, one studies the agreement in the event rates and shapes of various kinematic and topological distributions of interest, between the observed number of events in data (N_{obs}) and the expected backgrounds from SM processes. Any significant deviation in a specific region in one of the relevant observables, for example in a reconstructed mass, $N_{\text{obs}} - N_{\text{bkg}}$, can be interpreted as a potential signal. Then, the significance of such difference—both local and global—can be determined using a profile-binned likelihood test, to determine the probability that a signal process of interest explains, within the associated statistical and systematic uncertainties, the discrepancy between data and the background [136–139].

2.2 JETS RECONSTRUCTION

Quarks and gluons are never observed as free particles because of colour confinement [140, 141]. Nevertheless, perturbative QCD treats them as the relevant short-distance degrees of freedom: factorization theorems and asymptotic freedom justify computing hard-scattering matrix elements for incoming and outgoing partons, even though QCD becomes non-perturbative at low scales [131]. The strong coupling α_s grows large and effectively "blows up" around the confinement scale Λ_{QCD} [21]. Consequently, something must happen to quarks and gluons before they reach the detector [110]. In practice, gluons and quarks, except for the top, hadronize producing cascades of baryons and mesons that themselves undergo further decays. Hadronization is modeled e.g. with the Lund string or cluster models [110, 140, 141]. At the LHC, these hadrons typically carry energies comparable to the electroweak scale, and relativistic boosts tend to collimate their decay products into narrow bunches [142]. Those collimated collections of hadrons are the jets we measure at hadron colliders and the objects we use to infer the partons produced in the hard interaction [124, 142].

Each high-energy parton produced in a collision, such as a quark from the process $gg \to q\bar{q}$, undergoes hadronization over a distance scale of $\sim 10^{-15}$ m, producing a jet of hadrons [110, 140]. The energy composition of these jets is phenomenologically well established and is the basis of particle-flow reconstruction: on average roughly $\sim 60\%$ of the jet energy is carried by charged particles (mostly $\pi^{\pm}, K^{\pm}$), $\sim 30\%$ by photons (from $\pi^0 \to \gamma\gamma$) and $\sim 10\%$ by neutral hadrons [126]. In high-energy jets, the particles can be too collimated to be resolved individually in coarse calorimeter segmentation. Nevertheless, the jet four-momentum is reconstructed from clustered PF candidates or calorimeter deposits and then corrected using jet energy corrections derived from simulation and in-situ data [106, 111, 126].

Phenomenologically one usually assumes that each high-energy parton yields a jet and that the measured jet four-momentum can, to useful accuracy, be related to the original parton four-momentum [143, 144]. Jets are therefore defined operationally using recombination (clustering) algorithms such as Cambridge–Aachen [145] or the (anti-)kT family [124]. Experimentally this means grouping a large number of energy depositions (or particle-flow candidates) observed in the calorimeters and tracker into a much smaller set of jets or sub-jets [126]. Nothing in the raw detector data, however, indicates a priori how many jets there should be: the clustering procedure and the choice of a resolution scale fix the outcome [142]. In practice one must either specify the desired number of final jets or choose a resolution/stop criterion (for example a distance parameter R, a clustering distance cut, or a jet-mass/sub-jet-resolution threshold) that determines the smallest substructure to be considered a separate parton-like object [146].

Modern reconstruction techniques at the LHC typically use PF candidates as input together with infrared- and collinear-safe clustering algorithms to define jet four-momenta [111, 126]. The anti-k_T algorithm [124], implemented in `FastJet` [111], is widely used in ATLAS and CMS; it groups candidates by proximity in the rapidity–azimuth (y, ϕ) plane with a typical distance parameter $R \sim 0.4$–0.6 and is relatively insensitive to soft radiation and pileup when combined with area-based subtraction techniques [147]. After clustering, jet energy corrections (JEC) derived from simulation and in-situ calibrations compensate for detector response, pileup, and underlying-event effects [148], while jet-substructure and tagging algorithms (mass-drop, N-subjettiness, SoftDrop, etc.) help infer the flavour and origin of the initiating parton [146, 149, 150].

2.2.1 JET ALGORITHMS

Recombination (or sequential clustering) algorithms formalise the intuitive idea that parton showering produces collinear and soft splittings [142, 143, 145]: two nearby and kinematically compatible sub-jets are merged if they are more likely to have originated from a single parton [143, 145]. A practical implementation requires a measure of "distance" between objects [111, 143]; common choices combine an angular separation in the rapidity–azimuth plane, ΔR_{ij}, with a transverse-momentum weighting [124, 143]. Typical distance measures are [124, 143, 145]

$$\begin{aligned}
k_T: &\quad y_{ij} = \frac{\Delta R_{ij}}{R}\min(p_{T,i}, p_{T,j}), &\quad y_{iB} = p_{T,i},\\
C/A: &\quad y_{ij} = \frac{\Delta R_{ij}}{R}, &\quad y_{iB} = 1,\\
\text{anti-}k_T: &\quad y_{ij} = \frac{\Delta R_{ij}}{R}\min(p_{T,i}^{-1}, p_{T,j}^{-1}), &\quad y_{iB} = p_{T,i}^{-1}.
\end{aligned} \tag{2.8}$$

The parameter R balances jet–jet and jet–beam criteria and sets the geometric size of jets. In LHC analyses, typical values are $R \sim 0.4$–0.7 depending on the physics target [111].

Two operational modes are useful to distinguish. In an exclusive algorithm, one supplies a resolution scale y_{cut} and proceeds iteratively:

1. compute $y^{min} = \min_{i,j}\{y_{ij}, y_{iB}\}$;
2. if $y^{min} = y_{ij} < y_{cut}$ merge i and j and repeat;
3. if $y^{min} = y_{iB} < y_{cut}$ remove i as beam radiation and repeat;
4. stop when $y^{min} > y_{cut}$ and keep remaining sub-jets as jets.

An inclusive algorithm omits y_{cut} and instead declares a sub-jet a final-state jet when its jet–beam distance is the smallest quantity; iteration continues until no inputs remain. Inclusive algorithms therefore produce a variable number of jets, while exclusive algorithms deliver a scale-dependent fixed set.

A practical question is how to combine the kinematics of merged objects. The most common choice in modern experiments is the E-scheme: four-vectors are added, which preserves energy–momentum and yields a physical jet mass useful for substructure and boosted-object tagging. An alternative is to sum three-momenta and rescale the energy to enforce a massless jet. This might be appropriate when the analysis targets massless parton kinematics, but it discards potentially useful jet-mass information.

From a theoretical and experimental perspectives, the infrared and collinear safety considerations are important properties: a jet algorithm should yield stable results under the emission of soft particles or collinear splittings. The k_T, C/A, and anti-k_T families are constructed to satisfy these requirements. For practical use, these algorithms have the following particular properties: the k_T technique naturally follows the physical shower history through soft-first clustering, while the C/A has a purely geometric approach, useful for declustering and substructure studies, and lastly the anti-k_T approach produces regular cone-like jets that are experimentally robust and convenient.

Corrections for PU and underlying events are necessary at the LHC. These corrections depend on the jet area and are typically performed by estimating an event-wide transverse-momentum density and subtracting the corresponding contribution proportional to the jet area. Finally, because inclusive algorithms can produce jets arbitrarily close to the beam, a minimum jet p_T threshold, commonly ranging between 20–100 GeV, depending on the analysis, is imposed to ensure experimental observability and theoretical control.

2.2.2 τ tagging at multipurpose detectors

The τ lepton decays hadronically with a probability of $\sim 65\%$, producing a narrow "τ-jet" that contains only a few charged and neutral hadrons [21, 151]. Hadronic τ decays are dominated by one- and three-prong topologies and often include neutral pions that promptly decay to photon pairs, giving a sizable electromagnetic fraction in the calorimeters [21, 152]. When the τ momentum is large compared to its mass, the decay products are highly collimated [117, 151]: for $p_T > 50$ GeV roughly 90% of the visible energy is contained within a cone of radius $R = \sqrt{(\Delta\eta)^2 + (\Delta\varphi)^2} = 0.2$ [151]. These properties motivate the use of small signal cones and narrow isolation annuli in reconstruction [117, 151].

Identification algorithms exploit three complementary classes of observables [117, 126, 151, 152]:

- Calorimetric isolation and shower-shape variables [151, 152]: hadronic τ decays are characterized for localized energy deposits (showers) in the calimetry system (in the ECAL+HCAL subdetectors) [151]. Experiments use isolation sums and shape ratios to quantify peripheral activity [151, 152]. Example variables are

$$\Delta E_T^{12} = \frac{\sum_{0.1<\Delta R<0.2} E_{T,j}}{\sum_{\Delta R<0.4} E_{T,i}}, \quad P_{\text{ISOL}} = \sum_{\Delta R<0.40} E_T - \sum_{\Delta R<0.13} E_T, \quad (2.9)$$

  which suppress jets from QCD processes that populate the isolation ring [151].

- Charged-track isolation and prong topology [126, 151]: the few, collimated charged tracks of a τ jet candidate allow powerful selections. A common procedure defines a matching cone of radius R_m around the calorimeter jet axis to select candidate tracks above a p_T^{min} threshold. The leading track (tr_1) defines a narrow signal cone R_S (1- or 3-prong hypotheses) and a larger isolation cone R_I is scanned for additional tracks [126, 151]. The scalar sum of the p_T of all tracks between the tr_1 cone and the isolation cone, is expected to be small compared to the p_T of the leading track.

- Lifetime and vertexing observables [21, 129]: the finite τ lifetime ($c\tau \approx 87$ μm) produces displaced tracks and, for multi-prong decays, a reconstructible secondary vertex. Impact-parameter significances and secondary-vertex properties are exploited to separate genuine τ_h from prompt jets or leptons [21, 129].

Additional discriminants include the invariant mass of the visible decay products computed from tracks and calorimeter clusters, electromagnetic energy fractions (sensitive to $\pi^0 \to \gamma\gamma$), and dedicated shower-strip grouping for nearby photons. For example, invariant-mass reconstruction commonly uses a jet cone $\Delta R_{jet} \lesssim 0.4$ while excluding calorimeter clusters matched to tracks by a minimum separation $\Delta R_{track} \gtrsim 0.08$ to reduce double counting.

Reconstruction algorithms combine these inputs. CMS's Hadron-Plus-Strips (HPS) algorithm explicitly builds decay-mode hypotheses and uses strip-clustering of photons, complemented by modern methods using multivariate or deep-learning discriminators (DeepTau) to reject jets, electrons, and muons [117, 153]. ATLAS employs analogous calorimeter+track based MVAs and BDTs [154]. Typical working points trade efficiency versus background: medium points often give τ_h efficiencies of order 50–70% with light-jet misidentification rates in the per-mille to percent range, depending on kinematics and PU.

Practical implementations tune cone sizes, isolation thresholds, and MVA inputs to the kinematic region and analysis goals. The choice of working point is driven by the signal-to-background optimization for the search or measurement at hand.

2.2.3 B TAGGING AT MULTIPURPOSE DETECTORS

Jets originating from bottom quarks (b-jets) exhibit several distinctive properties that enable their identification. The relatively long lifetime of b hadrons (order 1.5 ps) produces displaced charged tracks and often reconstructible secondary vertices a few millimetres from the primary interaction point. The large b-hadron mass yields decay products with sizable transverse momentum relative to the jet axis, and semileptonic branching fractions produce soft electrons or muons inside the jet. These features form the basis for b-tagging [155].

Practical algorithms exploit individual signatures or combine them:

- **Track-counting:** counts tracks with large impact-parameter significance to identify a b-like topology [155].
- **Jet-probability:** evaluates the compatibility of the jet's track impact-parameter distribution with the primary vertex hypothesis [155].
- **Secondary-vertex:** explicitly reconstructs displaced vertices and uses their kinematic properties (decay length significance, vertex mass) [155].
- **Soft-lepton taggers:** identify low-p_T leptons inside jets from semileptonic b decays [155].

Modern taggers combine many observables in multivariate or deep learning classifiers to maximize discrimination power. Contemporary approaches exploit rich, low-level inputs (track by track and PF candidate information, vertex features and kinematics) and advanced network architectures (DeepCSV/DeepJet, RNN/sequence, graph/set networks) [116, 154, 155]. These developments yield measurable performance gains: modern deep classifiers typically improve b efficiency at fixed mistag rate relative to classical taggers and allow continuous discriminants with tunable operating points. Calibration with data-driven scale factors (from $t\bar{t}$, multijet or dilepton control samples) and propagation of associated systematic uncertainties remain essential for physics results [155].

- Deep feed-forward networks (e.g. DeepCSV/DeepJet) ingest a large set of high-level and per-track inputs to produce powerful binary or multi-class discriminants that separate b, c and light-flavour jets.
- Sequence models and recurrent networks (RNN-based taggers) process an arbitrary ordered list of track-level variables, improving sensitivity by directly exploiting per-track correlations and order-dependent information (impact-parameter sequences, track kinematics).
- Graph- and set-based architectures and combined particle+vertex networks (sometimes referred to as "DeepFlavour"-style models) aggregate heterogeneous inputs and return per-flavour probabilities, enabling natural multi-classification and calibrated operating points.

These developments yield measurable performance gains: modern deep classifiers typically improve b identification efficiencies at fixed mistag rates (or reduce mistag rates at fixed efficiency) relative to classical taggers. The continuous output of such networks permits analyses to choose operating points (loose/medium/tight) corresponding to desired efficiencies or mistag rate targets. Calibration remains essential: data-driven scale factors derived from control samples (e.g. $t\bar{t}$, multijet, dilepton) are applied to correct simulation, and systematic uncertainties from the calibration, flavour composition, and kinematic extrapolation are propagated to physics results.

Examples in use are CMS DeepCSV / DeepJet and ATLAS MV2 / DL1 [117, 154], which illustrate the transition from expert-designed high-level variables to large-scale machine learning leveraging low-level detector information. Typical medium working points yield b-tag efficiencies of order 60–80% with light-jet misidentification rates at or below the percent level. The precise choice of working point is tuned per analysis to optimize sensitivity while accounting for calibration and systematic uncertainties.

2.3 THE CMS DETECTOR

As previously mentioned, CMS is a general-purpose detector at the LHC [156]. The detector has a length of 21.6 m, a diameter of 14.6 m, and a weight of 14,000 tonnes. Its cylindrical geometry is divided into a central barrel section and two endcaps. This design provides hermetic coverage to accurately measure momentum and energy balance, which is crucial for identifying non-interacting particles such as neutrinos, through missing transverse energy.

The detector is constructed from concentric layers of sub-detectors, as illustrated in Fig. 2.5. The innermost component is the silicon tracker, comprising a pixel detector and silicon strip tracker. It reconstructs the trajectories of charged particles and measures their p_T with a resolution of $\approx 0.7\%$ for 10 GeV particles within a pseudorapidity range of $|\eta| < 2.5$.

Surrounding the tracker is the calorimeter system (ECAL and HCAL). The ECAL is made of dense lead-tungstate crystals. It is designed to measure electrons and photons with a high resolution of $\approx 0.6\%$ for 50 GeV electrons. The HCAL detector, located outside the ECAL, is a brass-scintillator sampling calorimeter that measures hadrons (e.g., charged pions, kaons, protons) with an energy resolution of $\approx 18\%$ for 50 GeV pions. Together, the ECAL and HCAL cover $|\eta| < 3$. The coverage is extended to $|\eta| < 5$ with steel and quartz-fiber hadron calorimeters in the forward regions.

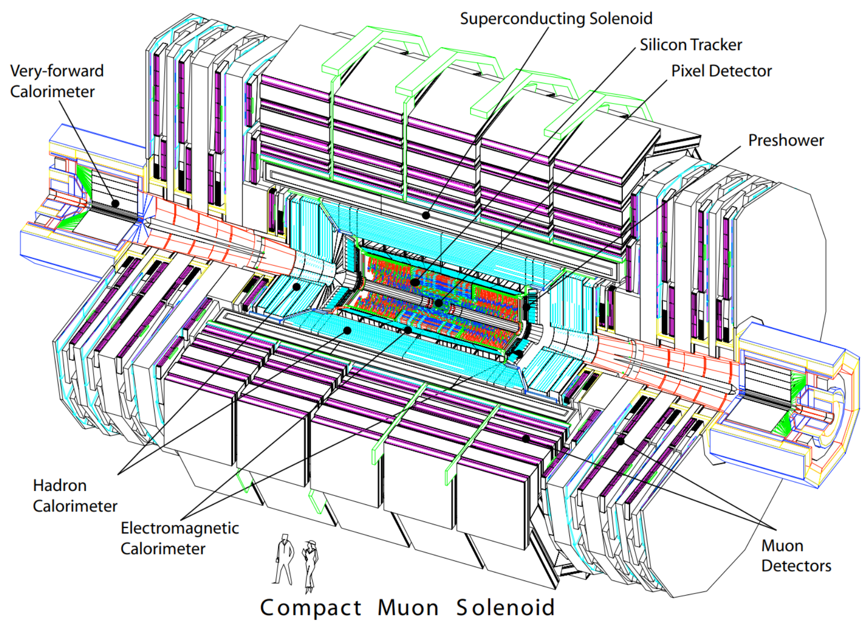

Figure 2.5: Layout of the CMS experiment at the CERN LHC. (retrieved from [156]).

A key feature of CMS is its large superconducting solenoid, which encloses the tracker and calorimeters. The solenoid is constructed from a niobium-titanium alloy and cooled to 4.2 K with liquid helium. It generates a uniform magnetic field of 3.8 T throughout the tracking volume, enabling precise momentum measurement from the curvature of charged particle tracks.

The outermost system is dedicated to the identification of muon objects. Gas-based ionization detectors are embedded in the steel flux-return yoke that surrounds the solenoid. This system provides triggering and tracking capabilities for muons up to $|\eta| < 2.4$. The combination of the inner tracker and the muon system allows for a robust identification and momentum measurement of muons across a wide kinematic range.

The geometrical segmentation of the barrel and endcaps defines the detector's acceptance in terms of pseudorapidity. The central barrel provides optimal coverage for $|\eta| \lesssim 1.5$, while the endcaps extend the acceptance to $|\eta| \lesssim 2.5$ for the tracker and calorimeters, and to $|\eta| \lesssim 2.4$ for the muon system.

This segmentation impacts the detection efficiency. The silicon trackers are highly efficient in the barrel, where particles cross the layers perpendicularly. In the endcaps, the reduced hit multiplicity from shallow-angle traversals leads to a slight decrease in tracking efficiency and resolution. The calorimeters are also optimized to maintain performance across η, though the material budget and granularity vary.

Muon reconstruction performance exhibits regional differences. In the barrel, drift tubes (DTs) provide high spatial resolution, while in the endcaps, cathode strip chambers (CSCs) and resistive plate chambers (RPCs) are used to handle higher background rates and non-uniform magnetic fields. The assumed identification efficiency for muons (electrons) is 95% (85%), with a mis-identification rate of 0.3% (0.6%) [121, 127, 128].

For the identification of heavy-flavor jets, we adopt the DeepCSV algorithm [155]. In our simulated data, we use the value corresponding to the "medium" working point, which provides a b-tagging efficiency of 70% with a light-flavor jet misidentification rate of approximately 1% across the entire p_T spectrum. The "loose" (85% efficiency, 10% mis-id) and "tight" (45% efficiency, 0.1% mis-id) working points were also explored during the analysis optimization.

For hadronically decaying τ leptons (τ_h), we use the DeepTau algorithm [117], which employs a deep neural network combining isolation and lifetime information to identify τ_h decay modes, as explained in Section 2.2.2. The "medium" working point is chosen for this analysis, providing a τ_h identification efficiency of 70% and a misidentification rate of 0.5% for jets originating from light quarks and gluons. This working point was selected through an optimization process that maximized the discovery reach of the analysis.

2.4 PHENOMENOLOGICAL PIPELINE

The estimation of signal and background event yields is performed through a comprehensive Monte Carlo (MC) simulation pipeline [104, 105, 157, 158]. This approach, a cornerstone of high-energy physics research, enables robust studies of BSM scenarios by emulating the entire data collection and processing chain of a collider experiment [106, 110]. The key advantages of this methodology include [104, 111]:

- The ability to perform automated calculations of theoretical quantities such as cross-sections and decay widths for complex processes.
- Conducting feasibility studies and optimizing analysis strategies prior to data acquisition.
- Estimating the efficiency of complex event selection criteria and the geometric acceptance of the detector.
- Predicting the rates and kinematical distributions of both irreducible and reducible background processes.
- Comparing and distinguishing between different theoretical hypotheses for a potential discovered signal.

The simulation workflow is modular, reflecting the logical progression from a theoretical Lagrangian to simulated detector-level observables [104, 105, 157, 158]. A schematic view of this pipeline is presented in Fig. 2.6 [104, 106].

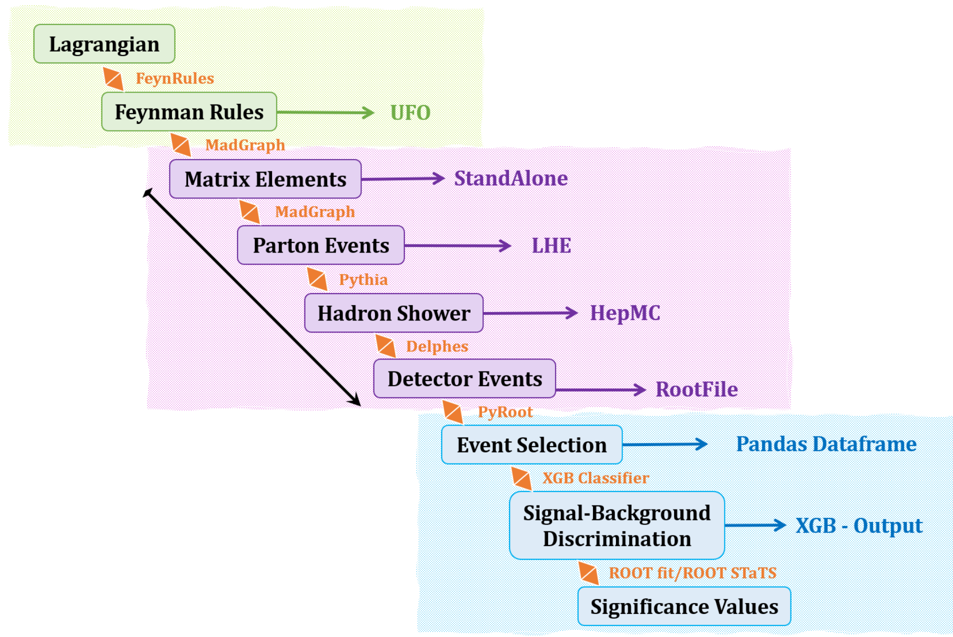

Figure 2.6: Schematic overview of the phenomenological MC pipeline: model definition (FeynRules) -> UFO export -> matrix-element generation (MadGraph) -> parton shower and hadronization (PYTHIA) -> fast detector simulation (DELPHES) -> analysis ntuples (ROOT).

The process begins with the implementation of the theoretical model in `FeynRules` (v2.3.43) [105, 157]. The Lagrangian of the new physics scenario, including all particle definitions, parameters, and interactions, is translated into a set of Feynman rules and exported in the Universal FeynRules Output (UFO) format [158], interoperable with modern matrix-element generators [104].

This UFO module, accompanied by a parameter card defining numerical values for masses and couplings, serves as input to `MadGraph5_aMC@NLO` (v3.5.7) [104, 159]. Within `MadGraph`, the hard process and corresponding matrix elements are generated and stored in Les Houches event (LHE) files. The PDF choices (here NNPDF3.0 NLO [112]) and matching/merging settings (MLM/CKKW-type) are configured to control radiation and multi-jet overlap [160, 161]. Parton-level LHE events are passed to `PYTHIA 8` for showering, hadronization and decays [110], and the generator output is exchanged in HepMC format for downstream processing [162].

To accurately model processes featuring significant interference effects between the new physics signal (e.g., a Z' boson) and the SM backgrounds, the full squared amplitude (often referred to as the Signal-Discriminated Events or SDE strategy) is employed for the phase-space integration. The `MadEvent` submodule then generates unweighted parton-level events, which are stored in the LHE format, containing the four-momenta of all final-state particles. The generation is optimized through careful configuration of the `run_card`, setting appropriate kinematic cuts on final-state partons to avoid wasting computational resources on events that would subsequently be rejected by the detector simulation.

Given the presence of additional jet radiation, the MLM matching scheme [160] is applied to mitigate the double-counting of jet emission between the matrix element calculation and the subsequent parton shower. This ensures a smooth transition between the hard process and softer radiative effects.

The parton-level LHE events are then passed to PYTHIA (v8.2.44) [110] for the modeling of QCD and QED radiation (parton showering), hadronization, and particle decays. This step translates the colored partons into stable, color-singlet hadrons and resonances that form the observable final state. The resulting events, which include a full list of generator-level particles, are saved in the HepMC2 format.

Detector effects are simulated using DELPHES (v3.4.2) [106], a fast parametric detector simulation framework. The `delphes_card_CMS.tcl` configuration card is used to emulate the response of the CMS detector, including the geometric acceptance, tracking efficiency, calorimeter energy resolution and segmentation, and the inner and outter magnetic field. Key reconstruction algorithms are applied within DELPHES:

- Jets are clustered from calorimeter towers using the anti-k_t algorithm [124] with a distance parameter of $R = 0.4$, and b-tagging is simulated based on the efficiency and mis-tag rate of the CMS performance.

- Muons and electrons are identified with efficiency maps that are functions of p_T and η.

- The $\vec{p}_T^{\,\text{miss}}$ is calculated from the negative vector sum of all reconstructed particle momenta, as it was defined in Equation 2.1.

The final output, containing reconstructed physics objects (jets, leptons, $|\vec{p}_T^{\,\text{miss}}|$), is stored in ROOT format [163].

At this stage, the analysis of the simulated samples converges with the methodology applied to real collider data. The subsequent steps involve applying event selection criteria, calibrating and scaling the reconstructed objects (e.g., applying Jet Energy Corrections), and performing statistical interpretation. The reliability of the simulation is validated by comparing the modeling of well-known SM processes (e.g., Drell-Yan, $t\bar{t}$ production) against published results and data-driven control regions. Dominant theoretical systematic uncertainties, such as those arising from the choice of factorization and renormalization scales, PDF variations, and parton shower modeling, are evaluated and propagated through the analysis.

2.5 MEASUREMENT OF THE POWER OF AN ANALYSIS

In high energy physics experiments, data is often discretized into bins (e.g., histograms of collision events versus energy or momentum) to test competing hypotheses [164]. The fundamental framework compares two scenarios: the *null hypothesis* (H_0), representing background-only processes (only a b_i number of events in each bin i), and the *alternative hypothesis* (H_1), including both signal (s_i) and background events ($s_i + b_i$) [165]. Event counts (n_i) in a collider experiment follow a Poissonian distribution. Therefore, the likelihood for observing the data under each hypothesis is the product of Poisson probabilities per bin. And, because of this, it is written as a binned-likelihood [98, 164]:

$$\mathcal{L}(n_i \mid \lambda_i) = \frac{e^{-\lambda_i}\lambda_i^{n_i}}{n_i!}, \quad \text{where } \lambda_i = \begin{cases} b_i & \text{for } H_0, \\ s_i + b_i & \text{for } H_1. \end{cases} \tag{2.10}$$

The Neyman-Pearson lemma [139, 165] provides a rigorous framework for hypothesis testing by establishing that the *likelihood ratio* $Q = \mathcal{L}(\text{data} \mid H_1)/\mathcal{L}(\text{data} \mid H_0)$ is the most powerful test statistic for distinguishing between two simple hypotheses, H_0 and H_1 [98, 165]. This forms the basis for quantifying the evidence for new physics signals against known backgrounds [98, 136]. For binned analyses in particle physics, we define the likelihood ratio Q_i for each bin i as [98, 164],

$$Q_i = \frac{\mathcal{L}(n_i \mid s_i + b_i)}{\mathcal{L}(n_i \mid b_i)} = e^{-s_i}\left(1 + \frac{s_i}{b_i}\right)^{n_i}, \tag{2.11}$$

where n_i is the observed event count, s_i the expected signal, and b_i the expected background in bin i, as explained before [98, 164].

The test for the full analysis is constructed as the product of individual bin likelihood ratios [98, 164]:

$$Q = \prod_{i=1}^{N} Q_i, \tag{2.12}$$

where N is the total number of bins [164]. Under this formulation, each bin is treated as an independent experiment, allowing us to analyze the data in a modular way. This is convenient when combining results from multiple search channels or energy ranges [98, 136].

For convenience and to connect with asymptotic results, one commonly works with the log-likelihood ratio:

$$-2\ln Q = 2\sum_{i=1}^{N}\left[s_i - n_i \ln\left(1 + \frac{s_i}{b_i}\right)\right], \tag{2.13}$$

and, by Wilks' theorem, its asymptotic distribution under the null hypothesis is chi-square distributed in regular cases [98, 166].

In practice, the Neyman-Pearson lemma motivates the use of a test statistic t that quantifies the evidence for a signal against the background-only hypothesis, which can be written as

$$t = -2\ln Q = \sum_{i=1}^{N}\left[2s_i - 2n_i w_i\right], \tag{2.14}$$

with the optimal weight of each bin given by $w_i = \ln\left(1 + \frac{s_i}{b_i}\right)$.

The discovery significance κ quantifies the statistical separation of t if n is distributed according to the background-only hypothesis (H_0) versus the signal-plus-background hypothesis (H_1), normalized by the standard deviation of the H_1 distribution (σ_{H_1}),

$$\kappa = \frac{\langle t \rangle_{H_0} - \langle t \rangle_{H_1}}{\sigma_{H_1}}. \tag{2.15}$$

The expected behavior differs under the signal-plus-background (H_1) and background-only (H_0) hypotheses:

- **Under** H_1 we expect that the n_i data distribution follows $\text{Pois}(s_i + b_i)$:

$$\langle -2\ln Q \rangle_{s+b} = \sum_i \left[2s_i - 2(s_i + b_i)w_i\right] \implies \sigma^2_{s+b} = 4\sum_i (s_i + b_i)w_i^2. \tag{2.16}$$

- **Under** H_0 we expect that the n_i data distribution follows $\text{Pois}(b_i)$

$$\langle -2\ln Q \rangle_{b} = \sum_i \left[2s_i - 2b_i w_i\right] \implies \sigma^2_{b} = 4\sum_i b_i w_i^2 \tag{2.17}$$

Substituting in κ gives a useful expression for the discovery significance,

$$\kappa = \frac{\sum s_i w_i}{\sqrt{\sum (s_i + b_i) w_i^2}} \tag{2.18}$$

It quantifies the separation between the signal+background ($s + b$) and the background-only hypotheses in units of standard deviations (σ), where $\kappa = 5$ corresponds to the traditional 5σ discovery threshold, $\kappa = 3$ to a 3σ evidence to the traditional anomaly detection threshold, and $\kappa = 1.69$ to the 95% confidence level (CL) exclusion limit.

This figure of merit automatically optimizes sensitivity through the logarithmic weights $w_i = \ln(1 + s_i/b_i)$, which naturally emphasize bins with either high signal-to-background ratios (s_i/b_i) or large absolute signal contributions (s_i). In asymptotic limits, κ simplifies to intuitive forms: for dominant signals ($s_i \gg b_i$), it approaches $\sqrt{\sum s_i}$ (Poisson counting), while in background-dominated regimes ($s_i \ll b_i$), it reduces to an inverse-variance-weighted sum $\sum s_i / \sqrt{\sum b_i (s_i/b_i)^2}$. This dual behavior ensures optimal discrimination power across all signal regimes.

In practice, we must take into account systematic effects by incorporating nuisance parameters into the likelihood and profiling over uncertainty ranges. The power calculation can be extended to include systematic uncertainties by modifying the denominator as,

$$\boxed{\kappa_{\text{sys}} = \frac{\sum_i s_i w_i}{\sqrt{\sum_i \left[(s_i + b_i) + \delta^2_{\text{sys,signal},i} + \delta^2_{\text{sys,bkg},i}\right] w_i^2}},} \tag{2.19}$$

where δ_{sys} terms represent the systematic uncertainties on signal and background predictions.

This framework not only provides a figure of merit for an analysis but also serves as a roadmap for experimental optimization. The expected signal and background in each bin, s_i and b_i, are not fundamental inputs but are themselves products of the experimental setup and analysis choices. They can be expressed in terms of more fundamental experimental parameters (with acceptance absorbed into the selection efficiencies):

$$s_i = \sigma_{s,i} \cdot L \cdot \epsilon_{s,i},$$
$$b_i = \sigma_{b,i} \cdot L \cdot \epsilon_{b,i},$$

where, following Equation 2.7, $\sigma_{s,i}$ and $\sigma_{b,i}$ are the fiducial cross-sections for signal and background processes in bin i, L is the integrated luminosity, and $\epsilon_{s,i}$ and $\epsilon_{b,i}$ are the cumulative or total efficiencies (selection efficiency combined with detector acceptance and reconstruction effects).

Substituting these expressions into the significance κ reveals the multi-dimensional parameter space available for optimization:

$$\kappa = \frac{\sum_i \sigma_{s,i} \cdot \epsilon_{s,i} \cdot w_i}{\sqrt{\sum_i \left[(\sigma_{s,i}\epsilon_{s,i} + \sigma_{b,i}\epsilon_{b,i}) + \delta_{sys}^2\right] \cdot w_i^2}} \cdot \sqrt{L}.$$

This decomposition shows that the discovery significance can be enhanced through several distinct strategies. The primary handles are:

- **Increasing integrated luminosity** (L): The $\sqrt{L}$ scaling represents the fundamental statistical limit - doubling sensitivity requires quadrupling data collection time. This drives the construction of higher-luminosity colliders and longer data-taking campaigns.

- **Reducing systematic uncertainties**: The δ_{sys} terms encompass uncertainties from theoretical predictions, detector calibration, background estimation methods, and luminosity measurement. Their reduction requires dedicated calibration measurements, improved Monte Carlo simulations, and sophisticated data-driven background estimation techniques.

- **Improving detector performance**: Effective efficiencies $\epsilon_{s,i}$ and $\epsilon_{b,i}$ can be improved through better detector design, increased coverage, and enhanced reconstruction and calibration algorithms that recover and correctly identify more signal events while controlling backgrounds.

- **Choosing optimal observables**: The weights $w_i = \ln(1 + s_i/b_i)$ are maximized when the analysis uses variables that provide the best separation between signal and background. This motivates the development of advanced feature engineering and the use of multivariate methods that automatically learn the most discriminating variables.

- **Optimizing selection criteria**: Signal efficiency $\epsilon_{s,i}$ can be maximized while background efficiency $\epsilon_{b,i}$ is minimized through sophisticated trigger algorithms, multivariate analysis techniques, and machine learning classifiers that exploit subtle differences between signal and background event features.

Therefore, the power of an analysis, quantified by κ, is the result of a concerted effort across accelerator operation, detector performance, and analysis strategy.

The key limitation of the binned formulation in Eq. 2.19 is its treatment of bins as independent experiments, which discards valuable information from inter-bin correlations. This approximation becomes particularly evident in regions of high sensitivity, where the shape information of distributions becomes crucial. In such cases, multivariate methods that exploit the full correlation structure (such as matrix element methods, deep learning classifiers, or template fits) typically outperform simple binned significance estimates.

However, the formalism presented here provides theoretical insight and a useful approximation for quick sensitivity estimates. In the asymptotic limit and for counting experiments, this approach yields results consistent with statistical packages commonly used in high energy physics, such as `RooStats` and `RooFit`. These frameworks implement more rigorous statistical procedures that fully account for the likelihood structure, parameter correlations, and systematic uncertainties through nuisance parameters.

Despite this limitation, the κ metric remains invaluable for establishing *experimental sensitivity*, which is defined as the minimum signal strength required to achieve a certain significance level (e.g., 95% CL exclusion or 5σ discovery potential). It provides a practical tool for guiding analysis design, optimizing selection criteria, and prioritizing experimental efforts.

For experimental final results and interpretation, full statistical treatments using profile likelihood methods within frameworks such as `RooStats` remain the gold standard, as they properly account for all correlations and systematic uncertainties. In this work, we are not interested in the final statistical interpretation of data, but rather in understanding and optimizing the experimental sensitivity to new physics signals. Therefore, the κ metric serves as a practical and insightful tool for guiding analysis design and experimental strategy.

2.6 ML ENHANCED SIGNAL-BACKGROUND DISCRIMINATION

As shown in Sec. 2.5, the sensitivity of a search depends on optimally separating signal and background processes [98, 167]. Traditional cut-based analyses, which apply sequential selection criteria to individual observables, cannot fully exploit the discriminatory information contained in the high-dimensional feature space of collision events [167, 168]. In this approach, for an event described by a feature vector $\mathbf{x} = (x_1, x_2, \ldots, x_N)$, event selection criteria are applied in the form [169]

$$\text{Selection:} \quad x_1 > c_1 \text{ AND } x_2 > c_2 \text{ AND } \ldots \text{ AND } x_N > c_N. \tag{2.20}$$

This method has several limitations that become apparent when considering correlations among kinematic variables [167, 168]. A typical LHC event contains a large number of observables, and an optimal discriminator must consider these variables and their correlations simultaneously [114, 169]. Tight event selection criteria might severely limit the available phase space, discarding events that are signal-like in multivariate space but fall just outside univariate boundaries [167, 168]. The challenge of dimensionality also arises, as optimizing many cuts becomes unstable and prone to statistical fluctuations [168, 170]. Finally, sequential cuts cannot capture non-linear relationships and complex decision boundaries that often provide the strongest discrimination [167, 168].

Supervised learning addresses these limitations directly [167, 168]. It learns a function $f(\mathbf{x})$ that maps the high-dimensional input space to a continuous score approximating the posterior probability [171, 172]:

$$f : \mathbb{R}^N \to [0, 1], \quad f(\mathbf{x}) \approx P(\text{signal} \mid \mathbf{x}). \tag{2.21}$$

This score incorporates correlations and non-linearities present in the training data, providing a powerful, continuous discriminant [167, 168].

Formally, the classification problem can be stated as follows [168]. Each collision event is represented by a feature vector $\mathbf{x} = (x_1, x_2, \ldots, x_N)$, where the components correspond to reconstructed kinematic variables or high-level observables [114, 126]. The task is to assign a label

$$y = \begin{cases} 1 & \text{if the event originates from the signal process,} \\ 0 & \text{if the event originates from the background.} \end{cases} \tag{2.22}$$

Rather than predicting a hard label, modern classifiers return a continuous score $f(\mathbf{x}) \in [0, 1]$ that estimates the probability of an event being signal given its features. This formulation allows the classifier to exploit multidimensional correlations and complex decision boundaries that cut-based methods cannot capture [167, 171].

Logistic regression, SVMs [173], Random Forests [174] and boosted trees [170, 175] are common choices; see [168, 169] for comparisons and practical guidance.

Several algorithms are commonly employed in this context. Logistic regression is often used as a baseline due to its simplicity and transparency. It assumes a linear decision boundary in the feature space, with the discriminant

$$f(\mathbf{x}) = \sigma(\mathbf{w} \cdot \mathbf{x} + b), \quad \sigma(z) = \frac{1}{1 + e^{-z}}, \tag{2.23}$$

where $\mathbf{w}$ are model parameters and b is a bias term. While it cannot capture complex non-linear relationships, logistic regression remains useful when signal and background are approximately linearly separable, and it provides a clear reference point against which more sophisticated methods can be compared.

Support Vector Machines (SVMs) instead seek to maximize the margin between signal and background classes. For non-linear problems, SVMs employ kernel functions $K(\mathbf{x}_i, \mathbf{x})$ that implicitly map the inputs to a higher-dimensional space where linear separation becomes possible. The decision function is

$$f(\mathbf{x}) = \text{sign}\left(\sum_{i=1}^{N} \alpha_i y_i K(\mathbf{x}_i, \mathbf{x}) + b\right), \tag{2.24}$$

where α_i are Lagrange multipliers. SVMs are effective in high-dimensional spaces and have strong theoretical guarantees, but they scale poorly to large datasets and are highly sensitive to kernel choice and hyperparameter tuning.

Tree-based ensembles are among the most widely used methods. Random Forests combine multiple decision trees trained on bootstrap samples of the data, with random feature selection at each split:

$$F(\mathbf{x}) = \frac{1}{B} \sum_{b=1}^{B} T_b(\mathbf{x}), \tag{2.25}$$

where B is the number of trees and T_b is the prediction of the b-th tree. This approach reduces variance and mitigates overfitting through averaging. Random Forests are robust, parallelizable, and provide natural feature importance measures, though they typically require more trees than boosted methods and may yield slightly lower performance on well-tuned tasks.

Boosted Decision Trees (BDTs) have become a standard tool in particle physics because they balance interpretability and performance. A single decision tree partitions the feature space through binary splits (e.g., "Is $x_i <$ threshold?") and assigns class probabilities to terminal nodes. On their own, trees are high-variance learners, but boosting combines many weak learners (typically shallow trees) into a strong ensemble:

$$F_M(\mathbf{x}) = \sum_{m=1}^{M} \gamma_m h_m(\mathbf{x}), \tag{2.26}$$

where each new tree $h_m(\mathbf{x})$ corrects the errors of the current ensemble $F_{m-1}(\mathbf{x})$, and γ_m is its weight. This sequential correction process produces a powerful classifier. BDTs are robust to outliers and non-Gaussian distributions, handle mixed variable types naturally, and perform implicit feature selection, often revealing which observables are most discriminating. These properties explain their widespread adoption in LHC analyses.

Finally, Deep Neural Networks (DNNs) represent the most expressive class of models, capable of learning highly complex, hierarchical representations of the input data. A deep network with multiple hidden layers can be written as

$$f(\mathbf{x}) = \sigma^{(L)}\left(W^{(L)}\sigma^{(L-1)}\left(\cdots \sigma^{(1)}(W^{(1)}\mathbf{x} + b^{(1)}) \cdots\right) + b^{(L)}\right), \tag{2.27}$$

where L is the number of layers. DNNs excel at capturing intricate patterns and correlations, but they require large training datasets, careful regularization, and extensive hyperparameter tuning. Their black-box nature also complicates interpretability and the assessment of systematic uncertainties.

In practice, Random Forests are often used as robust, low-maintenance alternatives, while SVMs have largely been superseded by tree-based methods and neural networks due to scalability issues. DNNs can outperform other methods on very complex problems with sufficient data, but they demand significantly more computational resources. For most LHC searches, BDTs—particularly implementations such as XGBoost—provide the best balance between performance, interpretability, and computational efficiency. In Sec. 3.4, and in Tab. 3.3, we compare the performance of different methods and show that the gain in accuracy from DNNs is marginal compared to BDTs, while the training time is substantially larger.

2.6.1 XGBOOST: OPTIMIZED GRADIENT BOOSTING

XGBoost (eXtreme Gradient Boosting) is a widely used implementation of gradient boosting that has become standard in high energy physics due to its efficiency, predictive power, and robustness.

A single decision tree is a weak classifier: it partitions the feature space through binary splits but is highly sensitive to fluctuations in the training data. Boosting addresses this by constructing an ensemble of trees sequentially. At each step, a new tree is trained to predict the residual errors of the current ensemble. This iterative approach allows the classifier to improve gradually, with later trees focusing on events that were previously misclassified.

The algorithm minimizes a regularized objective function:

$$\mathcal{L} = \sum_{i=1}^{n} l(y_i, \hat{y}_i) + \sum_{m=1}^{M} \Omega(f_m), \tag{2.28}$$

where $l(y_i, \hat{y}_i)$ measures the prediction error and $\Omega(f_m)$ penalizes complex trees to prevent overfitting. The regularization term is:

$$\Omega(f) = \gamma T + \tfrac{1}{2}\lambda \|\mathbf{w}\|^2 + \alpha \|\mathbf{w}\|_1, \tag{2.29}$$

where T is the number of leaves, $\mathbf{w}$ are the leaf weights, and γ, λ, α control tree complexity.

The model is built additively:

$$\hat{y}_i^{(t)} = \hat{y}_i^{(t-1)} + \eta f_t(\mathbf{x}_i), \tag{2.30}$$

where η is the learning rate. Each new tree is selected to minimize:

$$f_t = \arg\min_f \sum_{i=1}^{n} \left[g_i f(\mathbf{x}_i) + \tfrac{1}{2} h_i f^2(\mathbf{x}_i) \right] + \Omega(f), \tag{2.31}$$

with g_i and h_i the first and second derivatives of the loss function.

The performance of XGBoost depends on finding the right balance between underfitting and overfitting. Underfitting occurs when the model is too simple to capture the relevant patterns in the data, leading to poor performance on both training and test sets. In this case the model is characterized by high bias and low variance. Overfitting, on the other hand, arises when the model learns the training data too closely, including statistical fluctuations and noise. This yields very good performance on the training set but poor generalization to new data, with the model showing low bias and high variance.

Several hyperparameters play a central role in controlling this balance:

- **n_estimators**: Number of boosting rounds. Too few trees lead to underfitting, while too many lead to overfitting. Early stopping is commonly used to determine the optimal number by monitoring validation performance.

- **Learning rate (η)**: Step size shrinkage applied at each boosting step. Small values (e.g. 0.01–0.1) improve generalization but require more trees; larger values speed up training but can overfit.

- **max_depth**: Maximum depth of individual trees. Shallower trees (4–6) tend to be more stable, while deeper ones (7–10) can capture complex correlations but risk overfitting.

- **Regularization parameters**:

  – γ: Minimum loss reduction required for a split. Larger values make the algorithm more conservative.

  – λ: L2 regularization on leaf weights, which limits large values and stabilizes the model.

  – α: L1 regularization on leaf weights, which promotes sparsity and can serve as implicit feature selection.

Optimal hyperparameters are typically found through systematic search methods. The most common approach is *grid search with cross-validation* (GridSearchCV), which exhaustively tests all parameter combinations within predefined ranges. The core of this method is *k-fold cross-validation*, a robust technique for assessing model generalization.

The k-fold cross-validation procedure consists of the following steps: First, the available training data is randomly shuffled and partitioned into k equal-sized subsets called folds. This partitioning is typically stratified to preserve the class distribution in each fold. Then, the model is trained and evaluated k times in a round-robin fashion. For each iteration i (where i = 1 to k), the i-th fold is held out as validation data, while the remaining k-1 folds are used for training. The model's performance metric (typically negative log-loss, accuracy, or area under the ROC curve) is computed on the validation fold. After all k iterations are completed, the performance scores from each validation fold are averaged to produce a single estimation of the model's generalization error. This approach ensures that every data point is used exactly once for validation while being used k-1 times for training, providing an unbiased estimate of model performance that is robust to the specific partitioning of the data.

For XGBoost in HEP applications, we typically use k= 5 folds as it offers a good balance between computational cost and reliable error estimation. Each parameter combination is evaluated through this cross-validation process, ensuring that selected parameters generalize well beyond the training data and are not overly tuned to specific statistical fluctuations.

The grid search tests all combinations in the parameter space defined by ranges such as: `learning_rate` $\eta \in [0.01, 0.3]$, `max_depth` $\in [3, 10]$, `n_estimators` $\in [100, 1000]$, with regularization parameters γ, λ, and α typically explored in logarithmic scales.

While grid search is thorough, it becomes computationally expensive for high-dimensional parameter spaces. In such cases, more efficient methods like *randomized search* (which samples parameter combinations randomly) or *Bayesian optimization* (which uses probabilistic models to guide the search toward promising regions) can be employed.

The optimization process is iterative: initial broad searches identify promising parameter regions, followed by finer-grained searches around the best-performing configurations. Early stopping during training—monitoring validation performance and halting when no improvement is observed for a specified number of rounds—prevents overfitting and significantly reduces computational cost, making the hyperparameter optimization feasible for large-scale HEP analyses.

2.6.2 STANDARD ML ANALYSIS WORKFLOW

The XGBoost output score $f(\mathbf{x})$ transforms high-dimensional data into a single optimal discriminant. When binned, the resulting histogram gives expected yields:

$$s_i = \int_{\text{bin } i} \sigma_s \cdot \mathcal{L} \cdot \epsilon_s \cdot p_s(f)\, df, \tag{2.32}$$

$$b_i = \int_{\text{bin } i} \sigma_b \cdot \mathcal{L} \cdot \epsilon_b \cdot p_b(f)\, df, \tag{2.33}$$

where $p_s(f)$ and $p_b(f)$ are the output distributions.

Integrating machine learning into high-energy physics analysis follows a standardized workflow designed to maximize sensitivity while ensuring robustness against overfitting and systematic biases:

1. **Dataset Preparation and Balancing**: Monte Carlo simulations generate signal and background samples. The signal sample corresponds to the hypothetical new physics process, while background samples include all known Standard Model processes that can produce similar experimental signatures. To prevent classifier bias toward the

typically dominant background, datasets are balanced through undersampling (selecting a subset of the majority class) or, more commonly, event weighting using $w_i = \sigma \cdot \mathcal{L} \cdot \epsilon / N_{gen}$. Equal numbers of signal and background events are often used during training to ensure the algorithm learns both classes effectively, though the final evaluation uses proper physics weights.

2. **Feature Preprocessing**: Input variables (kinematic observables such as p_T, η, ϕ, invariant masses, and angular separations) are standardized using techniques like StandardScaler (transforming to zero mean and unit variance) or MinMaxScaler (scaling to a fixed range, typically [0, 1]). While tree-based methods like XGBoost are theoretically scale-insensitive, preprocessing improves numerical stability and convergence speed. Dimensionality reduction techniques like Principal Component Analysis (PCA) may be used for visualization or to address severe multicollinearity, though trees naturally handle correlated features.

3. **Model Training and Hyperparameter Optimization**: The classifier is trained on the preprocessed data using the procedures described in Sec. 2.6.1. Key hyperparameters—including learning rate, maximum tree depth, L1/L2 regularization strengths, and minimum child weight—are optimized via grid search, random search, or Bayesian optimization as detailed in the hyperparameter optimization strategy. Performance is evaluated using k-fold cross-validation to ensure generalizability and avoid overfitting, with the optimal configuration selected based on the best cross-validated performance.

4. **Output Score Generation**: Instead of binary class assignments, the trained model's continuous output is obtained using `predict_proba()`, which provides a per-event probability score $f(\mathbf{x}) \in [0, 1]$ indicating the likelihood of belonging to the signal class. This score serves as a powerful discriminant variable that encapsulates the multidimensional separation power.

5. **Histogram Construction and Weighting**: Events are binned based on their classifier score to form a one-dimensional histogram. Each bin's content is calculated using the appropriate physics-level weights:

$$N_i^{\text{bin}} = \sum_{\text{events in bin } i} w_j = \sum_{\text{events in bin } i} \left(\sigma \cdot \mathcal{L} \cdot \epsilon / N_{\text{gen}}\right)_j ,$$

yielding the expected signal (s_i) and background (b_i) yields per bin. The binning is typically optimized to maximize the expected sensitivity, often with finer binning in regions of better signal-to-background ratio.

6. **Sensitivity Measurement**: The final histogram, incorporating all relevant systematic uncertainties as nuisance parameters, serves as

input to the statistical model described in Sec. 2.5. The discovery significance κ (from Eq. 2.19) is computed, quantifying the analysis sensitivity and enabling comparison between different analysis strategies or machine learning approaches.

This end-to-end workflow seamlessly integrates machine learning into the established statistical framework of particle physics, transforming high-dimensional data into an optimized discriminant for sensitivity extraction.

3

$U(1)_{T^3_R}$ GAUGE EXTENSION OF THE STANDARD MODEL

Extensions of the SM that introduce new $U(1)$ gauge symmetries are among the most widely studied scenarios to address these phenomenological hints while maintaining theoretical consistency. In particular, the $U(1)_{T^3_R}$ has been explored in the context of left-right symmetric models [176–178], where $U(1)_{T^3_R}$ is identified as the diagonal, electrically neutral generator of $SU(2)_R$. It is often related to $U(1)_{B-L}$ through the breaking pattern

$$U(1)_{B-L} \times U(1)_{T^3_R} \to U(1)_Y.$$

This motivates the existence of a new, massive, electrically neutral gauge boson associated with the extra $U(1)$ symmetry [179–182].

In the minimal case, since the Higgs doublet is a singlet under $U(1)_{B-L}$, it acquires its hypercharge from $U(1)_{T^3_R}$. Its vacuum expectation value (VEV) links the symmetry-breaking scales of $U(1)_Y$ and $U(1)_{T^3_R}$. Alternatively, these scales can be decoupled by introducing an additional $U(1)_G$ group, under which SM fermions are singlets but the Higgs is charged. The inclusion of this symmetry provides model-building freedom to explore a wider range of phenomenological scenarios. In this case, the hypercharge is given by the linear combination

$$Y = Q_{T^3_R} + \frac{1}{2}Q_{B-L} + Q_G. \tag{3.1}$$

More generally, scenarios can be constructed where the hypercharge is not directly related to $U(1)_{T^3_R}$.

Nevertheless, the $U(1)_{T^3_R}$ symmetry has recently attracted attention for its potential to resolve some tensions of LFUV in the SM (see Sec. 1.4) by explaining $(g-2)_\mu$, B anomalies [183], and DM [184–186]. In this framework, right-handed SM fermions are charged under $U(1)_{T^3_R}$. Recent theoretical and phenomenological work has focused on models where the low-energy gauge symmetry of the SM is extended by this Abelian group, where the spontaneous breaking of $U(1)_{T^3_R}$ is not tied to electroweak symmetry breaking [183–189].

The corresponding gauge boson of the extra $U(1)$ is a neutral vector particle whose physical interpretation depends on its couplings and mass range. If the new boson couples directly to SM fermions with electroweak-strength interactions, it is often referred to as a Z'. If instead the new boson interacts only very weakly with the SM, typically through kinetic mixing with the hypercharge gauge boson, it is commonly called a dark photon A'. In either case, the gauge boson acquires mass through a Higgs-like mechanism. A complex scalar field ϕ, singlet under the SM gauge group, can provide the longitudinal degree of freedom. Its CP-odd component gives mass to the neutral vector boson, while its CP-even component can manifest as a dark Higgs, ϕ'.

To ensure anomaly cancellation, a right-handed neutrino ν_R is required for each SM generation that couples to $U(1)_{T^3_R}$. In addition, a set of new vector-like fermions $(\chi_u, \chi_d, \chi_\ell, \chi_\nu)$ is introduced to generate fermion masses in a UV-complete theory, following the universal see-saw mechanism [190–195]. This mechanism introduces a non-trivial coupling with the top quark, $\chi_u - t - \phi'$, allowing a vertex for the production of $t\chi_u\phi'$ final states via χ_u–t fusion (see Fig. 3.1)....AF: Las figuras deben aparecer en orden conforme se citan. Habla primero de la Figura 3.3, la cual aparece siete páginas después, y luego de las Figuras 3.1 y 3.2 que aparecen en la página siguiente. Since χ_u couples to SM quarks and gluons, it can be copiously produced. Its energetic decay products, together with a ϕ' mediator carrying significant transverse momentum, can be efficiently detected, especially if ϕ' decays to visible SM particles in the central detector region.

This strategy is effective for reducing SM backgrounds and enhances the LHC discovery potential for heavy top partners and GeV-scale mediators, which are otherwise challenging to probe at hadron colliders. Moreover, $t\chi_u\phi'$ final states can also arise from $\chi_u\bar{\chi}_u$ production via QCD vertices, where one χ_u decays to $t\phi'$ (see Fig. 3.2)....AF: Mover figura. The presence of energetic decay products and a mediator with substantial transverse momentum provides greater sensitivity than searches considering χ_u or ϕ' alone.

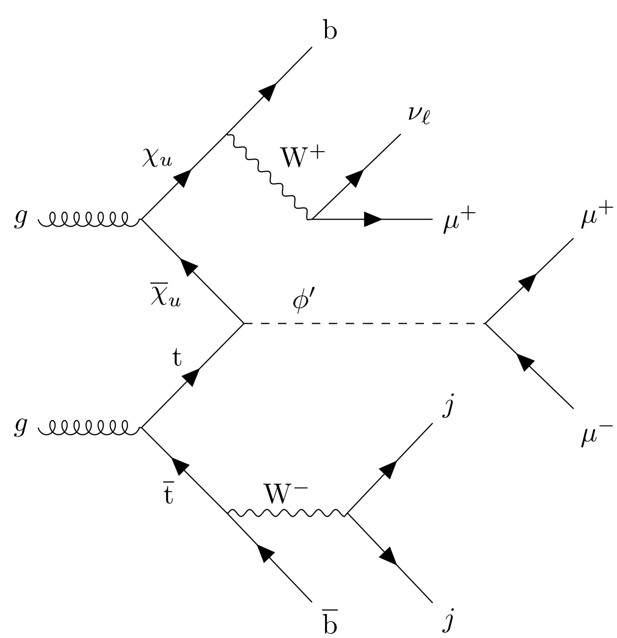

Figure 3.1: Representative Feynman diagram for the production of a ϕ' boson in association with a χ_u vector-like quark through the fusion of a top quark and χ_u vector-like quark. Once again, the ϕ' decays to a pair of muons, the top quark decays fully hadronically, and the χ_u decays semi-leptonically to muons, neutrinos and b-jets.

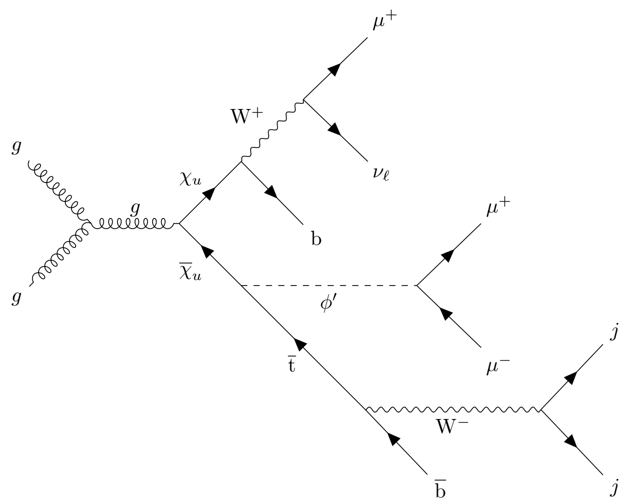

Figure 3.2: Representative Feynman diagram for the production of a ϕ' boson in association with a χ_u vector-like quark through the fusion of a gluon pair from incoming protons. The ϕ' decays to a pair of muons, the top quark that decays fully hadronically, and the χ_u decay semi-leptonically to muons, neutrinos and jets.

In this chapter, we present a phenomenological study of search strategies at the LHC for a light (GeV-scale) scalar ϕ' produced in association with a heavy (TeV-scale) top-partner χ_u. This work, that has been published as [2], focuses on the previously unexplored production channel $pp \to t\chi_u\phi'$. This contrasts with more commonly studied processes, such as heavy vector-like quarks (T), $pp \to TT \to t\phi' t\phi'$, and the di-photon ϕ' decay channels (see Sec. 4.1 and [196–200]).

We consider the case where ϕ' has family non-universal couplings to fermions, as proposed in [187]. Such couplings can address several open questions in the SM. Our analysis focuses on $\phi' \to \mu^+\mu^-$ decays, as muons are efficiently reconstructed and identified. This allows for low $p_T(\mu)$ triggers and provides a characteristically clean signature to suppress QCD multijet backgrounds.

To further maximize the sensitivity to this complex signal, a central component of our analysis is the use of ML. We employ an analysis based on Boosted Decision Trees (BDT) [170]. The BDT output is used in a profile-binned likelihood test to determine the signal significance for each model. The effectiveness of BDTs and other ML algorithms has been demonstrated in numerous experimental and phenomenological studies [201–210]. Our results show that the BDT approach significantly improves sensitivity.

The remainder of this chapter is organized as follows. Sec. 4.1 describes the minimal $U(1)_{T^3_R}$ model. Sec. 3.1 reviews current relevant LHC results.

Sec. 3.3 details the MC simulation samples used in this study. Sec. 3.4 discusses the motivation and implementation of the machine learning workflow, and Sec. 4.3 presents the main results.

3.1 CURRENT EXCLUSION LIMITS ON VECTOR-LIKE QUARKS

The ATLAS and CMS collaborations at CERN have conducted various searches for heavy vector-like quarks. These searches utilized pp collisions at center-of-mass energies of $\sqrt{s} = 8$ and 13 TeV. The studies primarily focused on T production through gluon-mediated QCD processes, either in pair production from quark-antiquark annihilation (Fig. 3.3) or in single-T production from electroweak processes involving associated quarks (Fig. 3.4).

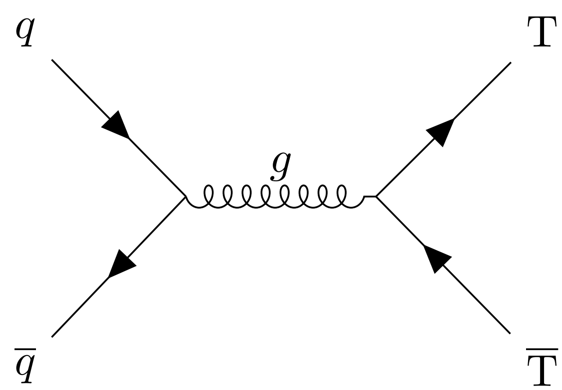

Figure 3.3: Representative Feynman diagram for T pair production via gluon-mediated QCD processes.

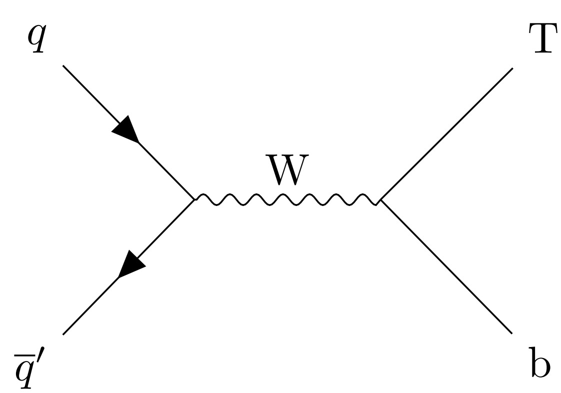

Figure 3.4: Representative Feynman diagram for single T production via electroweak processes.

In those studies, T decays into bW, tZ, or tH have been considered. In the context of T pair production, $T\bar{T}$, via QCD processes, the cross sections are well-known and solely depend on the mass of the vector-like quark. Assuming a narrow T decay width ($\Gamma/m(T) < 0.05$ or 0.1) and a 100% branching fraction to bW, tZ, or tH, these searches have set stringent bounds on $m(T)$, excluding masses below almost 1.5 TeV at 95% confidence level [211–218]. The most recent analysis from the CMS collaboration probes T-quark production via $pp \to Tqb$, in final states with $T \to tZ$ or $T \to tH$, considering scenarios with preferential couplings to third-generation fermions. The analysis sets 95% confidence level upper limits of $68 - 1260$ fb on the production cross section, for T masses ranging from 600-1200 GeV [212]. The latest studies from ATLAS probe vector-like quarks using the single-T production mode with the $T \to tH$ decay channel leading to a fully hadronic final state [213], the single-T production mode with the $T \to tZ$ decay channel leading to a multileptonic final state [214], the TT pair production mode with various T decay channels leading to multileptonic final states [215], and the TT pair production mode with various T decay channels leading to a single lepton plus missing momentum final state [216, 217]. The multilepton search offers the greatest sensitivity in most of the phase space, but the missing transverse energy based search has better sensitivity for low branching fraction $\mathfrak{B}(T \to Wb)$ and high $\mathfrak{B}(T \to Ht)$. These searches have similar sensitivities for the singlet and doublet models, resulting in exclusion bounds for masses below about 1.25 TeV and 1.41 TeV, respectively.

A key consideration in the model interpretations summarized above is that the T branching fractions depend on the chosen model. The excluded mass range is less restrictive for specific branching fraction scenarios, such as $\{\mathfrak{B}(T \to tZ), \mathfrak{B}(T \to bW), \mathfrak{B}(T \to tH)\} = \{0.2, 0.6, 0.2\}$, setting bounds on masses below about 0.95 TeV. Moreover, if the $T \to \phi' t$ decay is allowed, or if the branching fractions $\mathfrak{B}(T \to tH/bW)$ are lower, the limits previously quoted must be re-evaluated. The authors of Ref. [219] emphasize that bounds on $m(T)$ can be around 500 GeV when $T \to t\phi'$ decays are permitted. Therefore, to facilitate a comprehensive study, benchmark scenarios in this paper are considered down to $m(\chi_u) = 500$ GeV.

3.2 THE MINIMAL $U(1)_{T^3_R}$ MODEL

The model extends the SM by an Abelian gauge symmetry $U(1)_{T^3_R}$, under which only the right-handed fermions are charged. The symmetry breaking is achieved via two independent Higgs mechanisms: one with the SM Higgs doublet H for electroweak symmetry breaking, and another with a Higgs singlet ϕ for $U(1)_{T^3_R}$ breaking. These scalars acquire independent vacuum expectation values (VEVs), $\langle H \rangle = v_h/\sqrt{2}$ and $\langle \phi \rangle = v_\phi/\sqrt{2}$. In the Kibble parametrization, the fields are written as:

$$H = \begin{pmatrix} G_+ \\ \frac{1}{\sqrt{2}}\left(v_h + \rho_0 + iG_0\right) \end{pmatrix}, \tag{3.2}$$

$$\phi = \frac{1}{\sqrt{2}}\left(v_\phi + \rho_\phi + iG_\phi\right). \tag{3.3}$$

In Eqs. (3.2) and (3.3), $G_\pm$, G_0, and G_ϕ are the Goldstone bosons absorbed by the SM $W^\pm$ and Z bosons and the dark photon A' (associated with $U(1)_{T_R^3}$) to acquire mass. The fields ρ_0 and ρ_ϕ mix to form the physical mass eigenstates, the SM-like Higgs boson h and a dark Higgs ϕ':

$$\begin{pmatrix} h \\ \phi' \end{pmatrix} = \begin{pmatrix} \cos\alpha & -\sin\alpha \\ \sin\alpha & \cos\alpha \end{pmatrix} \begin{pmatrix} \rho_0 \\ \rho_\phi \end{pmatrix}. \tag{3.4}$$

This mixing arises from diagonalizing the mass matrix derived from the gauge-invariant scalar potential:

$$\begin{aligned} V(H,\phi) = {} & \mu_H^2 H^\dagger H + \mu_\phi^2 \phi^* \phi \\ & + \lambda (H^\dagger H)(\phi^*\phi) + \lambda_H (H^\dagger H)^2 + \lambda_\phi (\phi^*\phi)^2. \end{aligned} \tag{3.5}$$

Minimizing the potential yields the tadpole equations:

$$\frac{\partial V}{\partial H} = \frac{v_h}{\sqrt{2}} \left(\mu_H^2 + \lambda_H v_h^2 + \frac{1}{2} \lambda v_\phi^2 \right) = 0, \tag{3.6}$$

$$\frac{\partial V}{\partial \phi} = \frac{v_\phi}{\sqrt{2}} \left(\mu_\phi^2 + \lambda_\phi v_\phi^2 + \frac{1}{2} \lambda v_h^2 \right) = 0. \tag{3.7}$$

The physical scalar masses are given by:....Af: Sugiero expendir un poco más esta parte. Considero apropiado explicar al lector que se hace luego de encontrar los tadpole equations, mostrar explicitamente la forma de la matriz no diagonal de masas y luego explicar que al diagonalizar se encuentran los valores físicos de masas escalares de la 3.8. Tambien explicar un poco más de donde surge la tangente.

$$m_{h,\phi'}^2 = \frac{1}{2} \left(\lambda_H v_h^2 + \lambda_\phi v_\phi^2 \right) \pm \sqrt{\lambda^2 v_h^2 v_\phi^2 + \left(\lambda_H v_h^2 - \lambda_\phi v_\phi^2 \right)^2}, \tag{3.8}$$

and the mixing angle α satisfies:

$$\tan 2\alpha = \frac{-\lambda v_h v_\phi}{\lambda_\phi v_\phi^2 - \lambda_H v_h^2}. \tag{3.9}$$

The quartic couplings can be expressed in terms of the physical parameters:

$$\lambda_H = \frac{m_{\phi'}^2 + m_h^2 + (m_{\phi'}^2 - m_h^2)\cos 2\alpha}{4 v_h^2}, \tag{3.10}$$

$$\lambda_\phi = \frac{m_{\phi'}^2 + m_h^2 + (m_{\phi'}^2 - m_h^2)\cos 2\alpha}{4 v_\phi^2}, \tag{3.11}$$

$$\lambda = \frac{m_{\phi'}^2 - m_h^2}{2 v_h v_\phi} \sin 2\alpha. \tag{3.12}$$

Thus, the scalar sector has four free parameters: the masses m_h and $m_{\phi'}$, the mixing angle α, and the dark Higgs VEV v_ϕ. Similar to how v_h is fixed by the electroweak gauge boson masses, v_ϕ is related to the dark photon mass by $m_{A'}^2 = g_{T_R^3}^2 v_\phi^2$, where $g_{T_R^3}$ is the $U(1)_{T_R^3}$ gauge coupling. Depending on the value of $g_{T_R^3}$, this gauge boson can behave as a heavy Z' or a light dark photon. In this chapter, we assume $g_{T_R^3}$ is sufficiently small such that A' can be treated as a dark photon.

3.2.1 THE UNIVERSAL SEESAW MECHANISM

In this model, the masses of the SM fermions are generated through a universal seesaw mechanism by mixing with vector-like fermions χ_f. The relevant mass terms in the Lagrangian are:

$$-\mathcal{L} \supset Y_{f_L} \bar{f}'_L \chi'_{fR} H + Y_{f_R} \bar{\chi}'_{fL} f'_R \phi^* + m_{\chi'_f} \bar{\chi}'_{fL} \chi'_{fR} + \text{h.c.} \tag{3.13}$$

This leads to the mass matrix:

$$M_f = \begin{pmatrix} 0 & Y_{f_L} v_h/\sqrt{2} \\ Y_{f_R} v_\phi/\sqrt{2} & m_{\chi'_f} \end{pmatrix}. \tag{3.14}$$

The mass eigenstates (f, χ_f) are obtained by rotating the gauge eigenstates:

$$\begin{pmatrix} f_{L,R} \\ \chi_{f_{L,R}} \end{pmatrix} = \begin{pmatrix} \pm\cos\theta_{f_{L,R}} & \mp\sin\theta_{f_{L,R}} \\ \sin\theta_{f_{L,R}} & \cos\theta_{f_{L,R}} \end{pmatrix} \begin{pmatrix} f'_{L,R} \\ \chi'_{f_{L,R}} \end{pmatrix}, \tag{3.15}$$

such that $\mathcal{R}(\theta_{f_L}) M_f \mathcal{R}^{-1}(\theta_{f_R}) = \text{diag}(m_f, m_{\chi_f})$. For real parameters, the physical masses and mixing angles are given by:

$$m_f m_{\chi_f} = \frac{Y_{f_L} v_h Y_{f_R} v_\phi}{2}, \tag{3.16}$$

$$m_f^2 + m_{\chi_f}^2 = m_{\chi'_f}^2 + \frac{1}{2}\left(Y_{f_L}^2 v_h^2 + Y_{f_R}^2 v_\phi^2\right), \tag{3.17}$$

$$\tan\theta_{f_{L,R}} = \frac{\sqrt{2}}{m_{\chi'_f}} \left(\frac{Y_{f_{L,R}} v_{h,\phi}}{2} - \frac{m_f^2}{Y_{f_{L,R}} v_{h,\phi}} \right). \tag{3.18}$$

The Yukawa interactions of the physical fermions with the scalars h and ϕ' are:

$$-\mathcal{L}_{\text{yuk}} = h\, \bar{\psi}_{f_L}\, \mathcal{Y}_h\, \psi_{f_R} + \phi'\, \bar{\psi}_{f_L}\, \mathcal{Y}_\phi\, \psi_{f_R}, \tag{3.19}$$

where $\psi_f = (f, \chi_f)^T$. The Yukawa matrices are:

$$\mathcal{Y}_h = \frac{1}{\sqrt{2}} \mathcal{R}(\theta_{f_L}) \left(Y_{f_L} \sigma_+ \cos\alpha - Y_{f_R} \sigma_- \sin\alpha\right) \mathcal{R}^{-1}(\theta_{f_R}), \tag{3.20}$$

$$\mathcal{Y}_\phi = \frac{1}{\sqrt{2}} \mathcal{R}(\theta_{f_L}) \left(Y_{f_L} \sigma_+ \sin\alpha + Y_{f_R} \sigma_- \cos\alpha\right) \mathcal{R}^{-1}(\theta_{f_R}), \tag{3.21}$$

with $\sigma_\pm = (\sigma_1 \pm i\sigma_2)/2$ being the ladder Pauli matrices.

The expressions above provide a simplified, one-generation view. The complete model involves a non-trivial flavor structure where the mass matrices are general 3×3 matrices. The diagonalization of the full 6×6 mass matrices, the procedure for absorbing unphysical unitary rotations, and the emergence of the CKM matrix are detailed in Appendix A. Furthermore, the appendix contains a rigorous treatment of the mass eigenvalue problem, deriving the exact relationship between the fundamental parameters (m_L, m_R, m_χ) and the physical observables (m_f, m_F, θ_L), which leads to critical constraints on the model's parameter space to ensure perturbativity.

Field	$SU(3)_C$	$SU(2)_L$	$U(1)_Y$	$U(1)_{T_R^3}$
q'_L	**3**	**2**	1/6	0
ℓ'_L	**1**	**2**	-1/2	0
H	**1**	**2**	1/2	0
u'^c_R	**3**	**1**	-2/3	-2
d'^c_R	**3**	**1**	1/3	2
ℓ'^c_R	**1**	**1**	1	2
ν'^c_R	**1**	**1**	0	-2
ϕ	**1**	**1**	0	2
χ'_{u_L}	**3**	**1**	2/3	0
$\chi'^c_{u_R}$	**3**	**1**	-2/3	0
χ'_{d_L}	**3**	**1**	-1/3	0
$\chi'^c_{d_R}$	**3**	**1**	1/3	0
χ'_{ℓ_L}	**1**	**1**	-1	0
$\chi'^c_{\ell_R}$	**1**	**1**	1	0
χ'_{ν_L}	**1**	**1**	0	0
$\chi'^c_{\nu_R}$	**1**	**1**	0	0

Table 3.1: Minimal field content of the model and their representations under the SM and $U(1)_{T_R^3}$ gauge groups.

3.2.2 MINIMAL UV-COMPLETE THEORY

To generate non-zero masses for all SM fermions and ensure gauge anomaly cancellation, the model must include at least one full generation of vector-like fermions $\{\chi_u, \chi_d, \chi_\ell, \chi\}$ and the right-handed neutrinos ν_R for each SM generation. Their quantum numbers are listed in Tab. 3.1. The Yukawa interactions in the UV-complete theory are:

$$\begin{aligned}-\mathcal{L} \supset\; & Y^{ij}_{Lu}\bar{q}'^i_L\chi'^j_{uR}\widetilde{H} + Y^{ij}_{Ru}\bar{\chi}'^i_{uL}u'^j_R\phi^* + m^{ij}_{\chi_u}\bar{\chi}'^i_{uL}\chi'^j_{uR}\\ & + Y^{ij}_{Ld}\bar{q}'^i_L\chi'^j_{dR}H + Y^{ij}_{Rd}\bar{\chi}'^i_{dL}d'^j_R\phi + m^{ij}_{\chi_d}\bar{\chi}'^i_{dL}\chi'^j_{dR}\\ & + Y^{ij}_{L\ell}\bar{\ell}'^i_L\chi'^j_{\ell R}H + Y^{ij}_{R\ell}\bar{\chi}'^i_{\ell L}\ell'^j_R\phi + m^{ij}_{\chi_\ell}\bar{\chi}'^i_{\ell L}\chi'^j_{\ell R}\\ & + Y^{ij}_{L\nu}\bar{\ell}'^i_L\chi'^j_{\nu R}\widetilde{H} + Y^{ij}_{R\nu}\bar{\chi}'^i_{\nu L}\nu'^j_R\phi^* + m^{ij}_{\chi_\nu}\bar{\chi}'^i_{\nu L}\chi'^j_{\nu R} + \text{h.c.}\end{aligned} \tag{3.22}$$

Here, $i, j = 1, 2, 3$ are generation indices. The diagonalization of the mass matrices for each fermion type follows the structure outlined in Eqs. (3.16) and (3.17), while the Yukawa matrices generalize the structure of Eqs. (3.20) and (3.21), now encoding the CKM and PMNS mixing matrices. The neutrino sector has a more complex structure due to the possibility of a Majorana mass term for the vector-like neutrinos χ'_ν.

3.3 SAMPLES AND SIMULATION

The minimal $U(1)_{T_R^3}$ model described in Sec. 4.1 .....AF: No debería ser Sec. 3.2??is implemented *at tree level* into the `FeynRules` package [105], which generates the Feynman rules and exports them into a Universal FeynRules Output (UFO) [158]. The resulting UFO is utilized as input for a generator to produce the MC samples. We have used the implementation of the $U(1)_{T^3_R}$ model in Ref. [189]. Both signal and background events are generated with the MadGraph5_aMC@NLO v3.2.0 program [104, 159] at leading order (LO) in QCD, considering pp beams colliding with a center-of-mass energy of $\sqrt{s} = 13.6$ TeV. Each signal and background sample is generated separately, with no interference effects between the signal and background considered. The impact of these interference effects has been evaluated, and for all values of χ_u and ϕ' masses considered, the effect on the signal plus background cross section is found to be less than $< 0.5\%$. Additionally, the effect on the shape of the b-jet p_T distribution is less than 6% for $p_T < 300$ GeV and less than 2% for b-jet $p_T > 300$ GeV. We use the NNPDF3.0 NLO [112] set for parton distribution functions (PDFs) for all event generation. Parton-level events are then interfaced with PYTHIA (v8.2.44) [110] to account for parton showering and hadronization processes. Finally, we use DELPHES (v3.4.2) [106] to simulate smearing and other detector effects using the CMS detector geometric configurations and parameters for particle identification and reconstruction, using the CMS input card with 140 average pileup interactions.

All signal cross sections used in this analysis are obtained requiring the following kinematic criteria on leptons ℓ, b quarks, and light-quark/gluon jets (j) at parton level in MadGraph: $p_T(\ell) > 35$ GeV, $|\eta(b)| < 2.5$, $|\eta(\ell)| < 2.3$, $p_T(j) > 20$ GeV, and $|\eta(j)| < 5$. These parton-level selections were applied exclusively to the signal processes to restrict event generation to the relevant phase space regions. For background processes, these default parton level requirements in MadGraph were imposed: $p_T(\ell) > 10$ GeV, $|\eta(\ell)| < 2.5$, $p_T(j) > 20$ GeV, $|\eta(j)| < 5$, and $|\eta(b)| < 5$. This ensures that the phase space regions for the background near the analysis-level selection criteria are adequately described after parton showering since the pre-selections at the analysis level are more stringent than the parton-level requirements. Furthermore, we use the MLM algorithm for jet matching and jet merging. The parameters xqcut and qcut of the MLM algorithm are set to 30 and 45 respectively to ensure continuity of the differential jet rate as a function of jet multiplicity. Each simulated signal and background sample is produced separately at LO, with one million events at the generation level, neglecting potential interference effects between the signal and background due to the suppression caused by the different orders of magnitude in the coupling constants of the signal and background.

Signal samples are generated considering the production of a ϕ' boson, an associated χ_u vector-like quark, and a top quark ($pp \to \chi_u t \phi'$), inclusive in both α and α_s (see Figures 3.1-3.2). Signal samples were created considering coupling values of $Y_{t_R} = Y_{t_L} = 2\sqrt{2}$ in the range of masses $m(\phi') \in \{5, 10, 50, 100, 325\}$ GeV for the dark higgs and $m(\chi_u) \in \{0.50, 0.75, 1.0, 1.5, 2.0, 2.5\}$ TeV for the vector-like quark χ_u [220]. The production cross section for $pp \to \chi_u t \phi'$ is highly dependent on the choice of

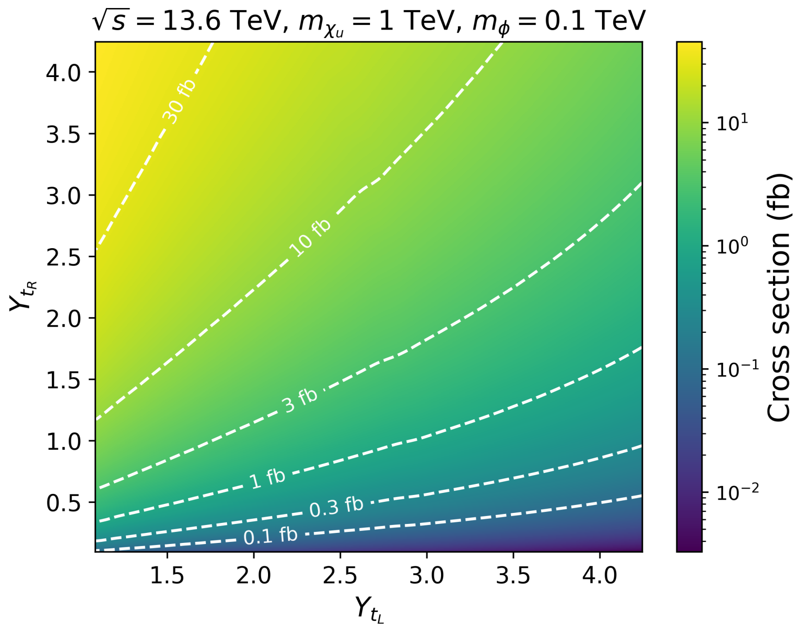

Figure 3.5: Signal production cross section, $pp \to \chi_u t\phi'$, in the Y_{t_R} versus Y_{t_L} plane, for a benchmark point with $m(\phi') = 100$ GeV and $m(\chi_u) = 1.00$ TeV. The white-dashed contours show specific cross section values in the two dimensional plane.

the Yukawa couplings in the Lagrangian. The χ_u−t fusion process, shown in Fig. 3.1, is dominated by the Y_{t_R} coupling. However, the decay $\chi_u \to t\phi'$ shown in Fig. 3.2 is inversely proportional to the Y_{t_L} coupling. This effect is shown in Fig. 3.5, which displays the total signal cross section, as a function of Y_{t_R} and Y_{t_L}, for a benchmark point with $m(\phi') = 100$ GeV and $m(\chi_u) = 1.0$ TeV.

We target signal events where the top quark decays hadronically into a bottom quark and two jets ($t \to bW \to bq\bar{q}'$), benefiting from its large branching ratio of $\approx 67.2\%$. In addition, the χ_u decays semileptonically into a b quark, lepton, and neutrino (via $\chi_u \to bW$ and $W \to \mu\nu_\mu$), while the ϕ' produces two muons. This final state provides clean signatures with relatively low trigger p_T thresholds. We emphasize again that the scalar ϕ' particle could result from the mixture of the SM Higgs boson and additional scalar fields, and the Yukawas of the fermions could additionally arise from the mixing of the SM fermions with additional copies of the associated vector-like fermions. Therefore, the ϕ' branching ratios are dependent on the chosen mechanism and model by which this mixture occurs, see for example, Refs. [75, 221–223]. For the purpose of this work, and similar to Refs. [187, 189], the considered benchmark signal scenarios have $\mathfrak{B}(\chi_u \to b\,W)$ of about 0.5 and $\mathfrak{B}(\phi' \to \mu^+\mu^-) = 1.00$. Fig. 3.7 shows the production cross section in fb, as a function of $m(\phi')$ and $m(\chi_u)$ masses, assuming the aforementioned decays, branching ratios, and couplings.

We note that for the parameter space of focus in this paper, the total mass of the t-χ_u system is larger than $m(\phi')$, thus the large rest energy of the t-χ_u system is converted into potentially large momentum values for the ϕ'. Similarly, the t-quark produced through the χ_u-t fusion interaction can also have large momentum values, and thus in some cases the hadronic t decay products cannot be fully reconstructed independently of each other. This results in three possible t reconstruction scenarios: a fully merged scenario where the $W \to jj$ system and the b quarks are very collimated and reconstructed as a single "fat jet" (henceforth referred to as a FatJet, FJ); a partially merged scenario, where the decay products of the W boson form a single FatJet but the b quark can still be separately identified; and an un-merged scenario where all decay products can be independently identified. Jets are clustered using the anti-k_t algorithm [224] as implemented in the `FastJet` (v3.4.2) [225] package, with a distance parameter of $R = 0.4$ for standard jets and $R = 0.8$ for fat jet objects. Each scenario has an associated identification efficiency and misidentification rate, which depends on the choice of the boosted t/W algorithm (our choice of efficiency and misidentification rates is described later).

Based on the details above, the final state of interest in this paper consists of three muons (two from the ϕ' decay and one from the χ_u decay), a (possibly boosted) top-tagged system, at least one b-tagged jet, and large $\vec{p}_T^{\,miss}$. For the partially merged and un-merged scenarios, there will be two b quarks present in the final state (one of which is part of the top tagged system).

We consider background sources from SM processes which can give similar objects in the final state as those expected for signal. Several background sources were considered and studied, such as QCD multijet events, production of vector boson pairs ($VV : WW, ZZ, WZ$), vector boson triplets ($VVV : WWZ, WZZ, ZZZ, WWW$), top-quark pairs in association with weak bosons ($t\bar{t}X$), and $t\bar{t}t\bar{t}$ processes. The dominant sources of SM background events are from the $t\bar{t}X$, ZZW, and $t\bar{t}t\bar{t}$ processes. The $t\bar{t}X$ background is primarily associated production of a Z/γ^* from $t\bar{t}$ fusion processes. The ZZW process becomes a background when one Z decays $b\bar{b}$, another Z decays to a pair of muons, and the W decays to a muon and a neutrino. Events from ZZW and $t\bar{t}t\bar{t}$ have been combined, after being weighted by their corresponding production cross section. The combination is presented as the "$b\bar{b}\mu\mu\mu\nu$" background in the remainder of this paper. The $t\bar{t}X$ process is presented as part of the "$t\bar{t}\mu^+\mu^-$" background. Figure 3.6 shows a representative Feynman diagram for the $t\bar{t}\mu^+\mu^-$ background process. Tab. 3.2 shows the production cross sections for the dominant background sources. The rest of the aforementioned background processes do not contribute meaningfully in our context, accounting for $\ll 1\%$ of the total expected background yield.

The identification of leptons, boosted top quarks, and bottom quarks plays an important role in the ability to identify signal events, the ability to minimize the rate of SM backgrounds, and thus also the discovery reach in the high-luminosity environment of the LHC. It is worth noting that the reconstruction and identification of leptons and the decay products of

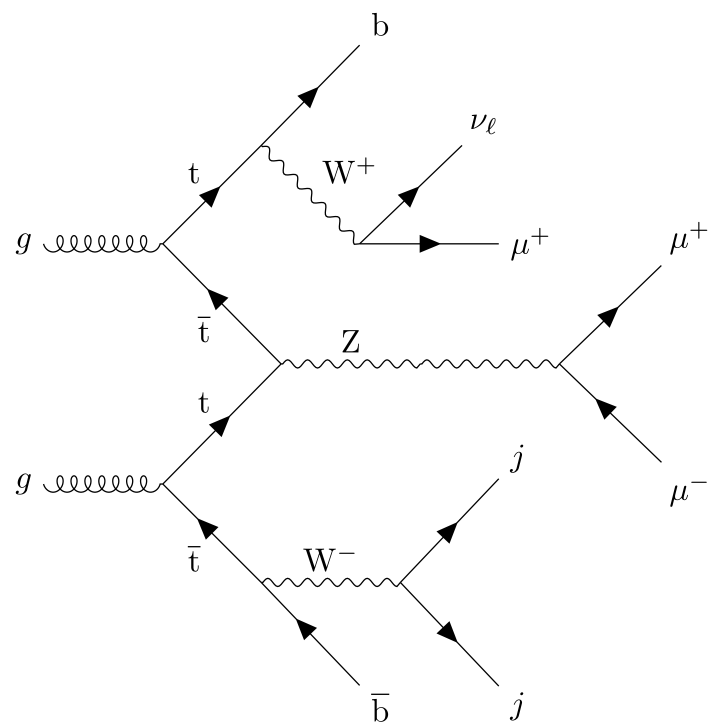

Figure 3.6: Representative Feynman diagram for a background event. A Z boson is produced in association with a top quark through the fusion of a top, anti top pair from incoming protons. The Z boson subsequently decays to a pair of muons and the two spectator top quarks decay semi-leptonically and purely hadronically to muons, neutrinos and jets, resulting in the same final states as the signal event.

Background Process	Cross-Section σ [pb]
$pp \to t\bar{t}\,\mu^+\mu^-$	2.574×10^{-3}
$pp \to b\bar{b}\,\mu\mu\mu\nu$	4.692×10^{-4}

Table 3.2: A summary of dominant SM backgrounds produced by pp collisions and their cross sections in pb, as computed by MadGraph with $n = 10^6$ events.

the top/bottom quarks may be non-trivial at the High-Luminosity LHC (HL-LHC) due to the presence of a potentially large number of in-time and out-of.time PU interactions. The impact of PU on the new physics discovery reach, and the importance of to mitigate its effects at CMS and ATLAS has been outlined in many articles, for example in Ref. [121]. We note the expected performance of the upgraded ATLAS and CMS detectors for the HL-LHC is beyond the scope of this work. However, the studies presented here do attempt to provide reasonable expectations by conservatively assuming some degradation in lepton and hadron identification efficiencies, using Ref. [121] as a benchmark, and considering the case of 140 average PU interactions in the DELPHES input cards, as described above.

For muons with $|\eta| < 1.5$, the assumed identification efficiency is 95% with a 0.3% misidentification rate [121, 128]. The performance degrades linearly with η for $1.5 < |\eta| < 2.5$, and we assume an identification efficiency of 65% with a 0.5% misidentification rate at $|\eta| = 2.5$. Similarly, the charged hadron tracking efficiency, which contributes to the jet clustering algorithm and $\vec{p}_T^{\,\text{miss}}$ calculation, is 97% for $1.5 < |\eta| < 2.5$, and degrades to about 85% at $|\eta| = 2.5$. These potential inefficiencies due to the presence of secondary pp interactions contribute to how well the lepton and top kinematics can be reconstructed. Following Refs. [226, 227], we consider the "Loose" working point for the identification of the fully merged (partially merged) t decays, which results in $80 - 85\%$ top (W) identification efficiency and $11 - 25\%$ misidentification rate, depending on the FatJet transverse momentum (p_T^{FJ}). Following Ref. [228], we consider the "Loose" working point of the DeepCSV algorithm [116], which gives a $70 - 80\%$ b-tagging efficiency and 10% light quark mis-identification rate. The choice of boosted t/W and b-tagging working points is determined through an optimization process that maximizes discovery reach. It is noted the contribution from SM backgrounds with a misidentified boosted t/W is negligible, and thus our discovery projections are not sensitive to uncertainties related to the boosted t/W misidentification rates.

3.4 DATA ANALYSIS USING MACHINE LEARNING

The analysis of signal and background events is performed utilizing machine learning techniques. A machine learning-based approach offers sizeable advantages when compared to traditional event classification techniques. Unlike conventional methods, machine learning models have the capability to simultaneously consider all kinematic variables, allowing them

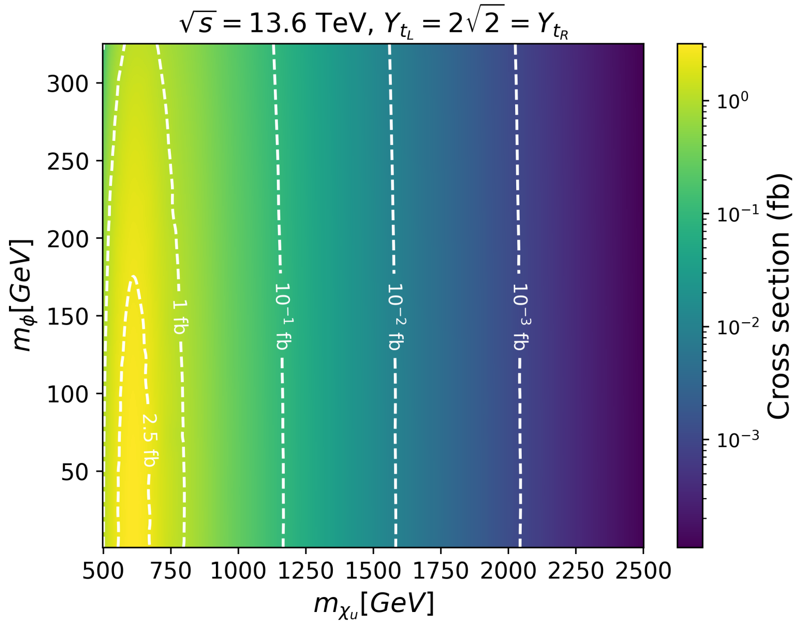

Figure 3.7: Projected cross section (fb) plot for $pp \to t\chi_u\phi'$ and subsequent decay as a function of $m(\chi_u)$ and $m(\phi')$.

to efficiently navigate the complex and high-dimensional space of event kinematics. Consequently, machine learning models can effectively enact sophisticated selection criteria that take into account the entirety of this high-dimensional space. This makes them ideal for high-energy physics applications.

The BDT method is a powerful machine learning technique that has proven its effectiveness in various applications, particularly in the field of collider physics. In this method, decision trees are trained greedily in a sequential manner, with each tree focusing on learning the discrepancies or residuals between its predictions and the expected values obtained from the previously trained tree. This iterative process aims to progressively minimize errors, making BDTs a particularly effective approach for enhancing model performance.

In the context of collider physics, BDTs have demonstrated their utility in addressing classification problems. In particular, BDTs can effectively discriminate between signal and background events, enabling accurate and efficient event classification. Their ability to handle subtle non-linear relationships within the data with high interpretability makes BDTs a valuable tool to handle large amounts of data with a large number of parameters for each event.

The first step in our workflow involves the use of a specialized `MadAnalysis Expert Mode` C++ script [229]. This script extracts essential kinematic and topological information from the simulated samples. The script will process the aforementioned variables contained within these files and transform them into a structured and informative CSV (Comma-Separated Values) format that can be used to train our machine learning models. These kinematic variables include crucial details about the events, such as particle momenta, energies, and topologies, providing the fundamental building blocks for our machine learning analysis.

To account for the differential significance of various events, we apply cross-section weighting. This ensures that the relative importance of signal and background events is appropriately balanced in the dataset. This weighting is crucial for addressing the varying likelihood of observing different types of events in high-energy physics experiments. The prepared and weighted datasets are then passed to our `MadAnalysis Expert Mode` C++ script, where the simulated signal and background events are initially filtered, before being passed to the CSV file for use by the machine learning algorithm. The filtering process requires at least one well-reconstructed and identified b-jet candidate, at least one jet (regular or FJ) not tagged as a b jet, and exactly three identified muons. The filtering selections are motivated by experimental constraints, such as the geometric constraints of the CMS/ATLAS detectors, the typical kinematic thresholds for the reconstruction of particle objects, and the available lepton triggers which also drive the minimal kinematic thresholds. Selected jets must have $p_T > 30$ GeV and $|\eta(j)| < 5.0$, while b-jet candidates with $p_T > 20$ GeV and $|\eta(b)| < 2.5$ are chosen. The μ object must pass a $p_T > 35$ GeV threshold and be within a $|\eta(\ell)| < 2.3$. We will refer to this filtering criteria as pre-selections. The efficiency of the pre-selections depends on $m(\phi')$ and $m(\chi_u)$, but is typically about $25 - 30\%$ for the signal samples. Events passing this pre-selection are used as input for the machine learning algorithm, which classifies them as signal or background, using a probability factor.

We explore the performance of a diverse set of machine learning models, specifically three neural networks of differing architectures and a BDT algorithm. To ensure robust model assessment, we employed a standard 90-10 train-test split of the dataset, partitioning it into a 90% portion for training and a 10% portion for testing. This division allows us to gauge the generalization capabilities of our models on unseen data.

The training and evaluation of the BDT were carried out in a high-performance computing environment. Specifically, an Nvidia A100 GPU was used. The canonical `PyTorch` [230] deep learning framework was employed for configuring, training, and evaluating the neural networks. PyTorch is well-regarded for its flexibility and performance in deep learning applications.

For the BDT algorithm, we used hyperparameters $\eta = 0.3$, $\gamma = 0$, and `max_depth` $= 6$. The `XGBoost` [175] library was used for the implementation of the Boosted Decision Tree algorithm. It offers high efficiency, optimization, and interpretability, making it a suitable choice for this particular task.

It is worth mentioning that we experimented with deep neural networks of various architectures. Although we found that they yield similar signal sensitivity to the BDT, the complex nature of the studies in this work

Model	Train/Test Acc.	Training Time
BDT	N.A./0.9993	6s
Neural Network 1	0.9999/0.9997	1h 58m
Neural Network 2	0.9999/0.9998	2h 12m
Neural Network 3	0.9999/0.9998	2h 32m

Table 3.3: Train/test results for the ML models.

(particle objects considered, experimental constraints in a high luminosity LHC, etc.) motivates the use of a BDT over a deep neural network because of its usefulness, efficiency, and simplicity in understanding the machine learning output in addition to significantly shorter training times. Therefore, we perform our proceeding analysis using the BDT. The outcomes of our model training and evaluation are presented in Table 3.

3.5 RESULTS

Figures 3.8, 3.9, and 3.10 show relevant kinematic distributions for two benchmark signal points and the dominant SM backgrounds, using the subset of events passing the pre-selections defined above. The signal benchmark points in these figures are $m(\phi') = 325\,\text{GeV}$, $m(\chi_u) = 2\,\text{TeV}$, and $m(\phi') = 1\,\text{GeV}$, $m(\chi_u) = 500\,\text{GeV}$. The distributions are normalized such that the area under the curve is unity. These distributions correspond to the reconstructed mass, $m(\mu_1, \mu_2)$, between the two muon candidates with the highest transverse momentum (μ_1 and μ_2), the transverse momentum of the b-jet candidate with the highest transverse momentum p_T (b_1), and the muon candidate with the highest transverse momentum p_T (μ_1), respectively. Note that the signal distributions exhibit tails that are significantly the backgrounds. These distributions are among the variables identified by the BDT algorithm with the highest signal to background discrimination power.

As can be seen from Fig. 3.8, the ϕ' mass can be reconstructed through its associated muon decay pair, which is observed as a peak in the $m(\mu_1, \mu_2)$ distribution around the expected $m(\phi')$ value, and has low- and high-mass tails which are a consequence of cases where the leading and/or subleading muon is not from the ϕ' decay, but rather from the associated W boson from the χ_u decay. For the backgrounds, muons come from Z (W) decays. Therefore, the $m(\mu_1, \mu_2)$ background distributions show a peak near $m_{W/Z}$, combined with a broad distribution indicative of the combination of two muon candidates from different decay vertices. We note that the $\phi' \to \mu^+\mu^-$ decay width depends on the square of the $\phi' \to \mu^+\mu^-$ coupling and $\frac{m_\mu^2}{m_{\phi'}^2}$ and is thus suppressed by the relatively small muon mass. For the new physics phase space considered in this paper, the ϕ' decay width is less than 1% of the ϕ' resonant mass. Furthermore, as indicated previously, the signal/background interference effects are

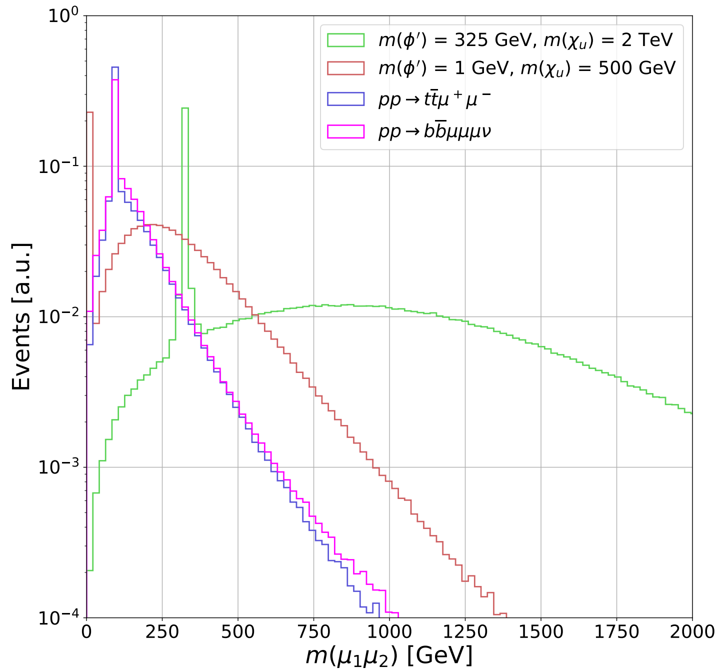

Figure 3.8: Invariant mass distribution of the muon pair with the highest and second highest transverse momentum. The distributions are shown for the two main SM background processes and two signal benchmark points.

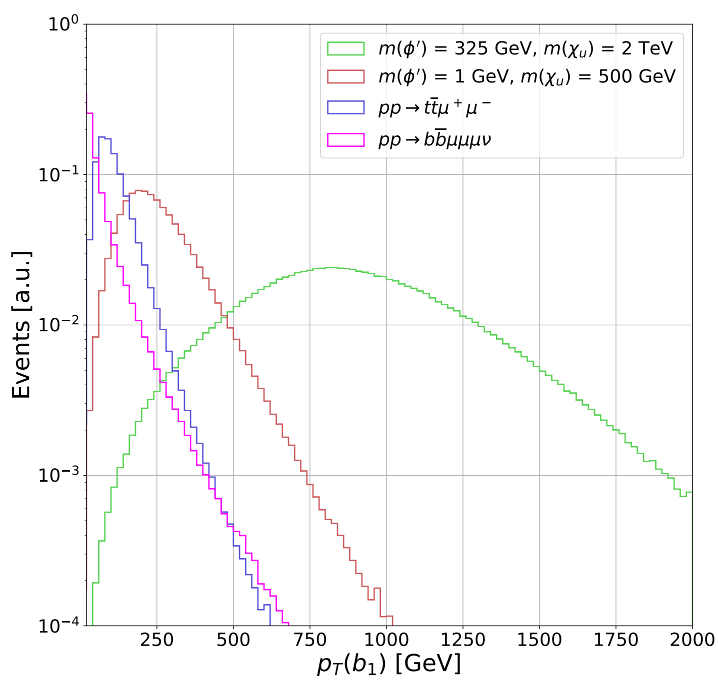

Figure 3.9: Transverse momentum distribution of the leading b-quark jet candidate. The distributions are shown for the two main SM background processes and two signal benchmark points.

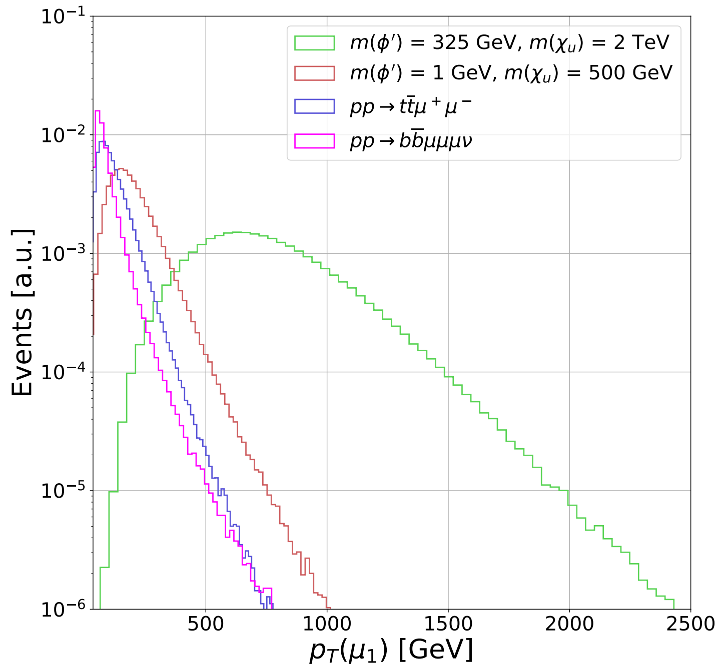

Figure 3.10: Transverse momentum distribution of the leading muon candidate. The distributions are shown for the two main SM background processes and two signal benchmark points.

small and negligible compared to effects from experimental resolution. Therefore, the width of the $m(\mu_1, \mu_2)$ signal distributions is driven by the experimental resolution in the reconstruction of the muon momenta, as well as the probability that the two leading muons are the correct pair from the ϕ' decay. Since the probability that the two highest-p_T muons are the correct pair from the $\phi' \to \mu^+\mu^-$ decay depends on $m(\phi')$ and $m(\chi_u)$, it is important to include all possible combinations of dimuon pairs (i.e., $m(\mu_1, \mu_3)$ and $m(\mu_2, \mu_3)$) in the training of the BDT.

Fig. 3.9 shows the distribution for the b-jet candidate with the highest p_T, $p_T(b_1)$, for the same simulated samples shown in Fig. 3.8. Based on the signal topology and our choice of parameter space (i.e., $m_{\chi_u} > m_t$), it is expected that the leading b-jet candidate comes from the χ_u decay, with an average p_T close to $\frac{m_{\chi_u} - m_W}{2}$, as observed in Fig. 3.9. For the $t\bar{t}\mu^+\mu^-$ background, the b-jet candidates come from top-quark decays. Therefore, their average transverse momentum is expected to be $\frac{m_t - m_W}{2} \approx 45$ GeV, as observed in Fig. 3.9. On the other hand, the b-jet candidates for the $b\bar{b}\mu\mu\mu\nu$ background can come from off-mass-shell Z^*/γ^*, and thus typically have an even softer spectrum in comparison to the $t\bar{t}\mu^+\mu^-$ background.

Fig. 3.10 shows the distribution for the muon candidate with the highest p_T, $p_T(\mu_1)$. Similar to Fig. 3.9, when $m(\chi_u) > m_t$ it is expected that the leading muon candidate comes from the χ_u decay, with an average p_T of approximately $\frac{m(\chi_u) - m_W}{4}$, as observed in Fig. 3.10. For the major SM backgrounds, the muon candidates come from $Z/W/\gamma^*$ decays. Therefore, their average transverse momentum is expected to be much lower, $\frac{m_{Z/W}}{4} \approx$

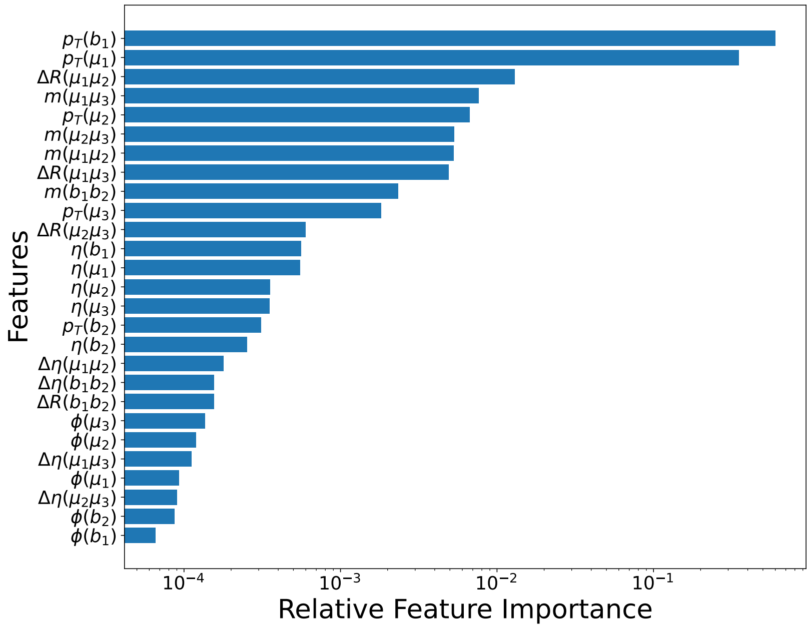

Figure 3.11: Relative importance of features in training for a benchmark signal scenario with $m(\phi') = 325\,\text{GeV}$ and $m(\chi_u) = 2000\,\text{GeV}$.

$40 - 45$ GeV. This kinematic feature provides a nice handle to discriminate high $m(\chi_u)$ signal events amongst the large SM backgrounds, which have lower average $p_T(\mu)$ constrained by the SM weak boson masses.

In addition to these aforementioned variables in Figures 3.8-3.10, several other kinematic variables were included as inputs to the BDT algorithm. In particular, 27 such variables were used in total, and these included the momenta of b and muon candidates; invariant masses of pairs of muons; angular differences between b jets and between the muons. Fig. 3.11 shows the features that are used for training the machine learning models and their importance for a benchmark point.

As mentioned above, the variables $m(\mu_i, \mu_j)$ for $i, j \neq 1$ provide some additional discrimination between signal and background when the leading muons are not a ϕ' decay candidate. The angular separation variables, such as $\Delta R(\mu_i, \mu_j)$, are designed to be sensitive to lower mass ϕ', since the low rest mass of those particles means they acquire more boost, and thus smaller angular separation ΔR between the muon candidates. The trained BDT returns the discriminating power of each of its inputs, and the feature importance for each variable is shown in Fig. 3.11 for a signal benchmark point with $m(\phi') = 325\,\text{GeV}$ and $m(\chi_u) = 2000\,\text{GeV}$.

Fig. 3.12 shows the distributions for the output of the BDT algorithm, normalized to unity, for the representative signal benchmark point of $m(\phi') = 1\,\text{GeV}$, $m(\chi_u) = 0.5\,\text{TeV}$ and the two dominant backgrounds. The output of the BDT algorithm is a value between 0 and 1, which quantifies the likelihood that an event is either background-like (BDT output near 1) or signal-like (BDT output near 0). Fig. 3.13 illustrates the true positive rate (TPR), defined as the probability of correctly selecting

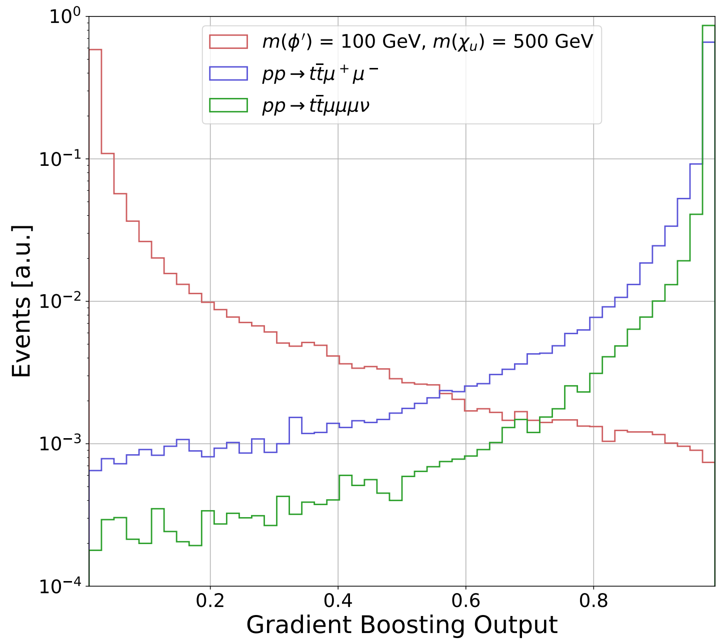

Figure 3.12: Output of the gradient boosting algorithm for a benchmark $m(\phi') =$ 100 GeV and $m(\chi_u) = 500$ GeV signal, and dominant backgrounds. The distributions are normalized to unity.

signal events using the BDT output, plotted against the false positive rate (FPR), defined as the probability of incorrectly selecting background events. For example, for $m(\phi') = 100$ GeV and $m(\chi_u) = 500$ GeV, when signal events are selected at 65% probability, the background is selected at about 10^{-3} probability. We note that the primary discriminating feature between the signal and background is the boosted b-jet p_T coming from the χ_u vector-like quark. The p_T of said b jet increases with $m(\chi_u)$, peaking at around $[m(\chi_u) - m(W)]/2$. This enhanced boost increases the separation between signal and background, improving the performance of the BDT algorithm as $m(\chi_u)$ increases.

The outputs from the BDT machine learning algorithm are used to perform a profile-bin likelihood analysis to estimate the signal significance for a luminosity of 3000 fb^{-1}, corresponding to the expected amount of collected data by the end of the LHC era. For this purpose, the BDT distributions are normalized to cross section times pre-selection efficiency times luminosity for the different signal models. The significance is then calculated using the expected bin-by-bin yields of the BDT output distribution in a profile likelihood fit, using the ROOTFit [132] package developed by CERN. The expected signal significance Z_{sig} is estimated using the probability of obtaining the same test statistic for the signal plus background and the signal-null hypotheses, defined as the local p-value. Similar to Refs. [231–237], the significance corresponds to the point where the integral of a Gaussian distribution between Z_{sig} and ∞ results in a value equal to the local p-value. The estimation of Z_{sig} incorporates systematic uncertainties. The uncertainty values have been included as nuisance parameters,

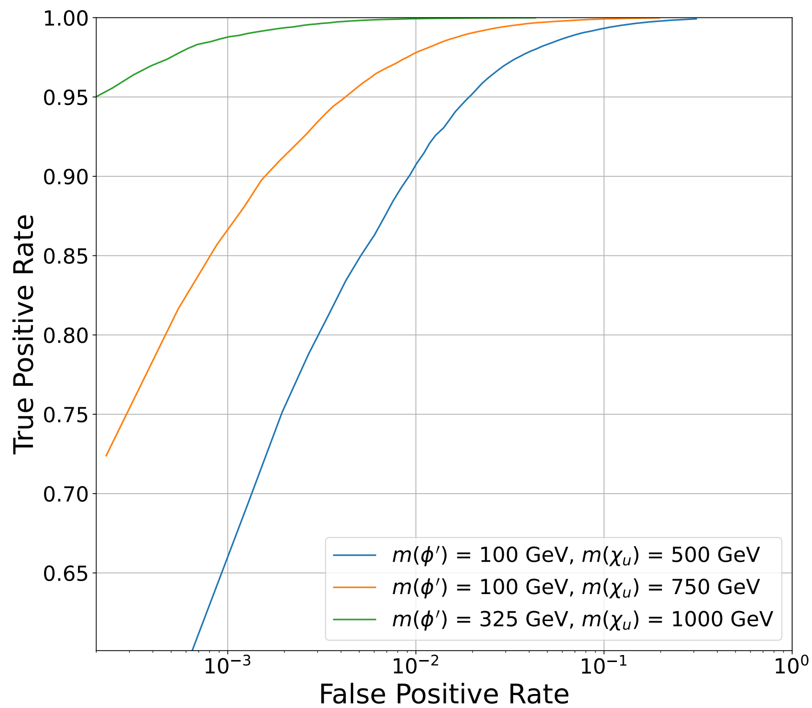

Figure 3.13: Receiver operating characteristic curve of the BDT algorithm for three different signal benchmark scenarios.

considering lognormal priors for normalization and Gaussian priors for uncertainties associated with the modeling of the shapes similar to Refs. [238, 239].

The systematic uncertainties that have been included result from experimental and theoretical constraints. A 1-5% systematic uncertainty, depending on the simulated MC sample, has been included to account for the choice of Parton Distribution Function (PDF) set. The systematic uncertainty effect was incorporated following the PDF4LHC [132] recommendations. This systematic uncertainty has a small impact on the expected event yields for signal and background, but it does not affect the shape of the BDT output distribution. We additionally considered theoretical uncertainties related to the absence of higher-order contributions to the signal cross sections, which can change the pre-selection efficiencies and the shapes of kinematic variables used as inputs to the BDT algorithm. This uncertainty was calculated by varying the renormalization and factorization scales by $\times 2$, and studying the resulting change in the bin-by-bin yields of the BDT distributions. They are found to be at most 2% in a given bin.

Regarding experimental uncertainties, following experimental measurements from CMS on the estimation of the integrated luminosity, a conservative 3% effect has been included [113]. A 5% systematic uncertainty associated with the reconstruction and identification of b-quark jets has been included, independent of p_T and η of the b-jet candidates. According to Ref. [228], this uncertainty is correlated between signal and background processes with genuine b-jets and is also correlated across BDT

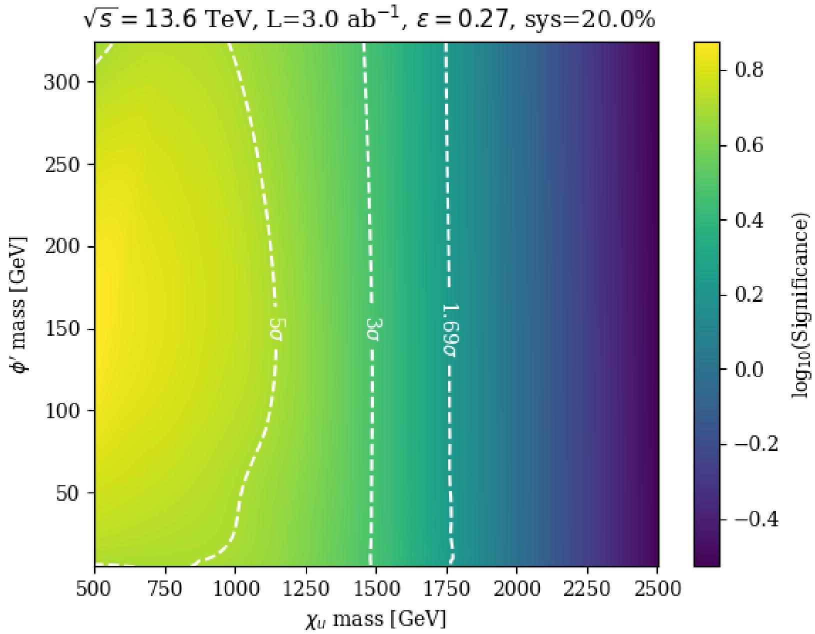

Figure 3.14: Signal significance for the high luminosity LHC era, considering with 3000 fb^{-1} of collected data.

bins for each process. For muons, we include a 2% uncertainty associated with the reconstruction, identification, and isolation requirements, and a 3% systematic uncertainty to account for scale and resolution effects on the momentum and energy measurement. We consider jet energy scale uncertainties ranging from $2-5\%$, contingent on η and p_T, resulting in shape-based uncertainties on the BDT output distribution. Jet energy scale uncertainties were assumed to range from $1-5\%$, contingent on η and p_T. These assumptions lead to shape-based uncertainties on the BDT output distribution, varying from $1-2\%$. Additionally, we include a 10% systematic uncertainty to account for errors in the signal and background predictions. Considering all the various sources of systematic uncertainties, our conservative estimate yields a total effect of about 20%.

Fig. 3.14 shows the expected signal significance considering an integrated luminosity of 3000 fb^{-1}. The significance is shown as a heat map in a two-dimensional plane for different ϕ' and χ_u masses. The x-axis corresponds to $m(\chi_u)$, the y-axis to $m(\phi')$, and the heat map to $\log_{10}(Z_{sig})$. The white dashed lines are contours of constant signal significances of 1.69σ, 3σ and 5σ to represent regions of possible exclusion, evidence of new physics, and discovery, respectively. Under these conditions, ϕ' (χ_u) masses ranging from 1 to 325 GeV (500 to 1800 GeV) can be probed. The range for a discovery with 5σ signal significance varies from χ_u masses from $m(\chi_u) =$ 770-1100 GeV, depending $m(\phi^{'})$. For large $m(\chi_u)$, the significance is almost independent of $m(\phi')$ because the primary discriminating feature—the boosted b-quark originating from ϕ'—is driven predominantly by the large $m(\chi_u)$, with the kinematic impact of $m(\phi')$ being relatively negligible.

3.6 DISCUSSION

The LHC will continue to run with pp collisions at $\sqrt{s} = 13.6$ TeV for the next decade. Given the increase in the integrated luminosity expected from the high-luminosity program, it is important to consider unexplored new physics phase space that diverges from the conventional assumptions made in many BSM theories, and which could have remained hidden in processes that have not yet been thoroughly examined. It is additionally crucial to explore advanced analysis techniques, in particular the use of artificial intelligence algorithms, to enhance the probability of detecting these rare corners where production cross sections are lower and discrimination from SM backgrounds is difficult.

In this work, we examine a model based on a $U(1)_{T_R^3}$ extension of the SM, which can address various conceptual and experimental issues with the SM, including the mass hierarchy between generations of fermions, the thermal dark matter abundance, and the muon $g-2$, $R_{(D)}$, and $R_{(D^*)}$ anomalies. This model contains a light scalar boson ϕ', with potential masses below the electroweak scale, and TeV-scale vector-like quarks χ_u. We consider the scenario where the scalar ϕ' has family non-universal fermion couplings and $m(\phi') \geqslant 1$ GeV, as was suggested in Ref. [187], and thus the ϕ' can primarily decay to a pair of muons. Previous works in Refs. [189, 199] considered scenarios motivating a search methodology with a merged diphoton system from $\phi' \to \gamma\gamma$ decays. The authors of Ref [189], in which $m(\phi') < 1$ GeV, indeed pointed out that if the ϕ' is heavier than about 1 GeV, then decays to $\mu^+\mu^-$ can become the preferable mode for discovery, which is the basis for the work presented in this paper. We further note that the final state topology studied in this paper would represent the most important mode for discovery at $m(\phi') < 2m_t$ where the $\phi' \to t\bar{t}$ decay is kinematically forbidden.

The main result of this paper is that we have shown that the LHC can probe the visible decays of new bosons with masses below the electroweak scale, down to the GeV-scale, by considering the simultaneous production of heavy QCD-coupled particles, which then decay to the SM particles that contain large momentum values and can be observed in the central regions of the CMS and ATLAS detectors. The boosted system combined with innovative machine learning algorithms allows for the signal extraction above the lower-energy SM background. The LHC search strategy described here can be used to discover the prompt decay of new light particles. An important conclusion from this paper is that the detection prospects for low-mass particles are enhanced when it is kinematically possible to simultaneously access the heavy degrees of freedom which arise in the UV completion of the low-energy model. This specific scenario in which the couplings of the light scalars are generationally dependent, with important coupling values to the top quark, is an ideal example which would be difficult to directly probe at low energy beam experiments.

The proposed data analysis represents a competitive alternative to complement searches already being conducted at the LHC, allowing us to probe ϕ' masses from 1 to 325 GeV, for $m(\chi_u)$ values up to almost 2 TeV, at the HL-LHC. Therefore, we strongly encourage the ATLAS and CMS Collaborations to consider the proposed analysis strategy in future new physics searches.

4

ON VECTORIAL LEPTOQUARKS SENSITIVITY AT THE LHC

As suggested in the introduction of Ch. 3, the patterns of LFUV discussed in Sec. 1.4 motivate the construction of gauge-complete theoretical frameworks that can naturally accommodate non-universal couplings to fermions. Such frameworks could potentially link these anomalies to the resolution of other open questions in the SM, such as the B-meson anomalies. In particular, efforts have been made to embed $U(1)_{T^3_R}$ in larger gauge groups, such as the Pati–Salam model [240], which unifies quarks and leptons in the same multiplet. This unification naturally leads to the presence of leptoquarks (LQs) in the particle spectrum, mediating quark–lepton transitions [73]. This was followed by intense theoretical development aiming to explain the anomalies via TeV-scale LQ exchange at tree level [41, 43, 64, 65, 73, 83, 84, 86, 241–248].

Leptoquarks are hypothetical bosons carrying both baryon and lepton number, enabling them to interact simultaneously with a lepton and a quark. They are a common feature of SM extensions where quarks and leptons belong to the same multiplet. Besides the Pati–Salam model [240], typical examples include $SU(5)$ GUT scenarios [249]. They can also appear in theories with strong dynamics, such as compositeness [250]. LQs have exotic couplings that allow quark–lepton transitions, resulting in a rich and diverse phenomenology which naturally leads to multiple constraints. A particularly stringent one arises from proton decay, which pushes the LQ mass close to the Planck scale unless baryon and lepton numbers are conserved. Even in models where these numbers are preserved, LQs remain subject to a wide variety of experimental and phenomenological bounds [42, 251–255], including limits from meson mixing, electric and magnetic dipole moments, atomic parity violation tests, rare decays, and direct searches. The relative importance of these bounds is, however, highly model dependent.

Before the end of 2022, it was generally agreed that, within proposed single LQ solutions, the only candidate capable of addressing all B-meson anomalies simultaneously and surviving all other constraints was a vector LQ (U_1), transforming as $(\mathbf{3}, \mathbf{1}, 2/3)$, and coupling mainly to third-generation fermions via $b\,\tau$ and $t\,\nu_\tau$ vertices [43, 73]. Despite a recent re-analysis of $R_{K^{(*)}}$ data showing this ratio to be compatible with the SM prediction [46, 51, 52, 67], the solution to the $R_{D^{(*)}}$ anomaly remains an

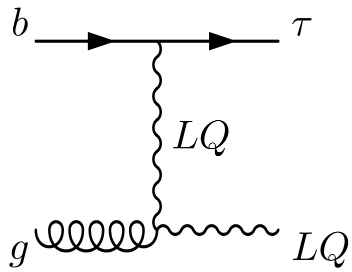

(a)

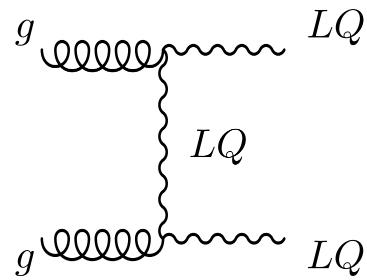

(b)

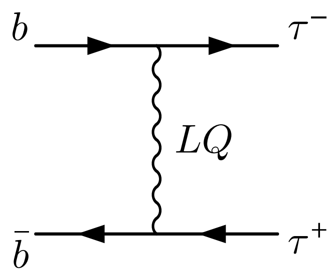

(c)

Figure 4.1: Representative Feynman diagrams of single (a), pair (b), and non-resonant (c) production leptoquarks in proton-proton collision experiments. In single and pair production, the diagrams shown involve t-channel LQ exchange, dominant for lower LQ mass. However, for larger mass there exist s-channel diagrams featuring a virtual bottom quark and gluon, respectively.

open question. This continues to be a valid motivation for the study of scenarios where new particles have preferential couplings to third-generation fermions. Thus, it is still of interest to continue exploring the possibility of observing the U_1 LQ at the LHC [248].

As expected, the theoretical community has extensively participated in probing LQ models by scrutinizing search strategies, recasting LHC results, and predicting the reach in the parameter space via different searches involving third-generation fermions (see for instance [97, 203, 256–263]). In addition, several 13 TeV searches for LQs decaying into t/b and τ/ν final states have been performed by the CMS [91, 264–271] and ATLAS [92, 272–277] collaborations.

Of the searches above, we find [91] particularly interesting. Here, the CMS collaboration explores signals corresponding to $t\,\nu\,b\,\tau$ and $t\,\nu\,\tau$ final states, with 137 fb^{-1} of pp collision data. The former is motivated by LQ pair production, with one LQ decaying into $t\,\nu$ and the other into $b\,\tau$, while the latter arises from a single LQ produced in association with a τ, with a subsequent LQ decay into $t\,\nu$ (see Fig. 4.1 for the corresponding diagrams). From the combination of both production channels, the search excludes U_1

masses under $1.3-1.7\,\text{TeV}$, with this range depending on the U_1 coupling to gluons and on its coupling g_U in the $b_L\,\tau_L$ vertex.

What makes this search particularly attractive is that, for the first time, an LHC collaboration directly places (mass dependent) bounds on g_U. This is important, since having information on this parameter is crucial in order to understand if the U_1 is really responsible for the $R_{D^{(*)}}$ anomaly. The inclusion of the single-LQ production mode is important, since its cross-section is directly proportional to g_U^2. However, as can be seen in Figure 6 of [91], the current constraints are dominated by pair production, with single-LQ production playing a subleading role. While this is expected [259], it still leads us to ponder the possibility of improving the sensitivity of LHC searches to single-LQ production, and thus on achieving better constraints on g_U. Other complementary and similar searches to [91] were carried out by both ATLAS [276] and CMS [271].

It is also well known, though, that searches for an excess in the high-p_T tails of τ lepton distributions can strongly probe g_U, up to very large LQ masses. Indeed, as shown in [96, 248], the new physics effective operators contributing to $R_D{}^{(*)}$ also contribute to an enhancement in the $pp \to \tau\tau$ production rates. This has motivated a large number of recasts [69, 70, 73, 74, 97, 248, 259, 278, 279], as well as a CMS search explicitly providing constraints in terms of U_1 [270]. Nevertheless, it is important to note that for these $pp \to \tau\tau$ processes, the LQ participates non-resonantly, so contributions to the $pp \to \tau\tau$ rates and kinematic distributions from non-LQ BSM diagrams containing possible virtual particles, such as a heavy neutral vector boson Z', could spoil a straightforward interpretation of any possible excess [97]. Thus, it is also necessary to understand how the presence of other virtual particles can affect the sensitivity of an analysis probing g_U.

In this work we study the projected LQ sensitivity at the LHC, considering already available pp data as well as the expected amount of data to be acquired during the HL-LHC runs. We explore a proposed analysis strategy which utilizes a combination of single-, double-, and non-resonant-LQ production, targeting final states with varying τ-lepton and b-jet multiplicities. The studies are performed considering various benchmark scenarios for different LQ masses and couplings, also taking into account distinct chiralities for the third-generation fermions in the LQ vertex. We also assess the impact of a companion Z', which is typical of gauge models, in non-resonant LQ probes, and find that interference effects can have a significant effect on the discovery reach. We consider this effect to be of high interest, given that non-resonant LQ production can have the largest cross-section, and thus could be an important channel in terms of discovery potential.

An important aspect of this work is that the analysis strategy is developed using a ML algorithm based on BDTs[170]. The output of the event classifier is used to perform a profile-binned likelihood test to extract the overall signal significance for each model considered in the analysis. The advantage of using BDTs and other ML algorithms has been demonstrated in several experimental and phenomenological studies [201–207]. In our studies, we find that the BDT algorithm gives sizeable improvement in signal significance.

4.1 A SIMPLIFIED MODEL FOR THE U_1 LEPTOQUARK

Extending the SM with a massive U_1 vector LQ is not straightforward, as one has to ensure the renormalizability of the model. Most of the theoretical community has focused on extensions of the Pati-Salam (PS) models which avoid proton decay, such as the scenario found in [176]. Other examples include PS models with vector-like fermions [280–282], the so-called 4321 models [71, 72, 93], the twin PS^2 model [85, 283], the three-site PS^3 model [284–286], as well as composite PS models [287–289].

In what follows, we shall restrict ourselves to a simplified non-renormalizable lagrangian, understood to be embedded into a more complete model. The SM is thus extended by adding the following terms featuring the U_1 LQ:

$$\begin{aligned}\mathcal{L}_{U_1} \;=\; & -\frac{1}{2}U^{\dagger}_{\mu\nu}U^{\mu\nu} + M_U^2\, U^{\dagger}_{1\mu}U_1^{\mu} \\ & -ig_s\, U^{\dagger}_{1\mu}\, T^a\, U_{1\nu}\, G^{a\mu\nu} - i\frac{2}{3}g'\, U^{\dagger}_{1\mu}U_{1\nu}B^{\mu\nu} \\ & +\frac{g_U}{\sqrt{2}}[U_{1\mu}(\bar{Q}_3\,\gamma^{\mu}L_3 + \beta_L^{s\tau}\,\bar{Q}_2\,\gamma^{\mu}L_3 \\ & +\beta_R\,\bar{b}_R\,\gamma^{\mu}\tau_R) + \text{h.c.}] \end{aligned} \tag{4.1}$$

where $U_{\mu\nu} \equiv \mathcal{D}_{\mu}U_{1\nu} - \mathcal{D}_{\nu}U_{1\mu}$, and $\mathcal{D}_{\mu} \equiv \partial_{\mu} + ig_sT^aG^a_{\mu} + i\frac{2}{3}g'B_{\mu}$. As evidenced by the second line above, we assume that the LQ has a gauge origin [1].

The third and fourth lines in in Eq. (4.1) shows the LQ interactions with SM fermions, with coupling g_U, which we have chosen as preferring the third generation [2]. These are particularly relevant for the LQ decay probabilities, as well as for the single-LQ production cross-section. The $\beta_L^{s\tau}$ parameter, which is the LQ $\to s\tau$ coupling in the β_L matrix (see footnote), is chosen to be equal to 0.2, following the fit done in [70], in order to simultaneously solve the $R_{D^{(*)}}$ anomaly and satisfy the $pp \to \tau^+\tau^-$ constraints. Although $\beta_L^{s\tau}$ technically alters the single-LQ production cross-section and LQ branching fractions, we have confirmed that a value of $\beta_L^{s\tau} = 0.2$ results in negligible impact on our collider results, and thus is ignored in our subsequent studies.

The LQ right-handed coupling is modulated with respect to the left-handed one by the β_R parameter. The choice of β_R is important phe-

[1] The couplings in the second line of Eq. (4.1) can be found in the literature as $g_s \to g_s(1-\kappa_U)$ and $g' \to g'(1-\tilde{\kappa}_U)$, in order to take into account the possibility of an underlying strong interaction.

[2] Before the demise of the $R_{K^{(*)}}$ anomaly [46, 51, 52, 67], a 3×3 β_L matrix would be used instead, with values fitted to solve all B meson anomalies.

nomenologically, as it affects the LQ branching ratios [3], as well as the single-LQ production cross-section. To illustrate the former, Fig. 4.2 (top) shows the LQ $\to b\tau$ and LQ $\to t\nu$ branching ratios as functions of the LQ mass, for two values of β_R. For large LQ masses, we confirm that with $\beta_R = 0$ then BR(LQ $\to b\,\tau$) $\approx$ BR(LQ $\to t\,\nu$) $\approx \frac{1}{2}$. However, for $\beta_R = -1$, as was chosen in [86], the additional coupling adds a new term to the total amplitude, leading to BR(LQ $\to b\,\tau$) $\approx \frac{2}{3}$. The increase in this branching ratio can thus weaken bounds from LQ searches targeting decays into $t\,\nu$ final states, which motivates exploring the sensitivity in $b\tau$ final states exclusively. Note that although a BR(LQ $\to b\,\tau$) ≈ 1 scenario is possible by having the LQ couple exclusively to right-handed currents (i.e, $g_U \to 0$, but $g_U\beta_R \neq 0$), it does not solve the observed anomalies in the $R_{D^{(*)}}$ ratios. Therefore, although some LHC searches assume BR(LQ $\to b\,\tau$) $= 1$, we stress that in our studies we assume values of the model parameters and branching ratios that solve the $R_{D^{(*)}}$ ratios.

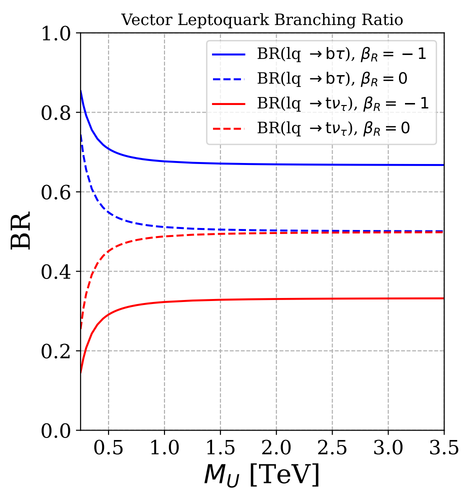

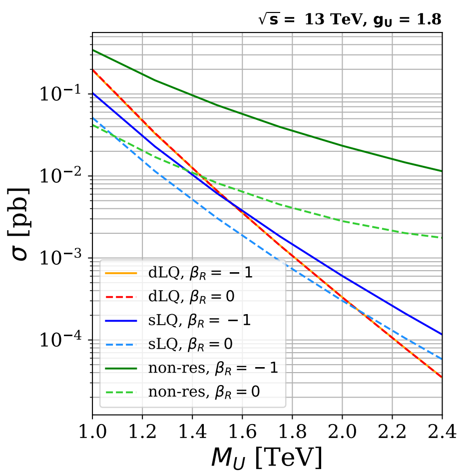

Figure 4.2: Left: The LQ $\to b\tau$ and LQ $\to t\nu$ branching ratios for $\beta_R = 0$ (solid lines) and $\beta_R = -1$ (dashed lines). Right: Signal cross-section as a function of the LQ mass, for $\sqrt{s} = 13$ TeV, with $g_U = 1.8$. We show single, pair, and non-resonant production, for $\beta_R = -1, 0$ in solid and dashed lines, respectively.

To further understand the role of β_R at colliders, Fig. 4.2 (bottom) shows the cross-section for single-LQ (sLQ), double-LQ (dLQ), and non-resonant (non-res) production, as a function of mass and for a fixed coupling $g_U = 1.8$, assuming $p\,p$ collisions at $\sqrt{s} = 13$ TeV. We note that this benchmark scenario with $g_U = 1.8$ results in a LQ $\to b\tau$ decay width that is <5% of the LQ mass, for mass values from 250 GeV to 2.5 TeV. In the Figure, we observe that, since dLQ production is mainly mediated by events from quantum chromodynamic processes, the choice of β_R does not affect the cross-section. However, for sLQ production, a non-zero value for β_R increases the cross-section by about a factor of 2 and by almost one order

[3] Having $\beta_L^{s\tau}$ different from zero also opens new decay channels. These, however, are either suppressed by $\beta_L^{s\tau}$ and powers of λ_{CKM}. In any case, this effect would decrease BR(LQ $\to b\,\tau$) and BR(LQ $\to t\,\nu$) by less than 3%.

of magnitude in the case of non-res production. These results shown in Fig. 4.2 are easily understood by considering the diagrams shown in Fig. 4.1. The LQ mass value where the sLQ production cross-section exceeds the dLQ cross-section depends on the choice of g_U.

We also note that to solve the $R_{D^{(*)}}$ anomaly, the authors of [70] point out that the wilson coefficient $C_U \equiv g_U^2\, v_{SM}^2/(4\, M_U^2)$ is constrained to a specific range of values, and this range depends on the value of the β_R parameter. Therefore, the allowed values of the coupling g_U depend on M_U and β_R, and thus our studies are performed in this multi-dimensional phase space.

We study the role of a Z' boson in $p\,p \to \tau\tau$ production. The presence of a Z' boson in LQ models has been justified in various papers, for example, in [97]. The argument is that minimal extensions of the SM which include a massive gauge U_1 LQ, uses the gauge group $SU(4) \times SU(3)' \times SU(2)_L \times U(1)_{T_R^3}$. Such an extension implies the presence of an additional massive boson, Z', and a color-octet vector, G', arising from the spontaneous symmetry breaking into the SM, see for example App. [**sec:4321**]. The Z' in particular can play an important role in the projected LQ discovery reach, as it can participate in $p\,p \to \tau\tau$ production by s-channel exchange, both resonantly and as a virtual mediator. To study the effect of a Z' on the $p\,p \to \tau\tau$ production cross-sections and kinematics, we extend our benchmark Lagrangian in Eq. (4.1) with further non-renormalizable terms involving the Z'. Accordingly, we assume the Z' only couples to third-generation fermions. Our simplified model is thus extended by:

Naively, the LQs are associated to the breaking of $SU(4) \to SU(3)_{[4]} \times U(1)_{B-L}$, the G' arises from $SU(3)_{[4]} \times SU(3)' \to SU(3)_c$, and the Z' comes from the breaking of $U(1)_{B-L} \times U(1)_{T_R^3} \to U(1)_Y$. Notice that the specific pattern of breaking, and the relations between the masses and couplings, are connected to the specific scalar potential used.

$$\begin{aligned}\mathcal{L}_{Z'} \;=\;& -\frac{1}{4}Z'_{\mu\nu}Z'^{\mu\nu} + \frac{1}{2}M_{Z'}^2 Z'_\mu Z'^\mu \\ &+\frac{g_{Z'}}{2\sqrt{6}}Z'^\mu(\zeta_q \bar{Q}_3\gamma_\mu Q_3 + \zeta_t \bar{t}_R\gamma_\mu t_R \\ &+\zeta_b \bar{b}_R\gamma_\mu b_R - 3\zeta_\ell \bar{L}_3\gamma_\mu L_3 - 3\zeta_\tau \bar{\tau}_R\gamma_\mu \tau_R)\end{aligned} \tag{4.2}$$

where the constants $M_{Z'}$, $g_{Z'}$, ζ_q, ζ_t, ζ_b, ζ_ℓ, ζ_τ, are model dependent.

We study two extreme cases for the Z' mass, following [290], namely $M_{Z'} = \sqrt{\frac{1}{2}}M_U < M_U$ and $M_{Z'} = \sqrt{\frac{3}{2}}M_U > M_U$. We also assume the LQ and Z' are uniquely coupled to left-handed currents, i.e. $\zeta_q = \zeta_\ell = 1$ and $\zeta_t = \zeta_b = \zeta_\tau = 0$. With these definitions, Fig. 4.3 shows the effect of the Z' on the $\tau\tau$ production cross-section, considering $g_U = 1$, $\beta_R = 0$, and different $g_{Z'}$ couplings. On the left, the cross-sections corresponding to the cases where $M_{Z'} = \sqrt{\frac{1}{2}}M_U$ are shown. As expected, the $\tau\tau$ production cross-section for the inclusive case (i.e., $g_{Z'} \neq 0$) is larger than that for the LQ-only non-res process ($g_{Z'} = 0$, depicted in blue). This effect increases with $g_{Z'}$ and, within the evaluated values, can exceed the LQ-only cross-section by up to two orders of magnitude. In contrast, a more intricate behaviour can be seen on the right of Fig. 4.3, which corresponds to $M_{Z'} = \sqrt{\frac{3}{2}}M_U$. Here, for low values of M_U, a similar increase in the cross-section is observed. However, for higher values of M_U, the inclusive $p\,p \to \tau\tau$ cross-section is smaller than the LQ-only $\tau\tau$ cross-section. This behaviour suggests the presence of a dominant destructive interference at high masses, leaving its imprint on the results.

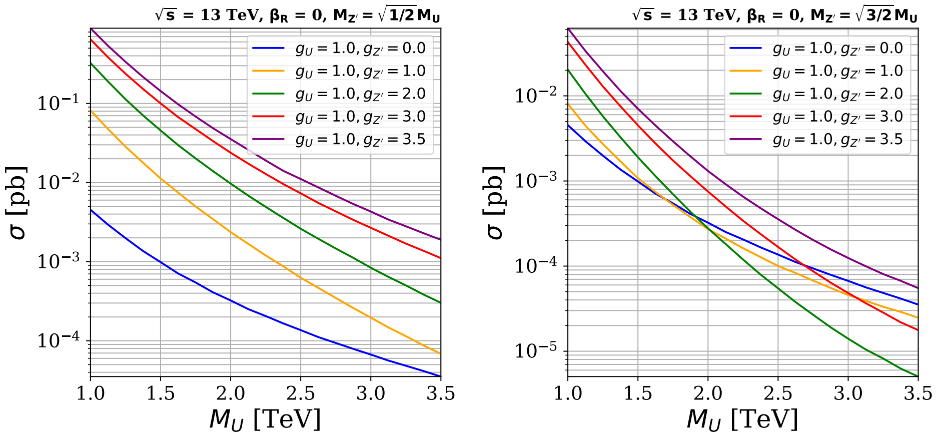

Figure 4.3: $\tau\tau$ cross-section as a function of the LQ mass for different values of g_U and $g_{Z'}$. The estimates are performed at $\sqrt{s} = 13\,\text{TeV}$, $\beta_R = 0$, $M_{Z'} = \sqrt{1/2}M_U$ (left), and $M_{Z'} = \sqrt{3/2}M_U$ (right).

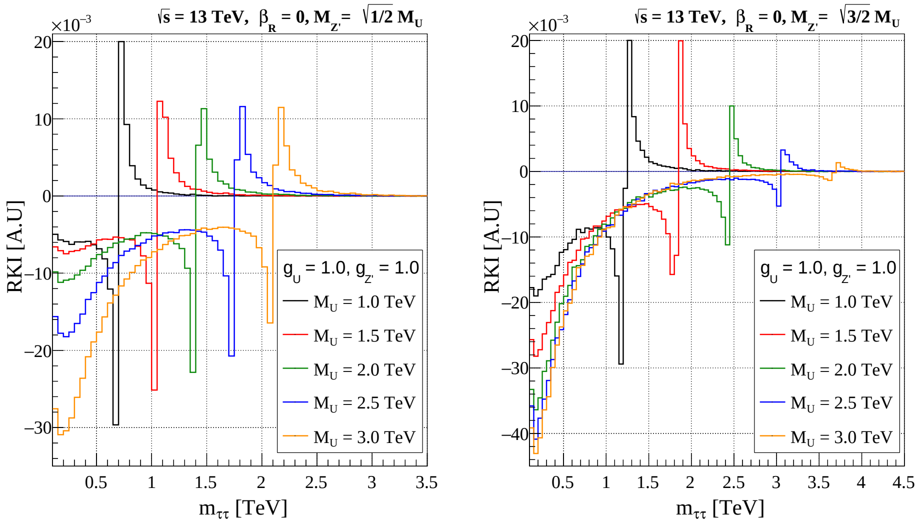

Figure 4.4: The relative kinematic interference (RKI), as a function of the reconstructed mass of two taus, for different LQ masses. The studies are performed assuming $\sqrt{s} = 13\,\text{TeV}$, $\beta_R = 0$, $g_U = 1.0$, $g_{Z'} = 1.0$, $M_{Z'} = \sqrt{1/2}M_U$ (left), and $M_{Z'} = \sqrt{3/2}M_U$ (right).

In order to further illustrate the effect, Fig. 4.4 shows the relative kinematic interference (RKI) as a function of the reconstructed invariant mass $m_{\tau\tau}$, for $g_{Z'} = 1$ and varying values of M_U. The RKI parameter is defined as

$$\text{RKI}(m_{\tau\tau}) = \frac{1}{\sigma_{LQ+Z'}}\left[\frac{d\sigma_{LQ+Z'}}{dm_{\tau\tau}} - \left(\frac{d\sigma_{LQ}}{dm_{\tau\tau}} + \frac{d\sigma_{Z'}}{dm_{\tau\tau}}\right)\right], \tag{4.3}$$

where σ_X is the production cross-section arising due to contributions from X particles. For example, $\sigma_{LQ+Z'}$ represents the inclusive cross-section where both virtual LQ and s-channel Z' exchange contribute. For both cases, we can observe the presence of deep valleys in the RKI curves when $m_{\tau\tau} \to 0$, indicating destructive interference between the LQ and the Z' contributions. This interference generates a suppression of the differential cross-section for lower values of $m_{\tau\tau}$ and, therefore, in the integrated cross-section.

The observed interference effects are consistent with detailed studies on resonant and non-res $p\,p \to t\bar{t}$ production, performed in reference [291].

4.2 SEARCH STRATEGY AND SIMULATION

Our proposed analysis strategy utilizes single-LQ (i.e. $p\,p \to \tau\,\mathrm{LQ}$), double-LQ (i.e. $p\,p \to \mathrm{LQ}\,\mathrm{LQ}$), and non-resonant LQ production (i.e. $p\,p \to \tau\tau$) as shown in Fig. 4.1. At leading order in α_s, since we focus on $U_1 \to b\,\tau$ decays, the sLQ process results in the $b\tau\tau$ mode, the dLQ process results in the $bb\tau\tau$ mode, and the non-res process results in the $\tau\tau$ mode. Therefore, in all cases we obtain two τ leptons, with either 0, 1, or 2 b jets. The τ leptons decay to hadrons (τ_h) or semi-leptonically to electrons or muons (τ_ℓ, $\ell = e$ or μ). To this end, we study six final states: $\tau_h\tau_{h/\ell}$, $b\,\tau_h\tau_{h/\ell}$, and $bb\,\tau_h\tau_{h/\ell}$, which can be naively associated to non-res, sLQ and dLQ production, respectively. Nevertheless, experimentally it is possible for b jets to not be properly identified or reconstructed, leading, for instance, to a fraction of dLQ signal events falling into the $b\,\tau_h\tau_{h/\ell}$ and $\tau_h\tau_{h/\ell}$ categories. Similarly, soft jets can fake b jets, such that non-res processes can contribute to the $b\,\tau_h\tau_{h/\ell}$ and $bb\,\tau_h\tau_{h/\ell}$ final states. This kind of signal loss and mixing is taken into account in our analysis[4].

The contributions of signal and background events are estimated using Monte Carlo (MC) simulations. We implemented the U_1 model from [97], adjusted to describe the lagrangian in Equations (4.1) and (4.2), using `FeynRules` (v2.3.43) [105, 157]. The branching ratios and cross-sections have been calculated using `MadGraph5_aMC` (v3.1.0) [104, 159], the latter at leading order in α_s. The corresponding samples are generated considering $p\,p$ collisions at $\sqrt{s} = 13\,\mathrm{TeV}$ and $\sqrt{s} = 13.6\,\mathrm{TeV}$. All samples are generated using the NNPDF3.0 NLO [112] set for parton distribution functions (PDFs) and using the full amplitude square SDE strategy for the phase-space optimization due to strong interference effects with the Z' boson. Parton level events are then interfaced with the `PYTHIA` (v8.2.44) [110] package to include parton fragmentation and hadronization processes, while `DELPHES` (v3.4.2) [106] is used to simulate detector effects, using the input card for the CMS detector geometric configurations, and for the performance of particle reconstruction and identification.

[4] Note that further signal mixing can also occur at the event generation level by including terms at larger order in α_s. For example, in the non-res diagram in Fig. 4.1, one of the initial b could come from a $g \to b\bar{b}$ splitting, leading to non resonant production of $b\,\tau_h\tau_{h/\ell}$. Simulating and studying the role of such NLO contributions is outside the scope of this work.

Variable	Threshold					
	$\tau_h\tau_h$	$b\tau_h\tau_h$	$bb\tau_h\tau_h$	$\tau_h\tau_\ell$	$b\tau_h\tau_\ell$	$bb\tau_h\tau_\ell$
$N(b)$	$= 0$	$= 1$	$\geqslant 2$	$= 0$	$= 1$	$\geqslant 2$
$p_T(b)$	-	$\geqslant 30\,\text{GeV}$		-	$\geqslant 30\,\text{GeV}$	
$\lvert\eta(b)\rvert$	-	$\leqslant 2.4$		-	$\leqslant 2.4$	
$N(\ell)$	$= 0$			$= 1$		
$p_T(e)$	-			$\geqslant 35\,\text{GeV}$		
$p_T(\mu)$	-			$\geqslant 30\,\text{GeV}$		
$\lvert\eta(\ell)\rvert$	-			$\leqslant 2.4$		
$N(\tau_h)$	$= 2$			$= 1$		
$p_T(\tau_h)$	$\geqslant 50$ GeV					
$\lvert\eta(\tau_h)\rvert$	$\leqslant 2.3$					
$\Delta R(p_i, p_j)$	$\geqslant 0.3$					

Table 4.1: Preliminary event selection criteria used to filter events before feeding them to the BDT algorithm. A $\Delta R(p_i, p_j) > 0.3$ requirement is imposed between all pairs of reconstructed particle candidates p_i, p_j.

At parton level, jets and leptons are required to have a minimum transverse momentum (p_T) of 20 GeV, while b jets are required to have a minimum p_T of 30 GeV. Additionally, we constrain the pseudorapidity (η) to $|\eta| < 2.5$ for b jets and leptons, and $|\eta| < 5.0$ for jets. The production cross-sections shown in the bottom panel of Figures 4.2 and 4.3 are obtained with the aforementioned selection criteria.

Tab. 4.1 shows the preliminary event selection criteria for each channel at analysis level. The channels are divided based on the multiplicity of b jets, $N(b)$, number of light leptons, $N(\ell)$, number of hadronic tau leptons, $N(\tau_h)$, and kinematic criteria based on η, p_T and spatial separation of particles in the detector volume ($\Delta R = \sqrt{(\Delta\eta)^2 + (\Delta\phi)^2}$). The minimum p_T thresholds for leptons are chosen following references [91, 270, 273], based on experimental constrains associated to trigger performance. Following reference [155], we use a flat identification efficiency for b jets of 70% across the entire p_T spectrum with misidentification rate of 1%. These values correspond with the "medium working point" of the CMS algorithm to identify b jets, known as DeepCSV. We also explored the "Loose" ("Tight") working point using an efficiency of 85% (45%) and mis-identification rate of 10% (0.1%). The "medium working point" was selected as it gives the best signal significance for the analysis.

For the performance of τ_h identification in DELPHES, we consider the latest technique described in [117], which is based on a deep neural network (i.e. DeepTau) that combines variables related to isolation and τ-lepton lifetime as input to identify different τ_h decay modes. Following [117],

Sample	$t\bar{t}$	single t	VV	V+jets	signals
$\mathbf{N_{events}} \times 10^{-6}$	24.31	11.50	32.35	39.45	0.60

Table 4.2: The number of simulated events for the signal and background samples.

we consider three possible DeepTau "working points": (i) the "Medium" working point of the algorithm, which gives a 70% τ_h-tagging efficiency and 0.5% light-quark and gluon jet mis-identification rate; (ii) the "Tight" working point, which gives a 60% τ_h-tagging efficiency and 0.2% light-quark and gluon jet mis-identification rate; and (iii) the "VTight" working point, which gives a 50% τ_h-tagging efficiency and 0.1% light-quark and gluon jet mis-identification rate. Similar to the choice of b-tagging working point, the choice of τ_h-tagging working point is determined through an optimization process which maximizes discovery reach. The "Medium" working point was ultimately shown to provide the best sensitivity and therefore chosen for this study. For muons (electrons), the assumed identification efficiency is 95% (85%), with a 0.3% (0.6%) mis-identification rate [121, 127, 128].

After applying the preliminary selection criteria, the primary sources of background are production of top quark pairs ($t\bar{t}$), and single-top quark processes (single t), followed by production of vector bosons with associated jets from initial or final state radiation (V+jets), and pair production of vector bosons (VV). The number of simulated MC events used for each sample is shown in Tab. 4.2.

We use two different sets of signal samples. The first set includes various $\{M_U, g_U\}$ scenarios, for two different values of $\beta_R \in \{0, -1\}$. We generate signal samples for M_U values between 250 GeV and 5000 GeV, in steps of 250 GeV. The considered g_U coupling values are between 0.25 and 3.5, in steps of 0.25. Although the signal cross-sections depend on both M_U and g_U, the efficiencies of our selections only depend on M_U (for all practical purposes) since the decay widths are relatively small compared to the mass of M_U ($\frac{\Gamma_U}{M_U} < 5\%$), and thus more sensitive to experimental resolution. In total there are 280 $\{M_U, g_U, \beta_R\}$ scenarios simulated for this first set of signal samples, and for each of these scenarios two subsets of samples are generated, which are used separately for the training and testing of the machine learning algorithm. The second set of signal samples is used to evaluate interference effects between LQs and the Z' bosons in non-res production. Using benchmark values $g_U = 1.8$ and $\beta_R = 0$, we consider various $\{M_U, g_{Z'}\}$ scenarios for two different Z' mass hypotheses, $(M_{Z'}/M_U)^2 \in \{\frac{1}{2}, \frac{3}{2}\}$. The M_U values vary between 500 GeV and 5000 GeV, in steps of 250 GeV. The $g_{Z'}$ coupling values are between 0.25 and 3.5, in steps of 0.25. Therefore, in total there are 280 $\{M_U, g_{Z'}, (M_{Z'}/M_U)^2\}$ scenarios simulated for this second set of signal samples, and for each of these scenarios a total of 6.0×10^5 MC events are generated.

As noted previously, the simulated signal and background events are initially filtered using selections which are motivated by experimental constraints, such as the geometric constraints of the CMS detector, the typical kinematic thresholds for reconstruction of particle objects, and the available triggers. The remaining events after the preliminary event selection criteria are used to train and execute a BDT algorithm for each signal point in the $\{M_U, g_U\}$ space, in order to maximize the probability to detect signal amongst background events. The BDT algorithm is implemented using the `scikit-learn` [114] and `xgboost` (XGB) [175] python libraries. We use the the `XGBClassifier` class from the `xgboost` library, a 10-fold cross validation using the `scikit-learn` method (`GridCV` [5]) for a grid in a hyperparameter space with 75, 125, 250, and 500 estimators, maximum depth in 3, 5, 7, 9, as well as learning rates of 0.01, 0.1, 1, and 10. For the cost function, we utilize the default mean square error (`MSE`). Additionally, we use the tree method based on the approximate greedy algorithm (histogram-optimized), referred to as `hist`, with a uniform sample method. These choices allow us to maximize the detection capability of the BDT algorithm by carefully tuning the hyperparameters, selecting an appropriate cost function, and utilizing an optimized tree construction method.

For each of the six analysis channels and $\{M_U, g_U\}$ signal point, the binary XGB classifier was trained (tested) with 20% (80%) of the simulated events, for each signal and background MC sample. Over forty kinematic and topological variables were studied as input for the XGB. These included the momenta of b jets and $\tau_{h,\ell}$ candidates; both invariant and transverse masses of pairs of τ objects and of $b\,\tau$ combinations; angular differences between b jets, between τ objects, and between the $\tau_{h,\ell}$ and b jets; and additional variables derived from the missing momentum in the events. After studying correlations between variables and their impact on the performance of the BDT, we found that only eight variables were necessary and responsible for the majority of the sensitivity of the analysis. The variable that provides the best signal to background separation is the scalar sum of the p_T of the final state objects (τ_h, $\tau_{h/\ell}$, and b jets) and the missing transverse momentum, referred to as S_T^{MET}:

$$S_T^{MET} = |\vec{p}_T^{\,miss}| + \sum_{\tau_h, \tau_{h/\ell}, b} |\vec{p}_T| \tag{4.4}$$

The S_T^{MET} variable has been successfully used in LQ searches at the LHC, since it probes the mass scale of resonant particles involved in the production processes. Other relevant variables include the magnitude of the vectorial difference in p_T between the two lepton candidates ($|\Delta\vec{p}_T|_{\tau_h\tau_{h/\ell}}$), the $\Delta R_{\tau_h\tau_{h/\ell}}$ separation between them, the reconstructed dilepton mass $m_{\tau_h\tau_{h/\ell}}$, and the product of their electric charges ($Q_{\tau_h} \times Q_{\tau_{h/\ell}}$). We also use the $|\Delta\vec{p}_T|$ between the τ_h candidate and $\vec{p}_T^{\,miss}$, and (if applicable) the $|\Delta\vec{p}_T|$ between the τ_h candidate and the leading b jet. For the final states including two τ_h candidates, the one with the highest p_T is used.

[5] GridCV is a method that allows to find the best combination of hyperparameter values for the model, as this choice is crucial to achieve an optimal performance.

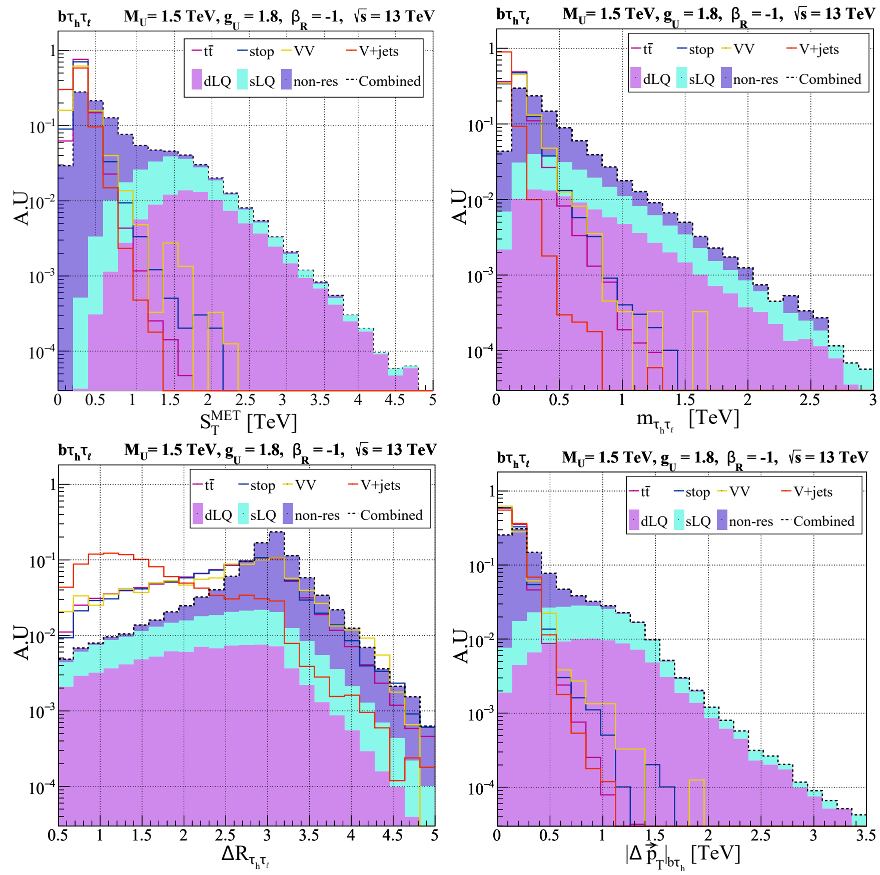

Figure 4.5: S_T^{MET}, $m_{\tau_h\tau_\ell}$, $\Delta R_{\tau_h\tau_\ell}$, $|\Delta\vec{p}_T|_{b\tau_h}$ signal and background distributions for the $b\tau_h\tau_\ell$ channel. The signal distributions are generated for a benchmark sample with LQ mass of 1.5 TeV maximally coupled to right-handed currents. The combined distribution (shown as a stacked histogram) is the sum of the distributions, correctly weighted according to their respective cross-sections, assuming a coupling $g_U = 1.8$.

Fig. 4.5 shows some relevant topological distributions, including S_T^{MET} on the top, for the $b\,\tau_h\tau_\ell$ category. In the Figure we include all signal production modes to this channel, with each component weighted with respect to their total contribution to the combined signal. The combined signal distribution is normalised to unity. We also show all background processes contributing to this channel, each of them individually normalised to unity. We find that the combined signal is dominated by sLQ production for large values of S_T^{MET}, while non-res production dominates for small S_T^{MET}. Interestingly, the backgrounds also sit at low S_T^{MET} values, since S_T^{MET} is driven by the mass scale of the SM particles being produced, in this case top quarks and Z/W bosons. This suggest that the sLQ and dLQ signals can indeed be separated from the SM background. As expected, the S_T^{MET} sLQ and dLQ signal distributions have a mean near M_U, representative of resonant production, and a broad width as expected for large mass M_U hypotheses when information about the z-components of the momenta of objects is not utilised in the S_T^{MET} calculation.

Fig. 4.5 (second from the top) shows the reconstructed mass of the ditau system, for the $b\tau_h\tau_\ell$ search channel. Since the two τ candidates in signal events arise from different production vertices (e.g., each τ candidate in dLQ production comes from a different LQ decay chain), the ditau mass distribution for signal scales as $m_{\tau_h\tau_\ell} \sim p_T(\tau_h) + p_T(\tau_\ell)$, and thus has a tail which depends on M_U and sits above the expected SM spectrum. On the other hand, the SM $m_{\tau_h\tau_\ell}$ distributions sit near $m_{Z/W}$ since the τ candidates in SM events arise from Z/W decays.

Fig. 4.5 (third from the top) shows the $\Delta R_{\tau_h\tau_\ell}$ distribution for the $b\tau_h\tau_\ell$ channel. In the case of the $pp \to \tau\tau$ non-res signal distribution, the two τ leptons must be back-to-back to preserve conservation of momentum. Therefore, the visible τ candidates, τ_h and τ_ℓ, give rise to a $\Delta R_{\tau_h\tau_\ell}$ distribution that peaks near π radians. In the case of sLQ production, although the LQ and associated τ candidate must be back-to-back, the second τ candidate arising directly from the decay of the LQ does not necessarily move along the direction of the LQ (since the LQ also decays to a b quark). As a result, the $\Delta R_{\tau_h\tau_\ell}$ distribution for the sLQ signal process is smeared out, is broader, and has a mean below π radians. On the other hand, the τ_h candidate in $t\bar{t}$ events is often a jet being misidentified as a genuine τ_h. When this occurs, the fake τ_h candidate can arise from the same top quark decay chain as the τ_ℓ candidate, thus giving rise to small $\Delta R_{\tau_h\tau_\ell}$ values. This difference in the signal and background distributions provides a nice way for the ML algorithm to help decipher signal and background processes.

As noted above, the $|\Delta\vec{p}_T|$ distribution between the visible τ candidates and the b-quark jets is an important variable to help the BDT distinguish between signal and background processes. The discriminating power can be seen in Fig. 4.5 (bottom), which shows the $|\Delta\vec{p}_T|$ between the τ_h and b-jet candidate of the $b\tau_h\tau_\ell$ channel. In the case of dLQ production, the b quarks and τ leptons from the LQ $\to b\tau$ decay acquire transverse momentum of $p_T \sim M_U/2$. However, when the τ lepton decays hadronically (i.e. $\tau \to \tau_h\nu$), a large fraction of the momentum is lost to the neutrino. Therefore, the $|\Delta\vec{p}_T|_{b\tau_h}$ distribution for the dLQ (and sLQ) process peaks below $M_U/2$. On the other hand, for a background process such as V+jets, the b jet arises due to initial state radiation, and thus must balance the momentum of the associated vector boson (i.e. $p_T(b) \sim p_T(V) \sim m_V$). Since the visible τ candidate is tyically produced from the V boson decay chain, its momentum (on average) is approximately $p_T(\tau_h) \sim p_T(V)/4 \sim m_V/4$. Therefore, to first order, the $|\Delta\vec{p}_T|$ distribution for the V+jets background is expected to peak below the m_V mass.

Lets us turn to the results of the $b\tau_h\tau_\ell$ BDT classifier, which is shown in Fig. 4.6 for the different signal production modes and backgrounds. Similar to Fig. 4.5, the distribution for each individual signal production mode is weighted with respect to their total contribution to the combined signal. The background distributions and combined signal distribution are normalized to an area under the curve of unity. Fig. 4.6 shows the XGB

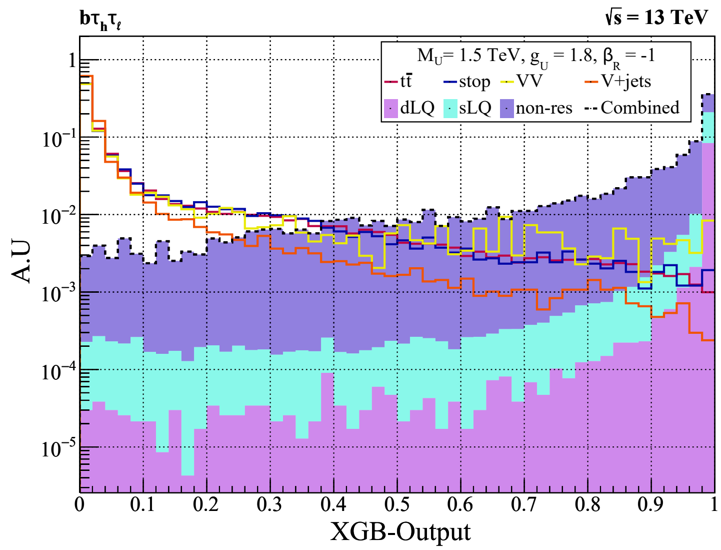

Figure 4.6: Postfit XGB-output normalised distribution in the $b\,\tau_h\tau_\ell$ channel, for LQ mass of 1.5 TeV, constant coupling $g_U = 1.8$, and maximally coupled to right-handed currents.

distributions for a signal benchmark point with $M_U = 1.5$ TeV, $g_U = 1.8$, and $\beta_R = -1$. The XGB output is a value between 0 and 1, which quantifies the likelihood that an event is either signal-like (XGB output near 1) or background-like (XGB output near 0). We see that the presence of the sLQ and dLQ production modes is observed as an enhancement near a XGB output of unity, while the backgrounds dominate over the low end of the XGB output spectrum, especially near zero. In fact, over eighty percent of the sLQ and dLQ distributions reside in the last two bins, XGB output greater than 0.96, while more than sixty percent of the backgrounds fall in the first two bins, XGB output less than 0.04. It is also interesting to note that in comparison to the sLQ and dLQ distributions in Fig. 4.6, non-res is broader and not as narrowly peaked near XGB output of 1, which is expected due to the differences in kinematics described above. Overall, if we focus on the last bin in this distribution, we find approximately 0.2% of the background, in contrast to 22% of the non-res, 78% of the sLQ, and 91% of the dLQ signal distributions. These numbers highlight the effectiveness of the XGB output in reducing the background in the region where the signal is expected.

The output signal and background distributions of the XGB classifier, normalised to their cross section times pre-selection efficiency times luminosity, are used to perform a profile binned likelihood statistical test in order to determine the expected signal significance. The estimation is performed using the `RooFit` [292] package, following the same methodology as in Refs. [231–236, 293–302]. The value of the significance (Z_{sig}) is measured using the probability to obtain the same outcome from the test statistic in the background-only hypothesis, with respect to the signal plus background hypothesis. This allows for the determination of the local p-value and thus the calculation of the signal significance, which corresponds to the point where the integral of a Gaussian distribution between Z_{sig} and ∞ results in a value equal to the local p-value.

Systematic uncertainties are incorporated as nuisance parameters, considering log-priors for normalization and Gaussian priors for shape uncertainties. Our consideration of systematic uncertainties includes both experimental and theoretical effects, focusing on the dominant sources of uncertainty. Following [113], we consider a 3% systematic uncertainty on the measurement of the integrated luminosity at the LHC. A 5% uncertainty arises due to the choice of the parton distribution function used for the MC production, following the PDF4LHC prescription [132]. The chosen PDF set only has an effect on the overall expected signal and background yields, but the effect on the shape of the XGB output distribution is negligible. Reference [117] reports a systematic uncertainty of 2-5%, depending on the p_T and η of the τ_h candidate. Therefore, we utilize a conservative 5% uncertainty per τ_h candidate, independent of p_T and η, which is correlated between signal and background processes with genuine τ_h candidates, and correlated across XGB bins for each process. We assumed a 5% τ_h energy scale uncertainty, independent of p_T and η, following the CMS measurements described in [117]. Finally, we assume a conservative 3% uncertainty per b-jet candidate, following reference [228], and an additional 10% uncertainty in all the background predictions to account for possible mismodeling by the simulated samples. The uncertainties on the background estimates are typically derived from collision data using dedicated control samples that have negligible signal contamination and are enriched with events from the specific targeted background. The systematic uncertainties on the background estimates are treated as uncorrelated between background processes.

4.3 RESULTS

The expected signal significance for sLQ, dLQ and non-res production, and their combination, is presented in Fig. 4.7. Here, the significance is shown as a heat map in a two dimensional plane of g_U versus M_U, considering exclusive couplings to left-handed currents, *i.e.* $\text{BR}(\text{LQ} \to b\,\tau) = \frac{1}{2}$. The dashed lines show the contours of constant signal significance. The 1.69σ contour represents exclusion at 95% confidence level, and the 3-5σ contours represent potential discovery. The grey band defines the set of $\{M_U, g_U\}$ values that can explain the B-meson anomalies, $C_U \sim 0.01$ for this scenario. The estimates are performed under the conditions for the second run, RUN-II, of the LHC ($\sqrt{s} = 13\,\text{TeV}$ and $L = 137\,\text{fb}^{-1}$). We find that the dLQ interpretation plot (Figure 4.7 second from the top) does not depend on g_U, which is expected due to dLQ production arising exclusively from interactions with gluons. For this reason, the dLQ production process provides the best mode for discovery when g_U is small. On the other

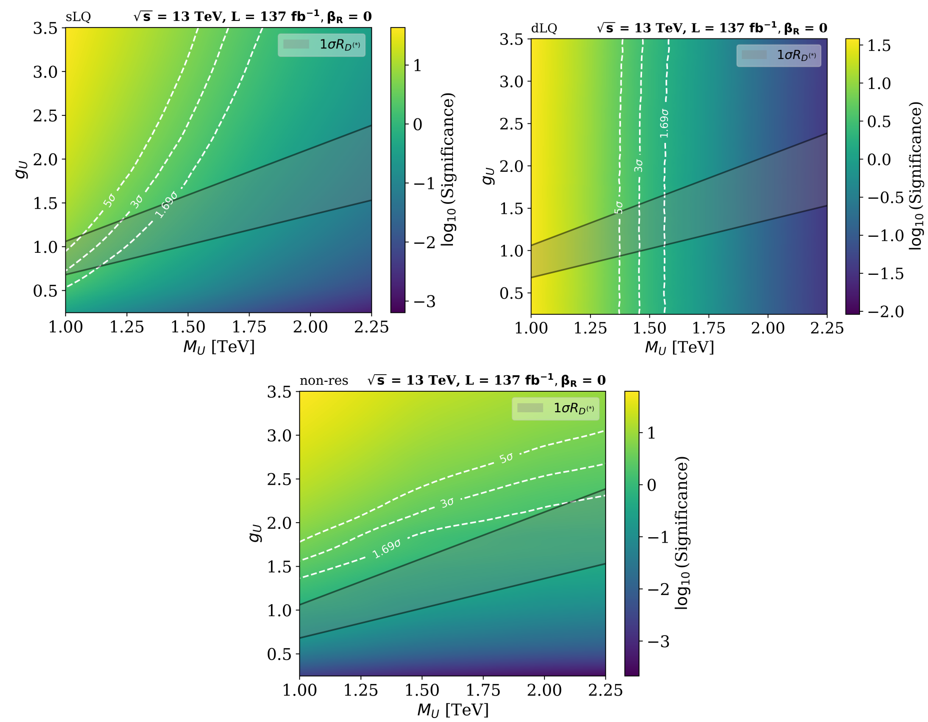

Figure 4.7: Signal significance for different coupling scenarios and LQ masses, without right-handed currents, using the combination of all search channels. The results pertaining to sLQ, dLQ and non-res production are displayed respectively from the top. These results are for $\sqrt{s} = 13\,\text{TeV}$ and $137\,\text{fb}^{-1}$.

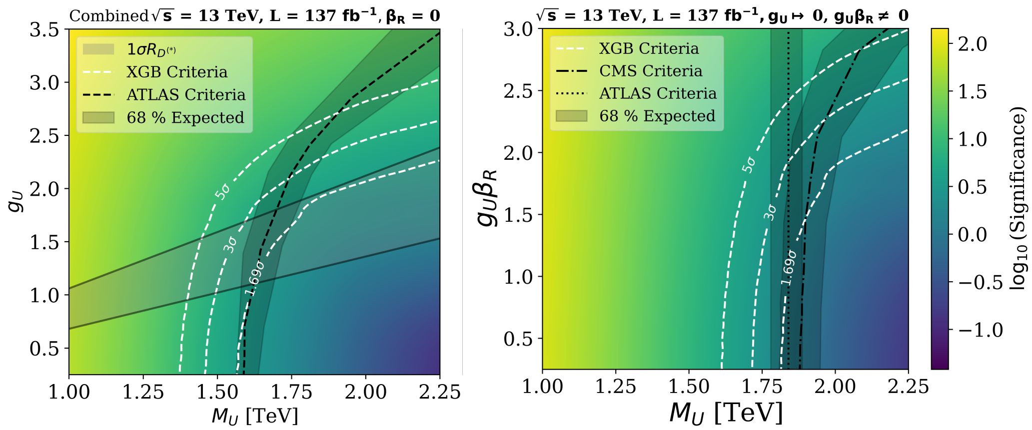

Figure 4.8: The top (bottom) panel shows signal significance comparison with ATLAS [276] (CMS and ATLAS [271, 277]) background only hypothesis, for the combination of all channels, with uniquely coupling to left-handed (right-handed) currents. The estimates are performed at $\sqrt{s} = 13$ TeV and 137 fb^{-1}.

hand, the non-res channel is more sensitive to changes in the coupling parameter g_U, as its production cross-section depends on g_U^4. Therefore, the non-res production process provides the best mode for discovery when g_U is large. These results confirm the expectations from previous analyses (see for instance [259]), in the sense that the dLQ and non-res processes complement each other nicely at low and high g_U scenarios. The sLQ channel combines features from both the dLQ and non-res channels, in principle making it an interesting option to explore different scenarios and gain a better understanding of LQ properties, but the evolution of the signal significance in the full phase space is more complicated as it involves resonant LQ production with a cross-section that depends non-trivially on M_U, g_U, and the LQ coupling to gluons. However, Fig. 4.7 shows that the sLQ production process can provide complementary and competitive sensitivity to the non-res and dLQ processes, in certain parts of the phase space.

The top panel of Fig. 4.8 presents the sensitivity of all signal production processes combined, and compares our expected exclusion region with the latest one from the ATLAS Collaboration [276]. The comparison suggests that our proposed analysis strategy provides better sensitivity than current methods being carried out at ATLAS, especially at large values of g_U. In particular, we find that with the pp data already available from RUN-II, our expected exclusion curves begin to probe solutions to the B-anomalies for LQ masses up to 2.25 TeV.

Fig. 4.8 shows the expected signal significance considering BR(LQ $\to$ b τ) $= 1$, in order to compare our analysis with the corresponding results from the CMS [271] and ATLAS [277] Collaborations. Let us emphasize again that BR(LQ $\to$ b τ) depends on β_R, as illustrated on the top panel of Fig. 4.2. Thus, although the BR(LQ $\to$ b τ) $= 1$ scenario is a possible physical case, it does not solve the observed anomalies in the $R_{D^{(*)}}$ ratios,

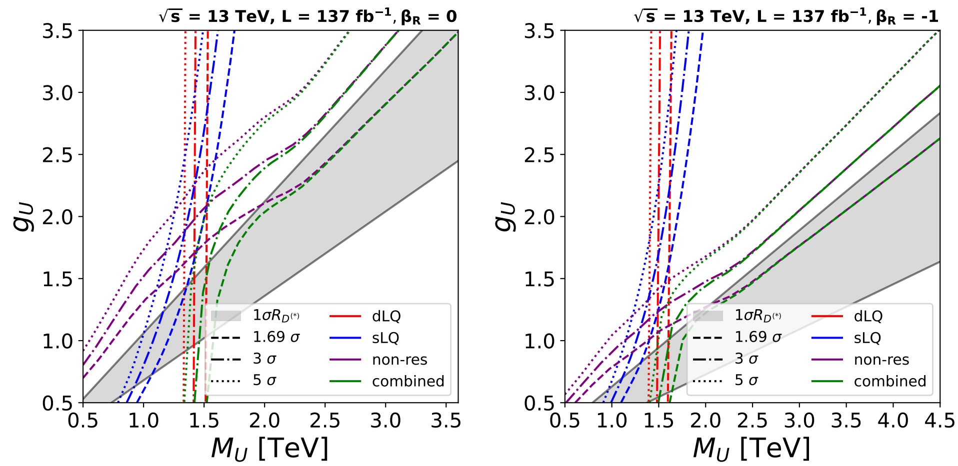

Figure 4.9: Signal significance for different coupling scenarios and LQ masses for all channels. This plot summarizes our results with $\beta_R = 0$ (without right-handed currents) and $\beta_R = -1$ (maximally coupled to right-handed currents). The estimates are performed at $\sqrt{s} = 13$ TeV and $137\,\text{fb}^{-1}$.

as it corresponds to the case where LQs couple exclusively to right-handed currents.

With this in mind, the scenario studied by CMS in [271] considers couplings only to left-handed currents, setting artificially the condition $\text{BR}(\text{LQ} \to b\,\tau) = 1$. In order to compare, we scale the efficiency$\times$acceptance of our selection criteria for $\beta_R = 0$, by a factor of 2.0 for sLQ and 4.0 for dLQ. According to Fig. 4.8, the ML approach that we have followed again suggests an optimisation of the signal and background separation, having the potential of improving the regions of exclusion (1.69 σ) with respect to that of CMS. In the bottom panel of the Figure we have also included a similar exclusion by ATLAS [277]. However, since ATLAS only considers dLQ production in the analysis, the results are not entirely comparable, so are included only as a reference.

We now turn to the role of β_R, and our capacity of probing the regions solving the B-meson anomalies. Fig. 4.9 shows the maximum significant contours, under LHC RUN-II conditions, for the different LQ production mechanisms and their combination, considering scenarios with only left-handed currents ($\beta_R = 0$, top) and with maximal right-handed currents ($\beta_R = -1$, bottom). We find a noticeable improvement in signal significance in all channels when taking $\beta_R = -1$, as is expected from the increase in $\text{BR}(\text{LQ} \to b\,\tau)$ branching ratio and production cross-sections (see Fig. 4.2). However, the region solving the B-meson anomalies also changes, preferring lower values of g_U, such that in both cases we find ourselves just starting to probe this region at large M_U.

The combined significance contours for the different BR scenarios that have been considered is presented in Fig. 4.10. These contours illustrate the regions of exclusion for the three cases of interest, namely exclusive left-handed currents ($\text{BR}(\text{LQ} \to b\,\tau) = \frac{1}{2}$, $\beta_R = 0$), maximal left and right

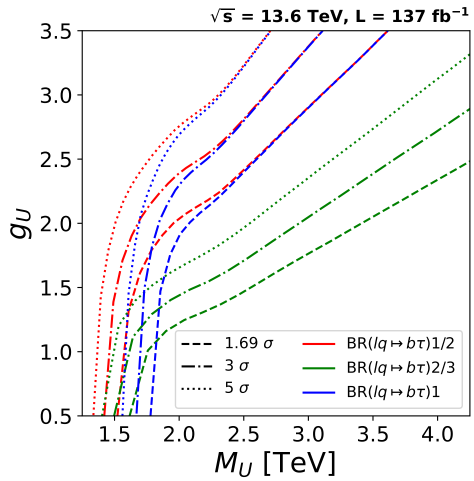

Figure 4.10: Signal significance for different coupling scenarios and LQ masses, considering the case without coupling to right-handed currents $\mathrm{BR}(\mathrm{LQ} \to b\,\tau) = \frac{1}{2}$, the case maximally coupled to right- and left-handed currents $\mathrm{BR}(\mathrm{LQ} \to b\,\tau) = \frac{2}{3}$, and the case uniquely coupled to right-handed currents $\mathrm{BR}(\mathrm{LQ} \to b\,\tau) = 1$. The estimates are performed at $\sqrt{s} = 13\,\mathrm{TeV}$ and $137\,\mathrm{fb}^{-1}$.

couplings ($\mathrm{BR}(\mathrm{LQ} \to b\,\tau) = \frac{2}{3}$, $\beta_R = -1$), and exclusive right-handed currents ($\mathrm{BR}(\mathrm{LQ} \to b\,\tau) = 1$, $g_U \to 0$, $g_U\beta_R = 1$). For small g_U, we find that the exclusive right-handed scenario is most sensitive, while the exclusive left-handed case is the worst. The reason for this is that this region is excluded principally by dLQ production, such that having the largest branching ratio is crucial in order to have a large number of events. For larger couplings, both exclusive scenarios end up having similar exclusion regions, with the $\beta_R = -1$ case being significantly more sensitive. The reason in this case is that the exclusion is dominated by non-res, which has a much larger production cross-section if both currents are turned on.

In order to finalise our analysis of the LQ-only model, we show in Fig. 4.11 the expected combined significance in the relatively near future. For this, considering $\sqrt{s} = 13.6\,\mathrm{TeV}$, we show contours for the sensitivity corresponding to integrated luminosities of $137\,\mathrm{fb}^{-1}$, $300\,\mathrm{fb}^{-1}$, and $3000\,\mathrm{fb}^{-1}$, for scenarios with only left-handed currents (top) and with maximal coupling to right-handed currents (bottom). Note that for $\beta_R = 0$ ($\beta_R = -1$), couplings g_U close to 3.18 (1.85) and $M_U = 5.0\,\mathrm{TeV}$ can be excluded with 1.69σ significance for the high luminosity LHC era, allowing us to probe the practically the entirety of the B-meson anomaly favored region. Note that the background yields for the high luminosity LHC might be larger due to pileup effects. Nevertheless, as it was mentioned in Sec. 4.2, we have included a conservative 10% systematic uncertainty associated with possible fluctuations on the background estimations. Although effects from larger pileup might be significant, they can be mitigated by improvements in the algorithms for particle reconstruction and identification, and also on the data-analysis techniques.

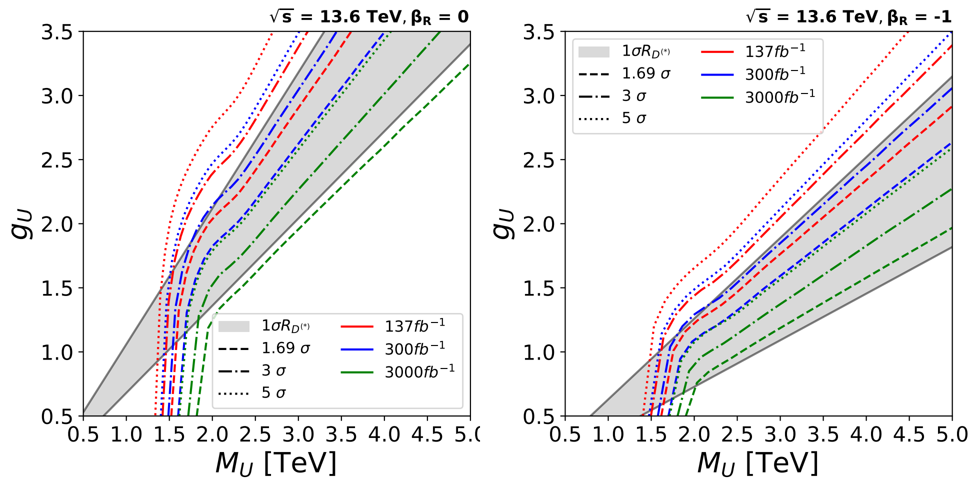

Figure 4.11: Projected signal significance for different coupling scenarios and LQ masses maximally coupled to right-handed currents. The estimates are performed at $\sqrt{s} = 13.6\,\text{TeV}$, $137\,\text{fb}^{-1}$, $300\,\text{fb}^{-1}$ and $3000\,\text{fb}^{-1}$.

As commented on the Introduction, non-res production can be significantly affected by the presence of a companion Z', which provides additional s-channel diagrams that add to the total cross-section and can interfere destructively with the LQ t-channel process (see Figures 4.3 and 4.4). From our previous results, we see that non-res always is of high importance in determining the exclusion region, particularly at large M_U and g_U, meaning it is crucial to understand how this role is affected in front of a Z' with similar mass.

The change in sensitivity on the non-res signal significance due this interference effect with the Z' boson is shown in Fig. 4.12. We consider two opposite cases for the Z' mass: $M_{Z'}^2 = M_U^2/2$ (top) and $M_{Z'}^2 = 3\,M_U^2/2$ (bottom). Our results are shown on the $g_{Z'}$ - M_U plane, for a fixed $g_U = 1.8$ and $\beta_R = 0$. For the $M_{Z'}^2 = M_U^2/2$ scenario, there is an overall increase in the total cross-section, with a larger $g_{Z'}$ implying a larger sensitivity. This means that our ability to probe smaller values of g_U could be enhanced, as a given observation would be reproduced with both a specific g_U and vanishing $g_{Z'}$, or a smaller g_U with large $g_{Z'}$. Thus, for a large enough $g_{Z'}$, it could be possible to enhance non-res to the point that the entire region favoured by B-anomalies could be ruled out. In contrast, for $M_{Z'}^2 = 3\,M_U^2/2$ the cross-section is strongly affected by the large destructive interference, such that a larger $g_{Z'}$ does not necessarily imply an increase in sensitivity. In fact, as can be seen in the bottom panel, for large M_U the significance is reduced as $g_{Z'}$ increases, leading to the opposite conclusion than above, namely, that a large $g_{Z'}$ could reduce the effectiveness of non-res.

The impact of the above can be seen in Fig. 4.13, which shows our previous sensitivity curves on the $M_U - g_U$ plane, but this time with a Z' contribution to non-res. We use the same values of $M_{Z'}$ as before, but fix $g_{Z'} = 3.5$. For smaller $M_{Z'}$ (top), the non-res contribution is enhanced so much, that both sLQ and dLQ play no role whatsoever in determining the

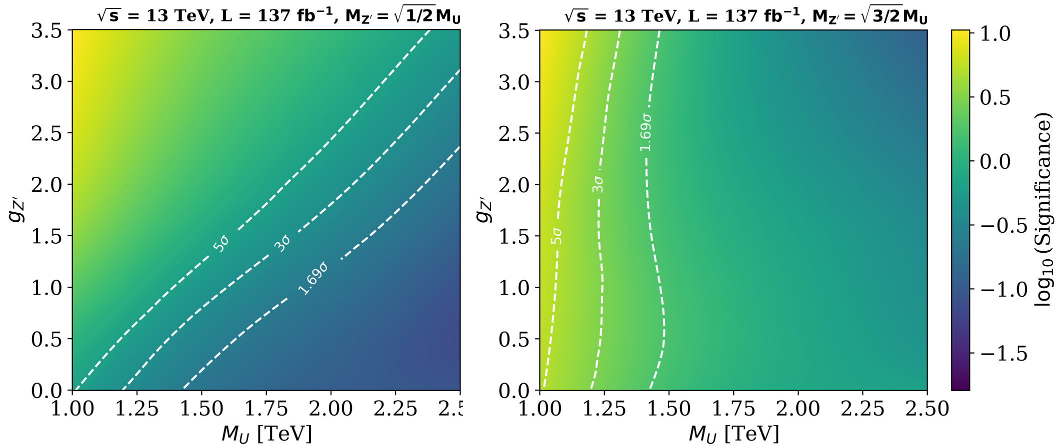

Figure 4.12: Change on the non-res signal significance for different Z' coupling scenarios and LQ masses. The estimates are performed at $\sqrt{s} = 13.0$ TeV, $\beta_R = 0$, $g_U = 1.8$, $M_{Z'} = \sqrt{1/2}M_U$ (top), and $M_{Z'} = \sqrt{3/2}M_U$ (bottom).

exclusion region. We find that, for small g_U, the sensitivity is dominated by Z' production such that, since M_U is related to $M_{Z'}$, LQ masses up to ~ 3 TeV are excluded. This bound is slightly relaxed for larger values of g_U, which is attributed to destructive interference effects due to an increased LQ contribution.

The bottom panel of Fig. 4.13 shows that case where $M_{Z'}$ is larger than M_U. As expected from our previous discussion, the behaviour and impact of non-res is modified. For small g_U, we again have the pure Z' production dominating the non-res cross-section, leading to a null sensitivity on g_U, similar to what happens in dLQ. In contrast, for very large g_U, we find that the pure LQ non-res production is the one that dominates, and we recover sensitivity regions with a slope similar to those shown in Figures 4.7-4.11, shifted towards larger values of g_U. For intermediate values of this coupling, the destructive interference have an important effect again, twisting the exclusion region slightly towards the left. Still, even in this case, we find that sLQ plays a marginal role in defining the combined exclusion region, and that the final result again depends primarily on dLQ and non-res production.

4.4 DISCUSSION AND CONCLUSIONS

Experimental searches for LQs with preferential couplings to third generation fermions are currently of great interest due to their potential to explain observed tensions in the R_D and R_{D^*} decay ratios of B mesons with respect to the SM predictions. Although the LHC has a broad physics program on searches for LQs, it is very important to consider the impact of each search within wide range of different theoretical assumptions within a specific model. In addition, in order to improve the sensitivity to detect possible signs of physics beyond the SM, it is also important to strongly consider

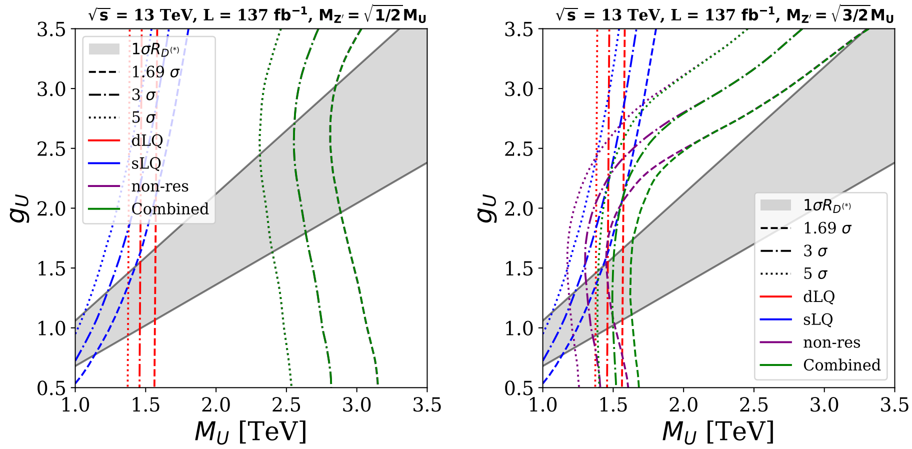

Figure 4.13: Signal significance for different coupling scenarios and LQ masses, for all channels, with an additional Z' contribution to non-res production. We set $\beta_R = 0$ and $g_{Z'} = 3.5$, taking $M^2_{Z'}$ equal to $M^2_U/2$ ($3M^2_U/2$) on the top (bottom) panel.

new computational techniques based on machine learning (ML). Therefore, we have studied the production of U_1 LQs with preferential couplings to third generation fermions, considering different couplings, masses and chiral currents. These studies have been performed considering pp collisions at $\sqrt{s} = 13$ TeV and 13.6 TeV and different luminosity scenarios, including projections for the high luminosity LHC. A ML algorithm based on boosted decision trees is used to maximize the signal significance. The signal to background discrimination output of the algorithm is taken as input to perform a profile binned-likelihood test statistic to extract the expected signal significance.

The expected signal significance for sLQ, dLQ and non-res production, and their combination, is presented as contours on a two dimensional plane of g_U versus M_U. We present results for the case of exclusive couplings to left-handed, mixed, and exclusive right-handed currents. For the first two, the region of the phase space that could explain the B meson anomalies is also presented. We confirm the findings of previous works that the largest production cross-section and best overall significance comes from the combination of dLQ and non-res production channels. We also find that the sensitivity to probe the parameter space of the model is highly dependent on the chirality of the couplings. Nevertheless, the region solving the B-meson anomalies also changes with each choice, such that in all evaluated cases we find ourselves just starting to probe this region at large M_U.

Our studies compare our exclusion regions with respect to the latest reported results from the ATLAS and CMS Collaborations. The comparison suggests that our ML approach has a better sensitivity than the standard cut-based analyses, especially at large values of g_U. In addition, our projections for the HL-LHC cover the whole region solving the B-anomalies, for masses up to 5.00 TeV.

Finally, we consider the effects of a companion Z' boson on non-res production. We find that such a contribution can have a considerable impact on the LQ sensitivity regions, depending on the specific masses and couplings. In spite of this, we still consider non-res production as an essential channel for probing LQs in the future.

A

ON THE UNIVERSAL SEESAW MECHANISM

The masses of the SM fermions are generated not through direct Yukawa couplings to the Higgs, but via a universal seesaw mechanism by mixing with new vector-like fermions χ_f. The most general gauge-invariant and renormalizable Lagrangian for the quark sector is given by:

$$\begin{aligned}\mathcal{L}_{\text{mass}}^{\text{quark}} \supset\ & \bar{Q}_L^i (Y_{uL})_{ij} \chi_{uR}^j \tilde{H} + \bar{Q}_L^i (Y_{dL})_{ij} \chi_{dR}^j H \\ & + \bar{\chi}_{uL}^i (Y_{uR})_{ij} u_R^j \phi^* + \bar{\chi}_{dL}^i (Y_{dR})_{ij} d_R^j \phi \\ & + \bar{\chi}_{uL}^i (m_{\chi u})_{ij} \chi_{uR}^j + \bar{\chi}_{dL}^i (m_{\chi d})_{ij} \chi_{dR}^j + \text{h.c.},\end{aligned} \tag{A.1}$$

where $i, j = 1, 2, 3$ are flavor indices. An entirely analogous set of terms exists for the lepton sector. The Yukawa matrices $Y_{uL}, Y_{dL}, Y_{uR}, Y_{dR}$ and the vector-like mass matrices $m_{\chi u}, m_{\chi d}$ are general complex 3×3 matrices, making the flavor structure highly non-trivial.

To make physical predictions, we must diagonalize these matrices. We express them in terms of their singular value decompositions (i.e., their diagonal forms) and the associated unitary mixing matrices:

$$\begin{aligned} Y_{uL} &= U_{LL}^\dagger Y_{uL}^d U_{LR}, & Y_{uR} &= U_{RL}^\dagger Y_{uR}^d U_{RR}, \\ Y_{dL} &= V_{LL}^\dagger Y_{dL}^d V_{LR}, & Y_{dR} &= V_{RL}^\dagger Y_{dR}^d V_{RR}, \\ m_{\chi u} &= W_{uL}^\dagger m_{\chi u}^d W_{uR}, & m_{\chi d} &= W_{dL}^\dagger m_{\chi d}^d W_{dR}. \end{aligned}$$

Here, the matrices Y^d and m^d are real, diagonal, and non-negative. The unitary matrices U, V, W are not physical by themselves but encode the mixing between flavor states.

We now perform a series of field redefinitions to absorb the maximal number of these unitary matrices into the definitions of the fermion fields. The goal is to make as many mass parameters diagonal as possible. The redefinitions are:

$$\begin{aligned} &Q_L \to U_{LL} Q_L, \quad \chi_{uR} \to W_{uR}\chi_{uR}, \quad \chi_{uL} \to W_{uL}\chi_{uL}, \quad u_R \to U_{RR} u_R, \\ &\chi_{dR} \to W_{dR}\chi_{dR}, \quad \chi_{dL} \to W_{dL}\chi_{dL}, \quad d_R \to V_{RR} d_R. \end{aligned}$$

Applying these transformations to the Lagrangian (A.1) and using the definitions above, we obtain the simplified form:

$$\begin{aligned}\mathcal{L}_{\text{Yuk}} =\ & \bar{Q}_L Y_{uL}^d (U_{LR} W_{uR}^\dagger) \chi_{uR} \tilde{H} + \bar{Q}_L (U_{LL} V_{LL}^\dagger) Y_{dL}^d (V_{LR} W_{dR}^\dagger) \chi_{dR} H \\ & + \bar{\chi}_{uL} (W_{uL} U_{RL}^\dagger) Y_{uR}^d u_R \phi^* + \bar{\chi}_{dL} (W_{dL} V_{RL}^\dagger) Y_{dR}^d d_R \phi \\ & + \bar{\chi}_{uL} m_{\chi u}^d \chi_{uR} + \bar{\chi}_{dL} m_{\chi d}^d \chi_{dR} + \text{h.c.}\end{aligned}$$

The matrix $\tilde{V}_{CKM} \equiv U_{LL} V_{LL}^\dagger$ is identified as the unitary matrix that will yield the observed Cabibbo-Kobayashi-Maskawa (CKM) quark mixing. For simplicity, and to focus on the essential mass generation mechanism, we adopt a *flavor-aligned* scenario. This assumes that all other unitary matrices (U_{LR}, W_{uR}, W_{uL}, U_{RL}, etc.) are equal to the identity matrix. This is a strong assumption that minimizes new sources of flavor violation beyond the SM. Under this assumption, the Lagrangian simplifies dramatically to:

$$\begin{aligned}\mathcal{L}_{\text{Yuk}} = &\bar{Q}_L Y^d_{uL} \chi_{uR} \tilde{H} + \bar{Q}_L \tilde{V}_{CKM} Y^d_{dL} \chi_{dR} H \\ &+ \bar{\chi}_{uL} Y^d_{uR} u_R \phi^* + \bar{\chi}_{dL} Y^d_{dR} d_R \phi \\ &+ \bar{\chi}_{uL} m^d_{\chi u} \chi_{uR} + \bar{\chi}_{dL} m^d_{\chi d} \chi_{dR} + \text{h.c.}\end{aligned}$$

All matrices Y^d and m^d are now diagonal. The only remaining off-diagonal flavor structure is in $\tilde{V}_{CKM}$.

After the electroweak symmetry breaking ($\langle H \rangle = v_h/\sqrt{2}$) and the $U(1)_{T^3_R}$ breaking ($\langle \phi \rangle = v_\phi/\sqrt{2}$), the mass terms for the up-type quarks (and analogously for down-type and leptons) are generated. For a single generation, the mass terms in the basis $(\bar{u}_L, \bar{\chi}_{uL})$, $(u_R, \chi_{uR})^T$ form a 2×2 matrix:

$$\mathcal{L}_{\text{mass}} = -\begin{pmatrix} \bar{u}_L & \bar{\chi}_{uL} \end{pmatrix} \begin{pmatrix} 0 & m_L \\ m_R & m_\chi \end{pmatrix} \begin{pmatrix} u_R \\ \chi_{uR} \end{pmatrix} + \text{h.c.}, \tag{A.2}$$

where the Dirac masses are:

$$\begin{aligned} m_L &= \frac{v_h}{\sqrt{2}} Y_{uL}, \\ m_R &= \frac{v_\phi}{\sqrt{2}} Y_{uR}. \end{aligned}$$

The entry m_χ is the vector-like mass. For three generations, this generalizes to a 6×6 matrix:

$$M_f = \begin{pmatrix} 0 & m_L \\ m_R & m_\chi \end{pmatrix}, \tag{A.3}$$

where each entry is now a 3×3 matrix: $m_L = \frac{v_h}{\sqrt{2}} Y^d_{fL}$, $m_R = \frac{v_\phi}{\sqrt{2}} Y^d_{fR}$, and $m_\chi = m^d_{\chi f}$.

The general mass matrix M_f is diagonalized by a bi-unitary transformation:

$$U_R^\dagger M_f U_L = M_f^d = \text{diag}(m_{f_1}, m_{f_2}, m_{f_3}, m_{F_1}, m_{F_2}, m_{F_3}), \tag{A.4}$$

where U_L and U_R are 6×6 unitary matrices. The physical masses are found by solving the eigenvalues of the Hermitian matrices $H_L = M_f M_f^\dagger$ and $H_R = M_f^\dagger M_f$, as U_L diagonalizes H_L and U_R diagonalizes H_R.

For the one-generation case, these matrices are:

$$\begin{aligned} H_L = M_f M_f^\dagger &= \begin{pmatrix} m_L m_L^\dagger & m_L m_\chi^\dagger \\ m_\chi m_L^\dagger & m_R m_R^\dagger + m_\chi m_\chi^\dagger \end{pmatrix} = \begin{pmatrix} |m_L|^2 & m_L m_\chi^* \\ m_\chi m_L^* & |m_R|^2 + |m_\chi|^2 \end{pmatrix}, \\ H_R = M_f^\dagger M_f &= \begin{pmatrix} m_R m_R^\dagger & m_R m_\chi^\dagger \\ m_\chi m_R^\dagger & m_L m_L^\dagger + m_\chi m_\chi^\dagger \end{pmatrix} = \begin{pmatrix} |m_R|^2 & m_R m_\chi^* \\ m_\chi m_R^* & |m_L|^2 + |m_\chi|^2 \end{pmatrix}. \end{aligned}$$

The eigenvalues λ of H_L (and H_R) are found from the characteristic equation $\det(H_L - \lambda \mathbb{I}) = 0$:

$$\begin{aligned} &\left||m_L|^2 - \lambda\right| \left||m_R|^2 + |m_\chi|^2 - \lambda\right| - |m_L|^2 |m_\chi|^2 = 0 \\ &\Rightarrow \lambda^2 - \lambda(|m_L|^2 + |m_R|^2 + |m_\chi|^2) + |m_L|^2 |m_R|^2 = 0. \end{aligned}$$

The solutions to this quadratic equation are the squared masses of the two mass eigenstates:

$$m_f^2 = \frac{1}{2}\left(m_\chi^2 + m_L^2 + m_R^2 - \sqrt{(m_\chi^2 + m_L^2 + m_R^2)^2 - 4m_L^2 m_R^2}\right), \qquad \text{(A.5)}$$

$$m_F^2 = \frac{1}{2}\left(m_\chi^2 + m_L^2 + m_R^2 + \sqrt{(m_\chi^2 + m_L^2 + m_R^2)^2 - 4m_L^2 m_R^2}\right), \qquad \text{(A.6)}$$

where we have now assumed all parameters are real for clarity. m_f is the light SM-like fermion mass, and m_F is the heavy vector-like partner mass.

Equation (A.5) is fundamental. It shows that the light mass m_f is not simply proportional to m_L (the SM Higgs VEV). We can solve Eq. (A.5) for m_L^2:

$$\begin{aligned} m_f^2(m_\chi^2 + m_L^2 + m_R^2 - m_f^2) &= m_L^2 m_R^2 \quad \text{(from the exact seesaw relation)} \\ m_L^2(m_R^2 - m_f^2) &= m_f^2(m_\chi^2 + m_R^2 - m_f^2) \\ m_L^2 &= m_f^2\left(\frac{m_\chi^2 + m_R^2 - m_f^2}{m_R^2 - m_f^2}\right) = m_f^2\left(1 + \frac{m_\chi^2}{m_R^2 - m_f^2}\right). \end{aligned}$$

Expressing this in terms of the original Yukawa couplings, where $m_L = \frac{v_h}{\sqrt{2}} Y_{fL}$ and the SM Yukawa is defined by $m_f = \frac{v_h}{\sqrt{2}} Y_f^{SM}$, we find:

$$Y_{fL}^2 = (Y_f^{SM})^2\left(1 + \frac{m_\chi^2}{m_R^2 - m_f^2}\right). \qquad \text{(A.7)}$$

This relation reveals the core of the universal seesaw mechanism: the Yukawa coupling Y_{fL} that couples the SM fermions to the Higgs is *enhanced* compared to the standard model value Y_f^{SM}. The enhancement factor is $\sqrt{1 + m_\chi^2/(m_R^2 - m_f^2)}$.

This has profound implications: On one hand, for light fermions $Y_f^{SM} \ll 1$. A large hierarchy $m_\chi^2 \gg m_R^2 \gg m_f^2$ can generate this tiny mass from a more "natural" $Y_{fL} \sim \mathcal{O}(0.1 - 1)$. On the other hand, for the top quark, $Y_t^{SM} \approx 1$ is already large. An enhancement could easily push Y_{tL} into the non-perturbative regime ($Y_{tL}^2/4\pi > 1$). To avoid this, we must require the enhancement factor to be $\mathcal{O}(1)$, which implies $m_\chi^2 \lesssim m_R^2 - m_t^2$. Since $m_R = \frac{v_\phi}{\sqrt{2}} Y_{fR}$, this suggests $v_\phi > m_\chi$ is a natural condition.

The bi-unitary transformation (A.4) is performed by matrices that can be parameterized by a mixing angle. For one generation, the left-handed mixing matrix is:

$$U_L = \begin{pmatrix} \cos\theta_L & \sin\theta_L \\ -\sin\theta_L & \cos\theta_L \end{pmatrix}. \qquad \text{(A.8)}$$

The angle θ_L quantifies the mixing between the SM fermion and its vector-like partner. The exact expressions for the fundamental parameters m_L, m_R, m_χ in terms of the physical masses m_f, m_F and the mixing angle θ_L can be found by equating $U_L^\dagger H_L U_L = \mathrm{diag}(m_f^2, m_F^2)$. This yields the system of equations:

$$\begin{aligned} m_L^2 &= m_f^2 \cos^2\theta_L + m_F^2 \sin^2\theta_L, \\ m_R^2 + m_\chi^2 &= m_f^2 \sin^2\theta_L + m_F^2 \cos^2\theta_L, \\ m_L m_\chi &= (m_F^2 - m_f^2)\sin\theta_L \cos\theta_L. \end{aligned}$$

Solving this system (and a similar one from H_R for θ_R) gives:

$$m_L^2 = \frac{1}{2}\left(m_f^2 + m_F^2 - (m_F^2 - m_f^2)\cos 2\theta_L\right), \tag{A.9}$$

$$m_R^2 = \frac{m_f^2 m_F^2}{m_L^2} = \frac{2m_f^2 m_F^2}{m_f^2 + m_F^2 - (m_F^2 - m_f^2)\cos 2\theta_L}, \tag{A.10}$$

$$m_\chi^2 = m_R^2 + m_F^2 + m_f^2 - m_L^2 - \frac{m_f^2 m_F^2}{m_L^2} = \frac{(m_F^2 - m_f^2)^2 \sin^2 2\theta_L}{4m_L^2}. \tag{A.11}$$

Substituting Eq. (A.9) into the expression for m_χ^2 yields the form shown in the original text.

The critical constraint to keep the top Yukawa perturbative is $m_\chi^2 < m_R^2$. Using Eqs. (A.10) and (A.11), the ratio is:

$$\frac{m_\chi^2}{m_R^2} = \frac{(m_F^2 - m_f^2)^2 \sin^2 2\theta_L}{4m_f^2 m_F^2} < 1. \tag{A.12}$$

For the top quark with $m_f = m_t \approx 173$ GeV and assuming a heavy partner $m_F \gg m_t$, this simplifies to:

$$\frac{m_F^4 \sin^2 2\theta_L}{4m_t^2 m_F^2} \approx \frac{m_F^2}{4m_t^2}\sin^2 2\theta_L < 1 \quad \Rightarrow \quad \sin^2 2\theta_L < \frac{4m_t^2}{m_F^2}. \tag{A.13}$$

This is a very strong constraint. For example, if $m_F = 1$ TeV, then $\sin^2 2\theta_L < 0.12$, meaning $\theta_L < 10°$. In the small θ_L limit, $\cos 2\theta_L \approx 1 - 2\theta_L^2$ and $\sin^2 2\theta_L \approx 4\theta_L^2$. Substituting this into Eq. (A.9):

$$\begin{aligned} m_L^2 &\approx \frac{1}{2}\left(m_t^2 + m_F^2 - (m_F^2 - m_t^2)(1 - 2\theta_L^2)\right) \\ &= \frac{1}{2}\left(m_t^2 + m_F^2 - m_F^2 + m_t^2 + 2(m_F^2 - m_t^2)\theta_L^2\right) \\ &= \frac{1}{2}\left(2m_t^2 + 2(m_F^2 - m_t^2)\theta_L^2\right) = m_t^2 + (m_F^2 - m_t^2)\theta_L^2. \end{aligned}$$

From the constraint (A.13), $\theta_L^2 < m_t^2/m_F^2$. Therefore:

$$m_L^2 < m_t^2 + (m_F^2 - m_t^2)\frac{m_t^2}{m_F^2} = m_t^2 + m_t^2 - \frac{m_t^4}{m_F^2} = 2m_t^2 - \frac{m_t^4}{m_F^2}. \tag{A.14}$$

Converting back to Yukawa couplings:

$$Y_{tL}^2 \lesssim (Y_t^{SM})^2 \left(2 - \frac{m_t^2}{m_F^2}\right). \tag{A.15}$$

This shows that the maximum enhancement for the top Yukawa is less than a factor of $\sqrt{2}$, which is perfectly perturbative.

The generalization to three generations involves the diagonalization of the full 6×6 matrices. The matrix $\tilde{V}_{CKM}$ introduced during field redefinition will manifest in the charged current weak interactions of the mass eigenstates. After diagonalization, the SM *W* boson will couple not only to the three light quarks but also to the heavy vector-like quarks, with couplings suppressed by the mixing angles θ_L^i. The observed 3×3 CKM matrix emerges as the effective mixing matrix among the three light quarks when the heavy states are integrated out.

The lepton sector follows an identical procedure for the charged leptons. The neutrino sector, however, offers further richness. The right-handed neutrinos ν_R can possess both Dirac masses (m_R) from coupling to ϕ and Majorana mass terms $M_R \bar{\nu}_R^c \nu_R$, which are allowed by the gauge symmetry. The vector-like neutrinos χ_ν can also have Majorana masses. This combination of Dirac and Majorana masses for both ν_R and χ_ν can generate a double or triple seesaw mechanism, providing a natural explanation for the tiny masses of the observed light neutrinos. The diagonalization of this extended neutrino mass matrix also generates the Pontecorvo-Maki-Nakagawa-Sakata (PMNS) mixing matrix.

B

THE 4321 MODEL

This appendix summarises the main features of the 4321 model presented in [71], based on the construction showed in [179]. The model is built upon the extended gauge group

$$\mathcal{G}_{4321} \equiv SU(4) \times SU(3)' \times SU(2)_L \times U(1)'.$$

The Standard Model (SM) gauge group, $\mathcal{G}_{321} \equiv SU(3)_c \times SU(2)_L \times U(1)_Y$, is embedded into $\mathcal{G}_{4321}$ through two key identifications.

First, the SM strong force is identified with the diagonal subgroup of the two $SU(3)$ factors:

$$SU(3)_c = \big(SU(3)_{[4]} \times SU(3)'\big)_{\text{diag}}, \tag{B.1}$$

where $SU(3)_{[4]} \subset SU(4)$. Second, and more crucially, the SM hypercharge is a linear combination of charges from the $SU(4)$ and $U(1)'$ sectors:

$$Y = Q_{B-L} + Y'. \tag{B.2}$$

Here, the baryon minus lepton number (Q_{B-L}) is generated by a diagonal $SU(4)$ generator, $Q_{B-L} = 2\sqrt{6}T^{15}/3$,

As we see in chapter 3, the $U(1)'$ charge could be identified with twice the third component of right-handed isospin, $Y' \equiv 2Q_{T^3_R}$. This specific embedding reveals the model's left-right symmetric foundation; the SM electric charge operator can now be expressed in the manifestly left-right symmetric form:

$$Q = Q_{T^3_L} + Q_{T^3_R} + \frac{1}{2}Q_{B-L}.$$

The spontaneous breaking of the full $\mathcal{G}_{4321}$ symmetry down to the SM $\mathcal{G}_{321}$ gives mass to the gauge bosons associated with the broken generators. The spectrum of these new massive vectors and their quantum numbers under the SM group are:

- A vector leptoquark, $U \sim (\mathbf{3}, \mathbf{1}, 2/3)$,
- A coloron, $g' \sim (\mathbf{8}, \mathbf{1}, 0)$,
- A massive neutral boson, $Z' \sim (\mathbf{1}, \mathbf{1}, 0)$.

Heuristically, each of these bosons originates from a distinct part of the symmetry breaking pattern: the leptoquark (U) emerges from the breaking $SU(4) \to SU(3)_{[4]} \times U(1)_{B-L}$, the coloron ($g'$) from $SU(3)_{[4]} \times SU(3)' \to SU(3)_c$, and the Z' from $U(1)_{B-L} \times U(1)_{T^3_R} \to U(1)_Y$.

The spontaneous breaking of the $\mathcal{G}_{4321}$ symmetry down to the Standard Model $\mathcal{G}_{321}$ and subsequently to electromagnetism is achieved through a scalar sector comprising four multiplets. The primary breaking $\mathcal{G}_{4321} \to \mathcal{G}_{321}$ is induced by the vacuum expectation values (vevs) of three scalar fields:

- $\Omega_1 \sim (\bar{\mathbf{4}}, \mathbf{1}, \mathbf{1}, -1/2)$,
- $\Omega_3 \sim (\bar{\mathbf{4}}, \mathbf{3}, \mathbf{1}, 1/6)$,
- $\Omega_{15} \sim (\mathbf{15}, \mathbf{1}, \mathbf{1}, 0)$ (taken to be a real field).

The final electroweak symmetry breaking, $\mathcal{G}_{321} \to U(1)_{\text{EM}}$, is triggered by the Higgs doublet $H \sim (\mathbf{1}, \mathbf{1}, \mathbf{2}, 1/2)$.

A suitable scalar potential (analysed in detail in Sec. **??**) allows for a vev configuration that ensures this breaking pattern. Phenomenological constraints suggest a clear hierarchy between these scales:

$$\langle \Omega_3 \rangle > \langle \Omega_1 \rangle \gg \langle \Omega_{15} \rangle \gg \langle H \rangle. \tag{B.3}$$

Given this hierarchy, we simplify the analysis by first considering the Ω_3 and Ω_1 system in isolation to understand the primary TeV-scale breaking. The effects of incorporating the smaller vevs of Ω_{15} and H will be discussed subsequently.

To analyze the Ω_3–Ω_1 subsystem, we represent these fields as a 4×3 matrix and a 4-vector, transforming as $\Omega_3 \to U_4^* \Omega_3 U_3^T$, and $\Omega_1 \to U_4^* \Omega_1$ under $SU(4) \times SU(3)'$, respectively. The desired vacuum configuration that breaks $\mathcal{G}_{4321}$ to $\mathcal{G}_{321}$ is:

$$\langle \Omega_3 \rangle = \frac{1}{\sqrt{2}} \begin{pmatrix} v_3 & 0 & 0 \\ 0 & v_3 & 0 \\ 0 & 0 & v_3 \\ 0 & 0 & 0 \end{pmatrix}, \qquad \langle \Omega_1 \rangle = \frac{1}{\sqrt{2}} \begin{pmatrix} 0 \\ 0 \\ 0 \\ v_1 \end{pmatrix}. \tag{B.4}$$

The most general renormalizable scalar potential that admits this vacuum as a stationary point, and in the limit where the bare masses vanish ($\mu_3 = \mu_1 = 0$) and the cubic coupling is absent ($\lambda_6 = 0$), can be written as:

$$\begin{aligned} V_{\Omega_3,\Omega_1} =& \mu_1^2 |\Omega_1|^2 + \mu_3^2 \,\mathrm{Tr}\left(\Omega_3^\dagger \Omega_3\right) \\ &+ \lambda_1 \left(\mathrm{Tr}\left(\Omega_3^\dagger \Omega_3\right) - \tfrac{3}{2} v_3^2\right)^2 + \lambda_2 \,\mathrm{Tr}\left(\Omega_3^\dagger \Omega_3 - \tfrac{1}{2} v_3^2 \mathbb{1}_3\right)^2 \\ &+ \lambda_3 \left(|\Omega_1|^2 - \tfrac{1}{2} v_1^2\right)^2 + \lambda_4 \left(\mathrm{Tr}\left(\Omega_3^\dagger \Omega_3\right) - \tfrac{3}{2} v_3^2\right) \left(|\Omega_1|^2 - \tfrac{1}{2} v_1^2\right) \\ &+ \lambda_5 \Omega_1^\dagger \Omega_3 \Omega_3^\dagger \Omega_1 + \lambda_6 \left([\Omega_3 \Omega_3 \Omega_3 \Omega_1]_1 + \text{h.c.}\right). \end{aligned} \tag{B.5}$$

Here, $\mathbb{1}_3$ denotes the 3×3 identity matrix. We have used a relative rephasing between the fields Ω_1 and Ω_3 to remove the phase of λ_6. The unique quartic term,

$$[\Omega_3 \Omega_3 \Omega_3 \Omega_1]_1 \equiv \epsilon_{\alpha\beta\gamma\delta} \epsilon^{abc} (\Omega_3)^\alpha_a (\Omega_3)^\beta_b (\Omega_3)^\gamma_c (\Omega_1)^\delta, \tag{B.6}$$

is required to avoid accidental global symmetries in the scalar potential that would lead to unwanted massless Goldstone bosons.

The inclusion of the other two representations, Ω_{15} and H, in the scalar potential can be safely considered as a perturbation. They are assumed to take the vevs $\langle \Omega_{15} \rangle = T_{15} v_{15}$ and $\langle H \rangle = \frac{1}{\sqrt{2}} (0, v)^T$, with $v = 246$ GeV. This treatment is justified because their vevs are subleading for phenomenological reasons and they do not alter the pattern of global symmetries of the Ω_3–Ω_1 potential. Finally, the decomposition of Ω_{15} under $\mathcal{G}_{321}$ is $\Omega_{15} \to (\mathbf{1},\mathbf{1},0) \oplus (\mathbf{3},\mathbf{1},2/3) \oplus (\bar{\mathbf{3}},\mathbf{1},-2/3) \oplus (\mathbf{8},\mathbf{1},0)$. The mixing of these states with those contained in $\Omega_{3,1}$ is parametrically suppressed by the ratio $v_{15}^2/v_{3,1}^2$, hence they play a subleading role in phenomenology.

Given the extended gauge group $\mathcal{G}_{4321}$, we denote the gauge fields by H_μ^α, $G_\mu'^a$, W_μ^i, B_μ'; the gauge couplings by g_4, g_3, g_2, g_1; and the generators by T^α, T^a, T^i, Y' (with indices $\alpha = 1,\ldots,15$, $a = 1,\ldots,8$, $i = 1,2,3$).

To determine the gauge boson spectrum, we start from the covariant derivatives acting on the scalar fields $\Omega_{3,1,15}$:

$$
\begin{aligned}
D_\mu\Omega_1 &= \left(\partial_\mu + ig_4 H_\mu^\alpha T^{\alpha *} - \tfrac{1}{2} i g_1 B_\mu'\right)\Omega_1, \\
D_\mu\Omega_3 &= \left(\partial_\mu + ig_4 H_\mu^\alpha T^{\alpha *} - i g_3 G_\mu'^a T^a + \tfrac{1}{6} i g_1 B_\mu'\right)\Omega_3, \\
D_\mu\Omega_{15} &= \partial_\mu\Omega_{15} - i g_4 \left[T^\alpha, \Omega_{15}\right] H_\mu^\alpha.
\end{aligned}
$$

We define the index $A = 9,\ldots,14$ to span the $SU(4)/(SU(3)_4 \times U(1)_4)$ coset. Neglecting electroweak symmetry breaking effects, the gauge boson masses are extracted from the canonically normalized kinetic terms of the scalar fields:

$$
\begin{aligned}
\mathcal{L} \supset &+ \frac{1}{2}\left(g_4^2 v_1^2 + g_4^2 v_3^2 + \frac{4}{3} g_4^2 v_{15}^2\right) H_\mu^A H^{\mu A} \\
&+ \frac{v_3^2}{4}\begin{pmatrix} H_\mu^a & G_\mu'^a \end{pmatrix}\begin{pmatrix} g_4^2 & -g_4 g_3 \\ -g_4 g_3 & g_3^2 \end{pmatrix}\begin{pmatrix} H^{b\mu} \\ G'^{b\mu} \end{pmatrix} \\
&+ \frac{3v_1^2 + v_3^2}{4}\begin{pmatrix} H_\mu^{15} & B_\mu' \end{pmatrix}\begin{pmatrix} \dfrac{g_4^2}{4} & -\dfrac{g_4 g_1}{2\sqrt{6}} \\ -\dfrac{g_4 g_1}{2\sqrt{6}} & \dfrac{g_1^2}{6} \end{pmatrix}\begin{pmatrix} H^{15\mu} \\ B'^\mu \end{pmatrix}.
\end{aligned}
\tag{B.7}
$$

Diagonalizing these mass matrices, we obtain the massive gauge boson spectrum:

$$
U_\mu^{1,2,3} = \frac{1}{\sqrt{2}}\left(H_\mu^{9,11,13} - iH_\mu^{10,12,14}\right), \quad M_U^2 = \frac{1}{4} g_4^2\left(v_1^2 + v_3^2 + \frac{4}{3} v_{15}^2\right), \tag{B.8}
$$

$$
g_\mu'^a = \frac{g_4 H_\mu^a - g_3 G_\mu'^a}{\sqrt{g_4^2 + g_3^2}}, \qquad M_{g'}^2 = \frac{1}{2}(g_4^2 + g_3^2) v_3^2, \tag{B.9}
$$

$$
Z_\mu' = \frac{g_4 H_\mu^{15} - \sqrt{\frac{2}{3}} g_1 B_\mu'}{\sqrt{g_4^2 + \frac{2}{3} g_1^2}}, \qquad M_{Z'}^2 = \frac{1}{4}\left(g_4^2 + \frac{2}{3} g_1^2\right)\left(v_1^2 + \frac{1}{3} v_3^2\right). \tag{B.10}
$$

The combinations orthogonal to (B.9) and (B.10) correspond to the massless $SU(3)_c \times U(1)_Y$ gauge bosons of $\mathcal{G}_{321}$ prior to electroweak symmetry breaking:

$$g_\mu^a = \frac{g_3 H_\mu^a + g_4 G_\mu^{\prime a}}{\sqrt{g_4^2 + g_3^2}}\,, \tag{B.11}$$

$$B_\mu = \frac{\sqrt{\frac{2}{3}} g_1 H_\mu^{15} + g_4 B_\mu'}{\sqrt{g_4^2 + \frac{2}{3} g_1^2}}\,. \tag{B.12}$$

The matching between the fundamental couplings g_4, g_3, g_1 and the SM couplings g_s, g_Y is readily obtained by acting with the covariant derivative on a field which transforms trivially under $SU(4)$. This yields:

$$g_s = \frac{g_4 g_3}{\sqrt{g_4^2 + g_3^2}}, \tag{B.13}$$

$$g_Y = \frac{g_4 g_1}{\sqrt{g_4^2 + \frac{2}{3} g_1^2}}. \tag{B.14}$$

Evolving the SM gauge couplings up to $\mu = 2$ TeV, we obtain $g_s = 1.02$ and $g_Y = 0.363$. Since $g_s \leqslant g_{4,3}$ and $g_Y \leqslant \sqrt{\frac{3}{2}} g_4, g_1$, the hierarchy $g_s \gg g_Y$ also implies $g_{4,3} \gg g_Y \simeq g_1$. In the limit $v_3 \gg v_1 \gg v_{15}$, the mass spectrum simplifies. For example, if the gauge couplings also satisfy $g_4 \sim g_3$, one finds $M_{g'} \simeq \sqrt{2} M_U$ and $M_{Z'} \simeq \frac{1}{\sqrt{2}} M_U$.

In the 4321 model, the observed SM fermion masses and mixings arise from the mixing between elementary chiral fermions—charged under $SU(3)' \times SU(2)_L \times U(1)'$ with SM-like quantum numbers—and three generations of vector-like fermions transforming as fundamentals of $SU(4)$. This mixing is triggered once the scalars Ω_1 and Ω_3 acquire VEVs (see Fig. B.1). The full matter content of the model is summarized in Tab. B.1.

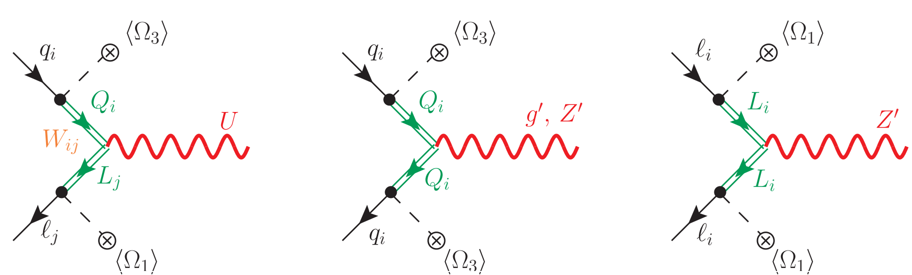

Figure B.1: Diagrammatic representation of the interactions between the SM fermions and the heavy vector-like fermions Ψ, induced by the Yukawa couplings to Ω_1 and Ω_3 after symmetry breaking.

Field	$SU(4)$	$SU(3)'$	$SU(2)_L$	$U(1)'$
$q_L^{\prime i}$	$\mathbf{1}$	$\mathbf{3}$	$\mathbf{2}$	$1/6$
$u_R^{\prime i}$	$\mathbf{1}$	$\mathbf{3}$	$\mathbf{1}$	$2/3$
$d_R^{\prime i}$	$\mathbf{1}$	$\mathbf{3}$	$\mathbf{1}$	$-1/3$
$\ell_L^{\prime i}$	$\mathbf{1}$	$\mathbf{1}$	$\mathbf{2}$	$-1/2$
$e_R^{\prime i}$	$\mathbf{1}$	$\mathbf{1}$	$\mathbf{1}$	-1
Ψ_L^i	$\mathbf{4}$	$\mathbf{1}$	$\mathbf{2}$	0
Ψ_R^i	$\mathbf{4}$	$\mathbf{1}$	$\mathbf{2}$	0
H	$\mathbf{1}$	$\mathbf{1}$	$\mathbf{2}$	$1/2$
Ω_1	$\bar{\mathbf{4}}$	$\mathbf{1}$	$\mathbf{1}$	$-1/2$
Ω_3	$\bar{\mathbf{4}}$	$\mathbf{3}$	$\mathbf{1}$	$1/6$
Ω_{15}	$\mathbf{15}$	$\mathbf{1}$	$\mathbf{1}$	0

Table B.1: Field content of the 4321 model. The index $i = 1, 2, 3$ runs over generations.

The mixing between the elementary fermions and the vector-like fermions is described by the Yukawa Lagrangian $\mathcal{L}_Y = \mathcal{L}_{\text{SM-like}} + \mathcal{L}_{\text{mix}}$, where

$$\mathcal{L}_{\text{SM-like}} = -\bar{q}_L'\, Y_d\, H d_R' - \bar{q}_L'\, Y_u\, \tilde{H} u_R' - \bar{\ell}_L'\, Y_e\, H e_R' + \text{h.c.}\,, \tag{B.15}$$

$$\mathcal{L}_{\text{mix}} = -\bar{q}_L'\, \lambda_q\, \Omega_3^T \Psi_R - \bar{\ell}_L'\, \lambda_\ell\, \Omega_1^T \Psi_R - \bar{\Psi}_L\, (M + \lambda_{15}\, \Omega_{15})\, \Psi_R + \text{h.c.}\,. \tag{B.16}$$

Here, $\tilde{H} = i\sigma_2 H^*$, and $Y_{u,d,e}$, $\lambda_{q,\ell,15}$, M are 3×3 matrices in flavour space.

The vector-like fermions transform under $\mathcal{G}_{4321}$ as

$$\Psi_{L,R} = \begin{pmatrix} Q_{L,R}' \\ L_{L,R}' \end{pmatrix} \sim (\mathbf{4}, \mathbf{1}, \mathbf{2}, 0). \tag{B.17}$$

Under the breaking $SU(4) \to SU(3)_{[4]} \times U(1)_{B-L}$, they decompose as $Q_{L,R}' \sim (\mathbf{3}, \mathbf{2}, 1/6)$ and $L_{L,R}' \sim (\mathbf{1}, \mathbf{2}, -1/2)$. Their vector-like masses are generated by the M term and are split by the VEV of Ω_{15}:

$$M_Q = M + \frac{\lambda_{15}\, v_{15}}{2\sqrt{6}}\,, \qquad M_L = M - \frac{3\,\lambda_{15}\, v_{15}}{2\sqrt{6}}\,. \tag{B.18}$$

To comply with flavour constraints, the authors on [179] employ the following Yukawa textures as a starting point

$$\begin{aligned}
&\lambda_q = \hat{\lambda}_q \equiv \text{diag}\left(\lambda_{12}^q, \lambda_{12}^q, \lambda_3^q\right)\,, \\
&\lambda_\ell = \hat{\lambda}_\ell\, W^\dagger \equiv \text{diag}\left(\lambda_1^\ell, \lambda_2^\ell, \lambda_3^\ell\right) \begin{pmatrix} 1 & 0 & 0 \\ 0 & \cos\theta_{LQ} & -\sin\theta_{LQ} \\ 0 & \sin\theta_{LQ} & \cos\theta_{LQ} \end{pmatrix}\,, \\
&\lambda_{15} \propto \hat{M} \propto \mathbb{1}\,.
\end{aligned} \tag{B.19}$$

After the $SU(3)_{[4]} \times SU(3)' \to SU(3)_c$ symmetry breaking, the 6×6 fermion mass matrices for the quarks read:

$$\mathcal{M}_u = \begin{pmatrix} V^\dagger\, \hat{Y}_u\, \frac{v}{\sqrt{2}} & \hat{\lambda}_q\, \frac{v_3}{\sqrt{2}} \\ 0 & \hat{M}_Q \end{pmatrix}\,, \quad \mathcal{M}_d = \begin{pmatrix} \hat{Y}_d\, \frac{v}{\sqrt{2}} & \hat{\lambda}_q\, \frac{v_3}{\sqrt{2}} \\ 0 & \hat{M}_Q \end{pmatrix}\,. \tag{B.20}$$

Similarly, after the $U(1)_{B-L} \times U(1)_{T^3_R} \to U(1)_Y$ symmetry breaking, the 6×6 fermion mass matrices for the leptons read:

$$\mathcal{M}_N = \begin{pmatrix} 0 & \hat{\lambda}_\ell \frac{v_1}{\sqrt{2}} \\ 0 & \hat{M}_L \end{pmatrix}, \qquad \mathcal{M}_e = \begin{pmatrix} \hat{Y}_e \frac{v}{\sqrt{2}} & \hat{\lambda}_\ell W^\dagger \frac{v_1}{\sqrt{2}} \\ 0 & \hat{M}_L \end{pmatrix}. \tag{B.21}$$

Here, $\hat{Y}_{u,d,e}$ and $\hat{\lambda}_{q,\ell}$ are diagonal matrices, V and W are unitary Cabibbo-like mixing matrices, and M_Q, M_L are proportional to the identity matrix.

The structure of the mass matrices in Eqs. (B.21) allows them to be diagonalized by unitary transformations of the form $\psi'_x = U_x \psi_x$, where ψ_x $(x = q, u, d, \ell, e, N)$ denotes a 6-dimensional vector containing both the chiral and vector-like fermions, and the unprimed fields represent the mass eigenstates.

For the neutrinos, since we do not include a ν_R field, the vector ψ_N is actually 3-dimensional, containing only the right-handed components $N_R \subset \Psi_R$. For notational simplicity, however, we treat it as a 6-dimensional vector.

The chosen flavour structure in Eq. (B.19) ensures that in the limit $W \to \mathbb{1}$, the mixing is family-specific: each vector-like fermion generation mixes predominantly with only one generation of chiral fermions (up to CKM rotations). At leading order, the unitary mixing matrices are given by:

$$\begin{aligned}
U_q &\approx \mathcal{R}_{14}(\theta_{q_1})\,\mathcal{R}_{25}(\theta_{q_2})\,\mathcal{R}_{36}(\theta_{q_3}), \quad & U_\ell &\approx \mathcal{R}_{14}(\theta_{\ell_1})\,\mathcal{R}_{25}(\theta_{\ell_2})\,\mathcal{R}_{36}(\theta_{\ell_3}), \\
U_u &\approx \mathcal{R}_{14}(\theta_{u_R})\,\mathcal{R}_{25}(\theta_{c_R})\,\mathcal{R}_{36}(\theta_{t_R}), \quad & U_e &\approx \begin{pmatrix} \mathbb{1} & 0 \\ 0 & W \end{pmatrix} \mathcal{R}_{14}(\theta_{e_R})\,\mathcal{R}_{25}(\theta_{\mu_R})\,\mathcal{R}_{36}(\theta_{\tau_R}), \\
U_d &\approx \mathcal{R}_{14}(\theta_{d_R})\,\mathcal{R}_{25}(\theta_{s_R})\,\mathcal{R}_{36}(\theta_{b_R}), \quad & U_N &\approx \begin{pmatrix} 0 & 0 \\ 0 & W \end{pmatrix}.
\end{aligned}$$

Here, we have adopted a flavour basis for the SM $SU(2)_L$ fermion multiplets defined by:

$$q^i = \begin{pmatrix} V^*_{ji}\, u^j_L \\ d^i_L \end{pmatrix}, \qquad \ell^\alpha = \begin{pmatrix} \nu^\alpha_L \\ e^\alpha_L \end{pmatrix}, \tag{B.22}$$

where V is the CKM matrix. The mixing angles are related to the Lagrangian parameters by:

$$\begin{aligned}
\sin\theta_{q_i} &= \frac{\lambda^q_i v_3}{\sqrt{|\lambda^q_i|^2 v_3^2 + 2\hat{M}_Q^2}}, \quad & \cos\theta_{q_i} &= \frac{\sqrt{2}\,\hat{M}_Q}{\sqrt{|\lambda^q_i|^2 v_3^2 + 2\hat{M}_Q^2}}, \\
\sin\theta_{\ell_i} &= \frac{\lambda^\ell_i v_1}{\sqrt{|\lambda^\ell_i|^2 v_1^2 + 2\hat{M}_L^2}}, \quad & \cos\theta_{\ell_i} &= \frac{\sqrt{2}\,\hat{M}_L}{\sqrt{|\lambda^\ell_i|^2 v_1^2 + 2\hat{M}_L^2}}, \\
\sin\theta_{u^i_R} &= \frac{m_{u_i}}{M_{Q_i}} \tan\theta_{q_i}, \quad & \sin\theta_{d^i_R} &= \frac{m_{d_i}}{M_{Q_i}} \tan\theta_{q_i}, \\
\sin\theta_{e^i_R} &= \frac{m_{e_i}}{M_{L_i}} \tan\theta_{\ell_i}, \quad & \cos\theta_{f^i_R} &= 1 \quad (f = u, d, e).
\end{aligned} \tag{B.23}$$

In these expressions, m_i and M_i denote the physical fermion masses. Up to corrections of $\mathcal{O}(m_i^2/M_i^2)$, these are given by:

$$\begin{aligned}
M_{L_i} &= \sqrt{\frac{|\lambda^\ell_i|^2 v_1^2}{2} + \hat{M}_L^2}, \quad M_{Q_i} = \sqrt{\frac{|\lambda^q_i|^2 v_3^2}{2} + \hat{M}_Q^2}, \\
m_{f_i} &\approx |\hat{Y}^i_f| \cos\theta_{f_i} \frac{v}{\sqrt{2}} \qquad (f = u, d, e).
\end{aligned} \tag{B.24}$$

The interaction terms of the massive gauge bosons with the fermions in the interaction basis are derived from the covariant derivative. For the left-handed fields, we find:

$$\begin{aligned}
\mathcal{L}_L = {} & \frac{g_4}{\sqrt{2}} \bar{Q}_L' \gamma^\mu L_L' \, U_\mu + \text{h.c.} \\
& + g_s \left(\frac{g_4}{g_3} \, \bar{Q}_L' \gamma^\mu T^a Q_L' - \frac{g_3}{g_4} \, \bar{q}_L' \gamma^\mu T^a q_L' \right) g_\mu'^a \\
& + g_Y \left(\sqrt{\frac{3}{2}} \, \frac{g_4}{g_1} \, Y(Q_L') \, \bar{Q}_L' \gamma^\mu Q_L' - \sqrt{\frac{2}{3}} \, \frac{g_1}{g_4} \, Y(q_L') \, \bar{q}_L' \gamma^\mu q_L' \right) Z_\mu' \\
& + g_Y \left(\sqrt{\frac{3}{2}} \, \frac{g_4}{g_1} \, Y(L_L') \, \bar{L}_L' \gamma^\mu L_L' - \sqrt{\frac{2}{3}} \, \frac{g_1}{g_4} \, Y(\ell_L') \, \bar{\ell}_L' \gamma^\mu \ell_L' \right) Z_\mu' \, ,
\end{aligned} \tag{B.25}$$

and for the right-handed fields:

$$\begin{aligned}
\mathcal{L}_R = {} & \frac{g_4}{\sqrt{2}} \bar{Q}_R' \gamma^\mu L_R' \, U_\mu + \text{h.c.} \\
& + g_s \left(\frac{g_4}{g_3} \, \bar{Q}_R' \gamma^\mu T^a Q_R' - \frac{g_3}{g_4} \, \bar{u}_R' \gamma^\mu T^a u_R' - \frac{g_3}{g_4} \, \bar{d}_R' \gamma^\mu T^a d_R' \right) g_\mu'^a \\
& + g_Y \left(\sqrt{\frac{3}{2}} \, \frac{g_4}{g_1} \, Y(Q_R') \, \bar{Q}_R' \gamma^\mu Q_R' - \sqrt{\frac{2}{3}} \, \frac{g_1}{g_4} \, Y(u_R') \, \bar{u}_R' \gamma^\mu u_R' - \sqrt{\frac{2}{3}} \, \frac{g_1}{g_4} \, Y(d_R') \, \bar{d}_R' \gamma^\mu d_R' \right) Z_\mu' \\
& + g_Y \left(\sqrt{\frac{3}{2}} \, \frac{g_4}{g_1} \, Y(L_R') \, \bar{L}_R' \gamma^\mu L_R' - \sqrt{\frac{2}{3}} \, \frac{g_1}{g_4} \, Y(e_R') \, \bar{e}_R' \gamma^\mu e_R' \right) Z_\mu' \, .
\end{aligned} \tag{B.26}$$

The SM hypercharges are: $Y(Q_L') = Y(Q_R') = Y(q_L') = \frac{1}{6}$, $Y(u_R') = \frac{2}{3}$, $Y(d_R') = -\frac{1}{3}$, $Y(L_L') = Y(L_R') = Y(\ell_L') = -\frac{1}{2}$, and $Y(e_R') = -1$.

To express the interactions in Eqs. (B.25) and (B.26) in the fermion mass basis, we collect the fields into 6-dimensional multiplets, ψ_x ($x = q, u, d, \ell, e$), and apply the corresponding unitary transformations U_x. Neglecting the right-handed rotations—which are suppressed by the small masses of the SM fermions—we obtain:

$$\begin{aligned}
\mathcal{L}_U &= \frac{g_4}{\sqrt{2}} U_\mu \left[\beta \, \bar{\psi}_q \gamma^\mu \psi_\ell + W \, \bar{Q}_R \gamma^\mu L_R \right] + \text{h.c.} \, , \\
\mathcal{L}_{g'} &= g_s \, \frac{g_4}{g_3} \, g_\mu'^a \left[\kappa_q \, \bar{\psi}_q \gamma^\mu T^a \psi_q + \kappa_u \, \bar{\psi}_u \gamma^\mu T^a \psi_u + \kappa_d \, \bar{\psi}_d \gamma^\mu T^a \psi_d \right] \, , \\
\mathcal{L}_{Z'} &= \frac{g_Y}{2\sqrt{6}} \, \frac{g_4}{g_1} \, Z_\mu' \left[\zeta_q \, \bar{\psi}_q \gamma^\mu \psi_q + \zeta_u \, \bar{\psi}_u \gamma^\mu \psi_u \right. \\
& \qquad \left. + \zeta_d \, \bar{\psi}_d \gamma^\mu \psi_d - 3 \zeta_\ell \, \bar{\psi}_\ell \gamma^\mu \psi_\ell - 3 \zeta_e \, \bar{\psi}_e \gamma^\mu \psi_e \right] \, .
\end{aligned} \tag{B.27}$$

The coupling matrices are defined as follows (with indices $A, B = 4, 5, 6$ spanning the heavy vector-like states, and $\alpha, \beta = 1, \ldots, 6$ spanning the full 6-dimensional space):

$$
\begin{aligned}
\beta^{\alpha\beta} &= [U_q]^*_{A\alpha}[W]_{AB}[U_\ell]_{B\beta}\,, \\
\kappa_q^{\alpha\beta} &= [U_q]^*_{A\alpha}[U_q]_{A\beta} - \frac{g_3^2}{g_4^2}\delta_{\alpha\beta}\,, \qquad \kappa_u \approx \kappa_d \approx \begin{pmatrix} 0 & 0 \\ 0 & \mathbb{1}_{3\times 3} \end{pmatrix} - \frac{g_3^2}{g_4^2}\mathbb{1}_{6\times 6}\,, \\
\zeta_q^{\alpha\beta} &= [U_q]^*_{A\alpha}[U_q]_{A\beta} - \frac{2g_1^2}{3g_4^2}\delta_{\alpha\beta}\,, \qquad \zeta_u \approx \zeta_d \approx \begin{pmatrix} 0 & 0 \\ 0 & \mathbb{1}_{3\times 3} \end{pmatrix} - \frac{2g_1^2}{3g_4^2}\mathbb{1}_{6\times 6}\,, \\
\zeta_\ell^{\alpha\beta} &= [U_\ell]^*_{A\alpha}[U_\ell]_{A\beta} - \frac{2g_1^2}{3g_4^2}\delta_{\alpha\beta}\,, \qquad \zeta_e \approx \begin{pmatrix} 0 & 0 \\ 0 & \mathbb{1}_{3\times 3} \end{pmatrix} - \frac{2g_1^2}{3g_4^2}\mathbb{1}_{6\times 6}\,.
\end{aligned}
\tag{B.28}
$$

A key result of the assumed flavour structure is that the matrix W cancels due to unitarity in the Z' and g' interactions. This cancellation is crucial for suppressing unwanted flavour-changing neutral currents (FCNCs) in these sectors.

Assuming $W = \mathcal{R}_{56}(\theta_{LQ})$ and no CP violation in the mixing angles, the left-handed coupling matrices can be explicitly written as:

$$
\beta \approx \begin{pmatrix} \mathrm{diag}(s_{q_1}s_{\ell_1}, s_{q_2}s_{\ell_2}, s_{q_3}s_{\ell_3})W & -\mathrm{diag}(s_{q_1}c_{\ell_1}, s_{q_2}c_{\ell_2}, s_{q_3}c_{\ell_3})W \\ \mathrm{diag}(c_{q_1}s_{\ell_1}, c_{q_2}s_{\ell_2}, c_{q_3}s_{\ell_3})W & -\mathrm{diag}(c_{q_1}c_{\ell_1}, c_{q_2}c_{\ell_2}, c_{q_3}c_{\ell_3})W \end{pmatrix},
\tag{B.29}
$$

$$
\kappa_q \approx \begin{pmatrix} \mathrm{diag}(s_{q_1}^2, s_{q_2}^2, s_{q_3}^2) & -\frac{1}{2}\mathrm{diag}(s_{2q_1}, s_{2q_2}, s_{2q_3}) \\ -\frac{1}{2}\mathrm{diag}(s_{2q_1}, s_{2q_2}, s_{2q_3}) & \mathrm{diag}(c_{q_1}^2, c_{q_2}^2, c_{q_3}^2) \end{pmatrix} - \frac{g_3^2}{g_4^2}\mathbb{1}_{6\times 6},
\tag{B.30}
$$

$$
\zeta_q \approx \begin{pmatrix} \mathrm{diag}(s_{q_1}^2, s_{q_2}^2, s_{q_3}^2) & -\frac{1}{2}\mathrm{diag}(s_{2q_1}, s_{2q_2}, s_{2q_3}) \\ -\frac{1}{2}\mathrm{diag}(s_{2q_1}, s_{2q_2}, s_{2q_3}) & \mathrm{diag}(c_{q_1}^2, c_{q_2}^2, c_{q_3}^2) \end{pmatrix} - \frac{2g_1^2}{3g_4^2}\mathbb{1}_{6\times 6},
\tag{B.31}
$$

$$
\zeta_\ell \approx \begin{pmatrix} \mathrm{diag}(s_{\ell_1}^2, s_{\ell_2}^2, s_{\ell_3}^2) & -\frac{1}{2}\mathrm{diag}(s_{2\ell_1}, s_{2\ell_2}, s_{2\ell_3}) \\ -\frac{1}{2}\mathrm{diag}(s_{2\ell_1}, s_{2\ell_2}, s_{2\ell_3}) & \mathrm{diag}(c_{\ell_1}^2, c_{\ell_2}^2, c_{\ell_3}^2) \end{pmatrix} - \frac{2g_1^2}{3g_4^2}\mathbb{1}_{6\times 6}.
\tag{B.32}
$$

Following the flavour structure in [43], the assumption of a single $U(2)_q$ breaking spurion in both the leptoquark and SM Yukawa couplings implies the relation $\beta_L^{13} = V_{td}^*/V_{ts}^*\,\beta_L^{23}$. More generally, from $U(2)$ symmetries acting on both quark and lepton sectors, we expect the hierarchy:

$$
|\beta_L^{31}| \ll |\beta_L^{23}|, |\beta_L^{32}| \ll |\beta_R^{33}|, |\beta_L^{33}| = \mathcal{O}(1),
$$

and analogously for the $\zeta_{\ell,e,Q}^{ij}$ and κ_Q^{ij} couplings.

This structure can be achieved with a specific choice of the λ parameters in the potential, leading to particular values for the mixing angles θ_{q_i} and θ_{ℓ_i}. To explain the B-physics anomalies, a large mixing angle θ_{ℓ_3} is required, while the other two angles $\theta_{\ell_{1,2}}$ must be small to avoid large contributions to muon and electron observables. The quark mixing angles

θ_{q_i} should be small for the first two generations to avoid large contributions to meson mixing observables, while a moderate value of θ_{q_3} is needed to explain the B-physics anomalies.

BIBLIOGRAPHY

[1] A. Flórez et al. "On the sensitivity reach of LQ production with preferential couplings to third generation fermions at the LHC". In: *The European Physical Journal C* 83.11 (Nov. 2023), p. 1023. ISSN: 1434-6052. DOI: 10.1140/epjc/s10052-023-12177-4.

[2] Umar Sohail Qureshi et al. "Probing light scalars and vector-like quarks at the high-luminosity LHC". In: *Eur. Phys. J. C* 85.4 (2025), p. 379. DOI: 10.1140/epjc/s10052-025-14085-1. arXiv: 2410.17854 [hep-ph].

[3] W Greiner. *Relativistic Quantum Mechanics. Wave Equations*. Springer, 2000. ISBN: 9783540674573.

[4] Stefan Pokorski. *Gauge field theories*. Cambridge Monographs on Mathematical Physics. Cambridge University Press, 2000. ISBN: 9780521478168.

[5] David Tong. *Quantum Field Theory University of Cambridge Part III Mathematical Tripos*. Vol. 45. 12. 1995.

[6] Herbert Goldstein, Charles P Poole, and John L Safko. *Classical mechanics*. 3rd ed. Addison Wesley, 2001. ISBN: 9780201657029,0201657023.

[7] J V José and E J Saletan. *Classical Dynamics: A Contemporary Approach*. Cambridge University Press, 1998. ISBN: 9780521636360.

[8] Roberto Martínez. *Teoría cuántica de campos*. Colección Textos. Universidad Nacional de Colombia, Facultad de Ciencias, Departamento de Física, 2002. ISBN: 9789587011203.

[9] Steven Weinberg. *The Quantum Theory of Fields, Volume 3: Supersymmetry*. Cambridge University Press, 2005. ISBN: 0521670551,9780521670555.

[10] D.A. Bromley Walter Greiner Joachim Reinhardt. *Field quantization*. 1st ed. Springer, 1996. ISBN: 3540591796,9783540591795.

[11] Dan V. Schroeder Michael E. Peskin. *An Introduction To Quantum Field Theory*. Frontiers in Physics. Westview Press, 1995. ISBN: 9780201503975.

[12] P C W Davies N. D. Birrell. *Quantum fields in curved space*. CUP. Cambridge Monographs on Mathematical Physics. Cambridge University Press, 1984. ISBN: 9780521278584,0521278589.

[13] Amitabha Lahiri and Palash B Pal. *A First Book of Quantum Field Theory*. Alpha Science International, 2006, p. 380. ISBN: 1842652494.

[14] Reinhold A. Bertlmann. *Anomalies in Quantum Field Theory*. Oxford University Press, 1996. ISBN: 9780198520476.

[15] Daniel Z. Freedman and Antoine Van Proeyen. *Supergravity*. Cambridge University Press, 2012. ISBN: 9780521194013.

[16] Diego Gallego. *Estudio de uplifts efectivos en compactificaciones de supercuerdas tipo-IIB*. Tech. rep. Tunja: Universidad Pedagógica y Tecnológica de Colombia, 2016, p. 96.

[17] Antoine Van Proeyen. "Tools for Supersymmetry". In: *Physics AUC* 9.I (1999), pp. 1–49. arXiv: 9910030 [hep-th].

[18] Stephen P. Martin. "TASI 2011 lectures notes: two-component fermion notation and supersymmetry". In: *arXiv* (2012). arXiv: 1205.4076.

[19] M Robinson. *Symmetry and the Standard Model: Mathematics and Particle Physics*. 1st ed. SpringerLink : Bucher. New York: Springer-Verlag, 2011. ISBN: 9781441982674. DOI: 10.1007/978-1-4419-8267-4.

[20] "Physics: 1963-1970". In: Nobel lectures, including presentation speeches and laureates' biographies. Elsevier Publishing Company, 1972.

[21] P.A. Zyla et al. "Review of Particle Physics". In: *PTEP* 2020.8 (2020), p. 083C01. DOI: 10.1093/ptep/ptaa104.

[22] F. J. Dyson. "The Radiation Theories of Tomonaga, Schwinger, and Feynman". In: *Phys. Rev.* 75 (3 1949), pp. 486–502. DOI: 10.1103/PhysRev.75.486.

[23] Cristian Rodriguez. "Evaluacion del Lagrangiano de Supergravedad $\mathcal{N} = 1$ utilizando el formalismo Superconforme." BA thesis. UPTC, 2018.

[24] C. S. Wu et al. "Experimental Test of Parity Conservation in Beta Decay". In: *Phys. Rev.* 105 (4 1957), pp. 1413–1415. DOI: 10.1103/PhysRev.105.1413.

[25] Tadao Nakano and Kazuhiko Nishijima. "Charge Independence for V-particles*". In: *Progress of Theoretical Physics* 10.5 (Nov. 1953), pp. 581–582. ISSN: 0033-068X. DOI: 10.1143/PTP.10.581.

[26] B. Odom et al. "New Measurement of the Electron Magnetic Moment Using a One-Electron Quantum Cyclotron". In: *Phys. Rev. Lett.* 97 (3 2006), p. 030801. DOI: 10.1103/PhysRevLett.97.030801.

[27] Steven Weinberg. "A Model of Leptons". In: *Phys. Rev. Lett.* 19 (21 1967), pp. 1264–1266. DOI: 10.1103/PhysRevLett.19.1264.

[28] Sheldon L. Glashow. "Partial-symmetries of weak interactions". In: *Nuclear Physics* 22.4 (1961), pp. 579–588. ISSN: 0029-5582. DOI: https://doi.org/10.1016/0029-5582(61)90469-2.

[29] John F. Donoghue. "General relativity as an effective field theory: The leading quantum corrections". In: *Phys. Rev. D* 50 (1994), pp. 3874–3888. DOI: 10.1103/PhysRevD.50.3874. arXiv: gr-qc/9405057.

[30] C. P. Burgess. "Quantum gravity in everyday life: General relativity as an effective field theory". In: *Living Rev. Rel.* 7 (2004), pp. 5–56. DOI: 10.12942/lrr-2004-5. arXiv: gr-qc/0311082.

[31] Steven Weinberg. "The Cosmological Constant Problem". In: *Rev. Mod. Phys.* 61 (1989). Ed. by Jong-Ping Hsu and D. Fine, pp. 1–23. DOI: 10.1103/RevModPhys.61.1.

[32] Planck Collaboration. "Planck 2018 results. VI. Cosmological parameters". In: *Astronomy & Astrophysics* 641 (2020), A6. DOI: 10.1051/0004-6361/201833910. arXiv: 1807.06209 [astro-ph.CO].

[33] LZ Collaboration. "First Dark Matter Search Results from the LZ Experiment". In: (2022). arXiv: 2207.03764 [hep-ex].

[34] LZ Collaboration. "Improved constraints on WIMP-nucleon interactions from LZ". In: (2023). arXiv: 2307.15711 [hep-ex].

[35] XENON Collaboration. "Search for WIMP dark matter with XENONnT". In: (2023). arXiv: 2307.08808 [hep-ex].

[36] A. D. Sakharov. "Violation of CP Invariance, C asymmetry, and baryon asymmetry of the universe". In: *Pisma Zh. Eksp. Teor. Fiz.* 5 (1967), pp. 32–35. DOI: 10.1070/PU1991v034n05ABEH002497.

[37] Sacha Davidson, Enrico Nardi, and Yosef Nir. "Leptogenesis". In: *Physics Reports* 466 (2008), pp. 105–177. DOI: 10.1016/j.physrep.2008.06.002. arXiv: 0802.2962 [hep-ph].

[38] David E. Morrissey and Michael J. Ramsey-Musolf. "Electroweak baryogenesis". In: *New Journal of Physics* 14 (2012), p. 125003. DOI: 10.1088/1367-2630/14/12/125003. arXiv: 1206.2942 [hep-ph].

[39] DESI Collaboration. "DESI 2024 VI: Cosmological constraints from DESI 2024 BAO measurements". In: (2024). arXiv: 2404.03000 [astro-ph.CO].

[40] Alejandro Rivero and Andre Gsponer. *The strange formula of Dr. Koide*. 2005. DOI: 10.48550/ARXIV.HEP-PH/0505220.

[41] G. Hiller and M. Schmaltz. "R_K and future $b \to s\ell\ell$ physics beyond the standard model opportunities". In: *Phys. Rev. D* 90 (2014), p. 054014. DOI: 10.1103/PhysRevD.90.054014. arXiv: 1408.1627 [hep-ph].

[42] I. Doršner et al. "Physics of leptoquarks in precision experiments and at particle colliders". In: *Phys. Rept.* 641 (2016), pp. 1–68. DOI: 10.1016/j.physrep.2016.06.001. arXiv: 1603.04993 [hep-ph].

[43] D. Buttazzo et al. "B-physics anomalies: a guide to combined explanations". In: *JHEP* 11 (2017), p. 044. DOI: 10.1007/JHEP11(2017)044. arXiv: 1706.07808 [hep-ph].

[44] Y. Fukuda et al. "Evidence for oscillation of atmospheric neutrinos". In: *Phys. Rev. Lett.* 81 (1998), pp. 1562–1567. DOI: 10.1103/PhysRevLett.81.1562. arXiv: hep-ex/9807003.

[45] Q. R. Ahmad et al. "Direct evidence for neutrino flavor transformation from neutral current interactions in the Sudbury Neutrino Observatory". In: *Phys. Rev. Lett.* 89 (2002), p. 011301. DOI: 10.1103/PhysRevLett.89.011301. arXiv: nucl-ex/0204008.

[46] M. Ciuchini et al. “Constraints on lepton universality violation from rare B decays”. In: *Phys. Rev. D* 107 (5 2023), p. 055036. DOI: 10.1103/PhysRevD.107.055036.

[47] LHCb Collaboration. “Test of lepton universality using $B^+ \to K^+\ell^+\ell^-$ decays”. In: *Phys. Rev. Lett.* 113 (2014), p. 151601. DOI: 10.1103/PhysRevLett.113.151601. arXiv: 1406.6482 [hep-ex].

[48] LHCb Collaboration. “Test of lepton universality with $B^0 \to K^{*0}\ell^+\ell^-$ decays”. In: *JHEP* 08 (2017), p. 055. DOI: 10.1007/JHEP08(2017)055. arXiv: 1705.05802 [hep-ex].

[49] LHCb Collaboration. “Search for lepton-universality violation in $B^+ \to K^+\ell^+\ell^-$ decays”. In: *Phys. Rev. Lett.* 122.19 (2019), p. 191801. DOI: 10.1103/PhysRevLett.122.191801. arXiv: 1903.09252 [hep-ex].

[50] LHCb Collaboration. “Test of lepton universality in beauty-quark decays”. In: *Nature Phys.* 18.3 (2022), pp. 277–282. DOI: 10.1038/s41567-021-01478-8. arXiv: 2103.11769 [hep-ex].

[51] LHCb Collaboration. “Test of lepton universality in $b \to \ell^+\ell^-$ decays”. In: (2022). DOI: 10.48550/arXiv.1705.05802. arXiv: 2212.09152 [hep-ex].

[52] LHCb Collaboration. “Measurement of lepton universality parameters in $B^+ \to K^+\ell^+\ell^-$ and $B^0 \to K^{*0}\ell^+\ell^-$ decays”. In: (2022). DOI: 10.48550/arXiv.2212.09153. arXiv: 2212.09153 [hep-ex].

[53] BaBar Collaboration. “Evidence for an excess of $\bar{B} \to D^{(*)}\tau^-\bar{\nu}_\tau$ decays”. In: *Phys. Rev. Lett.* 109 (2012), p. 101802. DOI: 10.1103/PhysRevLett.109.101802. arXiv: 1205.5442 [hep-ex].

[54] BaBar Collaboration. “Measurement of an excess of $\bar{B} \to D^{(*)}\tau^-\bar{\nu}_\tau$ decays and implications for charged Higgs bosons”. In: *Phys. Rev. D* 88.7 (2013), p. 072012. DOI: 10.1103/PhysRevD.88.072012. arXiv: 1303.0571 [hep-ex].

[55] Belle Collaboration. “Measurement of the branching ratio of $\bar{B} \to D^{(*)}\tau^-\bar{\nu}_\tau$ relative to $\bar{B} \to D^{(*)}\ell^-\bar{\nu}_\ell$ decays with hadronic tagging at Belle”. In: *Phys. Rev. D* 92.7 (2015), p. 072014. DOI: 10.1103/PhysRevD.92.072014. arXiv: 1507.03233 [hep-ex].

[56] LHCb Collaboration. “Measurement of the ratio of branching fractions $\mathcal{B}(\bar{B}^0 \to D^{*+}\tau^-\bar{\nu}_\tau)/\mathcal{B}(\bar{B}^0 \to D^{*+}\mu^-\bar{\nu}_\mu)$”. In: *Phys. Rev. Lett.* 115.11 (2015). [Erratum: Phys.Rev.Lett. 115, 159901 (2015)], p. 111803. DOI: 10.1103/PhysRevLett.115.111803. arXiv: 1506.08614 [hep-ex].

[57] LHCb Collaboration. “Test of lepton flavor universality by the measurement of the $B^0 \to D^{*-}\tau^+\nu_\tau$ branching fraction using three-prong τ decays”. In: *Phys. Rev. D* 97.7 (2018), p. 072013. DOI: 10.1103/PhysRevD.97.072013. arXiv: 1711.02505 [hep-ex].

[58] LHCb Collaboration. “Measurement of the ratios of branching fractions $\mathcal{R}(D^*)$ and $\mathcal{R}(D^0)$”. In: (2023). DOI: 10.48550/arXiv.2302.02886. arXiv: 2302.02886 [hep-ex].

[59] Y. Amhis et al. "Averages of b-hadron, c-hadron, and $$\tau $$-lepton properties as of 2018". In: *The European Physical Journal C* 81.3 (2021). DOI: 10.1140/epjc/s10052-020-8156-7.

[60] M. Antonelli et al. "An Evaluation of $|V_{us}|$ and precise tests of the Standard Model from world data on leptonic and semileptonic kaon decays". In: *Eur. Phys. J. C* 69 (2010), pp. 399–424. DOI: 10.1140/epjc/s10052-010-1406-3. arXiv: 1005.2323 [hep-ph].

[61] ATLAS Collaboration et al. "Test of the universality of τ and μ lepton couplings in W-boson decays from $t\bar{t}$ events with the ATLAS detector". In: *arXiv preprint arXiv:2007.14040* (2020).

[62] S. Schael et al. "Precision electroweak measurements on the Z resonance". In: *Phys. Rept.* 427 (2006), pp. 257–454. DOI: 10.1016/j.physrep.2005.12.006. arXiv: hep-ex/0509008.

[63] Bernat Capdevila et al. "Patterns of New Physics in $b \to s\ell^+\ell^-$ transitions in the light of recent data". In: *Journal of High Energy Physics* 2018.1 (2018). DOI: 10.1007/jhep01(2018)093.

[64] R. Alonso, B. Grinstein, and J. M. Camalich. "Lepton universality violation and lepton flavor conservation in B-meson decays". In: *JHEP* 10 (2015), p. 184. DOI: 10.1007/JHEP10(2015)184. arXiv: 1505.05164 [hep-ph].

[65] L. Calibbi, A. Crivellin, and T. Ota. "Effective field theory approach to $b \to s\ell\ell^{(\prime)}$, $B \to K^{(*)}\nu\bar{\nu}$ and $B \to D^{(*)}\tau\nu$ with third generation couplings". In: *Phys. Rev. Lett.* 115 (2015), p. 181801. DOI: 10.1103/PhysRevLett.115.181801. arXiv: 1506.02661 [hep-ph].

[66] Wolfgang Altmannshofer and David M. Straub. "New physics in $b \to s$ transitions after LHC run 1". In: *The European Physical Journal C* 75.8 (2015). DOI: 10.1140/epjc/s10052-015-3602-7.

[67] A. Greljo et al. "Rare b decays meet high-mass Drell-Yan". In: *JHEP* 2023.5 (2023). DOI: 10.1007/jhep05(2023)087.

[68] W. Altmannshofer et al. "The Belle II Physics Book". In: *PTEP* 2019.12 (2019). Ed. by E. Kou and P. Urquijo. [Erratum: PTEP 2020, 029201 (2020)], p. 123C01. DOI: 10.1093/ptep/ptz106. arXiv: 1808.10567 [hep-ex].

[69] A. Angelescu et al. "Closing the window on single leptoquark solutions to the B-physics anomalies". In: *JHEP* 10 (2018), p. 183. DOI: 10.1007/JHEP10(2018)183. arXiv: 1808.08179 [hep-ph].

[70] C. Cornella et al. "Reading the footprints of the B-meson flavor anomalies". In: *JHEP* 08 (2021), p. 050. DOI: 10.1007/JHEP08(2021)050. arXiv: 2103.16558 [hep-ph].

[71] L. Di Luzio, A. Greljo, and M. Nardecchia. "Gauge leptoquark as the origin of B-physics anomalies". In: *Phys. Rev. D* 96.11 (2017), p. 115011. DOI: 10.1103/PhysRevD.96.115011. arXiv: 1708.08450 [hep-ph].

[72] Admir Greljo and Ben A. Stefanek. “Third family quark–lepton unification at the TeV scale”. In: *Phys. Lett. B* 782 (2018), pp. 131–138. DOI: 10.1016/j.physletb.2018.05.033. arXiv: 1802.04274 [hep-ph].

[73] A. Angelescu et al. “Single leptoquark solutions to the B-physics anomalies”. In: *Phys. Rev. D* 104.5 (2021), p. 055017. DOI: 10.1103/PhysRevD.104.055017. arXiv: 2103.12504 [hep-ph].

[74] L. Allwicher et al. “Drell-Yan tails beyond the standard model”. In: *JHEP* 2023.3 (2023). DOI: 10.1007/jhep03(2023)064.

[75] Gianluca Blankenburg, Gino Isidori, and Joel Jones-Perez. “Neutrino Masses and LFV from Minimal Breaking of $U(3)^5$ and $U(2)^5$ flavor Symmetries”. In: *Eur. Phys. J. C* 72 (2012), p. 2126. DOI: 10.1140/epjc/s10052-012-2126-7. arXiv: 1204.0688 [hep-ph].

[76] Belle Collaboration. “Measurement of $\mathcal{R}(D)$ and $\mathcal{R}(D^*)$ with a semileptonic tagging method”. In: (2019). DOI: 10.48550/arXiv.1904.08794. arXiv: 1904.08794 [hep-ex].

[77] Belle Collaboration. “Measurement of the τ lepton polarization and $R(D^*)$ in the decay $\bar{B} \to D^*\tau^-\bar{\nu}_\tau$ with one-prong hadronic τ decays at Belle”. In: *Phys. Rev. D* 97 (2018), p. 012004. DOI: 10.1103/PhysRevD.97.012004. arXiv: 1709.00129 [hep-ex].

[78] Belle Collaboration. “Measurement of the branching ratio of $\bar{B}^0 \to D^{*+}\tau^-\bar{\nu}_\tau$ relative to $\bar{B}^0 \to D^{*+}\ell^-\bar{\nu}_\ell$ decays with a semileptonic tagging method”. In: *Phys. Rev. D* 94 (2016), p. 072007. DOI: 10.1103/PhysRevD.94.072007. arXiv: 1607.07923 [hep-ex].

[79] Belle Collaboration. “Measurement of the τ lepton polarization and $R(D^*)$ in the decay $\bar{B} \to D^*\tau^-\bar{\nu}_\tau$”. In: *Phys. Rev. Lett.* 118 (2017), p. 211801. DOI: 10.1103/PhysRevLett.118.211801. arXiv: 1612.00529 [hep-ex].

[80] Belle Collaboration. “Measurement of the branching ratio of $\bar{B} \to D^{(*)}\tau^-\bar{\nu}_\tau$ relative to $\bar{B} \to D^{(*)}\ell^-\bar{\nu}_\ell$ decays with hadronic tagging at Belle”. In: *Phys. Rev. D* 92 (2015), p. 072014. DOI: 10.1103/PhysRevD.92.072014. arXiv: 1507.03233 [hep-ex].

[81] LHCb Collaboration. “Measurement of the ratio of branching fractions $\mathcal{B}(\bar{B}^0 \to D^{*+}\tau^-\bar{\nu}_\tau)/\mathcal{B}(\bar{B}^0 \to D^{*+}\mu^-\bar{\nu}_\mu)$”. In: *Phys. Rev. Lett.* 115 (2015). [Erratum: Phys.Rev.Lett. 115, 159901 (2015)], p. 111803. DOI: 10.1103/PhysRevLett.115.111803. arXiv: 1506.08614 [hep-ex].

[82] LHCb Collaboration. “Measurement of the ratio of the $B^0 \to D^{*-}\tau^+\nu_\tau$ and $B^0 \to D^{*-}\mu^+\nu_\mu$ branching fractions using three-prong τ-lepton decays”. In: *Phys. Rev. Lett.* 120 (2018), p. 171802. DOI: 10.1103/PhysRevLett.120.171802. arXiv: 1708.08856 [hep-ex].

[83] M. Bauer and M. Neubert. “Minimal leptoquark explanation for the $R_{D^{(*)}}$, R_K, and $(g-2)_\mu$ anomalies”. In: *Phys. Rev. Lett.* 116.14 (2016), p. 141802. DOI: 10.1103/PhysRevLett.116.141802. arXiv: 1511.01900 [hep-ph].

[84] A. Crivellin, D. Muller, and T. Ota. "Simultaneous explanation of $R(D^*)$ and $b \to \mu^+\mu^-$:the last scalar leptoquark standing". In: *JHEP* 09 (2017), p. 040. DOI: 10.1007/JHEP09(2017)040. arXiv: 1703.09226 [hep-ph].

[85] S. F. King. "Twin Pati-Salam theory of flavour with a TeV scale vector leptoquark". In: *JHEP* 11 (2021), p. 161. DOI: 10.1007/JHEP11(2021)161. arXiv: 2106.03876 [hep-ph].

[86] C. Cornella, J. Fuentes-Martín, and G. Isidori. "Revisiting the vector leptoquark explanation of the B-physics anomalies". In: *JHEP* 07 (2019), p. 168. DOI: 10.1007/JHEP07(2019)168. arXiv: 1903.11517 [hep-ph].

[87] T. Aoyama et al. "The anomalous magnetic moment of the muon in the Standard Model". In: *Phys. Rept.* 887 (2020), pp. 1–166. DOI: 10.1016/j.physrep.2020.07.006. arXiv: 2006.04822 [hep-ph].

[88] B. Abi et al. "Measurement of the Positive Muon Anomalous Magnetic Moment to 0.46 ppm". In: *Physical Review Letters* 126.14 (2021). DOI: 10.1103/physrevlett.126.141801.

[89] G. W. Bennett et al. "Final Report of the Muon E821 Anomalous Magnetic Moment Measurement at BNL". In: *Phys. Rev. D* 73 (2006), p. 072003. DOI: 10.1103/PhysRevD.73.072003. arXiv: hep-ex/0602035.

[90] Thomas Blum et al. *The Muon (g-2) Theory Value: Present and Future*. 2013. DOI: 10.48550/ARXIV.1311.2198.

[91] CMS Collaboration. "Search for singly and pair-produced leptoquarks coupling to third-generation fermions in proton-proton collisions at s=13 TeV". In: *Phys. Lett. B* 819 (2021), p. 136446. DOI: 10.1016/j.physletb.2021.136446. arXiv: 2012.04178 [hep-ex].

[92] ATLAS Collaboration. "Searches for third-generation scalar leptoquarks in $\sqrt{s} = 13$ TeV pp collisions with the ATLAS detector". In: *JHEP* 06 (2019), p. 144. DOI: 10.1007/JHEP06(2019)144. arXiv: 1902.08103 [hep-ex].

[93] L. Di Luzio et al. "Maximal flavour violation: a Cabibbo mechanism for leptoquarks". In: *JHEP* 11 (2018), p. 081. DOI: 10.1007/JHEP11(2018)081. arXiv: 1808.00942 [hep-ph].

[94] G. Aad et al. "The ATLAS Experiment at the CERN Large Hadron Collider". In: *JINST* 3 (2008), S08003. DOI: 10.1088/1748-0221/3/08/S08003.

[95] S. Chatrchyan et al. "The CMS Experiment at the CERN LHC". In: *JINST* 3 (2008), S08004. DOI: 10.1088/1748-0221/3/08/S08004.

[96] D. A. Faroughy, A. Greljo, and J. F. Kamenik. "Confronting lepton flavor universality violation in B decays with high-p_T tau lepton searches at LHC". In: *Phys. Lett. B* 764 (2017), pp. 126–134. DOI: 10.1016/j.physletb.2016.11.011. arXiv: 1609.07138 [hep-ph].

[97] M. J. Baker et al. "High-p_T signatures in vector–leptoquark models". In: *Eur. Phys. J. C* 79.4 (2019), p. 334. DOI: 10.1140/epjc/s10052-019-6853-x. arXiv: 1901.10480 [hep-ph].

[98] Glen Cowan et al. "Asymptotic formulae for likelihood-based tests of new physics". In: *Eur. Phys. J. C* 71 (2011). [Erratum: Eur.Phys.J.C 73, 2501 (2013)], p. 1554. DOI: 10.1140/epjc/s10052-011-1554-0. arXiv: 1007.1727 [physics.data-an].

[99] H.P. P Nilles. "Supersymmetry, supergravity and particle physics". In: *Physics Reports* 110.1-2 (1984), pp. 1–162. ISSN: 03701573. DOI: 10.1016/0370-1573(84)90008-5.

[100] Lisa Randall and Raman Sundrum. "A Large mass hierarchy from a small extra dimension". In: *Phys. Rev. Lett.* 83 (1999), pp. 3370–3373. DOI: 10.1103/PhysRevLett.83.3370. arXiv: hep-ph/9905221.

[101] G. F. Giudice. "Naturalness after LHC". In: *arXiv e-prints* (2013). arXiv: 1307.7879 [hep-ph].

[102] Gianfranco Bertone, Dan Hooper, and Joseph Silk. "Particle dark matter: evidence, candidates and constraints". In: *Physics Reports* 405 (2005), pp. 279–390. DOI: 10.1016/j.physrep.2004.08.031. arXiv: hep-ph/0404175 [hep-ph].

[103] P. K. Mohapatra, R. N. Mohapatra, and P. B. Pal. "Implications of E6 Grand Unification". In: *Phys. Rev. D* 33 (1986), p. 2010. DOI: 10.1103/PhysRevD.33.2010.

[104] J. Alwall et al. "The automated computation of tree-level and next-to-leading order differential cross sections, and their matching to parton shower simulations". In: *JHEP* 07 (2014), p. 079. DOI: 10.1007/JHEP07(2014)079. arXiv: 1405.0301 [hep-ph].

[105] A. Alloul et al. "FeynRules 2.0 - A complete toolbox for tree-level phenomenology". In: *Comput. Phys. Commun.* 185 (2014), pp. 2250–2300. DOI: 10.1016/j.cpc.2014.04.012. arXiv: 1310.1921 [hep-ph].

[106] DELPHES 3 Collaboration. "DELPHES 3, A modular framework for fast simulation of a generic collider experiment". In: *JHEP* 02 (2014), p. 057. DOI: 10.1007/JHEP02(2014)057. arXiv: 1307.6346 [hep-ex].

[107] Georges Aad et al. "Search for high-mass dilepton resonances using 139 fb^{-1} of pp collision data collected at $\sqrt{s}$ =13 TeV with the ATLAS detector". In: *Phys. Lett. B* 796 (2019), pp. 68–87. DOI: 10.1016/j.physletb.2019.07.016. arXiv: 1903.06248 [hep-ex].

[108] Albert M Sirunyan et al. "Search for resonant and nonresonant new phenomena in high-mass dilepton final states at $\sqrt{s}$ = 13 TeV". In: *JHEP* 07 (2021), p. 208. DOI: 10.1007/JHEP07(2021)208. arXiv: 2103.02708 [hep-ex].

[109] S. Schael et al. "Measurement of the W boson mass and width in e+e- collisions at LEP". In: *The European Physical Journal C* 47.2 (2006), pp. 309–335. DOI: 10.1140/epjc/s2006-02576-8.

[110] T. Sjöstrand et al. "An introduction to PYTHIA 8.2". In: *Comput. Phys. Commun.* 191 (2015), pp. 159–177. DOI: 10.1016/j.cpc.2015.01.024. arXiv: 1410.3012 [hep-ph].

[111] M. Cacciari, G. P. Salam, and G. Soyez. "FastJet User Manual". In: *Eur. Phys. J. C* 72 (2012), p. 1896. DOI: 10.1140/epjc/s10052-012-1896-2. arXiv: 1111.6097 [hep-ph].

[112] NNPDF Collaboration. "Parton distributions for the LHC Run II". In: *JHEP* 04 (2015), p. 040. DOI: 10.1007/JHEP04(2015)040. arXiv: 1410.8849 [hep-ph].

[113] Paul Lujan et al. *The Pixel Luminosity Telescope: A detector for luminosity measurement at CMS using silicon pixel sensors*. Tech. rep. CMS-DN-21-008. Accepted by Eur. Phys. J. C. 2022. arXiv: 2206.08870 [physics.ins-det]. URL: https://arxiv.org/abs/2206.08870.

[114] F. Pedregosa et al. "Scikit-learn: Machine Learning in Python". In: *J. Mach. Learn. Res.* 12 (2011), pp. 2825–2830. ISSN: 1532-4435. DOI: 10.48550/arXiv.1201.0490.

[115] T. Chen and C. Guestrin. "XGBoost: A Scalable Tree Boosting System". In: *Proceedings of the 22nd ACM SIGKDD International Conference on Knowledge Discovery and Data Mining*. KDD '16. San Francisco, California, USA: ACM, 2016, pp. 785–794. ISBN: 978-1-4503-4232-2. DOI: 10.1145/2939672.2939785.

[116] E. Bols et al. "Jet flavour classification using DeepJet". In: *Journal of Instrumentation* 15.12 (2020), P12012. DOI: 10.1088/1748-0221/15/12/P12012.

[117] CMS Collaboration. "Identification of hadronic tau lepton decays using a deep neural network". In: *JINST* 17.07 (2022), P07023. DOI: 10.1088/1748-0221/17/07/P07023. arXiv: 2201.08458 [hep-ex].

[118] Lyndon Evans and Philip Bryant. "LHC Machine". In: *Journal of Instrumentation* 3.08 (2008), S08001–S08001. DOI: 10.1088/1748-0221/3/08/s08001.

[119] ATLAS Collaboration. "Observation of a new particle in the search for the Standard Model Higgs boson with the ATLAS detector at the LHC". In: *Physics Letters B* 716 (2012). ATLAS Higgs-discovery paper; verify metadata if needed, pp. 1–29. DOI: 10.1016/j.physletb.2012.08.020.

[120] CMS Collaboration. "Observation of a new boson at a mass of 125 GeV with the CMS experiment at the LHC". In: *Physics Letters B* 716 (2012). CMS Higgs-discovery paper; verify metadata if needed, pp. 30–61. DOI: 10.1016/j.physletb.2012.08.021.

[121] CMS Collaboration. *Study of the Discovery Reach in Searches for Supersymmetry at CMS with 3000/fb*. CMS Physics Analysis Summary CMS-PAS-FTR-13-014. Accessed on January 07, 2023. CERN, 2013. URL: https://cds.cern.ch/record/1607141.

[122] G. Apollinari et al. *High-Luminosity Large Hadron Collider (HL-LHC): Technical and performance projections*. Tech. rep. CERN Yellow Report / TBD. HL-LHC technical design / projection report; please verify exact report number/title and replace placeholder fields as desired. CERN, 2017.

[123] D. Bertolini et al. "Pileup Per Particle Identification". In: *JHEP* 10 (2014). Introduces the PUPPI algorithm for per-particle pileup mitigation; ampliamente usado en ATLAS/CMS analyses., p. 59. arXiv: 1407.6013 [hep-ph].

[124] Matteo Cacciari, Gavin P. Salam, and Gregory Soyez. "The anti-kt jet clustering algorithm". In: *Journal of High Energy Physics* 2008.04 (2008), p. 063. DOI: 10.1088/1126-6708/2008/04/063.

[125] Izaak Neutelings. *CMS coordinate system*. URL: https://tikz.net/axis3d_cms.

[126] CMS Collaboration. "Particle-flow reconstruction and global event description with the CMS detector". In: *JINST* 12 (2017). Resumen del algoritmo de reconstrucción particle-flow utilizado en CMS; útil para la discusión de PF en el texto., P10003.

[127] A.M. Sirunyan et al. "Electron and photon reconstruction and identification with the CMS experiment at the CERN LHC". In: *JINST* 16.05 (2021), P05014. DOI: 10.1088/1748-0221/16/05/P05014.

[128] A.M. Sirunyan et al. "Performance of the reconstruction and identification of high-momentum muons in proton-proton collisions at $\sqrt{s} = 13$ TeV". In: *JINST* 15.02 (2020), P02027. DOI: 10.1088/1748-0221/15/02/P02027.

[129] The CMS Collaboration. "Description and performance of track and primary-vertex reconstruction with the CMS tracker". In: *Journal of Instrumentation* 9.10 (Oct. 2014), P10009–P10009. ISSN: 1748-0221. DOI: 10.1088/1748-0221/9/10/p10009.

[130] André Rubbia. *Phenomenology of Particle Physics*. Cambridge, UK: Cambridge University Press, June 2022. ISBN: 978-1-316-51934-9, 978-1-009-02342-9.

[131] John C. Collins, Davison E. Soper, and George F. Sterman. "Factorization of Hard Processes in QCD". In: *Adv. Ser. Direct. High Energy Phys.* 5 (1989), pp. 1–91. DOI: 10.1142/9789814503266_0001. arXiv: hep-ph/0409313.

[132] J. Butterworth, S. Carrazza, A. Cooper-Sarkar, A. De Roeck, J. Feltesse, S. Forte, J. Gao, S. Glazov, J. Huston, Z. Kassabov, R. McNulty, A. Morsch, P. Nadolsky, V. Radescu, J. Rojo and R. Thorne. "PDF4LHC recommendations for LHC Run II". In: *J. Phys. G* 43 (2016), p. 023001. DOI: 10.1088/0954-3899/43/2/023001. arXiv: 1510.03865 [hep-ph].

[133] Albert M Sirunyan et al. "Performance of missing transverse momentum reconstruction in proton-proton collisions at $\sqrt{s} = 13$ TeV using the CMS detector". In: *JINST* 14.07 (2019), P07004. DOI: 10.1088/1748-0221/14/07/P07004. arXiv: 1903.06078 [hep-ex].

[134] Lawrence Lee et al. "Collider Searches for Long-Lived Particles Beyond the Standard Model". In: *Prog. Part. Nucl. Phys.* 106 (2019). [Erratum: Prog.Part.Nucl.Phys. 122, 103912 (2022)], pp. 210–255. DOI: 10.1016/j.ppnp.2019.02.006. arXiv: 1810.12602 [hep-ph].

[135] William R. Leo. *Techniques for Nuclear and Particle Physics Experiments*. Springer, 1994. ISBN: 978-3-540-57280-0, 978-3-642-57920-2. DOI: 10.1007/978-3-642-57920-2.

[136] Alexander L. Read. "Presentation of search results: The CL_s technique". In: *J. Phys. G* 28 (2002). Ed. by M. R. Whalley and L. Lyons, pp. 2693–2704. DOI: 10.1088/0954-3899/28/10/313.

[137] Wolfgang A. Rolke, Angel M. López, and Jan Conrad. "Limits and confidence intervals in the presence of nuisance parameters". In: *Nuclear Instruments and Methods in Physics Research Section A: Accelerators, Spectrometers, Detectors and Associated Equipment* 551.2–3 (Oct. 2005), 493–503. ISSN: 0168-9002. DOI: 10.1016/j.nima.2005.05.068.

[138] Gary J. Feldman and Robert D. Cousins. "Unified approach to the classical statistical analysis of small signals". In: *Physical Review D* 57.7 (Apr. 1998), 3873–3889. ISSN: 1089-4918. DOI: 10.1103/physrevd.57.3873.

[139] Alejandro Segura and Angie Catalina Parra. "A Practical Guide to Statistical Techniques in Particle Physics". In: (Nov. 2024). arXiv: 2411.00706 [hep-ph].

[140] Bo Andersson et al. "Parton Fragmentation and String Dynamics". In: *Phys. Rept.* 97 (1983), pp. 31–145. DOI: 10.1016/0370-1573(83)90080-7.

[141] B. R. Webber. "A QCD Model for Jet Fragmentation Including Soft Gluon Interference". In: *Nucl. Phys. B* 238 (1984), pp. 492–528. DOI: 10.1016/0550-3213(84)90333-X.

[142] Gavin P. Salam. "Towards Jetography". In: *Eur. Phys. J. C* 67 (2010), pp. 637–686. DOI: 10.1140/epjc/s10052-010-1314-6. arXiv: 0906.1833 [hep-ph].

[143] S. Catani et al. "Longitudinally invariant K_t clustering algorithms for hadron hadron collisions". In: *Nucl. Phys. B* 406 (1993), pp. 187–224. DOI: 10.1016/0550-3213(93)90166-M.

[144] Stephen D. Ellis and Davison E. Soper. "Successive combination jet algorithm for hadron collisions". In: *Phys. Rev. D* 48 (1993), pp. 3160–3166. DOI: 10.1103/PhysRevD.48.3160. arXiv: hep-ph/9305266.

[145] Yuri L. Dokshitzer et al. “Better jet clustering algorithms”. In: *JHEP* 08 (1997), p. 001. DOI: 10.1088/1126-6708/1997/08/001. arXiv: hep-ph/9707323.

[146] Jesse Thaler and Ken Van Tilburg. “Identifying Boosted Objects with N-subjettiness”. In: *JHEP* 03 (2011), p. 015. DOI: 10.1007/JHEP03(2011)015. arXiv: 1011.2268 [hep-ph].

[147] M. Cacciari, G. P. Salam, and G. Soyez. “The catchment area of jets”. In: *JHEP* 04 (2008). Detalla conceptos de área de jets y técnicas relacionadas con la resta de pile-up., p. 005. DOI: 10.1088/1126-6708/2008/04/005.

[148] Garvita Agarwal. “Jet Energy Scale and Resolution Measurements in CMS”. In: *PoS* ICHEP2022 (2022), p. 652. DOI: 10.22323/1.414.0652. arXiv: 2301.02175 [hep-ex].

[149] Jonathan M. Butterworth et al. “Jet substructure as a new Higgs search channel at the LHC”. In: *Phys. Rev. Lett.* 100 (2008), p. 242001. DOI: 10.1103/PhysRevLett.100.242001. arXiv: 0802.2470 [hep-ph].

[150] Andrew J. Larkoski et al. “Soft Drop”. In: *JHEP* 05 (2014), p. 146. DOI: 10.1007/JHEP05(2014)146. arXiv: 1402.2657 [hep-ph].

[151] A. M. Sirunyan et al. “Performance of reconstruction and identification of τ leptons decaying to hadrons and ν_τ in pp collisions at $\sqrt{s} = 13$ TeV”. In: *JINST* 13.10 (2018), P10005. DOI: 10.1088/1748-0221/13/10/P10005. arXiv: 1809.02816 [hep-ex].

[152] Georges Aad et al. “Identification and energy calibration of hadronically decaying tau leptons with the ATLAS experiment in pp collisions at $\sqrt{s}$=8 TeV”. In: *Eur. Phys. J. C* 75.7 (2015), p. 303. DOI: 10.1140/epjc/s10052-015-3500-z. arXiv: 1412.7086 [hep-ex].

[153] CMS Collaboration. “Performance of the CMS Level-1 trigger in proton-proton collisions at $\sqrt{s} = 13$ TeV”. In: *J. Inst.* 17.05 (2022), P05024. DOI: 10.31526/lhep.2022.195. arXiv: 2202.08678 [hep-ex].

[154] ATLAS Collaboration. “Measurement of the energy response of the ATLAS calorimeter to charged pions from $W^\pm \to \tau^\pm(\to \pi^\pm\nu_\tau)\nu_\tau$ events in Run 2 data”. In: *Eur. Phys. J. C* 82.3 (2022), p. 223. DOI: 10.1140/epjc/s10052-022-10933-6. arXiv: 2202.13948 [hep-ex].

[155] CMS Collaboration. “Identification of heavy-flavour jets with the CMS detector in pp collisions at 13 TeV”. In: *JINST* 13.04 (2018), P05011. DOI: 10.1088/1748-0221/13/05/P05011. arXiv: 1712.07158 [hep-ex].

[156] The CMS Collaboration. “The CMS experiment at the CERN LHC”. In: *Journal of Instrumentation* 3.08 (2008), S08004–S08004. DOI: 10.1088/1748-0221/3/08/s08004.

[157] N. D. Christensen and C. Duhr. “FeynRules - Feynman rules made easy”. In: *Comput. Phys. Commun.* 180 (2009), pp. 1614–1641. DOI: 10.1016/j.cpc.2009.02.018. arXiv: 0806.4194 [hep-ph].

[158] Celine Degrande et al. "UFO - The Universal FeynRules Output". In: *Comput. Phys. Commun.* 183 (2012), pp. 1201–1214. DOI: 10.1016/j.cpc.2012.01.022. arXiv: 1108.2040 [hep-ph].

[159] J. Alwall et al. "Computing decay rates for new physics theories with FeynRules and MadGraph 5_aMC@NLO". In: *Comput. Phys. Commun.* 197 (2015), pp. 312–323. DOI: 10.1016/j.cpc.2015.08.031. arXiv: 1402.1178 [hep-ph].

[160] Johan Alwall et al. "Comparative study of various algorithms for the merging of parton showers and matrix elements in hadronic collisions". In: *Eur. Phys. J. C* 53 (2008), pp. 473–500. DOI: 10.1140/epjc/s10052-007-0490-5. arXiv: 0706.2569 [hep-ph].

[161] Andy Buckley et al. "LHAPDF6: parton density access in the LHC precision era". In: *Eur. Phys. J. C* 75 (2015), p. 132. DOI: 10.1140/epjc/s10052-015-3318-8. arXiv: 1412.7420 [hep-ph].

[162] Matt Dobbs and Jorgen Beck Hansen. "The HepMC C++ Monte Carlo event record for High Energy Physics". In: *Comput. Phys. Commun.* 134 (2001), pp. 41–46. DOI: 10.1016/S0010-4655(00)00189-2.

[163] Rene Brun and Fons Rademakers. "ROOT — An object oriented data analysis framework". In: *Nucl. Instrum. Meth. A* 389.1-2 (1997). Ed. by M. Werlen and D. Perret-Gallix, pp. 81–86. DOI: 10.1016/s0168-9002(97)00048-x.

[164] Steve Baker and Robert D. Cousins. "Clarification of the Use of Chi Square and Likelihood Functions in Fits to Histograms". In: *Nucl. Instrum. Meth.* 221 (1984), pp. 437–442. DOI: 10.1016/0167-5087(84)90016-4.

[165] Jerzy Neyman and Egon Sharpe Pearson. "On the Problem of the Most Efficient Tests of Statistical Hypotheses". In: *Phil. Trans. Roy. Soc. Lond. A* 231.694-706 (1933), pp. 289–337. DOI: 10.1098/rsta.1933.0009.

[166] S. S. Wilks. "The Large-Sample Distribution of the Likelihood Ratio for Testing Composite Hypotheses". In: *Annals Math. Statist.* 9.1 (1938), pp. 60–62. DOI: 10.1214/aoms/1177732360.

[167] Dan Guest, Kyle Cranmer, and Daniel Whiteson. "Deep Learning and its Application to LHC Physics". In: *Ann. Rev. Nucl. Part. Sci.* 68 (2018), pp. 161–181. DOI: 10.1146/annurev-nucl-101917-021019. arXiv: 1806.11484 [hep-ex].

[168] Trevor Hastie, Robert Tibshirani, and Jerome Friedman. *The Elements of Statistical Learning*. Springer, 2009. ISBN: 978-0-387-84857-0, 978-0-387-84858-7. DOI: 10.1007/978-0-387-84858-7.

[169] A. Hoecker et al. *TMVA - Toolkit for Multivariate Data Analysis*. 2009. arXiv: physics/0703039 [physics.data-an].

[170] J. H. Friedman. "Greedy function approximation: A gradient boosting machine." In: *The Annals of Statistics* 29.5 (2001). Publisher: Institute of Mathematical Statistics, pp. 1189–1232. ISSN: 0090-5364, 2168-8966. DOI: 10.1214/aos/1013203451. (Visited on 09/05/2022).

[171] Kyle Cranmer, Juan Pavez, and Gilles Louppe. "Approximating Likelihood Ratios with Calibrated Discriminative Classifiers". In: (June 2015). arXiv: 1506.02169 [stat.AP].

[172] John Platt. *Probabilistic Outputs for Support Vector Machines and Comparisons to Regularized Likelihood Methods*. Tech. rep. Microsoft Research, 1999.

[173] Corinna Cortes and Vladimir Vapnik. "Support-vector networks". In: *Machine Learning* 20.3 (1995), pp. 273–297. DOI: 10.1007/BF00994018.

[174] Leo Breiman. "Random Forests". In: *Machine Learning* 45.1 (2001), pp. 5–32. DOI: 10.1023/A:1010933404324.

[175] T. Chen and C. Guestrin. "XGBoost: A scalable tree boosting system". In: *Proceedings of the 22nd ACM SIGKDD International Conference on Knowledge Discovery and Data Mining*. KDD '16. New York, NY, USA: Association for Computing Machinery, 2016, pp. 785–794. ISBN: 978-1-4503-4232-2. DOI: 10.1145/2939672.2939785. (Visited on 09/05/2022).

[176] N. Assad, B. Fornal, and B. Grinstein. "Baryon Number and Lepton Universality Violation in Leptoquark and Diquark Models". In: *Phys. Lett. B* 777 (2018), pp. 324–331. DOI: 10.1016/j.physletb.2017.12.042. arXiv: 1708.06350 [hep-ph].

[177] R. N. Mohapatra and J. C. Pati. ""Natural" left-right symmetry". In: *Physical Review D* 11.9 (May 1975), pp. 2558–2561. DOI: 10.1103/PhysRevD.11.2558.

[178] G. Senjanovic and R. N. Mohapatra. "Exact left-right symmetry and spontaneous violation of parity". In: *Physical Review D* 12.5 (Sept. 1975), pp. 1502–1505. DOI: 10.1103/PhysRevD.12.1502.

[179] Luca Di Luzio et al. "Maximal flavour violation: a Cabibbo mechanism for leptoquarks". In: *Journal of High Energy Physics* 2018.11 (Nov. 13, 2018), p. 81. ISSN: 1029-8479. DOI: 10.1007/JHEP11(2018)081. URL: https://doi.org/10.1007/JHEP11(2018)081.

[180] Michael J. Baker et al. "High-$$p_T$$signatures in vector–leptoquark models". In: *The European Physical Journal C* 79.4 (2019), p. 334. ISSN: 1434-6052. DOI: 10.1140/epjc/s10052-019-6853-x.

[181] Lisa Michaels and Felix Yu. "Probing new $U(1)$ gauge symmetries via exotic $Z \to Z'\gamma$ decays". In: *JHEP* 03 (2021), p. 120. DOI: 10.1007/JHEP03(2021)120. arXiv: 2010.00021 [hep-ph].

[182] P. S. Bhupal Dev et al. "Searching for Z′ bosons at the P2 experiment". In: *JHEP* 06 (2021), p. 039. DOI: 10.1007/JHEP06(2021)039. arXiv: 2103.09067 [hep-ph].

[183] Bhaskar Dutta et al. "Explaining $g_\mu - 2$ and $R_{K^{(*)}}$ using the light mediators of $U(1)_{T3R}$". In: *Physical Review D* 105.1 (Jan. 2022), p. 015011. DOI: 10.1103/PhysRevD.105.015011.

[184] Bhaskar Dutta, Sumit Ghosh, and Jason Kumar. "Sub-GeV dark matter model". In: *Physical Review D* 100.7 (Oct. 2019), p. 075028. DOI: 10.1103/PhysRevD.100.075028.

[185] Bhaskar Dutta, Sumit Ghosh, and Jason Kumar. "Contributions to $\acute{}N_{\text{eff}}$ from the dark photon of $U(1)_{T3R}$". In: *Physical Review D* 102.1 (July 2020), p. 015013. DOI: 10.1103/PhysRevD.102.015013.

[186] Bhaskar Dutta, Sumit Ghosh, and Jason Kumar. "$U(1)_{T3R}$ Extension of Standard Model: A Sub-GeV Dark Matter Model". In: *Snowmass 2021*. Mar. 2022. arXiv: 2203.07786 [hep-ph].

[187] Bhaskar Dutta, Sumit Ghosh, and Jason Kumar. "Opportunities for probing $U(1)_{T3R}$ with light mediators". In: *Physical Review D* 102.7 (Oct. 2020), p. 075041. DOI: 10.1103/PhysRevD.102.075041.

[188] Valentina De Romeri et al. "Dark matter in the scotogenic model with spontaneous lepton number violation". In: *Phys. Rev. D* 107 (9 2023), p. 095019. DOI: 10.1103/PhysRevD.107.095019.

[189] Bhaskar Dutta et al. "Probing an MeV-scale scalar boson in association with a TeV-Scale top-quark partner at the LHC". In: *Journal of High Energy Physics* 2023.3 (Mar. 2023), p. 164. ISSN: 1029-8479. DOI: 10.1007/JHEP03(2023)164.

[190] Z.G. Berezhiani. "The weak mixing angles in gauge models with horizontal symmetry — A new approach to quark and lepton masses". In: *Physics Letters B* 129.1 (1983), pp. 99–102. ISSN: 0370-2693. DOI: 10.1016/0370-2693(83)90737-2.

[191] Darwin Chang and Rabindra N. Mohapatra. "Small and calculable Dirac neutrino mass". In: *Phys. Rev. Lett.* 58 (16 1987), pp. 1600–1603. DOI: 10.1103/PhysRevLett.58.1600.

[192] Aharon Davidson and Kameshwar C. Wali. "Universal seesaw mechanism?" In: *Phys. Rev. Lett.* 59 (4 1987), pp. 393–395. DOI: 10.1103/PhysRevLett.59.393.

[193] S. Rajpoot. "See-Saw Masses for quarks and leptons in an ambidextrous electroweak interaction model". In: *Modern Physics Letters A* 02.05 (1987), pp. 307–315. DOI: 10.1142/S0217732387000422.

[194] K. S. Babu and Rabindra N. Mohapatra. "CP violation in seesaw models of quark masses". In: *Phys. Rev. Lett.* 62 (10 1989), pp. 1079–1082. DOI: 10.1103/PhysRevLett.62.1079.

[195] K. S. Babu and Rabindra N. Mohapatra. "Solution to the strong CP problem without an axion". In: *Phys. Rev. D* 41 (4 1990), pp. 1286–1291. DOI: 10.1103/PhysRevD.41.1286.

[196] Akanksha Bhardwaj et al. "Roadmap to explore vectorlike quarks decaying to a new scalar or pseudoscalar". In: *Physical Review D* 106.9 (Nov. 2022). ISSN: 2470-0029. DOI: 10.1103/physrevd.106.095014.

[197] Akanksha Bhardwaj et al. "Discovery prospects of a vectorlike top partner decaying to a singlet boson". In: *Physical Review D* 106.7 (Oct. 2022). ISSN: 2470-0029. DOI: 10.1103/physrevd.106.075024.

[198] Jai Bardhan et al. "Machine learning-enhanced search for a vectorlike singlet B quark decaying to a singlet scalar or pseudoscalar". In: *Physical Review D* 107.11 (June 2023). ISSN: 2470-0029. DOI: 10.1103/physrevd.107.115001.

[199] Shankha Banerjee et al. "Implications of a high-mass diphoton resonance for heavy quark searches". In: *Journal of High Energy Physics* 2016.11 (Nov. 2016). ISSN: 1029-8479. DOI: 10.1007/jhep11(2016)154.

[200] João M. Alves et al. "Vector-like singlet quarks: A roadmap". In: *Physics Reports* 1057 (Mar. 2024), 1–69. ISSN: 0370-1573. DOI: 10.1016/j.physrep.2023.12.004.

[201] X. Ai et al. "Probing highly collimated photon-jets with deep learning". In: *JPCS* 2438.1 (2023), p. 012114. DOI: 10.1088/1742-6596/2438/1/012114.

[202] ATLAS Collaboration. "Search for the standard model Higgs boson produced in association with top quarks and decaying into a $b\bar{b}$ pair in pp collisions at $\sqrt{s} = 13$ TeV with the ATLAS detector". In: *Phys. Rev. D* 97.7 (2018), p. 072016. DOI: 10.1103/PhysRevD.97.072016. arXiv: 1712.08895 [hep-ex].

[203] A. Biswas et al. "Collider signature of U_1 leptoquark and constraints from $b \to c$ observables". In: *J. Phys. G* 47.4 (2020), p. 045005. DOI: 10.1088/1361-6471/ab6948. arXiv: 1808.04169 [hep-ph].

[204] Y. L. Chung, S. C. Hsu, and B. Nachman. "Disentangling boosted Higgs boson production modes with machine learning". In: *JINST* 16 (2021), P07002. DOI: 10.1088/1748-0221/16/07/P07002. arXiv: 2009.05930 [hep-ph].

[205] J. Feng et al. "Improving heavy Dirac neutrino prospects at future hadron colliders using machine learning". In: *JHEP* 2022.9 (2022). DOI: 10.1007/jhep09(2022)141.

[206] D. Barbosa et al. "Probing a Z' with non-universal fermion couplings through top quark fusion, decays to bottom quarks, and machine learning techniques". In: *EPJC* 83.413 (2023). DOI: 10.1140/epjc/s10052-023-11506-x.

[207] S. Chigusa et al. "Deeply learned preselection of Higgs dijet decays at future lepton colliders". In: *Phys. Lett. B* 833 (2022), p. 137301. DOI: 10.1016/j.physletb.2022.137301. arXiv: 2202.02534 [hep-ph].

[208] Ernesto Arganda et al. “LHC study of third-generation scalar leptoquarks with machine-learned likelihoods”. In: *Phys. Rev. D* 109 (5 2024), p. 055032. DOI: 10.1103/PhysRevD.109.055032.

[209] S. Ajmal et al. “Searching for exclusive leptoquarks with the Nambu-Jona-Lasinio composite model at the LHC and HL-LHC”. In: *Journal of High Energy Physics* 2024.8 (Aug. 2024). ISSN: 1029-8479. DOI: 10.1007/jhep08(2024)176.

[210] Bhaskar Dutta et al. “Probing compressed bottom squarks with boosted jets and shape analysis”. In: *Physical Review D* 92.9 (Nov. 2015). ISSN: 1550-2368. DOI: 10.1103/physrevd.92.095009.

[211] CMS Collaboration. *Review of searches for vector-like quarks, vector-like leptons, and heavy neutral leptons in proton-proton collisions at $\sqrt{s} = 13$ TeV at the CMS experiment*. 2024. arXiv: 2405.17605 [hep-ex].

[212] CMS Collaboration. *Search for production of a single vector-like quark decaying to tH or tZ in the all-hadronic final state in pp collisions at $\sqrt{s} = 13$ TeV*. 2024. arXiv: 2405.05071 [hep-ex].

[213] Georges Aad et al. “Search for single production of a vectorlike T quark decaying into a Higgs boson and top quark with fully hadronic final states using the ATLAS detector”. In: *Phys. Rev. D* 105.9 (2022), p. 092012. DOI: 10.1103/PhysRevD.105.092012. arXiv: 2201.07045 [hep-ex].

[214] Georges Aad et al. “Search for singly produced vectorlike top partners in multilepton final states with 139 fb-1 of pp collision data at s=13 TeV with the ATLAS detector”. In: *Phys. Rev. D* 109.11 (2024), p. 112012. DOI: 10.1103/PhysRevD.109.112012. arXiv: 2307.07584 [hep-ex].

[215] Georges Aad et al. “Search for pair-production of vector-like quarks in pp collision events at s=13 TeV with at least one leptonically decaying Z boson and a third-generation quark with the ATLAS detector”. In: *Phys. Lett. B* 843 (2023), p. 138019. DOI: 10.1016/j.physletb.2023.138019. arXiv: 2210.15413 [hep-ex].

[216] Georges Aad et al. “Search for pair-produced vector-like top and bottom partners in events with large missing transverse momentum in pp collisions with the ATLAS detector”. In: *Eur. Phys. J. C* 83.8 (2023), p. 719. DOI: 10.1140/epjc/s10052-023-11790-7. arXiv: 2212.05263 [hep-ex].

[217] Georges Aad et al. “Search for single production of vector-like T quarks decaying into Ht or Zt in pp collisions at $\sqrt{s} = 13$ TeV with the ATLAS detector”. In: *JHEP* 08 (2023), p. 153. DOI: 10.1007/JHEP08(2023)153. arXiv: 2305.03401 [hep-ex].

[218] Georges Aad et al. *Exploration at the high-energy frontier: ATLAS Run 2 searches investigating the exotic jungle beyond the Standard Model*. Mar. 2024. arXiv: 2403.09292 [hep-ex].

[219] Giacomo Cacciapaglia et al. "Exotic decays of top partners: mind the search gap". In: *Phys. Lett. B* 798 (2019), p. 135015. DOI: 10.1016/j.physletb.2019.135015. arXiv: 1908.07524 [hep-ph].

[220] A. C. Canbay and O. Cakir. "Investigating the single production of vectorlike quarks decaying into a top quark and *W* boson through hadronic channels at the HL-LHC". In: *Phys. Rev. D* 108 (9 2023), p. 095006. DOI: 10.1103/PhysRevD.108.095006.

[221] Giacomo Cacciapaglia, Aldo Deandrea, and Shahram Vatani. "Is the muon a third family lepton?" In: *Physical Review D* 108.1 (July 2023). ISSN: 2470-0029. DOI: 10.1103/physrevd.108.016010.

[222] Joel Jones-Perez. "RGE behaviour of $U(2)^3$ symmetry in SUSY". In: *J. Phys. Conf. Ser.* 447 (2013). Ed. by Gustavo C. Branco et al., p. 012060. DOI: 10.1088/1742-6596/447/1/012060. arXiv: 1302.6133 [hep-ph].

[223] L. Calibbi et al. "SU(3) Flavour Symmetries and CP Violation". In: *PoS* EPS-HEP2009 (2009), p. 167. DOI: 10.22323/1.084.0167. arXiv: 0909.2501 [hep-ph].

[224] Matteo Cacciari, Gavin P Salam, and Gregory Soyez. "The anti-ktjet clustering algorithm". In: *Journal of High Energy Physics* 2008.04 (Apr. 2008), 063–063. ISSN: 1029-8479. DOI: 10.1088/1126-6708/2008/04/063.

[225] Matteo Cacciari, Gavin P. Salam, and Gregory Soyez. "FastJet user manual: (for version 3.0.2)". In: *The European Physical Journal C* 72.3 (Mar. 2012). ISSN: 1434-6052. DOI: 10.1140/epjc/s10052-012-1896-2.

[226] Albert M Sirunyan et al. "Identification of heavy, energetic, hadronically decaying particles using machine-learning techniques". In: *JINST* 15.06 (2020), P06005. DOI: 10.1088/1748-0221/15/06/P06005. arXiv: 2004.08262 [hep-ex].

[227] Morad Aaboud et al. "Performance of top-quark and *W*-boson tagging with ATLAS in Run 2 of the LHC". In: *Eur. Phys. J. C* 79.5 (2019), p. 375. DOI: 10.1140/epjc/s10052-019-6847-8. arXiv: 1808.07858 [hep-ex].

[228] A.M. Sirunyan et al. "Identification of heavy-flavour jets with the CMS detector in pp collisions at 13 TeV". In: *JINST* 13 (2018), P05011. DOI: 10.1088/1748-0221/13/05/P05011. arXiv: 1712.07158 [hep-ex].

[229] Eric Conte, Benjamin Fuks, and Guillaume Serret. "MadAnalysis 5, a user-friendly framework for collider phenomenology". In: *Computer Physics Communications* 184.1 (2013), pp. 222–256. ISSN: 0010-4655. DOI: 10.1016/j.cpc.2012.09.009.

[230] Adam Paszke et al. *PyTorch: An Imperative Style, High-Performance Deep Learning Library*. 2019. arXiv: 1912.01703 [cs.LG].

[231] A. Flórez et al. “Probing axionlike particles with $\gamma\gamma$ final states from vector boson fusion processes at the LHC”. In: *Phys. Rev. D* 103.9 (2021), p. 095001. DOI: 10.1103/PhysRevD.103.095001. arXiv: 2101.11119 [hep-ph].

[232] A. Flórez et al. “Anapole dark matter via vector boson fusion processes at the LHC”. In: *Phys. Rev. D* 100.1 (2019), p. 016017. DOI: 10.1103/PhysRevD.100.016017. arXiv: 1902.01488 [hep-ph].

[233] A. Flórez et al. “Probing heavy spin-2 bosons with $\gamma\gamma$ final states from vector boson fusion processes at the LHC”. In: *Phys. Rev. D* 99.3 (2019), p. 035034. DOI: 10.1103/PhysRevD.99.035034. arXiv: 1812.06824 [hep-ph].

[234] A. Flórez et al. “Expanding the reach of heavy neutrino searches at the LHC”. In: *Phys. Lett. B* 778 (2018), pp. 94–100. DOI: 10.1016/j.physletb.2018.01.009. arXiv: 1708.03007 [hep-ph].

[235] A. Flórez et al. “Searching for new heavy neutral gauge bosons using vector boson fusion processes at the LHC”. In: *Phys. Lett. B* 767 (2017), pp. 126–132. DOI: 10.1016/j.physletb.2017.01.062. arXiv: 1609.09765v2 [hep-ph].

[236] A. Flórez et al. “Probing the stau-neutralino coannihilation region at the LHC with a soft tau lepton and a jet from initial state radiation”. In: *Phys. Rev. D* 94.7 (2016), p. 073007. DOI: 10.1103/PhysRevD.94.073007. arXiv: 1606.08878 [hep-ph].

[237] R. Leonardi et al. “Phenomenology at the LHC of composite particles from strongly interacting Standard Model fermions via four-fermion operators of NJL type”. In: *The European Physical Journal C* 80.4 (Apr. 2020). ISSN: 1434-6052. DOI: 10.1140/epjc/s10052-020-7822-0.

[238] Cardona Natalia et al. *Long-term LHC Discovery Reach for Compressed Higgsino-like Models using VBF Processes*. 2021. arXiv: 2102.10194 [hep-ph].

[239] Andrés Flórez et al. “Probing axionlike particles with $\gamma\gamma$ final states from vector boson fusion processes at the LHC”. In: *Phys. Rev. D* 103 (9 2021), p. 095001. DOI: 10.1103/PhysRevD.103.095001.

[240] J. C. Pati and A. Salam. “Lepton number as the fourth color”. In: *Phys. Rev. D* 10 (1974). [Erratum: Phys.Rev.D 11, 703-703 (1975)], pp. 275–289. DOI: 10.1103/PhysRevD.10.275.

[241] B. Gripaios, M. Nardecchia, and S. A. Renner. “Composite leptoquarks and anomalies in B-meson decays”. In: *JHEP* 05 (2015), p. 006. DOI: 10.1007/JHEP05(2015)006. arXiv: 1412.1791 [hep-ph].

[242] S. Fajfer and N. Košnik. “Vector leptoquark resolution of R_K and $R_{D^{(*)}}$ puzzles”. In: *Phys. Lett. B* 755 (2016), pp. 270–274. DOI: 10.1016/j.physletb.2016.02.018. arXiv: 1511.06024 [hep-ph].

[243] D. Bečirević et al. “Palatable leptoquark scenarios for lepton flavor violation in exclusive $b \to s\ell_1\ell_2$ modes”. In: *JHEP* 11 (2016), p. 035. DOI: 10.1007/JHEP11(2016)035. arXiv: 1608.07583 [hep-ph].

[244] G. D’Amico et al. “Flavour anomalies after the R_{K^*} measurement”. In: *JHEP* 09 (2017), p. 010. DOI: 10.1007/JHEP09(2017)010. arXiv: 1704.05438 [hep-ph].

[245] G. Hiller and I. Nisandzic. “R_K and R_{K^*} beyond the standard model”. In: *Phys. Rev. D* 96.3 (2017), p. 035003. DOI: 10.1103/PhysRevD.96.035003. arXiv: 1704.05444 [hep-ph].

[246] D. Bečirević et al. “Scalar leptoquarks from grand unified theories to accommodate the B-physics anomalies”. In: *Phys. Rev. D* 98.5 (2018), p. 055003. DOI: 10.1103/PhysRevD.98.055003. arXiv: 1806.05689 [hep-ph].

[247] Geneviève Belanger et al. “Leptoquark manoeuvres in the dark: a simultaneous solution of the dark matter problem and the $R_{D^{(*)}}$ anomalies”. In: *JHEP* 02 (2022), p. 042. DOI: 10.1007/JHEP02(2022)042. arXiv: 2111.08027 [hep-ph].

[248] J. Aebischer et al. “Confronting the vector leptoquark hypothesis with new low- and high-energy data”. In: *The European Physical Journal C* 83.2 (Feb. 16, 2023), p. 153. ISSN: 1434-6052. DOI: 10.1140/epjc/s10052-023-11304-5.

[249] H. Georgi and S. L. Glashow. “Unity of all elementary particle forces”. In: *Phys. Rev. Lett.* 32 (1974), pp. 438–441. DOI: 10.1103/PhysRevLett.32.438.

[250] B. Schrempp and F. Schrempp. “Light leptoquarks”. In: *Phys. Lett. B* 153 (1985), pp. 101–107. DOI: 10.1016/0370-2693(85)91450-9.

[251] M. Leurer. “A comprehensive study of leptoquark bounds”. In: *Phys. Rev. D* 49 (1994), pp. 333–342. DOI: 10.1103/PhysRevD.49.333. arXiv: hep-ph/9309266.

[252] S. Davidson, D. C. Bailey, and B. A. Campbell. “Model independent constraints on leptoquarks from rare processes”. In: *Z. Phys. C* 61 (1994), pp. 613–644. DOI: 10.1007/BF01552629. arXiv: hep-ph/9309310.

[253] M. Leurer. “Bounds on vector leptoquarks”. In: *Phys. Rev. D* 50 (1994), pp. 536–541. DOI: 10.1103/PhysRevD.50.536. arXiv: hep-ph/9312341.

[254] J. L. Hewett and T. G. Rizzo. “Much ado about leptoquarks: A comprehensive analysis”. In: *Phys. Rev. D* 56 (1997), pp. 5709–5724. DOI: 10.1103/PhysRevD.56.5709. arXiv: hep-ph/9703337.

[255] F. S. Queiroz, K. Sinha, and A. Strumia. “Leptoquarks, Dark Matter, and Anomalous LHC Events”. In: *Phys. Rev. D* 91.3 (2015), p. 035006. DOI: 10.1103/PhysRevD.91.035006. arXiv: 1409.6301 [hep-ph].

[256] B. Diaz, M. Schmaltz, and Y. Zhong. "The leptoquark Hunter's guide: Pair production". In: *JHEP* 10 (2017), p. 097. DOI: 10.1007/JHEP10(2017)097. arXiv: 1706.05033 [hep-ph].

[257] I. Doršner and A. Greljo. "Leptoquark toolbox for precision collider studies". In: *JHEP* 05 (2018), p. 126. DOI: 10.1007/JHEP05(2018)126. arXiv: 1801.07641 [hep-ph].

[258] N Vignaroli. "Seeking leptoquarks in the $t\bar{t}$ plus missing energy channel at the high-luminosity LHC". In: *Phys. Rev. D* 99 (3 2019), p. 035021. DOI: 10.1103/PhysRevD.99.035021. arXiv: 1808.10309 [hep-ph].

[259] M. Schmaltz and Y. Zhong. "The leptoquark Hunter's guide: large coupling". In: *JHEP* 01 (2019), p. 132. DOI: 10.1007/JHEP01(2019)132. arXiv: 1810.10017 [hep-ph].

[260] U. Haisch and G. Polesello. "Resonant third-generation leptoquark signatures at the Large Hadron Collider". In: *JHEP* 05 (2021), p. 057. DOI: 10.1007/JHEP05(2021)057. arXiv: 2012.11474 [hep-ph].

[261] A. Bhaskar et al. "Improving third-generation leptoquark searches with combined signals and boosted top quarks". In: *Phys. Rev. D* 104.7 (2021), p. 075037. DOI: 10.1103/PhysRevD.104.075037. arXiv: 2106.07605 [hep-ph].

[262] J. Bernigaud et al. "LHC signatures of τ-flavoured vector leptoquarks". In: *JHEP* 08 (2022), p. 127. DOI: 10.1007/JHEP08(2022)127. arXiv: 2112.12129 [hep-ph].

[263] R. Leonardi et al. "Phenomenology at the LHC of composite particles from strongly interacting Standard Model fermions via four-fermion operators of NJL type". In: *EPJC* 80.309 (2020). DOI: 10.1140/epjc/s10052-020-7822-0. arXiv: 1810.11420 [hep-ph].

[264] CMS Collaboration. "Search for heavy neutrinos or third-generation leptoquarks in final states with two hadronically decaying τ leptons and two jets in proton-proton collisions at $\sqrt{s} = 13$ TeV". In: *JHEP* 03 (2017), p. 077. DOI: 10.1007/JHEP03(2017)077. arXiv: 1612.01190 [hep-ex].

[265] CMS Collaboration. "Search for third-generation scalar leptoquarks and heavy right-handed neutrinos in final states with two tau leptons and two jets in proton-proton collisions at $\sqrt{s} = 13$ TeV". In: *JHEP* 07 (2017), p. 121. DOI: 10.1007/JHEP07(2017)121. arXiv: 1703.03995 [hep-ex].

[266] CMS Collaboration. "Search for third-generation scalar leptoquarks decaying to a top quark and a τ lepton at $\sqrt{s} = 13$ TeV". In: *Eur. Phys. J. C* 78 (2018), p. 707. DOI: 10.1140/epjc/s10052-018-6143-z. arXiv: 1803.02864 [hep-ex].

[267] CMS Collaboration. "Constraints on models of scalar and vector leptoquarks decaying to a quark and a neutrino at $\sqrt{s} = 13$ TeV". In: *Phys. Rev. D* 98.3 (2018), p. 032005. DOI: 10.1103/PhysRevD.98.032005. arXiv: 1805.10228 [hep-ex].

[268] CMS Collaboration. "Search for a singly produced third-generation scalar leptoquark decaying to a τ lepton and a bottom quark in proton-proton collisions at $\sqrt{s} = 13$ TeV". In: *JHEP* 07 (2018), p. 115. DOI: 10.1007/JHEP07(2018)115. arXiv: 1806.03472 [hep-ex].

[269] CMS Collaboration. "Search for heavy neutrinos and third-generation leptoquarks in hadronic states of two τ leptons and two jets in proton-proton collisions at $\sqrt{s} = 13$ TeV". In: *JHEP* 03 (2019), p. 170. DOI: 10.1007/JHEP03(2019)170. arXiv: 1811.00806 [hep-ex].

[270] CMS Collaboration. "Searches for additional Higgs bosons and for vector leptoquarks in $\tau\tau$ final states in proton-proton collisions at $\sqrt{s} = 13$ TeV". In: (2022). DOI: 10.48550/arXiv.2208.02717. arXiv: 2208.02717 [hep-ex].

[271] CMS Collaboration. "The search for a third-generation leptoquark coupling to a τ lepton and a b quark through single, pair and nonresonant production at $\sqrt{s} = 13$ TeV". In: (2022). URL: https://inspirehep.net/literature/2110188.

[272] ATLAS Collaboration. "Search for a scalar partner of the top quark in the all-hadronic $t\bar{t}$ plus missing transverse momentum final state at $\sqrt{s} = 13$ TeV with the ATLAS detector". In: *Eur. Phys. J. C* 80.8 (2020), p. 737. DOI: 10.1140/epjc/s10052-020-8102-8. arXiv: 2004.14060 [hep-ex].

[273] ATLAS Collaboration. "Search for pair production of third-generation scalar leptoquarks decaying into a top quark and a τ-lepton in pp collisions at $\sqrt{s} = 13$ TeV with the ATLAS detector". In: *JHEP* 06 (2021), p. 179. DOI: 10.1007/JHEP06(2021)179. arXiv: 2101.11582 [hep-ex].

[274] ATLAS Collaboration. "Search for new phenomena in final states with b-jets and missing transverse momentum in $\sqrt{s} = 13$ TeV pp collisions with the ATLAS detector". In: *JHEP* 05 (2021), p. 093. DOI: 10.1007/JHEP05(2021)093. arXiv: 2101.12527 [hep-ex].

[275] ATLAS Collaboration. "Search for new phenomena in pp collisions in final states with tau leptons, b-jets, and missing transverse momentum with the ATLAS detector". In: *Phys. Rev. D* 104.11 (2021), p. 112005. DOI: 10.1103/PhysRevD.104.112005. arXiv: 2108.07665 [hep-ex].

[276] ATLAS Collaboration. "Search for leptoquarks decaying into the $b\tau$ final state in pp collisions at $\sqrt{s} = 13$ TeV with the ATLAS detector". In: (2023). DOI: 10.48550/arXiv.2305.15962. arXiv: 2305.15962 [hep-ex].

[277] ATLAS Collaboration. *Search for pair production of third-generation leptoquarks decaying into a bottom quark and a τ-lepton with the ATLAS detector*. 2023. DOI: 10.48550/arXiv.2303.01294. arXiv: 2303.01294 [hep-ex].

[278] A. Bhaskar et al. "Precise limits on the charge-2/3 U1 vector leptoquark". In: *Phys. Rev. D* 104.3 (2021), p. 035016. DOI: 10.1103/PhysRevD.104.035016. arXiv: 2101.12069 [hep-ph].

[279] U. Haisch, L. Schnell, and S. Schulte. "Drell-Yan production in third-generation gauge vector leptoquark models at NLO+PS in QCD". In: *JHEP* 2023.2 (2023). DOI: 10.1007/jhep02(2023)070.

[280] L. Calibbi, A. Crivellin, and T. Li. "Model of vector leptoquarks in view of the B-physics anomalies". In: *Phys. Rev. D* 98.11 (2018), p. 115002. DOI: 10.1103/PhysRevD.98.115002. arXiv: 1709.00692 [hep-ph].

[281] M. Blanke and A. Crivellin. "B Meson anomalies in a Pati-Salam model within the Randall-Sundrum background". In: *Phys. Rev. Lett.* 121.1 (2018), p. 011801. DOI: 10.1103/PhysRevLett.121.011801. arXiv: 1801.07256 [hep-ph].

[282] S. Iguro et al. "TeV-scale vector leptoquark from Pati-Salam unification with vectorlike families". In: *Phys. Rev. D* 104.7 (2021), p. 075008. DOI: 10.1103/PhysRevD.104.075008. arXiv: 2103.11889 [hep-ph].

[283] M. Fernández-Navarro and S. F. King. "B-anomalies in a twin Pati-Salam theory of flavour including the 2022 LHCb $R_{K^{(*)}}$ analysis". In: *JHEP* 2023.2 (2023). DOI: 10.1007/jhep02(2023)188.

[284] M. Bordone et al. "A three-site gauge model for flavor hierarchies and flavor anomalies". In: *Phys. Lett. B* 779 (2018), pp. 317–323. DOI: 10.1016/j.physletb.2018.02.011. arXiv: 1712.01368 [hep-ph].

[285] M. Bordone et al. "Low-energy signatures of the PS^3 model: from B-physics anomalies to LFV". In: *JHEP* 10 (2018), p. 148. DOI: 10.1007/JHEP10(2018)148. arXiv: 1805.09328 [hep-ph].

[286] Javier Fuentes-Martín et al. "Flavor hierarchies, flavor anomalies, and Higgs mass from a warped extra dimension". In: *Phys. Lett. B* 834 (2022), p. 137382. DOI: 10.1016/j.physletb.2022.137382. arXiv: 2203.01952 [hep-ph].

[287] B. Gripaios. "Composite leptoquarks at the LHC". In: *JHEP* 02 (2010), p. 045. DOI: 10.1007/JHEP02(2010)045. arXiv: 0910.1789 [hep-ph].

[288] R. Barbieri, C. W. Murphy, and F. Senia. "B-decay anomalies in a composite leptoquark model". In: *Eur. Phys. J. C* 77.1 (2017), p. 8. DOI: 10.1140/epjc/s10052-016-4578-7. arXiv: 1611.04930 [hep-ph].

[289] R. Barbieri and A. Tesi. "B-decay anomalies in Pati-Salam SU(4)". In: *Eur. Phys. J. C* 78.3 (2018), p. 193. DOI: 10.1140/epjc/s10052-018-5680-9. arXiv: 1712.06844 [hep-ph].

[290] J. Fuentes-Martín et al. "Vector leptoquarks beyond tree level. III. Vectorlike fermions and flavor-changing transitions". In: *Phys. Rev. D* 102 (11 2020), p. 115015. DOI: 10.1103/PhysRevD.102.115015.

[291] A. Djouadi et al. "Interference effects in $t\bar{t}$ production at the LHC as a window on new physics". In: *JHEP* 03 (2019), p. 119. DOI: 10.1007/JHEP03(2019)119. arXiv: 1901.03417 [hep-ph].

[292] The ROOT team. "ROOT - An Object Oriented Data Analysis Framework". In: *Nucl. Inst. & Meth. in Phys. Res. A* 389 (1997). Proceedings AIHENP'96 Workshop, Lausanne, Sep. 1996. See also "ROOT"[software], Release v6.18/02, and https://root.cern/manual/roofit/, pp. 81–86. DOI: 10.5281/zenodo.3895860.

[293] D. Barbosa et al. "Probing a Z' with non-universal fermion couplings through top quark fusion, decays to bottom quarks, and machine learning techniques". In: *Eur. Phys. J. C* 83.5 (2023), p. 413. DOI: 10.1140/epjc/s10052-023-11506-x. arXiv: 2210.15813 [hep-ph].

[294] B. Dutta et al. "Probing an MeV-Scale Scalar Boson in Association with a TeV-Scale Top-Quark Partner at the LHC". In: *JHEP* 03.164 (2023). DOI: 10.1007/JHEP03%282023%29164. arXiv: 2202.08234 [hep-ph].

[295] R. Arnowitt et al. "Determining the Dark Matter Relic Density in the Minimal Supergravity Stau-Neutralino Coannihilation Region at the Large Hadron Collider". In: *Phys. Rev. Lett.* 100 (2008), p. 231802. DOI: 10.1103/PhysRevLett.100.231802. arXiv: 0802.2968 [hep-ph].

[296] B. Dutta et al. "Supersymmetry Signals of Supercritical String Cosmology at the Large Hadron Collider". In: *Phys. Rev. D* 79 (2009), p. 055002. DOI: 10.1103/PhysRevD.79.055002. arXiv: 0808.1372 [hep-ph].

[297] C. Avila et al. "Connecting Particle Physics and Cosmology: Measuring the Dark Matter Relic Density in Compressed Supersymmetry at the LHC". In: *Physics of the Dark Universe* 27 (2020), p. 100430. DOI: 10.1016/j.dark.2019.100430. arXiv: 1801.03966 [hep-ph].

[298] B. Dutta et al. "Vector Boson Fusion Processes as a Probe of Supersymmetric Electroweak Sectors at the LHC". In: *Phys. Rev. D* 87 (2013), p. 035029. DOI: 10.1103/PhysRevD.87.035029. arXiv: 1210.0964 [hep-ph].

[299] A. Delannoy et al. "Probing Dark Matter at the LHC using Vector Boson Fusion Processes". In: *Phys. Rev. Lett.* 111 (2013), p. 061801. DOI: 10.1103/PhysRevLett.111.061801. arXiv: 1304.7779 [hep-ph].

[300] B. Dutta et al. "Probing Compressed Sleptons at the LHC using Vector Boson Fusion Processes". In: *Phys. Rev. D* 91 (2015), p. 055025. DOI: 10.1103/PhysRevD.91.055025. arXiv: 1411.6043 [hep-ph].

[301] B. Dutta et al. "Probing Compressed Top Squarks at the LHC at 14 TeV". In: *Phys. Rev. D* 90 (2014), p. 095022. DOI: 10.1103/PhysRevD.90.095022. arXiv: 1312.1348 [hep-ph].

[302] B. Dutta et al. "Probing Compressed Bottom Squarks with Boosted Jets and Shape Analysis". In: *Phys. Rev. D* 92 (2015), p. 095009. DOI: 10.1103/PhysRevD.92.095009. arXiv: 1507.01001 [hep-ph].